Université de Toulouse

THÈSE

En vue de l'obtention du

DOCTORAT DE L'UNIVERSITÉ DE TOULOUSE

Délivré par *Institut National Polytechnique de Toulouse*
Discipline ou spécialité : *Hydraulique, Hydrochimie, Sols, Environnement*

Présentée et soutenue par **Khalil ALASTAL**
Le 16 Mai 2012

Titre :

Ecoulements oscillatoires et effets capillaires en milieux poreux partiellement saturés et non saturés : applications en hydrodynamique côtière

---

JURY

John SELKER (Prof.)	Oregon State University, USA
Peter NIELSEN (Prof.)	University of Queensland, Australia
Jérôme BROSSARD (Prof.)	Université du Havre, France
Vincent REY (Prof.)	Université du Sud-Toulon-Var, France
Olivier EIFF (Prof.)	Institut National Polytechnique de Toulouse, France
Rachid ABABOU (dir. thèse)	Institut National Polytechnique de Toulouse, France
Dominique ASTRUC (co-dir. thèse)	Institut National Polytechnique de Toulouse, France

---

Ecole doctorale : *Sciences de l'Univers, de l'Environnement et de l'Espace (SDU2E)*
Unité de recherche : *Institut de Mécanique des Fluides de Toulouse (IMFT)*
Directeur(s) de Thèse : *Rachid ABABOU & Dominique ASTRUC*

Thesis Title

Oscillatory Flows and Capillary Effects in Partially Saturated and Unsaturated Porous Media: Applications to Beach Hydrodynamics

Ecoulements oscillatoires et effets capillaires en milieux poreux partiellement saturés et non saturés : applications en hydrodynamique côtière

Résumé étendu

Dans cette thèse, on étudie les écoulements oscillatoires en milieux poreux (non saturés ou partiellement saturés) dus à des oscillations tidales des niveaux d'eau dans des milieux ouverts adjacents aux milieux poreux. L'étude est centrée sur le cas des plages de sable en hydrodynamique côtière, mais les applications concernent, potentiellement et plus généralement, les problèmes d'oscillation et de variation temporelle des niveaux d'eau dans des systèmes couplés, lorsque ceux-ci mettent en jeu des interactions entre les écoulements de sub-surface (milieux poreux) et les eaux de surface (milieux ouverts) : plages naturelles et artificielles; digues portuaires; barrages en terre; berges de fleuves; estuaires.

Le forçage tidal des écoulements souterrains est représenté et modélisé ici, tant expérimentalement que numériquement, par une oscillation quasi-statique du niveau d'eau dans un réservoir externe ouvert, connecté au domaine poreux. On s'intéresse plus particulièrement aux écoulements verticaux forcés par une pression oscillatoire imposée au bas d'une colonne de sol. Sur le plan expérimental, ce type de forçage est obtenu par une machine à marée équipée d'un arbre rotatif.

Au total, on utilise dans ce travail trois types d'approches (expérimentale, numérique, analytique), l'objectif étant d'étudier le mouvement vertical de la surface "libre" et l'écoulement non saturé sus-jacent, de façon à prendre en compte aussi bien les pertes de charge dans la zone saturée que les gradients de pression capillaire dans la zone non saturée.

D'une part, on met en œuvre des expérimentations sur colonnes de sols en laboratoire. Ces colonnes sont équipées de tensiomètres à céramique poreuse pour mesurer les pressions positives et les succions (entre autres mesures). Les oscillations dans la colonne sont provoquées par une pression oscillatoire positive imposée au bas de la colonne grâce à la machine à marée1.

D'autre part, on met en œuvre une série de simulations numériques d'écoulements oscillatoires à l'aide du code de calcul BIGFLOW 3D, qui résoud l'Equation aux Dérivées Partielles (EDP) de Richards par une méthode de volumes finis implicite (méthode itérative de Picard modifiée pour l'EDP nonlinéaire, et gradients conjugués pour la résolution du système linéarisé). De plus, on développe une méthode de calage optimal des paramètres hydrodynamiques du sol (algorithme génétique). On cale les paramètres pour une fréquence de forçage donnée, puis les simulations ainsi calées sont comparées aux résultats expérimentaux pour d'autres fréquences (non calées).

Enfin, on développe une famille de solutions quasi-analytiques de type "multi-front" pour le problème des oscillations tidales. Celles-ci constituent une extension de l'approche "Green-Ampt"

[1] Une autre expérimentation 2D sur une maquette bi-plaque en section verticale, contenant une plage de sable inclinée, a été récemment construite et instrumentée (recherche collaborative en cours).

des écoulements piston. On obtient des systèmes d'Equations Différentielles Ordinaires (EDO), non linéaires et non autonomes, à conditions initiales (systèmes dynamiques). Les solutions de ces systèmes multi-front sont testées et comparées aux solutions volumes finis de l'équation de Richards sur maille fine. Les solutions multi-front s'avèrent cent fois plus rapides à calculer, et leur accord avec l'EDP de Richards est excellent même pour un sol limoneux à fort effet capillaire (le nombre de fronts requis reste modéré, N≈10 à 20 au plus). La méthode multi-front est alors utilisée pour générer un grand nombre de simulations oscillatoires, afin d'analyser les fluctuations de flux et niveau d'eau dans le système poreux pour une large gamme de fréquences de forçages. Les résultats, exprimés en termes de moyennes et d'amplitudes des variables hydrodynamiques, font apparaître une fréquence caractéristique, qui dépend des propriétés hydrodynamiques du milieu poreux, et qui sépare les régimes d'écoulement "haute fréquence" / "basse fréquence" dans le poreux.

Mots-Clés : Milieux poreux; non saturés; partiellement saturés; loi de Darcy; équation de Richards; effets capillaires; oscillations tidales; hydrodynamique côtière; plages; eaux souterraines; Green-Ampt; multi-front; surface libre; machine à marée; tensiomètre; succion; problème inverse; algorithme génétique; réponse fréquentielle.

Oscillatory Flows and Capillary Effects in Partially Saturated and Unsaturated Porous Media: Applications to Beach Hydrodynamics

Abstract

In this thesis, we study hydrodynamic oscillations in porous bodies (unsaturated or partially saturated), due to tidal oscillations of water levels in adjacent open water bodies. The focus is on beach hydrodynamics, but potential applications concern, more generally, time varying and oscillating water levels in coupled systems involving subsurface / open water interactions (natural and artificial beaches, harbor dykes, earth dams, river banks, estuaries). The tidal forcing of groundwater is represented and modeled (both experimentally and numerically) by quasi-static oscillations of water levels in an open water reservoir connected to the porous medium. Specifically, we focus on vertical water movements forced by an oscillating pressure imposed at the bottom of a soil column. Experimentally, a rotating tide machine is used to achieve this forcing. Overall, we use three types of methods (experimental, numerical, analytical) to study the vertical motion of the groundwater table and the unsaturated flow above it, taking into account the vertical head drop in the saturated zone as well as capillary pressure gradients in the unsaturated zone. Laboratory experiments are conducted on vertical sand columns, with a tide machine to force water table oscillations, and with porous cup tensiometers to measure both positive pressures and suctions along the column (among other measurement methods)[2]. Numerical simulations of oscillatory water flow are implemented with the BIGFLOW 3D code (implicit finite volumes, with conjugate gradients for the matrix solver and modified Picard iterations for the nonlinear problem). In addition, an automatic calibration based on a genetic optimization algorithm is implemented for a given tidal frequency, to obtain the hydrodynamic parameters of the experimental soil. Calibrated simulations are then compared to experimental results for other non calibrated frequencies. Finally, a family of quasi-analytical multi-front solutions is developed for the tidal oscillation problem, as an extension of the Green-Ampt piston flow approximation, leading to nonlinear, non-autonomous systems of Ordinary Differential Equations with initial conditions (dynamical systems). The multi-front solutions are tested by comparing them with a refined finite volume solution of the Richards equation. Multi-front solutions are at least 100 times faster, and the match is quite good even for a loamy soil with strong capillary effects (the number of fronts required is small, no more than $N \approx 10$ to 20 at most). A large set of multi-front simulations is then produced in order to analyze water table and flux fluctuations for a broad range of forcing frequencies. The results, analyzed in terms of means and amplitudes of hydrodynamic variables, indicate the existence, for each soil, of a characteristic frequency separating low frequency / high frequency flow regimes in the porous system.

Key Words. Porous media; Unsaturated; Partially saturated; Darcy's law; Richards equation; Capillary effects; Tidal oscillations; Beach hydrodynamics; Groundwater; Green-Ampt; Multi-front; Water table; Tide machine; Tensiometer; Suction; Inverse problem; Genetic Algorithm; Frequency response.

---

[2] Another experiment involving a 2D slab of soil with a sloping sand beach has been recently constructed and instrumented (ongoing collaborative work).

Dedication

I dedicate this thesis to my beloved father

who passed away in April 2011…

Acknowledgements

First of all, I thank ALLAH, the almighty, for giving me the strength and courage to accomplish the different tasks of my PhD thesis and for blessing me with many great people who have been my greatest support in both my personal and professional life.

I am extremely indebted to my advisor Prof. Rachid Ababou for his academic, morale and social support and guidance throughout the thesis work. Really I appreciate his advice, guidance, instruction, understanding, patience, support and time. My special thanks go to Mr. Dominique Astruc, to be my co-supervisor and to support me with their meaningful discussions, invaluable advices and rich ideas.

My thanks also go to the members of my PhD committee, Professors John Selker (Oregon State University, USA), Peter Nielsen (University of Queensland, Australia) and Jérôme Brossard (Université du Havre, France) for reading previous drafts of this dissertation and providing many valuable comments and suggestions that improved its presentation and contents. I would like to thank also the other members of my PhD committee, Professors Vincent Rey (Université du Sud Toulon-Var, France) and Olivier Eiff (Institut National Polytechnique de Toulouse, France) for their helpful advice and suggestions.

Special thanks deserve the persons from different technical services and research groups at the IMFT. Without their support it would be impossible for me to complete the experimental part of my research. In particular, I appreciate the indisputable support that I received from the mechanical design service and also from Signals and Images service. I would like to thank Jean-Marc Sfedj, Sebastien Cazin and Hervé Ayroles for their immense help and support whenever it was needed. I also appreciate the support I received from the technical staff of my two research groups (GEMP and OTE). My keen appreciation goes to Ruddy Soeparno and Serge Font for their valuable technical assistance.

A special acknowledgement is necessary for the administrative staff for their continuous effort. I owe my deepest gratitude to Suzy Bernard, Sylvie Senny and Celine Perles.

I would like to thank all my present and former colleagues at IMFT for making the inspiring atmosphere at the institute. I would also express special thanks to David Bailly, Yunli Wang, Hassan Fatmi, Nahla Mansouri and Bastien Caplain for their social attitude and friendship.

I would like to acknowledge the Consulate General of France in Jerusalem for my PhD study grant. I would like to thank also the personnel at the CROUS Toulouse, special thanks to Mr. Pierre Dedieu and Mrs Stéphanie Desco for their support and help.

I would like to express my heartfelt gratitude to my parents, brothers and sister, for their endless encouragement and well wishes. Father, today I got my PhD degree, fulfilling your wish before your sudden departure the last year. Although I cannot directly address to you anymore, deeply in my mind I always acknowledge and remember you.

Last, but not least, I would like to thank my wife for her continuous understanding and love. Her support and encouragement were in the end what made this thesis possible. I don’t forget my children who have always understood my absence and at the end gave me a lot of smiles and love.

Table of Contents

List of Figures

List of Tables

Introduction (en français)

1. Nature et contenu de l'étude

Les interactions entre écoulements superficiels et souterrains concernent un large éventail d'applications. Ces interactions se produisent dans les milieux aquatiques d'eau douce et d'eau salée, en milieux naturels et artificiels. On les rencontre par exemple dans les plages, les berges de fleuves, les digues poreuses et les barrages en terre et enrochements (**Fig. F.1**).

Les fluctuations dans les eaux de surfaces affectent les eaux souterraines auxquelles elles sont connectées. Les fluctuations temporelles qui se produisent dans les eaux de surface peuvent être d'origine naturelle ou anthropique : précipitations, crues, oscillations tidales (marées), ondes de surface, lâchers de barrages, etc. (Boutt, 2010).

Dans cette thèse, on s'intéresse à l'hydrodynamique souterraine des plages en zone côtière. Il est reconnu que les écoulements souterrains en zone côtière influencent le transport de sédiments et les processus morphologiques (érosion et dépôt) notamment dans la zone de jet de rive (Baird and Horn, 1996, Jeng et al., 2005b).[3] Les eaux souterraines côtières contrôlent aussi les conditions biologiques, le cycle des nutriments, et les transferts de contaminants au voisinage de la surface libre de la nappe côtière (Chen and Pinder, 2011, Hinz, 1998). Enfin, les écoulements souterrains affectent la stabilité des structures bâties sur des sols sableux près des plages (Nielsen, 1990).

[3] La zone de jet de rive est communément dénommée zone de "swash" en hydrodynamique côtière.

Fig. F.1: Photographies illustrant les couplages entre écoulements superficiels et souterrains en hydrologie et en hydrodynamique côtière. En haut à gauche: cas d'une plage de sable dont la nappe est couplée aux fluctuations du niveau de la mer. En haut à droite: cas d'une rive ou d'un îlot de sable et galets en milieu fluvial. En bas à gauche: cas d'un barrage en terre et enrochements, avec son lac-réservoir dont le niveau peut fluctuer. En bas à droite: cas d'une île de sable artificielle, "Palm beach", construite récemment à Dubaï.

En hydrodynamique côtière (plages) on peut distinguer deux types de "forçages" oscillatoires :

- les phénomènes basse fréquence ou ondes longues, de type "tidal" : cette catégorie désigne ici les ondes de marée de période 12h ou 24h, ou encore, d'autre phénomènes basse fréquence mais de périodes parfois plus courte (*seiches*), ou au contraire, les fluctuations non stationnaires de plus longue période (marées d'équinoxes, etc.);
- les phénomènes haute fréquence ou ondes courtes : cette catégorie désigne ici les ondes complexes et déferlantes, les processus de flux et reflux dans la zone de jet de rive (zone de *swash*), ainsi que les processus d'érosion (transports solides) qui accompagnent ces phénomènes en bord de plage dans la zone de *swash*.

Dans cette thèse, on se concentre sur les oscillations "tidales" au sens défini plus haut.

Plus précisément, on s'intéresse aux écoulements oscillatoires à l'intérieur d'un milieu poreux partiellement saturé / non saturé (plage) sous l'action d'oscillations tidales du niveau d'eau dans un milieu ouvert environnant (océan, mer, lac, estuaire), lequel est connecté au massif poreux. Dans ce travail, le forçage tidal des eaux souterraines sera représenté, ou idéalisé, par des oscillations quasi-statiques du niveau d'eau dans un réservoir de pleine eau connecté au domaine poreux (*ceci sera précisé par la suite*).

2. Objectifs et méthodologie

L'objectif général de cette thèse est d'améliorer la compréhension des phénomènes d'écoulements oscillatoires ou rapidement variés en milieux poreux partiellement saturés et/ou non saturés (plages de sable, digues portuaires, barrages en terre, berges fluviales, estuaires, etc.).

Plus particulièrement, le but de cette thèse est d'étudier les interactions entre eaux souterraines et eaux de surface, en prenant en compte tant la zone saturée que la zone non saturée, et donc, en incluant dans l'étude non seulement la surface libre de la nappe mais aussi la zone capillaire sus-jacente. Les résultats attendus concernent la réponse hydrodynamique du milieu poreux (plage) lorsqu'il est soumis à des oscillations périodiques du niveau de la mer (le forçage "tidal" défini plus haut).

Pour atteindre ces objectifs, trois types d'approches sont mises en œuvre :

- I). Expériences de laboratoire sur des colonnes verticales, avec une machine à marée pour générer des oscillations tidales imposées par le bas de la colonne, et en utilisant des tensiomètres pour mesurer aussi bien les pressions positives dans la zone saturée que les succions dans la zone non saturée (entre autres méthodes).[4]
- II) Simulations numériques des écoulements oscillatoires en milieux poreux partiellement saturés / non saturés au comportement hydrodynamique fortement

[4] Une autre expérimentation sur une maquette bi-plaque 2D, avec sable de plage inclinée, a été récemment construite et instrumentée (recherche collaborative en cours).

non linéaire. La méthode numérique est celle implémentée dans le code BIGFLOW (volumes finis 3D implicite, avec une méthode itérative point fixe ou Picard pour le problème non linéaire). De plus, une méthode de calage automatique a été implémentée afin d'optimiser les paramètres hydrodynamiques du sol expérimental (algorithme génétique).[5]

- III) Développement et mise en œuvre de solutions quasi-analytiques pour le calcul des écoulements oscillatoires dans une colonne de sol partiellement saturée / non saturée. Ceci inclut en particulier une nouvelle approche multi-front, basée sur une série de généralisations de l'approche de Green et Ampt des écoulements piston, et conduisant à des systèmes d'Equations Différentielles Ordinaires non linéaires et non autonomes, qui permettent d'obtenir rapidement les solutions de l'équation de Richards en présence de forçages temporels oscillatoires et fortement variables.

3. Plan de la thèse

Cette thèse est composée de neuf chapitres comme suit.

- **Le Chapitre 1** (ce chapitre introductif) présente une vue d'ensemble du travail, ses objectifs, les méthodes utilisées, et le plan du mémoire de thèse.
- **Le Chapitre 2** présente une revue de la littérature sur l'hydrodynamique souterraine des plages de sable en réponse aux fluctuations d'origine tidale.
- **Le Chapitre 3** introduit les concepts de base et les équations régissant les écoulements en milieux poreux non saturés, ou partiellement saturés: équations de Darcy, de conservation de masse, et de Richards. Les relations constitutives ($\theta(h)$, $K(h)$) requises pour résoudre l'équation de Richards sont également analysées (paramétrisation): à partir du modèle de van Genuchten / Mualem, une étude paramétrique est effectuée, et une interprétation physique des paramètres est

[5] De plus, le code de calcul BIGFLOW a été amélioré de la façon suivante au cours de ce travail : on a implémenté et testé le cas de conditions limites temporellement variables (signaux de pression); on a amélioré et automatisé les visualisations spatio-temporelles des champs de pression et de teneur en eau; et l'on a conçu une nouvelle interface MATLAB interface à menus déroulants, comme alternative à l'interface Python existante.

développée, en particulier, l'échelle de longueur capillaire (*voir également l'échelle de temps gravitaire dans le chapitre suivant*).

- **Le Chapitre 4** commence par présenter une revue du modèle numérique BIGFLOW, solveur de l'équation de Richards, utilisé dans une partie de cette thèse pour la simulation des écoulements oscillatoires en milieu poreux à saturation variable. Outre les aspects numériques (grille volumes finis 3D, domaine de calcul, conditions limites, fonctions auxiliaires non linéaires) -- les interfaces et processeurs graphiques du code sont aussi présentés. Enfin, on développe des tests de validation et de calage du code en exploitant certains concepts de la théorie de l'infiltration. Ceux-ci permettent, via des expériences numériques, de préciser l'interprétation physique des effets capillaires (sorptivité "S") ainsi que la compétition gravité/capillarité (temps gravitaire "t_{GRAV}").
- **Le Chapitre 5** contient une description détaillée du montage expérimental de la colonne de sol instrumentée (milieu poreux étudié à l'échelle de Darcy) ainsi que du système hydraulique et mécanique appelé "machine à marées". Ce chapitre discute aussi des méthodes de calage des capteurs (particulièrement les tensiomètres), ainsi que le protocole expérimental de remplissage de la colonne de sol. Les propriétés hydrodynamiques du sol de la colonne sont en partie mesurées directement, et en partie calées (sur ce dernier aspect, voir le chapitre 7).
- **Le Chapitre 6** présente les résultats expérimentaux obtenus sur la colonne de sol soumise à des oscillations via la machine à marées. Les résultats sont présentés en termes de signaux de pression interstitielle, pression totale (ou charge hydraulique), et cote de la surface libre de la nappe. On présente aussi les résultats en termes de profils verticaux de pression ou de charge. On étudie les déphasages, atténuations et structures temporelles des différents signaux, pour tout une gamme de paramètres expérimentaux (période tidale, amplitude, niveau d'eau statique). Ces résultats expérimentaux seront étendus à une gamme plus large de paramètres par simulations (cf. Chapitre 7 - analyses étendues en fonction de la fréquence de forçage).

- **Le Chapitre 7** a comme but d'étendre numériquement les résultats expérimentaux, c'est-à-dire, d'examiner les effets du forçage oscillatoire en dehors de la gamme des paramètres expérimentaux (gamme de fréquences, types de sols). On commence par procéder à un calage optimal des paramètres du sol à l'aide d'un algorithme génétique (ceci revient à résoudre un problème inverse pour identifier certains paramètres hydrodynamiques). Pour étudier la performance du calage, on cale les paramètres sur une seule expérience (fréquence ω_1 donnée), puis on tente de reproduire par simulation les résultats d'autres expériences (fréquences ω_2, ω_3, etc.). On présente ensuite une étude paramétrique étendue, visant à analyser la réponse de la nappe à une sollicitation en fréquence. Un des objectifs est de déceler une fréquence caractéristique permettant de distinguer deux régimes hydrodynamiques, haute fréquence et basse fréquence, selon le type de sol.
- **Le Chapitre 8** présente une approche théorique quasi-analytique de type "multi-front", qui permet de modéliser efficacement la réponse hydrodynamique d'une colonne de sol à un forçage fortement variable et/ou oscillatoire (temporel).[6] L'approche multi-front donne une famille de modèles à N fronts, généralisations successives de l'approche "écoulement piston" de Green et Ampt, adaptée au problème des oscillations tidales. Tout d'abord, un modèle à front unique est développé (Green-Ampt "inversé"). Ce modèle à 1 front est ensuite généralisé à 2 fronts puis N fronts. La paramétrisation du modèle est définie en termes des courbes non linéaires de teneur en eau et de conductivité hydraulique du sol ($\theta(h)$, $K(h)$). La performance du modèle multi-front est discutée et testée en utilisant des solutions fines de l'équation de Richards par le code volumes finis BIGFLOW, comme base de comparaison.
- **Le Chapitre 9** contient les conclusions sur les différentes parties du travail (expérimentales, numériques, théoriques), ainsi que les perspectives et recommandations en vue d'extensions futures de ce travail de recherche.

[6] Ce chapitre a été soumis, sous forme d'article, pour publication dans une revue scientifique internationale.

Chapter 1

Introduction

1.1 Nature and extent of the study

Surface/subsurface flow interactions concern a wide range of applications. Such interaction is found in both fresh and salt water environments and also in natural and man-made structures. This interaction encountered for example in beaches, river banks, porous dykes and earth dams (**Fig. 1.1**).

Surface water fluctuations strongly influence adjacent groundwater. Variations in surface water can arise from many natural and anthropogenic sources including precipitation and flood events, tidal oscillation, wave-induced displacement, dam releases, and associated reservoir drawdown (Boutt, 2010).

In this thesis, we are interested in beach groundwater hydrodynamics. Coastal groundwater flow has been recognized to influence the sediment transport and morphological processes like erosion and accretion in the swash zone (Baird and Horn, 1996, Jeng et al., 2005b), and to control the biological conditions, nutrient cycling and contaminant movement near the water table (Chen and Pinder, 2011, Hinz, 1998). Coastal groundwater flow also affects the stability of the structures founded on soils and sands near beaches (Nielsen, 1990).

Fig. 1.1: Photographs illustrating the coupling between surface and subsurface flows in hydrology and coastal hydrodynamics: the top left photograph illustrates the case of a sand beach with groundwater coupled to sea level fluctuations; the top right illustrates the case of a sand/gravel river bank or island; the bottom left shows an earth-fill dam with its reservoir lake shown at left; the bottom right is the artificial sand island "Palm Beach" designed recently in Dubai.

In the context of beach and coastal hydrodynamics, two main types of periodic "forcing" are encountered:

- low frequency / long tidal waves: this category designates slow "tidal" waves with long periods, e.g. 12h or 24h, as well as other phenomena with possibly somewhat shorter periods (such as "*seiches*");
- high frequency / short waves: this item designates complex nonlinear surface waves occurring in coastal areas; they may involve overspill phenomena (breaking waves), and run up/run down processes in the swash zone, as well as erosion processes (solid transport).

In this thesis, we focus on studying the effect of "tidal" oscillations taking place in porous bodies (partially saturated/unsaturated porous media). The tidal forcing of groundwater will be approximated, or idealized, by quasi-static oscillations of water levels in an open water reservoir adjacent to the porous medium.

1.2 Thesis objectives and methodology

The general objective of this thesis is to further advance the current understanding of oscillatory flows in porous bodies (sand beaches, harbor dykes, earth dams, river banks, estuaries, etc.).

More specifically, the aim in this thesis is to study beach groundwater /surface water interactions, taking into account both the saturated and unsaturated zones (including water table and capillary zone) under the effect of tidal forcing. The expected result should be a better understanding of the hydrodynamic response of the porous medium (the beach and its groundwater) when it is submitted to periodic tidal oscillations of sea water levels.

To fulfill the above objectives, three types of approaches are used:

- Laboratory experiments on vertical sand columns, with a tide machine to force the water table oscillations at the bottom of the column, and tensiometers to measure both positive pressures and suctions, among other measurement methods.[7]
- Numerical simulations of oscillatory water flow in partially saturated / unsaturated porous media with strongly non-linear behavior in porous media. The numerical simulation method is implemented in the BIGFLOW code (implicit 3D finite volumes, with fixed point or Picard iterations for the nonlinear problem). In addition, an

[7] Another experiment involving a 2D slab of soil with a sloping sand beach has been recently constructed and instrumented (ongoing collaborative work).

automatic calibration method was implemented to optimize the hydrodynamic parameters of the experimental soil based on a Genetic Algorithm.[8]

- Quasi-analytical solutions of oscillatory flows in a partially saturated/unsaturated porous column. This includes novel multi-front approaches, which generalize the Green-Ampt piston flow approach, leading to nonlinear differential equations.

It is worth noting that most of this thesis manuscript focuses on the effect of oscillations on homogeneous soils. However, other analyses on multilayered media were also presented (see Appendix E)

1.3 Thesis outline

This thesis is composed of nine chapters as follows:

- **Chapter 1** (this chapter) is an introductory chapter which provides an overview of the research study, its objectives, methodology and the outline of the dissertation.
- **Chapter 2** presents a review of the relevant scientific literature on beach groundwater hydrodynamics in response to fluctuations in open water bodies.
- **Chapter 3** introduces the basic definitions and the governing equations used to model variably saturated flow numerically, taking into account both saturated and unsaturated zones. The Darcy equation, mass conservation equation, and the resulting Richards equation (Partial Differential Equation) are presented. The constitutive relationships $[\theta(h), K(h)]$ required to solve the Richards equation are then reviewed. The van Genuchten / Mualem model is introduced; a parametric study is conducted, and a physical interpretation of the model parameters is given (capillary length scale).
- **Chapter 4** provides a review of the numerical code used in this thesis to simulate variably saturated flow in porous media (BIGFLOW). The main code, the pre- and post-processors, the computational domain, and the boundary conditions, are briefly

[8] Furthermore, the numerical code BIGFLOW was enhanced for this study in the following ways: the case of time varying Boundary Conditions was implemented and tested (input pressure signals); the 2D/3D space-time visualizations of water contents and pressure outputs was enhanced and automatized; and a new MATLAB interface was designed as an alternative to the existing Python interface.

discussed. Finally, a validation test for the numerical procedure is proposed and analyzed through the concepts of the infiltration theory; Physical interpretations of the results in terms of hydraulic conductivity, capillary effects, sorptivity and gravitational time scale are also given.

- **Chapter 5** contains a detailed description of the experimental setup of the Darcy-scale soil column and the associated hydro-mechanical system (tide machine). The chapter also discusses the methods used to calibrate the measurement sensors (especially tensiometers), and to fill and pack the sand into the column. The properties of the sand (used in the experiment) obtained from various measurements are presented (see also the calibration section in chapter 7).
- **Chapter 6** presents the experimental results of the oscillatory flow in the porous column / tide machine system. The results are presented in terms of the signals of pore water pressure, total pressure, and water table elevation, together with the profiles of pressure and total head. The attenuation, phase lag, and non harmonic structures of the different signals, are also discussed. Preliminary analyses and interpretations of the experimental results, based on the available range of forcing parameters (tidal period, tidal amplitude, and static level) are conducted. These experimental results are re-analyzed numerically in Chapter 7 below (extended analyses).
- **Chapter 7** extends the experimental study numerically, in order to examine the effect of oscillatory forcing outside the available range of the physical experiment (frequencies, type of soil). We start by implementing an optimal calibration of the numerical model using a Genetic Algorithm (this is equivalent to solving an inverse problem for the hydrodynamic parameters of the soil). Then we provide an extended numerical parametric study of the frequency response of the water table. One of the objectives is to identify a characteristic frequency separating low and high frequency regimes.

- **Chapter 8** provides the details of the semi-analytical multi-front approach developed to model the water table response to periodic forcing in porous columns.[9] The multi-front approach is the result of a series of generalizations of the Green-Ampt piston flow approach. First, a single front model is developed based on an "inverted" version of the classical Green-Ampt infiltration model, with a sharp "wetting front" separating the fully saturated and the totally dry regions. The model is then further extended to two fronts (N=2), and more generally to multi-front ($N \geq 2$). The parametrization of the model is defined in terms of the nonlinear water content and conductivity curves of the soil $[\theta(h), K(h)]$. The performance of the multi-front models is discussed and tested using a refined finite volume solution of the non linear Richards equation (BIGFLOW code) as a basis for comparisons.
- **Chapter 9** comprises the major conclusions for the whole thesis, together with recommendations and perspectives for future research (outlook).

In addition to the above chapters, this thesis includes the following appendices:

- **Appendix A:** deals with the effect of the acceleration (Eulerian and inertial accelerations) on the validity of using Darcy's equation.
- **Appendix B:** gives a comparison between our experiment results conducted on the sand column and the analytical model of Nielsen and Perrochet (2000) (complex effective porosity).
- **Appendix C:** provides preliminary optical measurements of the water content $[\theta(z,t)]$ using CCD camera.
- **Appendix D:** contains numerical simulations on homogeneous column under tidal forcing (a conference paper).
- **Appendix E:** contains additional simulation tests and analyses on a two-layered medium under tidal forcing (a conference paper).

[9] This chapter was submitted as an article for publication in an international scientific journal.

Chapter 2

Literature Review

2.1 Introduction

This chapter presents a review of the relevant scientific works on beach groundwater hydrodynamics in response to surface water fluctuations mainly due to tidal forcing. The chapter also presents the recent study involving vertical flows and capillary effects in the groundwater dynamic models.

2.2 Overview

Beach groundwater dynamics has been recognized to influence the morphological processes and sediment transport (erosion and accretion) of the swash zone (Baird and Horn, 1996, Jeng et al., 2005b) and to control the biological conditions, nutrient cycling and contaminant movement near the water table (Chen and Pinder, 2011, Hinz, 1998). It also affects the stability of the structures founded on soils and sands (Nielsen, 1990).

To understand and manage the behavior of coastal aquifers, it is required to accurately predict the dynamic groundwater hydraulics.

Beach groundwater hydrodynamics are a result of combined influence from tides and wave forcing. This thesis and consequently this literature review are concerned mainly with tidal forcing effects.

Fig. 2.1 shows a descriptive overview (and terminology) of the forcing at a coastal boundary. In this figure, the MSL is Mean Sea Level. The Still Water Surface (SWS) is the surface that would be measured in the absence of waves (the surface that oscillates with the tide only).The Mean Water Surface (MWS) is the water level, averaged over several wave periods, that indicates the set-up due to wave action. The Shoreline (SL) is defined as the intersection of the MWS with the sand surface. RL is the wave run-up limit. UENV and LENV are the upper and lower envelope boundaries of the water table oscillations. $\eta+$ is the total water table overheight as a result of sea forcing.

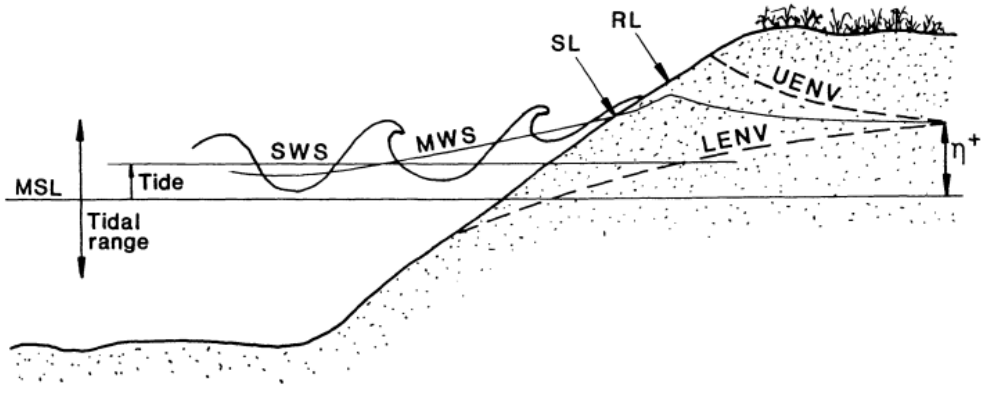

Fig. 2.1: Schematic of the forcing at a coastal boundary (Nielsen, 1999).

2.3 Beach groundwater behavior under tidal forcing

In this section, the behavior and observations of the beach groundwater under the effect of tidal oscillations in the adjacent water body are highlighted and summarized as following:

- Observations from the field and laboratory experiment show that the coastal aquifer responds to the tidal forcing which manifested as fluctuations in the water table of the adjacent aquifer (Li et al., 1997a) and also as fluctuations of the pore water pressure of the aquifer below the water table (Li et al., 2000a).
- The slope of the fluctuating water table is not flat, however the water table sloping seaward on a falling tide and landward on a rising tide and is generally steeper on a rising tide than on a falling tide (Horn, 2006, Raubenheimer et al., 1999).
- The groundwater fluctuations, as induced by the oceanic oscillations, affect water and mass exchange between the aquifer and ocean (Li et al., 2000a).
- The water table fluctuations propagate in the landward direction. (Nielsen et al., 1997) stated that the tidal oscillations vanished within 50m or so from the high water mark in an unconfined aquifer. However, their influence can be considerable up to few hundred meters inland from the shore (Lanyon et al., 1982, Li et al., 2000a). The propagation of these fluctuations is influenced primarily by oscillation frequency, modified by the aquifer parameters, vertical flow and capillarity (Horn, 2006).
- The amplitude of the tidal water table fluctuations is clearly attenuated in the landward direction (Raubenheimer et al., 1999, Baird et al., 1998, Nielsen, 1990).
- The time averaged of the fluctuating water table height may stand significantly above mean sea level (Raubenheimer et al., 1999, Turner et al., 1997). This is often referred to in the literature as an over-height or super-elevation. The lower the beach face slope and/or finer the sand of which it is composed, the higher coastal groundwater is anticipated to stand above mean sea level (Turner et al., 1997, Kang and Nielsen, 1996).

- Tidal water table fluctuations were asymmetrical in time as the beach fills more rapidly than it drains. In this context, (Turner et al., 1997) stated that: "the physical explanation for the significance of a sloping coastal boundary is straightforward to comprehend. Water can infiltrate vertically into the beach face during the flooding tide, but must seep essentially horizontally through the beach during the ebbing tide. In simple terms, a beach will 'fill' more easily that it can 'drain'. It is clear that a sloping beach face favors ocean inflow, implying a tendency for net super-elevation of the coastal water table and an accompanying skewness of the time variation for tidal water table fluctuations". It was observed also that the asymmetry increases in the landward direction (Horn, 2006).
- Water table oscillations have been shown to lag behind tidal oscillations. For a given geometry the lag in water table response is due to the hydraulic conductivity of the beach sediment. This lag increases in the landward direction (Horn, 2006).
- Decoupling between the water table and offshore water level occurs on fine-grained beaches near low tide (Turner, 1993b). In reality, across a low gradient beach face the water table typically decouples during tidal ebb, resulting in the formation of a seepage face that continues to increase in vertical extent through the falling tide (Turner et al., 1997).
- Beaches with low water table tend to accrete and beaches with high water table tend to erode (Grant, 1948, Li et al., 1997a, Baird et al., 1998).

Furthermore, the following is a summary of the behavior of the capillary effect on the coastal groundwater dynamics

- The capillary fringe significantly influence the water table dynamics specially for fine soils (Horn, 2006, Hinz, 1998, Li et al., 1997a, Li et al., 2000a); and has a considerable effects on the exchange of water between the ocean and the coastal aquifer (Horn, 2006).

- In the presence of capillary fringe, water table fluctuations propagate faster and decay more slowly (Nielsen and Turner, 2000, Cartwright et al., 2004).
- Capillarity effects provide a mechanism for the propagation inland of high-frequency sea level oscillations (Li et al., 1997a). It is observed also, that capillarity affects water table dynamics over a wider range of frequencies, including the tidal frequency (Nielsen and Perrochet, 2000a).

2.4 Beach groundwater modeling under tidal forcing

Many models have been developed to predict the groundwater response to periodic forcing in the adjacent water body (Baird et al., 1998, Kang and Nielsen, 1996, Nielsen, 1990, Raubenheimer et al., 1999, Song et al., 2007, Teo et al., 2003, Xia et al., 2010).

By scanning relevant works on this topic, most beach groundwater fluctuations models in coastal aquifer are based on the Boussinesq equation. Other models apply modification on Boussinesq equation to account for vertical flow and capillary effects. On the other hand, models based on the numerical solution of the Richards equations are also available. The following sub-sections briefly explore these models.

2.4.1 Partially saturated/unsaturated flow model with capillary effects: Richards equation

The Richards equation is a standard, frequently used approach for modeling flow in variably saturated/unsaturated porous media (Miller et al., 2006). It can be used with no need to modifications to simulate beach groundwater dynamics under tidal forcing including flows in the unsaturated zone and thus it takes into accounts vertical flows and the capillary effects.

Here we briefly introduce Richards equation (more details in chapter 3) which was formulated by Lorenzo A. Richards in 1931 (Richards, 1931). Richards equation is

obtained by combining Darcy's law with the mass conservation or continuity equation, under the assumption that the air phase remains at constant (atmospheric) pressure and the water phase is incompressible. It can be expressed as follows (mixed form of Richards Equation [(θ, h) form]):

$$\frac{\partial \theta(h,\vec{x})}{\partial t} = \text{div}\,\{K(h,\vec{x})\,\text{grad}(h + \hat{g}\cdot\vec{x})\} \qquad \textbf{Eq. 2.1}$$

where:

- $\theta(h,\vec{x})$: is the volumetric water content; it is function of the pressure head and can vary spatially.
- $K(h,\vec{x})$: is the hydraulic conductivity tensor, a symmetric second rank tensor. It is function of the pressure head and can vary spatially.
- $\hat{g}$: is the normalized gravitational vector; $\hat{g} = -\vec{g}/|g|$, ($|g| = 9.81\text{m/s}^2$).
- $\vec{x}$: is the point coordinate vector.

The water retention curve, $\theta(h)$, and the hydraulic conductivity characteristic, $K(h)$ are soil dependent hydraulic properties that have to be determined in order to model water flow by means of the Richards' equation. Many functional models were considered in the literature for these nonlinear curves. Richards' equation is highly nonlinear and therefore it is solved by employing numerical methods (for example: Finite element methods, Finite volume methods and Finite difference methods).

Detailed discussion on Darcy's equation, Richards equation and the corresponding constitutive relationship [$\theta(h)$ and $K(h)$] are presented in <u>the next chapter</u> [see section 3.4] as it is the core of the numerical code (BIGFLOW) used throughout this thesis.

2.4.2 Overview on Dupuit-Boussinesq-type models

Most of the proposed models are based on the Boussinesq equation which is derived from Darcy's law and a statement of mass conservation. These models are limited by the constraint of the Dupuit–Forchheimer approximation

Dupuit-Boussinesq models assume the following:

- **Vertical flow component:** Vertical circulations are neglected (because horizontal flows are much larger than vertical flows) ; the averaging procedure is based on vertically hydrostatic approximation of the real 3D flow (Ababou, 2008). Therefore, the flow is essentially horizontal.
- **Capillary fringe:** The thickness of the capillary is negligible compared to any other length entering the problem (Parlange et al., 1984). Therefore the sand drains instantaneously and the unsaturated zone located above the water table and the retarded flow to or from the unsaturated zone is neglected.

It should be noted that the sharp interface makes this an unusually appropriate problem for a Boussinesq-type approach.

Boussinesq's equation for one-dimensional horizontal flow in unconfined aquifer can be written as (Nielsen, 1990, Parlange et al., 1984):

$$\frac{\partial H(x,t)}{\partial t} = \frac{K}{n}\frac{\partial}{\partial x}\left(H(x,t)\frac{\partial H(x,t)}{\partial x}\right) \qquad \textbf{Eq. 2.2}$$

in which: $H(x,t)$ is the local groundwater table height from the horizontal, impermeable aquifer base; K is the hydraulic conductivity; x is the horizontal coordinate; t the time and n is the specific yield that represents the storage capacity of the aquifer due to storage/drainage of water during fluctuations of the water table; thus it is a fraction of the total porosity called efficient or effective porosity.

Notes about Boussinesq's equation:

- the above equation (Eq. 2.2) can be modified to consider sink/source terms representing fluxes through the roof or the floor of the aquifer (i.e. infiltration, upward leakage through the floor) see for example: (Ababou, 2008) . These terms are not taken into account because our attention at present is mainly focused on the effects of tidal oscillations.
- The Boussinesq equation (Eq. 2.2) is nonlinear and hardly has theoretical solutions in general (Sun et al., 2011). (Kacimov and Abdalla, 2010) stated that "no explicit analytical solution for a boundary condition corresponding to a tidal excitation (even for a simple harmonic) is known". However, integral estimates are possible. Philip (Philip, 1973) found an exact asymptotic solution for the steady part of $H(x,t)$ [or in other words, the time averaged of $H(x,t)$] which is higher than the mean sea level. Philip found that the asymptotic mean water table fluctuations (due to tidal forcing) as the landward distance approaches infinity has the following form:

$$H(\infty,t) = \sqrt{\overline{H^2(x,t)}} = \sqrt{D^2 + A^2/2} \qquad \textbf{Eq. 2.3}$$

where D is the mean sea level and A is the tidal amplitude.

This super-elevation or over-height was confirmed later by field and laboratory observations (Nielsen, 1990).

On the other hand, numerous approximation methods are mentioned in the literature to solve Boussinesq equation and the 2D flow equation; these methods are based mainly on perturbation approaches. We stated here some of the proposed methods:

2.4.3 Vertical beach models

For the simplified vertical beach case, Parlange et al. (Parlange et al., 1984) based on later work of Dagan (Dagan, 1967) derived an approximate solution of the non-linear Boussinesq equation using perturbation technique.

Parlange et al. use $\varepsilon_P = A/D$ as the perturbation parameter and they developed a second-order solution to the non-linear Boussinesq equation (Eq. 2.1) subjected to a tidal boundary condition. The second-order solution is of the form:

$$H(x,t) = D[1 + \varepsilon_P\, H_1(x,t) + \varepsilon_P^2\, H_2(x,t) + O(\varepsilon_P^3)] \qquad \textbf{Eq. 2.4}$$

subjected to the following conditions:

$$H(x=0,t) = D + Acos(\omega t) \qquad \textbf{Eq. 2.5}$$

and

$$\frac{\partial H}{\partial x} \to 0 \;\; as\; x \to \infty \qquad \textbf{Eq. 2.6}$$

The results are:

$$H_1(x,t) = cos(\omega t - \lambda x)e^{-\lambda x} \qquad \textbf{Eq. 2.7}$$

and

$$H_2(x,t) = \frac{1}{2}\left[cos\left(2\omega t - \sqrt{2}\lambda x\right)e^{-\sqrt{2}\lambda x} - cos[2(\omega t - \lambda x)]e^{-2\lambda x}\right] + \frac{1}{4}\left(1 - e^{-2\lambda x}\right) \qquad \textbf{Eq. 2.8}$$

where $\lambda = \sqrt{n\omega/(2KD)}$ is the wave number of the primary signal.

Their solution demonstrates that the nonlinear effects lead to the generation of higher harmonics in tidal water table fluctuations in a coastal aquifer (Eq. 2.8). The effects of these higher order components on tidal propagation are not negligible and if omitted they may lead to a significant error in predicting water table elevation. Parlange et al. solution also confirm the water table over-height obtained by Philip (Philip, 1973) in Eq. 2.3.

However, (Song et al., 2007) noted that the Parlange et al. approach is hindered by a secular term when extended to the third-order. To avoid this, Song et al. developed a new perturbation solution of the nonlinear Boussinesq equation. The solution adopts a perturbation parameter that gives consistency with the integral property (overheight) of the tidally fluctuating water table. The new perturbation parameter is $\varepsilon_s = A/D_\infty$ where D_∞ is the maximum time-averaged water table height given by Eq. 2.3.

By definition, the perturbation parameter (ε_s) is less than unit, and thus it is applicable to a wider range of physical conditions within the constraint of the Boussinesq approximation. With the second-order approximation, the solution is slightly more accurate than that of (Parlange et al., 1984)..

2.4.4 Sloping beach models

The more realistic case of sloping beach face was first treated by (Nielsen, 1990). The non-verticality of the beach slope results in a moving boundary condition in the mathematical formulation for groundwater fluctuations due to coastal tides.

Nielsen presents an analytical investigation where the assumption of a fixed location of the shoreline boundary condition is relaxed.

He derived a perturbation solution for small-amplitude fluctuations in the water table on the basis of the linearized Boussinesq equation by matching a prescribed series solution with the moving boundary condition. The linearization of Boussinesq equation has the following form:

$$\frac{\partial H}{\partial t} = \frac{KD}{n}\frac{\partial^2 H}{\partial x^2} \qquad \textbf{Eq. 2.9}$$

He introduces a new perturbation parameter $\xi = \lambda\, A\, cot\beta$; where (β) is the planar beach slope.

His model requires two boundary conditions:

- the water table oscillations die out far from the beach.
- the decoupling between the water table and the tide does not occur (i.e. no occurrence of seepage face).

For example, the first order approximation is given by:

$$H(x,t) = D + A\,cos(\omega t - \lambda x)e^{-\lambda x} + \xi A\left[\frac{1}{2} + \frac{\sqrt{2}}{2}cos\left(2\omega t + \frac{\pi}{4} - \sqrt{2}\lambda x\right)e^{-\sqrt{2}\lambda x}\right] \quad \textbf{Eq. 2.10}$$

Note that the solution in Eq. 2.10 includes an over-height of ($\xi A/2$) and higher harmonic (with frequency 2ω). Referring to (Nielsen, 1990), the over-height is due to three mechanisms: formation of seepage face at low tide (the decoupling of the exit point of the water table on the beach face and the tide), asymmetry of the boundary condition at the sloping beach face, and the nonlinearity of the governing equations.

Nielsen found that predictions using his analytical solution for a sloping boundary condition corresponded closely to observations of water tables in a microtidal beach except at low tide when the water table became decoupled from the tide.

(Li et al., 2000b) noted that the solutions derived by (Nielsen, 1990) did not satisfy the boundary condition at the beach face. The model was improved by Li et al. with their solution matching the seaward boundary condition exactly rather than approximately as in the case of (Nielsen, 1990).

(Li et al., 2000b) transformed the linearized Boussinesq equation [Eq. 2.9] into an advection–diffusion type equation with an oscillating velocity to account for the moving boundary effect.

$$\frac{\partial H}{\partial t} = \frac{KD}{n}\frac{\partial^2 H}{\partial x^{*2}} - v(t)\frac{\partial H}{\partial x^*} \quad \textbf{Eq. 2.11}$$

Where $x^* = x - X(t)$ is a transformed coordinate; $X(t) = \eta(t)\cot(\beta)$ is the x coordinate of the moving boundary; $\eta(t)$ is the tide induced oscillations of the mean sea level and $v(t) = \mathrm{d}X(t)/\mathrm{dt}$ is an oscillating velocity.

Maintaining the simplicity of the linearized Boussinesq equation, they presented a new perturbation approach to obtain approximate solutions to Eq. 2.11 with the same perturbation parameter as that of (Nielsen, 1990) [$\xi = \lambda\, A\, cot\beta$].

The first order approximation of Li et al. is given by:

$$H(x,t) = D + A\,cos(\omega t - \lambda x^*)e^{-\lambda x^*} + \frac{\xi A}{2}\left[1 + \sqrt{2}\,cos\left(2\omega t + \frac{\pi}{4} - \sqrt{2}\lambda x^*\right)e^{-\sqrt{2}\lambda x^*} - \sqrt{2}e^{-\lambda x^*}\left\{cos\left(2\omega t + \frac{\pi}{4} - \lambda x^*\right) + cos\left(\lambda x^* - \frac{\pi}{4}\right)\right\}\right] \quad \textbf{Eq. 2.12}$$

The solution in Eq. 2.12 predicts the same over-height ($\xi A/2$) as that of Nielsen's solution. However, Eq. 2.12 satisfies exactly the oceanic/land boundary moving boundary condition at the beach face while Eq. 2.10 only meets this condition approximately.

(Teo et al., 2003) noted that both (Nielsen, 1990) and (Li et al., 2000b) solutions had used a perturbation parameter ($\xi = \lambda\, A\, cot\beta$) that was dependent on the beach slope (β); restricting the range of applicability of their solutions to a certain beach slopes. Their solutions also lack higher order components as their models are based on the linearized Boussinesq equation.

(Teo et al., 2003) re-examined the shallow flow expansion similar to that used by (Parlange et al., 1984) for vertical beach, and derived a new analytical solution for water table fluctuations in a sloping beach. The capillary effects (and thus the unsaturated flow) and the effects of seepage face development are assumed negligible. Therefore, the potential head $\phi(x,z,t) = z + p/\rho g$ satisfies Laplace's equation:

$$\phi_{xx} + \phi_{zz} = 0, \qquad 0 \le z \le h(x,t) \quad \textbf{Eq. 2.13}$$

They introduced two perturbation parameters:

- the shallow water parameter ($\varepsilon_T = \sqrt{n\omega D/2K}$) representing the ratio of the still water table (D) to the decay length ($L = \sqrt{2KD/n\omega}$).
- the amplitude parameter ($\alpha_T = A/D$) representing the ratio of the maximum tidal variation to the average height of the water table.

Their solution was shown to significantly affect predictions of water table fluctuations in coastal aquifers.

Recently, (Stojsavljevic et al., 2012) had developed a new higher order semi-analytical solutions for tide-induced groundwater fluctuations in coastal aquifers, based on the model and methods introduced by (Teo et al., 2003). They noted that the high-order solution provides a better prediction of the fluctuations than previously derived solutions (especially for shallow beaches and where α_T is large). (Roberts et al., 2011) also extended (Teo et al., 2003) perturbation solution to higher-orders. They provided a general solution scheme, automated through Mathematica. The solution can, in principle, be extended to any arbitrary order.

Moreover, (Jeng et al., 2005a) instead of using the shallow water parameters (ε_T) that is used by (Teo et al., 2003); they derived a new analytical solution for tide-induced fluctuations in coastal aquifers, based on the wave steepness (ξ_J), given by:

$$\xi_J = \frac{A}{L} \qquad \textbf{Eq. 2.14}$$

Where A is the tidal amplitude and $L = \sqrt{2KD/n\omega}$ is the linear decay length; n is the soil porosity, K the hydraulic conductivity and ω the tidal frequency.

The (Jeng et al., 2005a) solution provided a wider applicable range to the free surface flow of groundwater compared with the conventional shallow-water expansion.

2.4.5 Models involving vertical flow effects

To account for vertical flows effects , (Nielsen et al., 1997) derived a new differential equation for flow in aquifers of intermediate depth. They attempted to relax the shallow aquifer assumption, based on Boussinesq equation. The new model considered only the case of a vertical beach and has the following form:

$$\frac{\partial \eta}{\partial t} = \frac{KD}{n} \tan\left(D\frac{\partial}{\partial x}\right)\frac{\partial \eta}{\partial x} \qquad \textbf{Eq. 2.15}$$

Where η is the fluctuation of the water table; n is porosity; D is aquifer depth; K is hydraulic conductivity; t is time; x is horizontal distance and $\tan(D\,\partial/\partial \mathrm{x})$ is an infinite order differential operator.

This model incorporate a pressure correction term to the hydrostatic pressure assumed in the non-linear Boussinesq equation. Therefore, the main insight of this model is that the groundwater movement in an aquifer which borders a hydrostatic reservoir cannot be described by a single ground-water wave mode, because all of the non-shallow wave modes are non-hydrostatic, while the clear-water reservoir would usually be hydrostatic.

2.4.6 Models involving capillary effects

Recent laboratory and field studies show that capillarity affects water table dynamics over a wider range of frequencies, including the tidal frequency (Nielsen and Perrochet, 2000a, Nielsen and Perrochet, 2000b, Turner, 1993a, Werner and Lockington, 2003). As the water table fluctuates, the pressure distribution above the water table will change, and thus an apparent local water exchange across the water table occurs (Li et al., 1997a).

(Parlange and Brutsaert, 1987) modified Boussinesq equation to incorporate the capillary effects. A capillary correction term was added to the equation to take into account the capillary influences above the water table (based on Green and Ampt approximation). Based on the linearized Boussinesq equation and applying the capillary correction, the following equation was resulted:

$$\frac{\partial H}{\partial t} = \frac{KD}{n}\frac{\partial^2 H}{\partial x^2} + \frac{DB}{n}\frac{\partial^3 H}{\partial t\,\partial x^2} \qquad \textbf{Eq. 2.16}$$

where B represents an average suction required to extract water held in the soil by capillarity. Other interpretations treated B as the average thickness of water held in the capillary zone above the water table.

(Parlange and Brutsaert, 1987) provided an estimation of the average suction B as follow:

$$B = \int_0^{\infty} (\theta - \theta_r)\ d\psi \qquad \textbf{Eq. 2.17}$$

Where θ_r is the residual water content and ψ is the soil water suction head.

(Ababou, 1991) suggested another estimation of the parameter B (λ_{CAP} in his notation) corresponds to the point of the inflection of the water retention curve $[\theta(\psi)]$ at which the specific moisture capacity $[C(\psi) = \partial\theta(\psi)/\partial\psi]$ is maximum. The suction head at this point can be treated as a global capillary length scale of the porous media which is defined by:

$$B = \frac{1}{\alpha}\left(1 - \frac{1}{n}\right)^{\frac{1}{n}} \qquad \textbf{Eq. 2.18}$$

where α and n are the van Genuchten model parameters.

(Parlange and Brutsaert, 1987) noted that this correction is important for relatively short times. (for times smaller than B/K which express the relative importance of capillarity and the gravity effects).

(Li et al., 2000a) considered the influences of unsaturated zone. They derived a new equation for groundwater waves by incorporating capillary effects into the intermediate-depth wave equation of (Nielsen et al., 1997) [Eq. 2.15].

Therefore, the new equation includes both the effects of vertical flows and capillarity and it is applicable to both intermediate-depth aquifers and high-frequency waves. To account for the unsaturated flow, the derivation of the model was based on Green-Ampt approximation applied to the capillary fringe similar to that used by (Parlange and Brutsaert, 1987). Their model has the following form:

$$\frac{\partial\eta}{\partial t} = \frac{K}{n}\tan\left(D\frac{\partial}{\partial x}\right)\frac{\partial\eta}{\partial x} + \frac{B}{n}\frac{\partial}{\partial t}\left[\tan\left(D\frac{\partial}{\partial x}\right)\frac{\partial\eta}{\partial x}\right] \qquad \textbf{Eq. 2.19}$$

where B is the thickness of the capillary fringe and the other terms as in Eq. 2.15. Note that the second term on the right-hand side of Eq. 2.19 accounts for capillary effects on groundwater dynamics. Or in other words, it accounts for the apparent water exchanges happened during the fluctuations of the water table.

(Li et al., 2000a) verified the new method by comparing its results to those obtained from direct numerical simulations of Richards equations (Eq. 2.1) using the finite element code "SUTRA". The new analytical solution was found to describe well the aquifer's responses to high-frequency boundary oscillations provided that the aquifer is of a shallow or intermediate depth.

(Li et al., 1997a) derived another equation to account for the capillary effects on the groundwater fluctuations. Capillary effects were incorporated into the model by modifying the kinematic boundary condition for the water table using an additional term suggested by (Parlange and Brutsaert, 1987). This condition accounts for mass transfer across the fluctuating water table due to pressure gradient variation that occurs in the capillarity effects during these fluctuations.

The modified kinematic boundary condition was incorporated into a boundary element method (BEM) developed previously by (Li et al., 1997b) which solves the two-dimensional flow equation subjected to free and moving boundary conditions, including the seepage dynamics at the beach face. The new capillary-involved model is as follow:

$$\frac{\partial \phi}{\partial t} = -\left[\frac{K}{n\ \cos\Theta}\ \frac{\partial \phi}{\partial \Omega}\right] - \left[\frac{B}{n \cos\Theta}\frac{\partial}{dt}\left(\frac{\partial \phi}{\partial \Omega}\right)\right] \qquad \textbf{Eq. 2.20}$$

where ϕ is the potential head defined as: $\phi(x, z, t) = z + p/\rho g$; $\partial\phi/\partial\Omega$ is the potential gradient in the normal direction to the water table; Θ is the angle between the free surface and the horizontal x-axis; n is the porosity and K is the hydraulic conductivity.

From the model presented in Eq. 2.20, (Li et al., 1997a) distinguished two mechanisms of beach water table fluctuations in response to sea oscillations:

- The first mechanism appears in the first term on the right-hand side. It is mainly due to a horizontal mass transport process which results from the boundary condition changes at the beach face.

- The second mechanism appears in the second term on the right-hand side and is due to a local mass transfer across the water table. This mass transfer process is a result of the pressure gradient changes at the water table.

Furthermore, (Li et al., 1997a) define a dimensionless number named coastal aquifer response (N_{CAR}) to quantify the importance of the capillary effects given by:

$$N_{CAR} = \frac{K}{B\omega} \qquad \textbf{Eq. 2.21}$$

Where $\omega = 2\pi/T_P$ is the forcing frequency.

The dimensionless number decreases with the increase of frequency and capillary fringe length, and increases as the hydraulic conductivity increases. Clearly, the first mechanism is dominant if N_{CAR} is large, while the second mechanism (capillary effects) prevails for small N_{CAR}. N_{CAR} can also be treated in terms of the response time of the capillary fringe ($T_f = B/K$) to the timescale for water table fluctuations ($T_w = 1/\omega$), this means that $N_{CAR} = T_w/T_f$.

On the other hand, Nielsen and Perrochet (Nielsen and Perrochet, 2000a, Nielsen and Perrochet, 2000b) accounted for the effects of the capillary fringe by introducing the concept of a complex effective porosity which describes the relationship between periodic fluctuations in the equivalent saturated height of total moisture (the sum of the water table height and the equivalent thickness of the capillary fringe) and those fluctuations of the water table height only. The complex effective porosity is defined by:

$$n_{ce}\frac{dh}{dt} = n\frac{dh_{tot}}{dt} \qquad \textbf{Eq. 2.22}$$

Where n_{ce} is the complex effective porosity; $n = \theta_s - \theta_r$ is the effective porosity; θ_s is the saturated water content; θ_r is the residual water content; h is the water table height; $h_{tot} = h + h_c$ is the equivalent saturated height of total moisture; h_c is the equivalent thickness of the capillary fringe [similar to that defined by (Parlange and Brutsaert, 1987) in Eq. 2.17].

It was stated by (Cartwright et al., 2004) that: "n_{ce} is complex in nature so as to mathematically account for the fact that fluctuations in the total moisture (h_{tot}) are both damped and lag those in the water table (h). These two processes are accounted for by $|n_{ce}|$ and Arg$\{n_{ce}\}$ respectively". (Nielsen and Perrochet, 2000a, Nielsen and Perrochet, 2000b) observed that within the range of experiments they conducted, n_{ce} is constant for a given soil and compaction and appears to be almost independent of the forcing frequency. However, this observation of constant n_{ce} was superseded by the more comprehensive dataset of (Cartwright et al., 2005) who found a definitive dependence of the effective porosity on $\omega B/K$. They recommend the following expression for n_{ce} which obtained by an empirical curve fit to their experimental data:

$$n_{ce} = \frac{n}{1 + 2.5(i\, n\omega B/K)^{2/3}} \qquad \textbf{Eq. 2.23}$$

They noted also that the form of this equation is similar but still clearly different from:

$$n_{ce} = \frac{n}{1 + i(n\omega B/K)} \qquad \textbf{Eq. 2.24}$$

which they derived from the Green-Ampt approximation model.

Finally it is worth noting that, the use of the complex effective porosity does not give any information about the dynamics of the moisture distribution in the unsaturated zone above the fluctuating water table (Cartwright et al., 2005, Horn, 2006).

From the previous literature review, it seems that neglecting the effect of the capillarity in the beach hydrodynamics models and analysis oversimplified the real case. The influence of the capillary effect increases for relatively high frequency forcing, low permeability small and grained porous media. To our knowledge, no detailed experimental works with suction pressure measurements in the unsaturated zone had been conducted to follow what happened above the fluctuating water table. In this thesis, we wish to improve the understanding of oscillatory flow processes and the capillary effects in partially saturated/unsaturated porous media, experimentally, numerically and analytically.

Chapter 3

Numerical Modeling of Variably Saturated Flow: Basic Definitions and Governing Equations

3.1 Introduction

This chapter introduces the basic definitions and the governing equations used to model variably saturated flow numerically, taking into account both saturated and unsaturated zones. Darcy equation, mass conservation equation, and the resulting Richards equation (Partial Differential Equation) are presented. The constitutive relationships $[\theta(h), K(h)]$ required to solve the Richards equation are then reviewed. The van Genuchten / Mualem model is introduced; a parametric study is conducted, and a physical interpretation of the model parameters is given.

The numerical code BIGFLOW 3D was used throughout this thesis to simulate variably saturated flow in porous media[10].

[10] See next chapter for more details on BIGFLOW.

3.2 Basic definitions

Porous media is a three phase material which consists of solid particles which make up the skeleton of porous media and voids that contains air and/or water. In the followings we recall a few basic concepts.

3.2.1 Saturated flow

It is a flow that occurs in a saturated porous media, in which all the voids are filled with water. The volumetric water content equals the porosity. The hydraulic conductivity is constant (not depending on the pressure head) and equals the saturated hydraulic conductivity.

3.2.2 Unsaturated flow

It is a water flow in unsaturated porous media, the voids being only partially filled with water and the rest with air. Resistance to air flow is neglected (air viscosity ≈ 0), air pressure equilibrates rapidly to atmospheric pressure. The moisture content is less than the porosity. The hydraulic conductivity and the moisture content are both functions of the pressure head.

3.2.3 Variably saturated flow or partially saturated flow

Water flow can occur either in fully saturated mode or unsaturated or both. Saturated and unsaturated zones may coexist, and their spatial pattern can evolve with time (as in wave action on an adjacent porous media)

3.2.4 Representative elementary volume (REV)

The Representative Elementary Volume, REV, concept was formalized by (Bear, 1972) for studies of transport in porous media. REV has been used to describe a scale at which the measured porous medium properties (porosity, permeability, etc.) are representative of the porous medium.

It can be defined as the minimum volume of a soil sample from which a given parameter becomes independent of the size of the sample (Al-Raoush and Papadopoulos, 2010).

The size of an REV ranges from a minimum bound, which is the transition from the microscale to the macroscale level, to a maximum bound, which is the transition from a homogenous to a heterogeneous state (Al-Raoush and Papadopoulos, 2010) as shown in **Fig. 3.1**.

Therefore, The REV must be (Dietrich et al., 2005) :

- Large enough to avoid undesirable fluctuations of the average properties.
- Small enough to render the spatial dependency of these properties.

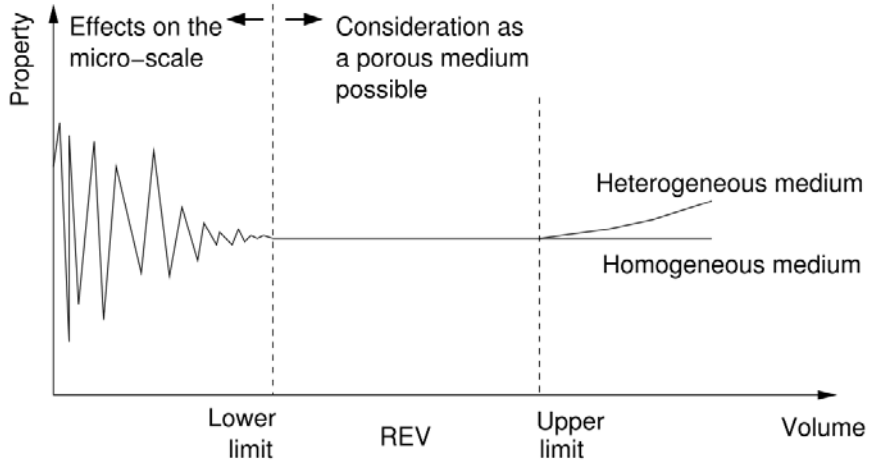

Fig. 3.1: Representative elementary volume (REV), (Dietrich et al., 2005).

3.2.5 Porosity (ϕ)

It is the ratio of the volume of voids (V_v) to the total volume of porous medium (V):

$$\phi = \frac{V_v}{V} \qquad \textbf{Eq. 3.1}$$

By definition, the porosity can only range from 0 to 1. [Typical porosity values [m^3/m^3] for unfractured, unconsolidated geologic media are: gravel (0.25 to 0.40); sand (0.25 to 0.50); silt (0.35 to 0.50); and clay (0.40 to 0.70), (Freeze and Cherry, 1979)].

3.2.6 Volumetric water content (θ)

It is the ratio of volume of water contained in the pores of porous medium (V_w) to the total volume of porous medium (V):

$$\theta = \frac{V_w}{V} \qquad \textbf{Eq. 3.2}$$

Theoretically, it can range from zero ($\theta = 0$) when the medium is completely dry to the value of the materials' porosity ($\theta = \theta_s = \phi$) at saturation.

However, there is a minimum volumetric water content known as the residual water content (θ_r) which represents the small amount of water which is adsorbed in thin films at low water potentials (at some large negative value of the pressure head) and which is barely mobile. [In water retention curve, the gradient $d\theta/dh$ becomes zero at when θ approaches both its saturated and residual values (van Genuchten, 1980)].

3.2.7 Degree of saturation (S_r)

It is the ratio of the volume of water (V_w) to the volume of voids (V_v) and is generally expressed as a percentage:

$$S_r = \frac{V_w}{V_v} \times 100 \qquad \textbf{Eq. 3.3}$$

For a dry soil S_r = 0. When the volume of the voids is fully occupied by water ($V_w = V_v$), S_r = 1 or 100%.

3.2.8 Viscosity (μ, υ)

It is a fluid property describing the ability of a given fluid to resist flow. Viscosity coefficients can be defined in two ways:

- Dynamic viscosity (or absolute viscosity) μ [N.s/m^2], the more usual one.
- Kinematic viscosity υ [m^2/s] is the *dynamic viscosity* divided by the density:

$$\upsilon = \mu/\rho. \qquad \textbf{Eq. 3.4}$$

3.2.9 Permeability, hydraulic conductivity (K)

The hydraulic conductivity (K) [m/s] is the term of proportionality between flux and hydraulic gradient in Darcy's law. It is not only a function of the porous media but also of the fluid. However, the intrinsic or specific permeability (k) [m^2] is a function of the medium alone. The hydraulic conductivity is related to the intrinsic permeability by the following relation (Freeze and Cherry, 1979):

$$K = \frac{k\rho g}{\mu} = \frac{kg}{\upsilon} \qquad \textbf{Eq. 3.5}$$

Where (μ, υ) are respectively the dynamic and kinematic viscosity of the fluid and g is the gravity acceleration.

Unlike the hydraulic conductivity, the intrinsic permeability (k) is a quantitative property of porous material and it is independent of fluid properties.

3.2.10 Capillary action, capillary fringe and air entry value:

Capillary action is a phenomenon where liquid spontaneously rises in a narrow space such as a thin tube, or in porous materials. This effect can cause liquids to flow against the force of gravity. It is the result of adhesion and surface tension.

Consider for example the soil layer shown in **Fig. 3.2**, pore water rises above the water table under capillary suction. The soil remains essentially saturated, described by the saturated water content (θ_s), until the suction head reaches the air-entry head, designated (h_a). The *air-entry head* may be defined as the suction head at which air initially begins to displace water from the soil pores. The saturated zone extending from the water table up to the air-entry head is commonly referred to as the *capillary fringe*.

Above the air-entry head, the water content decreases with increasing height (and increasing suction head), reflecting the fact that fewer and smaller capillary fingers are present for a given cross section of the soil column with increasing elevation.

At relatively large values of suction head, very little water is retained by the soil (defined previously as the residual water content, θ_r). Pore water within this regime is

primarily in the form of thin films surrounding the particle surfaces or disconnected ‘‘pendular’’ water menisci. (Lu and Likos, 2004).

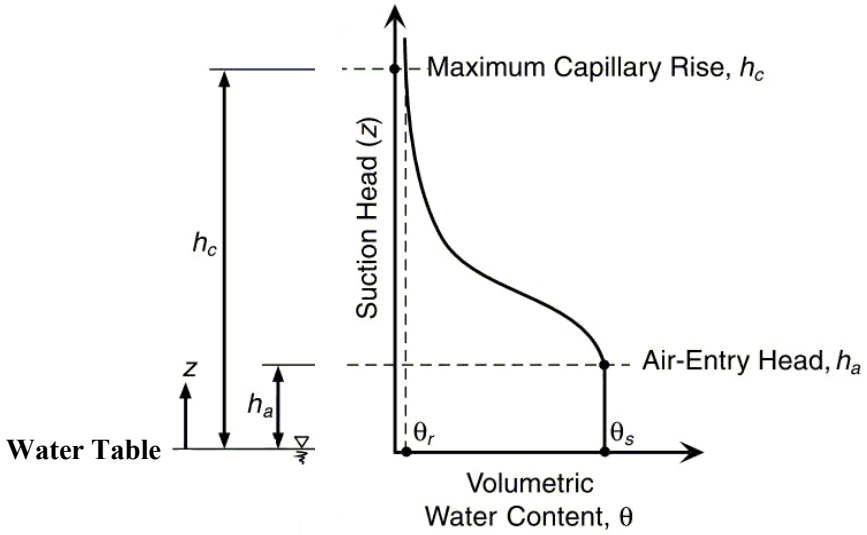

Fig. 3.2: Capillary rise and associated pore water retention in an unsaturated soil profile (Lu and Likos, 2004).

3.2.11 Total hydraulic head

The total hydraulic head H (or simply the hydraulic head) at any point in a porous medium is the summation of the pressure head (h) and the elevation head (z) at that point:

$$H = h + z = \frac{p_{water} - p_{atm}}{\rho_w g} + z \qquad \textbf{Eq. 3.6}$$

The elevation head (z) at a point is the vertical distance of that point measured from an assumed datum plane.

The pressure head (h) is the pore water pressure (p_{water}) at the point measured with respect to the atmospheric pressure (p_{atm}) and expressed in an equivalent meter water column (by dividing with the unit weight of water, $\rho_w g$). In the saturated zone, it is positive quantity and represent by the height to which water rises in a piezometer attached to this point.

On the other hand, the pressure head is negative in the unsaturated zone. This reflects the fact that water in the unsaturated zone is held in the soil pores under surface-tension

forces. A microscopic inspection would reveal a concave meniscus extending from grain to grain across each pore channel. Piezometers are no longer a suitable instrument for the measurement of h. Tensiometers are usually used to measure suction head (see chapter 4 for more details on tensiometers). Some references use the term *tension head* or *suction head* (denoted by ψ) to refer negative pressure head.

On the water table, the pressure head equals zero and therefore the total hydraulic head at any point on the water table must equal to the elevation z of the water table at that point.

3.3 Principles of flow in porous media: the governing equations

3.3.1 Darcy- Buckingham equation

Darcy's law describes the flow of a fluid through a porous medium as a linear relationship between the flux and pressure gradient. The law was formulated by Henry Darcy (1856) based on the results of 1D experiments of saturated flow through homogeneous and isotropic beds of sand. Darcy's Law was later modified by Buckingham (1907) for unsaturated flow to produce the Darcy-Buckingham law.

The generalized form of the Darcy-Buckingham equation for 3D variably saturated anisotropic porous medium can be expressed as follow:

$$\vec{q} = -K(h, \vec{x})\nabla H \qquad \textbf{Eq. 3.7}$$

Where:

$\vec{q}$ is the specific discharge or the flux density vector (m/s).

H is the total hydraulic head (m); $H = h + \hat{g} \cdot \vec{x}$

$\hat{g}$ is the normalized gravitational vector; $\hat{g} = -\vec{g}/|g|$, ($|g| = 9.81\mathrm{m/s^2}$).

$\vec{x}$ is the point coordinate vector.

h is the pressure head (m).

K is the hydraulic conductivity tensor, a symmetric second rank tensor. It is a function of the pressure head. This tensor can also be written in matrix form as:

$$K = \begin{bmatrix} K_{XX} & K_{XY} & K_{XZ} \\ K_{YX} & K_{YY} & K_{YZ} \\ K_{ZX} & K_{ZY} & K_{ZZ} \end{bmatrix} \quad \textbf{Eq. 3.8}$$

satisfying $K_{ij} = K_{ji}$. If the principal direction of anisotropy coincide with the *x*, *y* and *z* coordinate axes, the *K* tensor can also be reduced to (Freeze and Cherry, 1979):

$$K = \begin{bmatrix} K_{XX} & 0 & 0 \\ 0 & K_{YY} & 0 \\ 0 & 0 & K_{ZZ} \end{bmatrix} \quad \textbf{Eq. 3.9}$$

Note that Darcy's equation is not universally applicable. It is only valid for slow, laminar flow; usually, most groundwater flow cases fall in this category. The verification of laminar flow is done through the use of Reynolds number; a dimensionless parameter gives a measure of the ratio of inertial forces to viscous forces and consequently quantifies the relative importance of these two types of forces for given flow conditions:

$$R_e = qD/\upsilon \quad \textbf{Eq. 3.10}$$

where: q is the specific discharge (m/s), υ is the fluid kinematic viscosity (m^2/s) and D is a representative length dimension for the porous media (m).

(Bear, 1972) defined an *upper limit* of the validation of the linear Darcy's law, he stated that: "Darcy's law is valid as long as the Reynolds number based on average grain diameter does not exceed some value between 1 and 10, as shown in (**Fig. 3.3**).

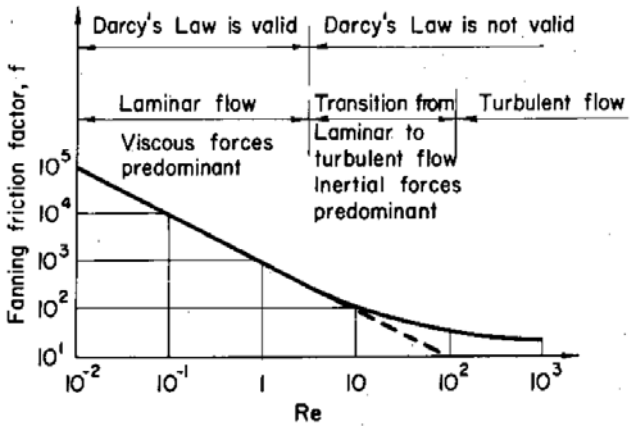

Fig. 3.3: Schematic classification of flow through porous media, (Bear, 1972)

3.3.2 Continuity equation (mass conservation equation)

The principle of mass conservation (or the continuity principle) states that for a given representative elementary volume (REV[11]) of porous media, the rate of water loss or gain is conservative and is equal to the net flux of in flow and out flow. It can be expressed as follows (Ababou, 2008):

$$\frac{\partial \theta_e(h)}{\partial t} = -\nabla \cdot \vec{q} \qquad \textbf{Eq. 3.11}$$

Where:

$\theta_e(h)$: is the effective volumetric water content at a given pressure head, (m^3/m^3) given by: $\theta_e(h) = \theta(h) - \theta_r$, and θ_r is the residual water content.

$\vec{q}$: is the flux vector (m/s)

The above equation (Eq. 3.11) is the governing continuity equation for transient incompressible fluid flow in porous media with no source term and is applicable to both saturated and unsaturated conditions.

3.3.3 Variably saturated 3D flow equation (generalized Richards' equation)

Richards' equation is a standard, frequently used approach for describing (and modeling) flow in variably saturated porous media (Miller et al., 2006). It was formulated by Lorenzo A. Richards in 1931. Richards' equation is obtained by combining Darcy-Buckingham's law with the mass conservation or continuity equation, under the assumption that the air phase remains at constant (atmospheric) pressure and the water phase is incompressible. It can be expressed as follows:

$$\frac{\partial \theta_e(h)}{\partial t} = \text{div}\{K(h, \vec{x})\ \text{grad}(h + \hat{g} \cdot \vec{x})\} \qquad \textbf{Eq. 3.12}$$

Eq. 3.12 represents the mixed form [(θ, h) form] of Richards Equation.

[11] While there is some debate regarding the appropriateness of the REV concept, it is useful in developing a continuity equation. In this sense, a REV is defined such that the medium and fluid properties are constant throughout its volume

This equation may be written in several forms, with either pressure head or water content or both as the dependent variable (Arampatzis et al., 2001). Three standard forms of the unsaturated flow equation may be identified:

- The "mixed" form as in the previous expression (Eq. 3.12),
- The "*h*-based" form:

$$C(h,\vec{x})\frac{\partial h}{\partial t} = \text{div}\,\{K(h,\vec{x})\,\text{grad}(h+\hat{g}\cdot\vec{x})\} \qquad \textbf{Eq. 3.13}$$

- The "θ-based" form:

$$\frac{\partial \theta_e(h)}{\partial t} = \text{div}\,\{D(\theta)\,\nabla\theta\} + \hat{g}\frac{\mathrm{d}K(\theta)}{\mathrm{d}\theta}\cdot\nabla\theta \qquad \textbf{Eq. 3.14}$$

Where:

$C(h)$ is the specific water capacity and it represents the slope of the water retention curve $\theta(h)$ [i.e., the change in water content in a unit volume of soil per unit change in matric potential]. It is given by the following expression:

$$C(h) = \frac{\partial\theta(h)}{\partial h} \qquad \textbf{Eq. 3.15}$$

And $D(\theta)$ is the soil-water diffusivity and it is the ratio of the hydraulic conductivity (K) to the specific water capacity (C) and is therefore defined as:

$$D(\theta) = \frac{K(\theta)}{C(\theta)} = K(\theta)\frac{\partial h(\theta)}{\partial\theta} \qquad \textbf{Eq. 3.16}$$

Richards' equation is strongly non-linear and cannot be solved analytically except for special cases. Consequently, numerical methods like finite element, finite difference and finite volume have been used to solve Richards' equation.

The water retention characteristic, $\theta(h)$, and the conductivity characteristic, $K(h)$ are soil dependent hydraulic properties that have to be determined in order to model water flow by means of the Richards' equation. Discussion on the characteristic curves is presented in the next sections.

3.3.4 Water retention curve ($\theta(h)$)

Essential to understanding unsaturated soil-water systems is the soil-water retention curve (WRC). The WRC is the relationship between soil suction (matric suction) and volumetric water content or degree of saturation (**Fig. 3.4**). The curve represents the storage capability of the soil and defines the amount of water retained in the pores under various matric suction values (Reinson et al., 2005). Usually, The water retention curve have the shape of a sigmoidal function (Leong and Rahardjo, 1997).

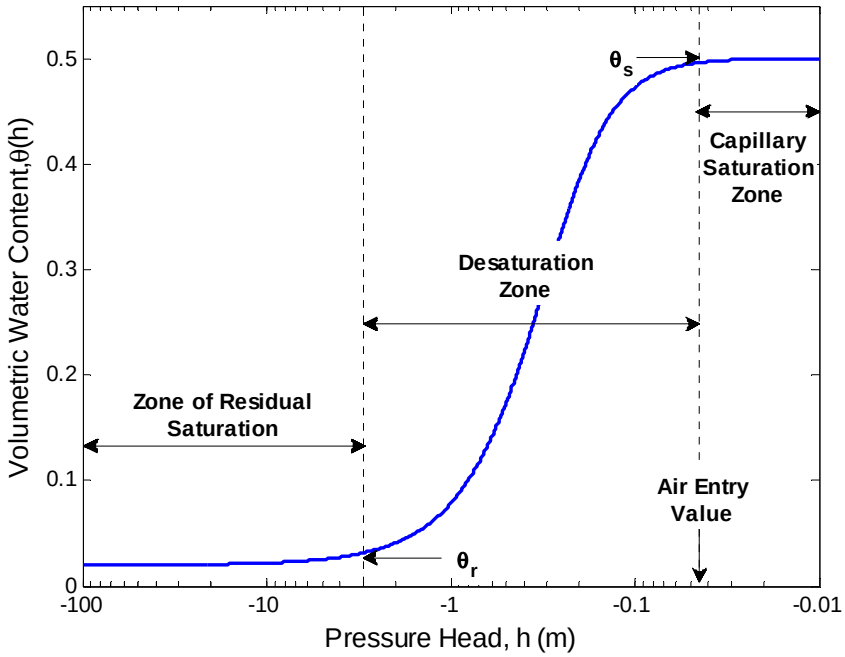

Fig. 3.4: A typical water retention curve showing approximate locations of the residual water content θ_r, the saturated water content θ_s and the air entry pressure ψ_A. The figure shows also the different zones within a drying cycle.

As shown in **Fig. 3.4**, three stages related to the process of desaturation (i.e. increasing soil suction) can be described as follows (Sillers et al., 2001):

A. Capillary saturation zone: the pore-water is in tension in this zone, however, the soil remains essentially saturated due to capillary forces. The capillary saturation zone continues up to the air entry value or bubbling pressure (h_b). The air-entry value describes the matric suction that must be exceeded before air recedes into the soil pores (and at which the largest pores begin to drain) (Reinson et al., 2005). The air-entry value

is a function of the size of the largest pores. Coarse-grained soils may start to drain immediately following the application of small matric suction.

B. Desaturation zone: after the air entry value, the volumetric water content decreases more rapidly, the liquid water within the pores is increasingly displaced by air in the desaturation zone. The desaturation zone ends at the residual water content θ_r, where pore-water becomes essentially immobile within the soil matrix. Increases in soil suction do not result in significant changes in water content and large suction change is required to remove additional water from the soil (Fredlund and Xing, 1994).

C. Zone of residual saturation: the liquid water is tightly held to the soil. In this zone, the term soil suction loses its physical significance and can then better be regarded as an equivalent term for the energy required for the withdrawal water from a unit mass of soil.

Fig. 3.5 shows three typical soil-water characteristic curves for a clay, silt and sand. The saturated water content (θ_r) generally increases with the plasticity of the soil (Fredlund and Xing, 1994) . The air entry (h_b) value for the soils tends to increase as the soil particles become finer. Also, the slope of the curve in the desaturation zone tends to become flatter as the soil particles become finer (Sillers et al., 2001).

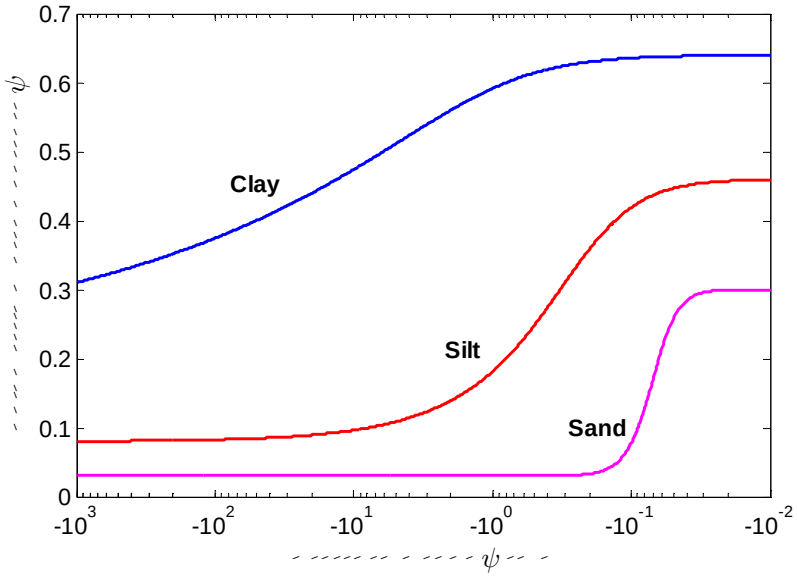

Fig. 3.5: Water retention curves for a clay, silt and sand.

Experimental data for the water retention curve can be obtained from laboratory tests. A mathematical function can then be fitted to the measured data. Many mathematical models have been proposed in the literature for representing the water retention curve. For example, Brooks and Corey (1964), Brutsaert (1966), Campbell (1974), van Genuchten (1980) and the Fredlund and Xing (1994). A summary of these models are given in Table 3.1.

Table 3.1 : Models of water retention curve $\boldsymbol{\theta(h)}$

Model Name	**Model**		**Fit. parameters**
Gardner (1956)	$\frac{\theta-\theta_r}{\theta_s-\theta_r}=\frac{1}{1+a\psi^n}$	**Eq. 3.17**	2 fit. parameters: a and n
Brooks and Corey (1964)	$\begin{cases}\frac{\theta-\theta_r}{\theta_s-\theta_r}=1 & \psi<a\\ \frac{\theta-\theta_r}{\theta_s-\theta_r}=\left(\frac{\psi}{a}\right)^{-n} & \psi>a\end{cases}$	**Eq. 3.18**	2 fit. parameters: a and n
Brutsaert (1966)	$\frac{\theta-\theta_r}{\theta_s-\theta_r}=\frac{1}{1+\left(\frac{\psi}{a}\right)^n}$	**Eq. 3.19**	2 fit. parameters: a and n
Tani (1982)	$\frac{\theta-\theta_r}{\theta_s-\theta_r}=\left(1+\frac{a-\psi}{a-n}\right)\exp\left(-\frac{a-\psi}{a-n}\right)$	**Eq. 3.20**	2 fit. parameters: a and n
McKee and Bumb (1984) *(Boltzman distribution)*	$\begin{cases}\frac{\theta-\theta_r}{\theta_s-\theta_r}=1 & \psi<a\\ \frac{\theta-\theta_r}{\theta_s-\theta_r}=\exp\left(\frac{a-\psi}{n}\right) & \psi>a\end{cases}$	**Eq. 3.21**	2 fit. parameters: a and n
van Genuchten (1980)	$\frac{\theta-\theta_r}{\theta_s-\theta_r}=\frac{1}{[1+(a\psi)^n]^m}$	**Eq. 3.22**	3 fit. parameters: a, n and m
	If m parameter is assumed to be a function of n (eliminating m as a fitting parameter), then:		2 fit. parameters: a and n
	+ Burdine (1953) $m=1-2/n$	**Eq. 3.23**	
	+ Mualem (1976) $m=1-1/n$	**Eq. 3.24**	
Fredlund and Xing (1994)	$\frac{\theta-\theta_r}{\theta_s-\theta_r}=\frac{1}{\left[\ln\left(\mathrm{e}+\left(\frac{\psi}{a}\right)^n\right)\right]^m}$	**Eq. 3.25**	3 fit. parameters: a, n and m

In the previous table; a, n and m are the fitting parameters of the model and can be generally described as follow:

- a parameter is related to the air entry value (Brooks and Corey, Fredlund and Xing, Brutsaert, McKee and Bumb) or to the inverse of the air entry value of the porous media (Gardner, van Genuchten) .
- n parameter is related to the pore size distribution of the porous media or the rate of change of the desaturation zone of the soil-water characteristic curve for most of the models above. In Brooks and Corey model n is termed the pore size index. In Tani model, n is equal to the soil suction at the inflection point.
- m parameter is related to the overall symmetry of the model about the infection point.

Note also that ψ is the matric suction and it is related to the pressure head by: $\psi = -h$

3.3.5 Other constitutive relationships

The first constitutive relationship which is the relation between θ and h was discussed in details previously and the mathematical expressions of many models cited in the literature were given.

However in this section, a summary of the constitutive relationships for only two models is given. These models are implemented in the numerical code BIGFLOW 3D used throughout this thesis to model variably saturated flow; the models are:

- Exponential model (a modified form of the Boltzman model).
- van Genuchten-Mualem model.

The section presents the mathematical expression of the following constitutive relationships (*expressed in the form used in the numerical code BIGFLOW 3D*):

- The water retention curve function: $S_e(h)$ or $h(S_e)$
- Hydraulic conductivity function: $K(S_e)$ or $K(h)$
- Specific water capacity: $C(S_e)$ or $C(h)$
- Hydraulic diffusivity: $D(S_e)$ or $D(h)$

Exponential Model

Here, the exponential model is expressed in the form used in the numerical code BIGFLOW. It is to some extent another form of the McKee and Bumb (1984) model given in Table 3.1.

In the exponential model, water retention function $\theta(h)$ is defined as:

$$S_e(h) = \frac{\theta_e(h)}{\theta_{es}} = \frac{\theta(h) - \theta_r}{\theta_s - \theta_r} = e^{\beta(h-h_b)} \quad \text{if } h \le h_b$$
$$S_e(h) = \frac{\theta(h) - \theta_r}{\theta_s - \theta_r} = 1 \quad \text{if } h > h_b \qquad \textbf{Eq. 3.26}$$

And the hydraulic conductivity function $K(h)$ is given by:

$$K(h) = K_s e^{\alpha(h-h_b)} \quad \text{if } h \le h_b$$
$$K(h) = K_s \quad \text{if h} > \text{h}_\text{b} \qquad \textbf{Eq. 3.27}$$

where:

h_b is the bubbling pressure head or the air entry value.

S_e is the effective saturation.

θ is the volumetric water content.

θ_r is the residual water content.

θ_s is the saturated water content.

θ_e is the effective water content (= $\theta - \theta_r$).

α, β are the model parameters.

Note that: It is common to normalize the hydraulic conductivity given in the above equations with respect to their maximum values at saturation (K_s). This normalized value, referred to as relative conductivity and it may be written as:

$$K_r = \frac{K}{K_s} = e^{\alpha(h-h_b)} \quad \text{if } h \le h_b$$
$$K_r = 1 \quad \text{if h} > \text{h}_\text{b} \qquad \textbf{Eq. 3.28}$$

The specific water capacity: (derived from Eq. 3.15)

$$C(h) = \beta\theta_{es}e^{\beta(h-h_b)} \quad \textbf{Eq. 3.29}$$

or in terms of S_e

$$C(S_e) = \beta\theta_{es}S_e \quad \textbf{Eq. 3.30}$$

The soil water diffusivity can also be deduced using Eq. 3.16 as follow:

$$D(S_e) = \frac{K_s}{\beta\theta_{es}}S_e^{(\alpha-\beta)/\beta} \quad \textbf{Eq. 3.31}$$

van Genuchten-Mualem Model

In this study, the van Genuchten (1980) soil water characteristic function coupled with Mualem (1976) conductivity function was adopted. van Genuchten model is generally thought to match experimental data more satisfactorily than others (Zhu, 2007).

The model proposed by van Genuchten is as follows:

$$S_e(h) = \frac{\theta_e(h)}{\theta_{es}} = \frac{\theta - \theta_r}{\theta_s - \theta_r} = \frac{1}{[1 + (-\alpha h)^n]^m} \quad \textbf{Eq. 3.32}$$

Where: α, n, m are the model shape parameters.

Note that the van Genuchten approach does not consider any effect of hysteresis; it formulates an average wetting/drainage behavior.

Furthermore, if $m = 1 - 1/n$ (Mualem (1976)); then the Mualem-based relative hydraulic conductivity can be written in terms of the parameters of Eq. 3.32.

$$K_r(S_e) = {S_e}^{1/2}\left[1 - \left(1 - {S_e}^{1/m}\right)^m\right]^2 \quad \textbf{Eq. 3.33}$$

Where $K_r = K/K_s$ and K_s is the saturated hydraulic conductivity.

Also we can express the relative hydraulic conductivity in terms of pressure head as:

$$K_r(h) = \frac{1}{(1 + (-\alpha h)^n)^{m/2}}\left(1 - \left[1 - \frac{1}{(1 + (-\alpha h)^n)}\right]^m\right)^2 \quad \textbf{Eq. 3.34}$$

Moreover; the specific moisture capacity can be derived using Eq. 3.15,

$$C(h) = \frac{mn\alpha\theta_{es}(-\alpha h)^{n-1}}{(1 + (-\alpha h)^n)^{m+1}} \quad \textbf{Eq. 3.35}$$

or in terms of S_e

$$C(S_e) = mn\alpha\theta_{es}{S_e}^{1+1/m}\left({S_e}^{-1/m} - 1\right)^{1-1/n} \quad \textbf{Eq. 3.36}$$

The soil water diffusivity can also be deduced using Eq. 3.16 as follow:

$$D(S_e) = \frac{(1-m)K_s}{\alpha m\theta_{es}} S_e^{0.5-1/m}\left[\left(1 - S_e^{1/m}\right)^{-m} + \left(1 - S_e^{1/m}\right)^{m} - 2\right] \quad \textbf{Eq. 3.37}$$

Another important property of the van Genuchten-Mualem model is the point of the inflection of the water retention curve at which the specific moisture capacity is maximum. The suction head at this point can be treated as a global capillary length scale of the porous media and is defined by:

$$\lambda_{CAP} = \frac{1}{\alpha}\left(1 - \frac{1}{n}\right)^{1/n} \quad \textbf{Eq. 3.38}$$

Note: Unless stated otherwise, the numerical simulations presented in this thesis are based on the van Genuchten-Mualem model.

The advantages of the van Genuchten-Mualem model can be summarized as follows:

- The van Genuchten-Mualem model is commonly referred to in the literature. It is one of the most widely used models (Hodnett and Tomasella, 2002).
- It provides a wide range of flexibility, allowing it to provide a reasonable fit of data from a variety of soils.
- It better captures the sigmoidal shape of typical curves. Smooth transitions at the air-entry pressure and for suction approaching the residual condition are more effectively captured (Lu and Likos, 2004).
- The model parameters have physical meaning; the effect of one soil parameter can be distinguished from the effect of the other two parameters. (Sillers et al., 2001).
- The m assumption ($m = 1 - 1/n$) reduces the f exibility of the van Genuchten model but signif cantly simplify it, thus resulting in greater stability during parameter optimization and permitting closed-form solution of the hydraulic conductivity function (Genuchten et al., 1991).

3.3.6 Nature of the van Genuchten-Mualem fitting parameters

As described previously, the van Genuchten-Mualem model has two fitting parameters: the α-parameter and the n-parameter.

With respect to the m-parameter, Mualem suggested a fixed relationship to be assumed between the n and m parameters (i.e. $m = 1 - 1/n$).

Fig. 3.6 shows a plot of the van Genuchten-Mualem model with a fixed n-parameter (i.e. n equal to 2.0) and a variable α-parameter. The α-parameter has units corresponding to the inverse of soil suction and it approximates the inverse of the air-entry head or the height of the capillary fringe. However, it is clear that the inverse of the α-parameter is larger than the air entry value.

As shown in **Fig. 3.6**, the α-parameter does not affect the shape of the curve but shifts the curve toward the higher or lower suction region of the plot. Porous media with relatively high air-entry pressure are characterized by smaller values of the α-parameter.

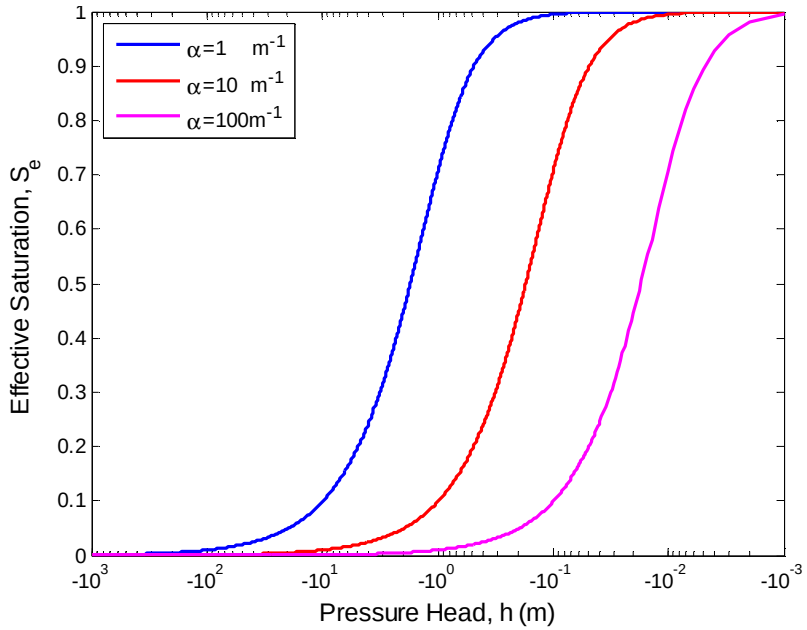

Fig. 3.6: Effect of the parameter "alpha" of the van Genuchten-Mualem model on the shape of the water retention curve, (alpha variable, n= 2, m=1-1/n).

On the other hand, **Fig. 3.7** shows the effect of varying the n-parameter with the α-parameter being constant (i.e. α= 1 m^{-1}). The n-parameter is related to the pore size distribution index. The more uniform the pore size in the soil, the larger the value of n. As shown in **Fig. 3.7**, the parameter n specif es the steepness of the water-release curve. If n is large, then the curve is steep, and the water content decreases quickly as the suction head becomes more negative. If n is small, then the change in water content is slow (Gau et al., 2006).

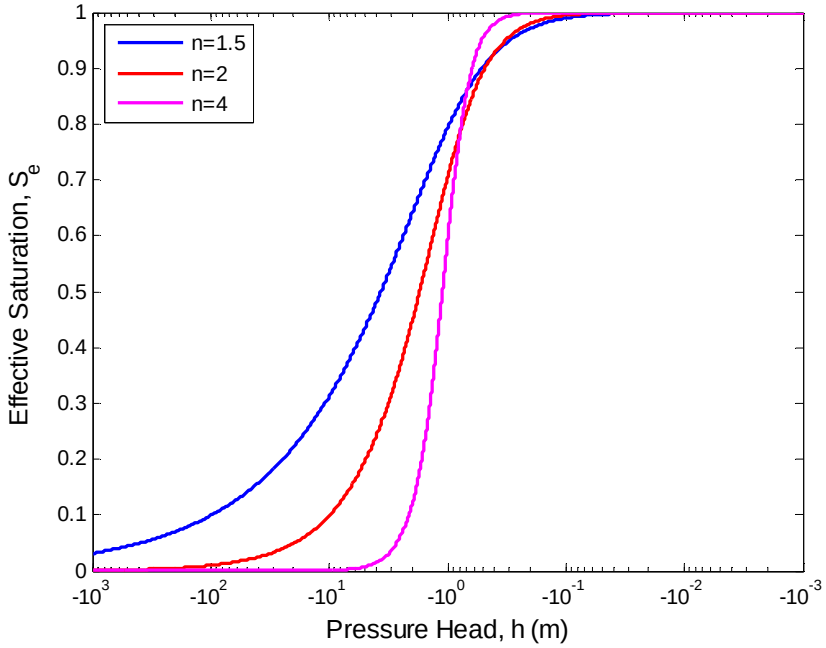

Fig. 3.7: Effect of the parameter n of the van Genuchten-Mualem model on the shape of the water retention curve, (alpha=1 m^{-1}, n= variable, m=1-1/n).

Chapter 4

Numerical Code Description and Validation Tests

(with Soil parameters and Time Characteristic Identification)

4.1 Introduction

This chapter provides a review of the numerical code used in this thesis to simulate variably saturated/unsaturated flow in porous media (BIGFLOW). The main code, the pre- and post-processors, the computational domain, and the boundary conditions, are briefly discussed. Finally, a validation test for the numerical procedure is proposed and analyzed through the concepts of the infiltration theory; physical interpretations of the results in terms of hydraulic conductivity, capillary effects, sorptivity and gravitational time scale are also given.

4.2 Numerical model description: BIGFLOW 3D code

4.2.1 Model review

The numerical code BIGFLOW 3D was initially developed at Massachusetts Institute of technology (MIT) (Ababou, 1988) as a research tool for high resolution simulation of 3D groundwater and was tested for high-performance computations (Ababou et al., 1992a). The current BIGFLOW package is the result of subsequent modifications over years aimed at enhancing its scope, flexibility and computational efficiency.

BIGFLOW can efficiently model large three dimensional (3D) flow systems in unsaturated, partially saturated or saturated heterogeneous porous media. It is able to represent multiple free surface dynamics in (x,y,z,t). Also, the model accounts for capillary effects in the unsaturated zone.

BIGFLOW code is based on implicit finite difference (or finite volumes), with sparse Preconditioned Conjugate Gradient matrix solver, and modified Picard iterations for nonlinear problems. The time step is generally variable and self adjusted.

The governing equations are discretized by a seven-point centered finite difference scheme in 3D space and a backwards (fully implicit) finite difference scheme in time. Since the discrete system is fully implicit in time, the case of a steady-state is handled by making the transient term zero and solving for only one (virtually infinite) time step. As explained above, the nonlinear flow problem, unsaturated or partially saturated, is approximately linearized by a modified Picard scheme. Thus, an approximate linear system has to be solved at each iteration step, and this is repeated for each time step. The linear or linearized finite difference system is solved by using a preconditioned iterative method (sparse Preconditioned Conjugate Gradient matrix solver). For the nonlinear case, this yields a doubly iterative cycle: outer iterations for linearization and inner iterations for solution of a linear system **Fig. 4.1** (Ababou and Bagtzoglou, 1993).

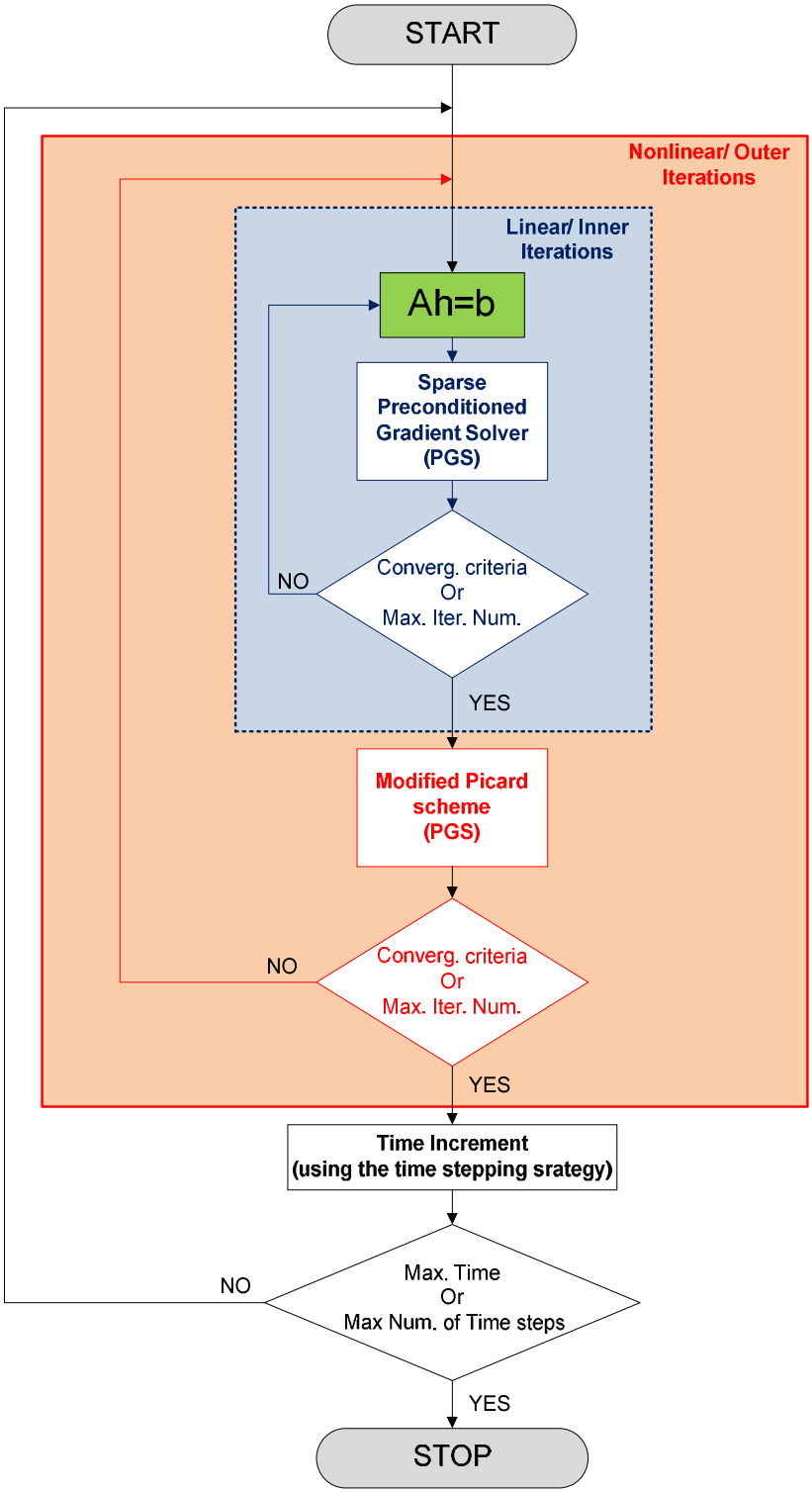

Fig. 4.1 Simplified schematic of the principle iterations in BIGFLOW 3D.

This model is fully 3D. However, 1D (column) or 2D (slice) simplified tests are simulated as "3D volumetric" by shrinking some dimensions to a few nodes, at least one interior node plus two boundary nodes along any unmodeled dimension. The 2D and 1D solution is obtained from the numerical output at the middle node for the 1D case and middle slice for the 2D case (Ababou and Bagtzoglou, 1993).

Hereafter we briefly described this numerical package. More details on BIGFLOW can be found in the literatures like: (Ababou, 2008, Ababou, 1991, Ababou and Al-Bitar, 2008, Ababou and Al-Bitar, 2004, Ababou and Bagtzoglou, 1993, Ababou et al., 1992c, Ababou et al., 1992b, Ababou and Trégarot, 2002, Bailly et al., 2009, Wang Y. et al., 2008, Trégarot, 2000).

4.2.2 BIGFLOW main processes

A graphical user interface (GUI) with Python 2.3 was developed to allow interactive data entry, manipulation, and analysis of the 3D numerical data sets. The interface allows an easier setup and diagnostics of the numerical experiments. It is also managed the different processes and simulation tasks in BIGFLOW. It comprises 3 main phases as follows (**Fig. 4.2**):

1. The preprocessing phase includes data entering and the creation of the input files (input1, input2, input3 to input9). In this stage the boundary conditions, initial conditions and material properties are defined and set up.
2. In the processing phase the simulator code is executed. The output results (head, water content, flux, mass balance and convergence) are saved in appropriate files.
3. The post-processing phase includes an auxiliary graphics display through the associated graphical tools.

Furthermore, a MatLab graphical user interface a complete *MatLab package programs* for further analysis and display of the output results have been developed in this thesis.

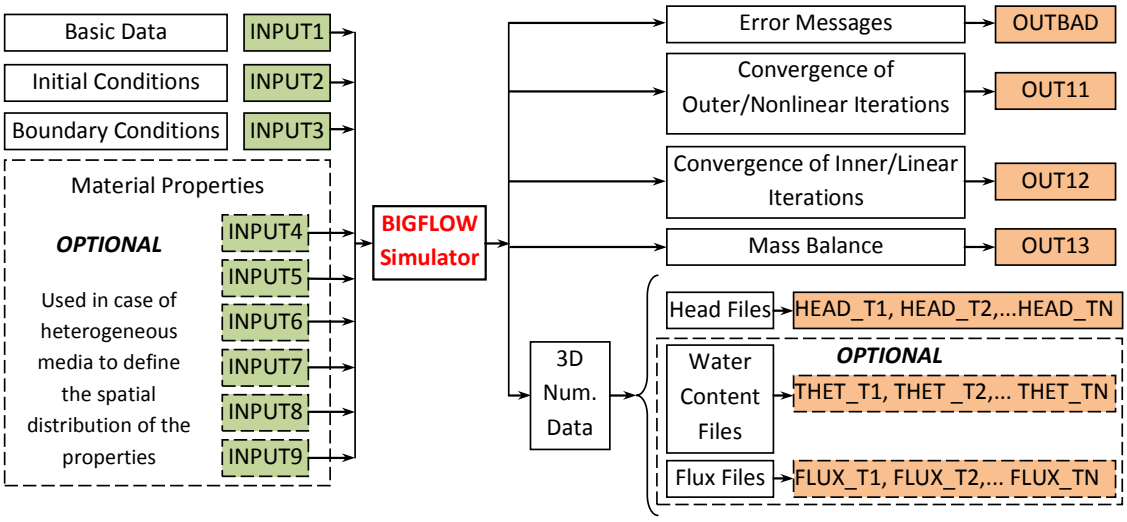

Fig. 4.2: Schematic of the input/output files in BIGFLOW 3D.

4.2.3 Computational domain

The computational domain is a rectangular parallelepiped, whose coordinate system may be inclined at arbitrary angles with respect to the natural, horizontal-vertical coordinate system. The later is done by changing the direction of the gravity vector with respect to the coordinate system attached to the flow domain.

4.2.4 Boundary conditions

The boundary conditions implemented in BIGFLOW are of three main types:

- Pressure conditions (Dirichlet).
- Normal flux condition (Neumann).
- Gravity drainage or null pressure gradient: it is peculiar to the unsaturated flow and can be implemented for the lower horizontal boundary.

Spatially variable and mixed-type boundary conditions can be applied separately for each of the six boundary planes. Mixed type means that the type of conditions can vary over the boundary plane.

Currently, R. Ababou, Y. Wang and K. Alastal (this thesis) modified BIGFLOW to handle oscillatory *random time-varying pressure head boundary condition* (pressure boundary conditions that vary with time). This modification is very important in order to simulate wave or tide action on a porous media. Details of implementing this type of boundary condition in BIGFLOW are presented in (Wang, 2010).

In this thesis, this type of boundary condition is used to:

- model an oscillatory pressure condition at a bottom boundary of 1D column.
- apply a time varying pressure head at the lateral side of the 2D numerical domain to simulate the effect of tides and waves on sandy beaches (with vertical and sloping beach face).

Furthermore, a new MatLab graphical user interface (GUI) was developed in this thesis to implement this new time varying boundary condition and also to enhance the code with respect to the input and output processes and visualizing.

4.2.5 Equational model implemented in BIGFLOW 3D

The equational model being solved is a generalized Richards equation (Darcy-type equation, with a mixed formulation of mass conservation, cf section 3.3), capable of simulating various types of flows within the same domain. BIGFLOW's generic equation, for 3D is of the form:

$$\begin{cases} \dfrac{\partial \theta_e(h)}{\partial t} = -\nabla \cdot \vec{q} \\ \vec{q} = -K(h,\vec{x})\nabla H \\ H = h + \hat{g} \cdot \vec{x} \end{cases} \qquad \textbf{Eq. 4.1}$$

Where only the first equation is actually solved, once the second and third equations have been inserted. As described previously in *chapter 2*, the first equation expresses mass conservation in a partially saturated medium with known water retention curve $\theta(h)$; the second equation is the generalized Darcy-Buckingham equation for saturated/unsaturated flow which considered as a nonlinear flux-gradient head loss law with tensorial hydraulic conductivity (K); and the third equation is the relation between total head (H) and pressure head (h) via a normalized gravitational vector ($\hat{g}$).

Two main functional models (constitutive relationships) are implemented in BIGFLOW for the nonlinear curves:

- van Genuchten-Mualem model(VGM).
- Exponential model (EXP).

Detailed description of these two models was given previously in chapter 3 (cf section 3.3.4, 3.3.5 and 3.3.6).

4.3 Validation test with continuous unsaturated infiltration

In this section, 1D continuous infiltration through a semi-infinite homogeneous soil is used to validate the numerical procedure, using the Van Genuchten/Mualem model in BIGFLOW 3D. The numerical results are compared with those of Philip's series solution, which was programmed in MatLab after the method of Vauclin et al (Vauclin et al., 1979). Permeability related parameter and sorptivity are identified from the numerical cumulative infiltration rate via an optimal fit procedure, and compared to the actual permeability and sorptivity (the latter is deduced from other parameters through Parlange's expression).

As noted previously, (c.f section 3.3.5), and due to many advantages, the numerical simulations presented in this thesis are almost based on the van Genuchten-Mualem model. Therefore, the validation test here is restricted to the case where the constitutive relationships is defined using this model.

4.3.1 Theoretical background: The infiltration theory

Over the past years, numerous analytical and semi-empirical equations for 1D infiltration have been developed (Green and Ampt, 1911, Horton, 1940, Philip, 1957).

Philip (Philip, 1969, Philip, 1957) develop a quasi-analytical solution for the theta-based form of Richards' equation (Eq.2.14) rewritten here:

$$\frac{\partial \theta}{\partial t} = \frac{\partial}{\partial z}\left(D(\theta)\frac{\partial \theta}{\partial z}\right) - \frac{\partial K(\theta)}{\partial z} \qquad \textbf{Eq. 4.2}$$

Philip assumed a semi-infinite medium with uniform initial conditions and constant head boundary conditions as follows:

Initial condition: $\mathrm{t} = 0\ ,\ z > 0,\ \theta = \theta_0$

Boundary condition: $t \geq 0,\ \ z = 0,\ \theta = \theta_1$ **Eq. 4.3**

The solution is assumed to be a power series of $t^{1/2}$:

$$z(\theta, t) = \sum_{n=1}^{N} \emptyset_n(\theta)\ t^{n/2} \qquad \textbf{Eq. 4.4}$$

where n is the number of terms in the series solution. For 4 terms, we get the following:

$$z(\theta, t) = \emptyset_1(\theta)\ t^{1/2} + \emptyset_2(\theta)\ t + \ \emptyset_3(\theta) t^{3/2} + \ \emptyset_4(\theta) t^2 \qquad \textbf{Eq. 4.5}$$

where the first term $[\emptyset_1(\theta)]$ embodies the influence of the capillary forces on the flow process, and the following terms $[\emptyset_2(\theta),\ \emptyset_3(\theta),\ \emptyset_4(\theta)]$ reflect the gravity effect on infiltration. The functions $\emptyset_i(\theta)$, are given by Philip as follows:

$$\int_{\theta_0}^{\theta} \emptyset_1 d\theta = -2\frac{D}{\emptyset_1'}$$

$$\int_{\theta_0}^{\theta} \emptyset_2 d\theta = \frac{D\emptyset_2'}{(\emptyset_1')^2} + (K(\theta) - K_0)$$

$$\int_{\theta_0}^{\theta} \emptyset_3 d\theta = \frac{2D}{3}\left[\frac{\emptyset_3'}{(\emptyset_1')^2} - \frac{(\emptyset_2')^2}{(\emptyset_1')^3}\right] \qquad \textbf{Eq. 4.6}$$

$$\int_{\theta_0}^{\theta} \emptyset_4 d\theta = \frac{D}{2}\left[\frac{\emptyset_4'}{(\emptyset_1')^2} - \frac{(\emptyset_2')^2}{(\emptyset_1')^3}\left\{2\frac{\emptyset_3'}{\emptyset_2'} - \frac{\emptyset_2'}{\emptyset_1'}\right\}\right]$$

Where the prime in the above equations signifies differentiation with respect to θ. (Vauclin et al., 1979) solved the above equation numerically. In this thesis, the numerical method proposed by Vauclin et al. was programmed in MatLab and used for comparison purposes as described later.

Furthermore, the cumulative infiltration $I(t)$ is obtained from:

$$I(t) - K_0 t = \int_0^{\infty} (\theta - \theta_0) dz = \int_{\theta_0}^{\theta_1} z\ d\theta \qquad \textbf{Eq. 4.7}$$

Where K_0 is the initial hydraulic conductivity. Putting Eq. 4.5 into Eq. 4.7 , we obtain the series solution of the cumulative infiltration I (in meters) as a function of time:

$$I(t) = St^{1/2} + (A_2 + K_0)t + A_3t^{3/2} + A_4t^2 + \cdots \quad \textbf{Eq. 4.8}$$

Where:

- $S = \int_{\theta_0}^{\theta_1} \emptyset_1 d\theta$ known as the sorptivity which characterizes the ability of the soil to absorb water by capillary diffusion (in the absence of gravity).
- $A_2, A_3, A_4 \ldots$ are given by $A_n = \int_{\theta_0}^{\theta_1} \emptyset_n d\theta \quad n = 2, 3, 4, \ldots$ reflect the effects of gravity.
- Note that: the sorptivity 'S' and the A's are not only soil characteristics but also depend on the initial (θ_0) and boundary (θ_1) conditions.

In practice, it is sufficient to use the two-parameter equation of the form:

$$I(t) = St^{1/2} + At \quad \textbf{Eq. 4.9}$$

The corresponding rate of infiltration $i(t)$ (m/s) is obtained by differentiating the cumulative infiltration $I(t)$ with respect to time:

$$i(t) = \frac{d\, I(t)}{dt} = \frac{1}{2}St^{-1/2} + A \quad \textbf{Eq. 4.10}$$

One of the problems involved in Philip's solution is that the time series solution becomes divergent for large times no matter how many terms are developed. Thus the above solution is valid only for a limited time range. The time limit is mostly set at t_{GRAV} (a time for which the gravity forces are supposed to become predominant over the capillary forces):

$$t_{GRAV} = \left(\frac{S(\theta_1, \theta_0,)}{K_1 - K_0}\right)^2 \quad \textbf{Eq. 4.11}$$

For large time, Philip derived a solution which is usually known as the solution at infinity.

In the case of horizontal infiltration, the gravity terms (the A's parameter in Eq. 4.8) are dropped and the cumulative infiltration is given by:

$$I(t) = St^{1/2} \qquad \textbf{Eq. 4.12}$$

Therefore, the sorptivity can be obtained from horizontal infiltration as: $S = I/t^{1/2}$

Finally, a different solution of infiltration was proposed by (Parlange, 1975) resulting in the following sorptivity expression:

$$S^2 = \int_{\theta_0}^{\theta_1} [\theta_1 + \theta - 2\theta_0] D(\theta) d\theta \qquad \textbf{Eq. 4.13}$$

4.3.2 Validation tests

In this test, unsaturated transient infiltration in a vertical column was simulated. A homogeneous soil column with the initial and boundary conditions shown in **Fig. 4.3** is used for simulating the 1D infiltration problem in BIGFLOW code. The initial condition is a uniform pressure head (equals $-h_0$). The pressure head at the upper boundary was held at a value corresponding to saturation ($h = 0$). The bottom boundary was held constant at the initial pressure head ($-h_0$). Transient infiltration of moisture in the vertical direction resulted from both capillary forces and gravity.

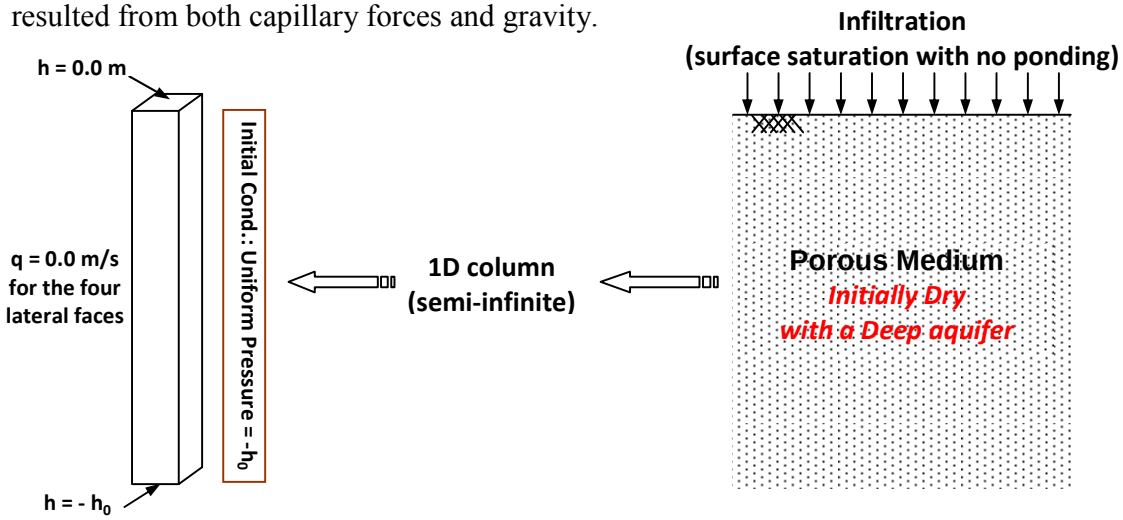

Fig. 4.3: Initial and boundary conditions used in the infiltration test for the different soils.

Three different porous media are used in the simulation: medium sand, fine sand and loam (named PM1, PM2 and PM3 respectively). Table 1 gives the hydraulic characteristics of these media. While the parameters of the first and third porous media (PM1 and PM3) were taken from the literature, the second porous medium was the same

as the one used by (Wang, 2010) in her wetting sand experiment. **Fig. 4.4** shows the water retention curves of these three PM.

(a)

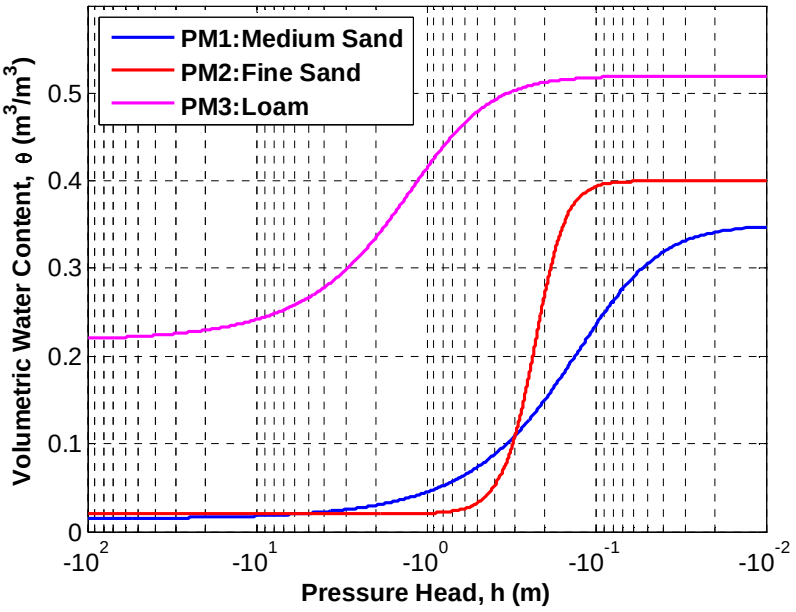

(b)

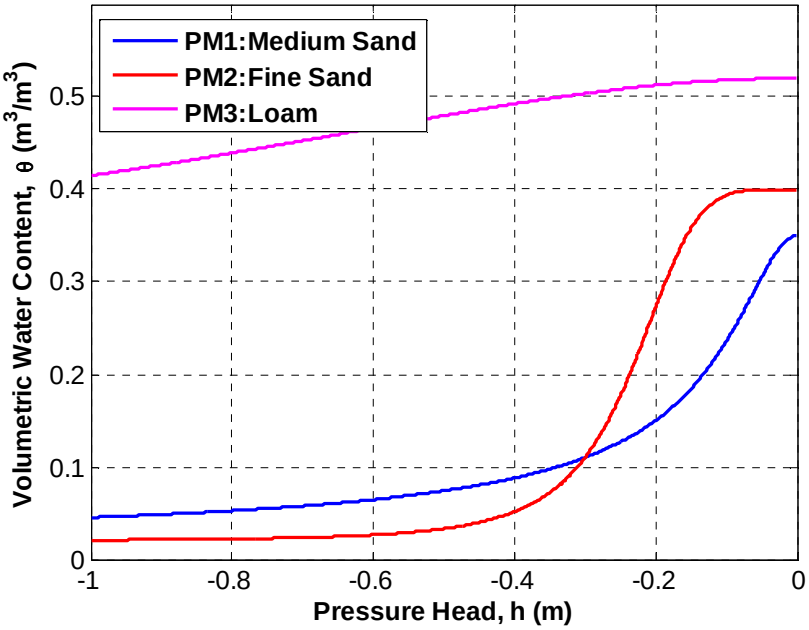

Fig. 4.4: Water retention curve for the three porous media used in the simulation. The figures are presented in different scale for the suction head: (a) in logarithmic scale, (b) in linear scale with a zoom taken between 0 and -1m of suction pressure.

Table 4.1 : Hydraulic characteristics of porous media used in the simulation

Parameters		**Soil No.1 Medium Sand**	**Soil No.2 Fine Sand**	**Soil No.3 Guelph Loam**
K_s (m/s)		2.0×10^{-4}	1.5×10^{-4}	3.66×10^{-6}
θ_s		0.35	0.40	0.52
θ_r		0.0147	0.02	0.218
VGM model parameters	α (m^{-1})	11.47	4.6	1.15
	$1/\alpha$ (cm)	8.71	21.74	86.95
	λ_{CAP} (cm)	6.11	20.79	62.25
	n	1.98	5	2.03

The validation procedure is as the following (see Fig. 4.5):

1. Perform 1D horizontal infiltration simulation using BIGFLOW 3D, this allows us to obtain the sorptivity parameter from Eq. 4.12 through a linear fitting of the I vs $\sqrt{t}$ relation. Then, compare this value to:
   - The sorptivity obtained by Philip's series solution via a MatLab code written in this thesis after the method of (Vauclin et al., 1979).
   - The sorptivity calculated by (Eq. 4.13) given by (Parlange, 1975) and programmed in this thesis in using the quadl MatLab function.
2. Perform 1D vertical infiltration simulation using BIGFLOW 3D, then:
   - Compare the BIGFLOW evoluted moisture content profile with those obtained from Philip's series solution.
   - Compare the *A*-parameter (Eq. 4.9) obtained from an optimal fit procedure of the $I/\sqrt{t}$ versus$\sqrt{t}$ curve resulted from BIGFLOW simulation to the saturated hydraulic conductivity K_s . The two terms are related by the simple relation : $A = \lambda K_s$. Where the interval of variation for the dimensionless ratio $\lambda = A/K_s$ is limited within the range: $1/3 \leq (\lambda = A/K_S) \leq 2/3$

     as suggested in the literature (Fuentes et al., 1992, Philip, 1969, Valiantzas, 2010)

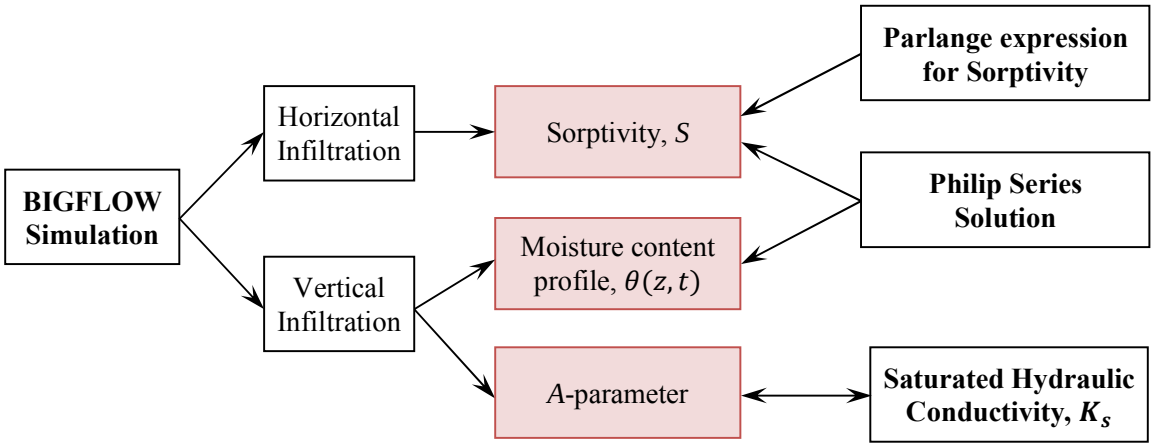

Fig. 4.5: Schematic diagram for the validation procedure and comparison.

4.3.3 Results and analysis

In the following, the results of horizontal and vertical infiltrations are presented. The numerical model results are compared to the quasi-analytical solutions.

In all simulations, suitable numerical parameters were chosen to obtain good numerical results in terms of mass balance (net boundary flux versus mass flux), and convergence of both nonlinear solver (Incremental Picard) and matrix solver (Preconditioned Conjugate Gradients with Diagonal Scaling).

Horizontal infiltration: Sorptivity comparison

Fig. 4.6, **Fig. 4.7** and **Fig. 4.8** show the result of BIGFLOW simulation of the horizontal infiltration for PM1, PM2 and PM3 respectively.

As shown in the figures, a stable linear and nonlinear convergence and a perfect mass balance are obtained.

The sorptivity values represent the slope of the line obtained by fitting a linear regression to I versus $\sqrt{t}$ points as shown in **Fig. 4.6**(d), **Fig. 4.7**(d) and **Fig. 4.8**(d).

The concept of sorptivity is addressed in some details here because it represents an important integral variable which links water retention and hydraulic conductivity characteristics and it may be helpful in obtaining a time-scale characteristic for PM.

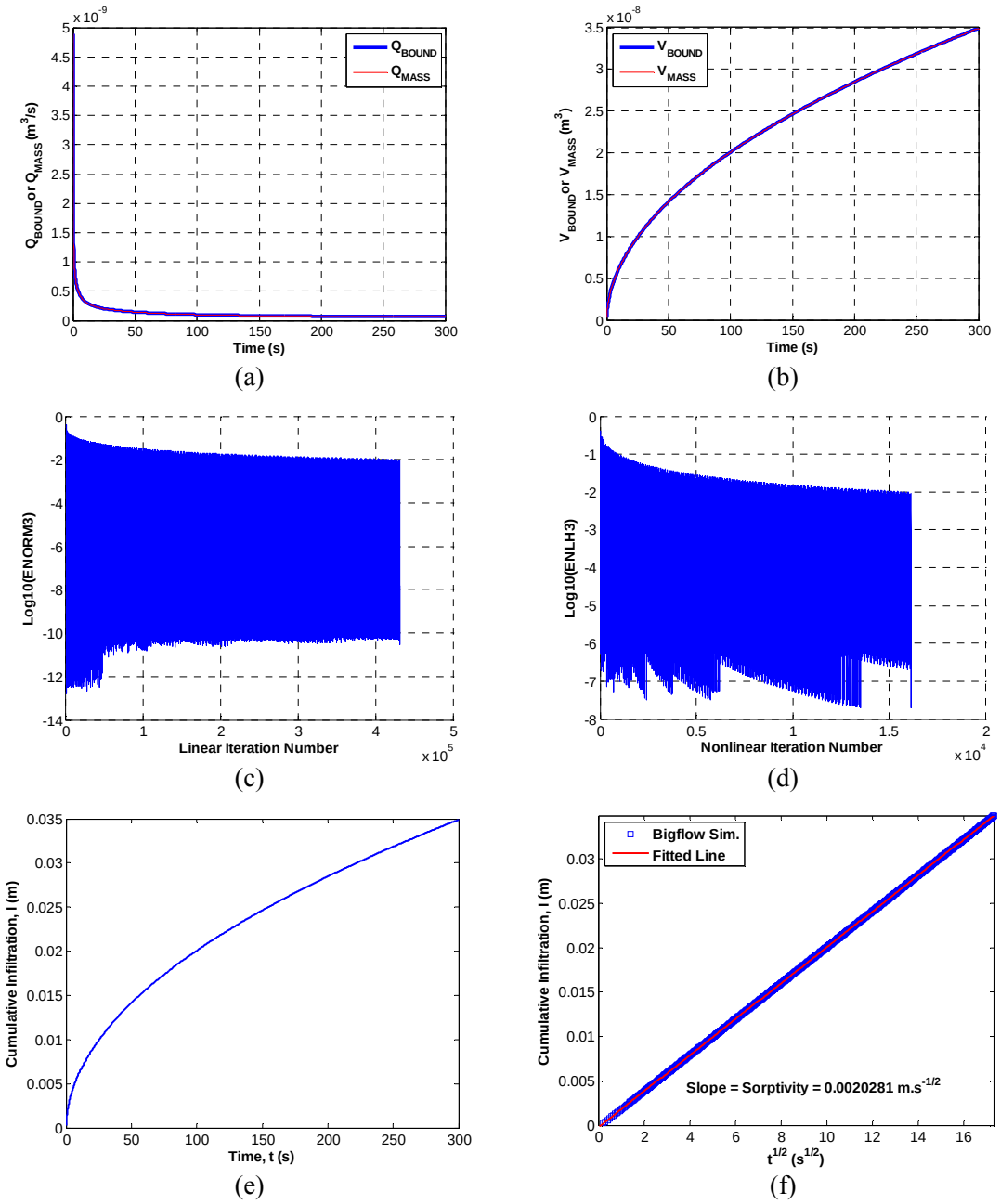

Fig. 4.6: BIGFLOW simulation results for horizontal infiltration case into medium sand (PM1): (a) Local mass balance: evolution of Q_{BOUND} and Q_{MASS}. (b) Global volume balance: evolution of V_{BOUND} and V_{MASS}. (c) Linear iteration convergence. (d) Nonlinear iteration convergence. (e) Evolution of the cumulative infiltration. (d) Sorptivity determination by fitting a linear regression line to I versus $\sqrt{t}$ data points.

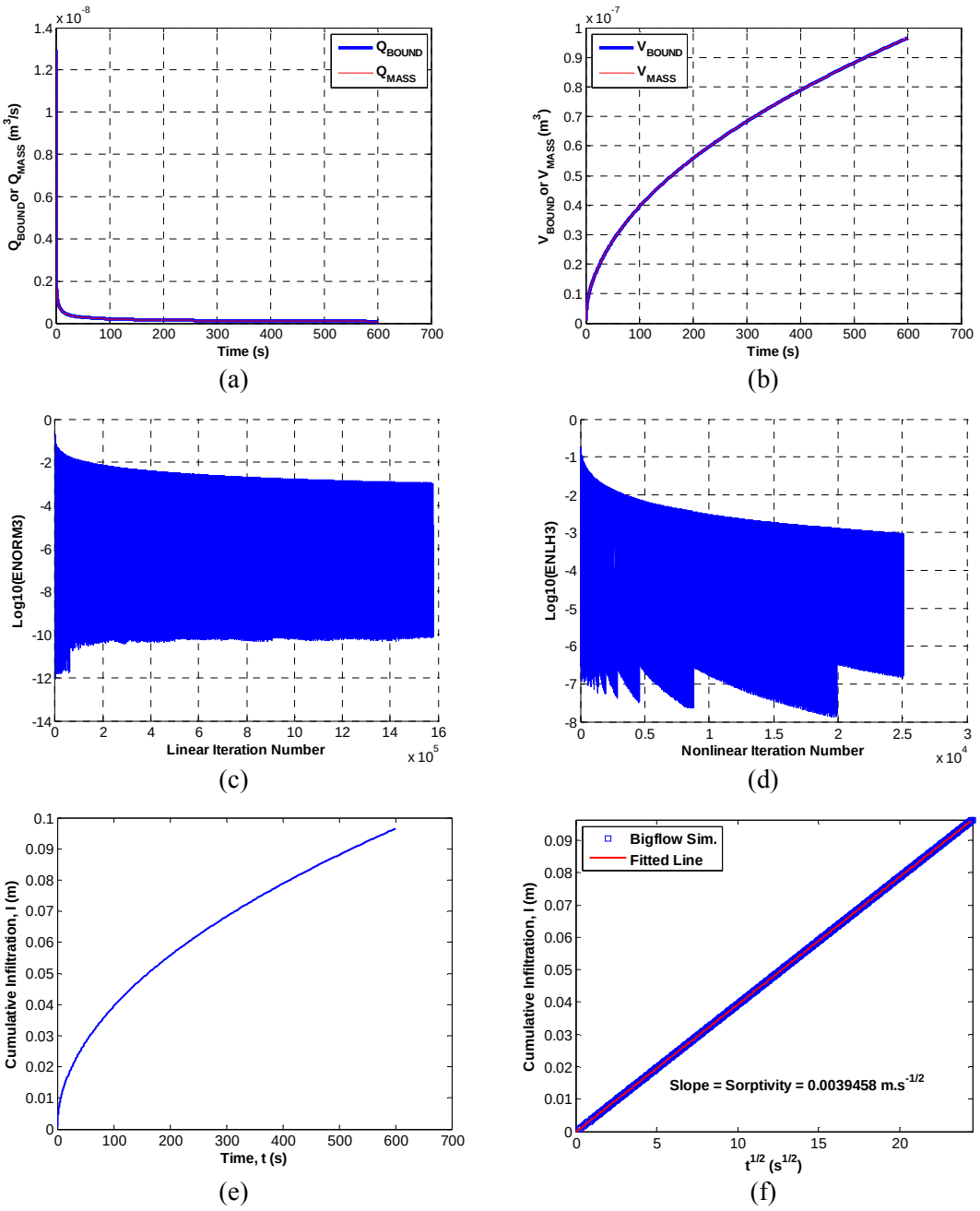

Fig. 4.7: BIGFLOW simulation results for horizontal infiltration case into fine sand (PM2): (a) Local mass balance: evolution of Q_{BOUND} and Q_{MASS}. (b) Global volume balance: evolution of V_{BOUND} and V_{MASS}. (c) Linear iteration convergence. (d) Nonlinear iteration convergence. (e) Evolution of the cumulative infiltration. (d) Sorptivity determination by fitting a linear regression line to I versus $\sqrt{t}$ data points.

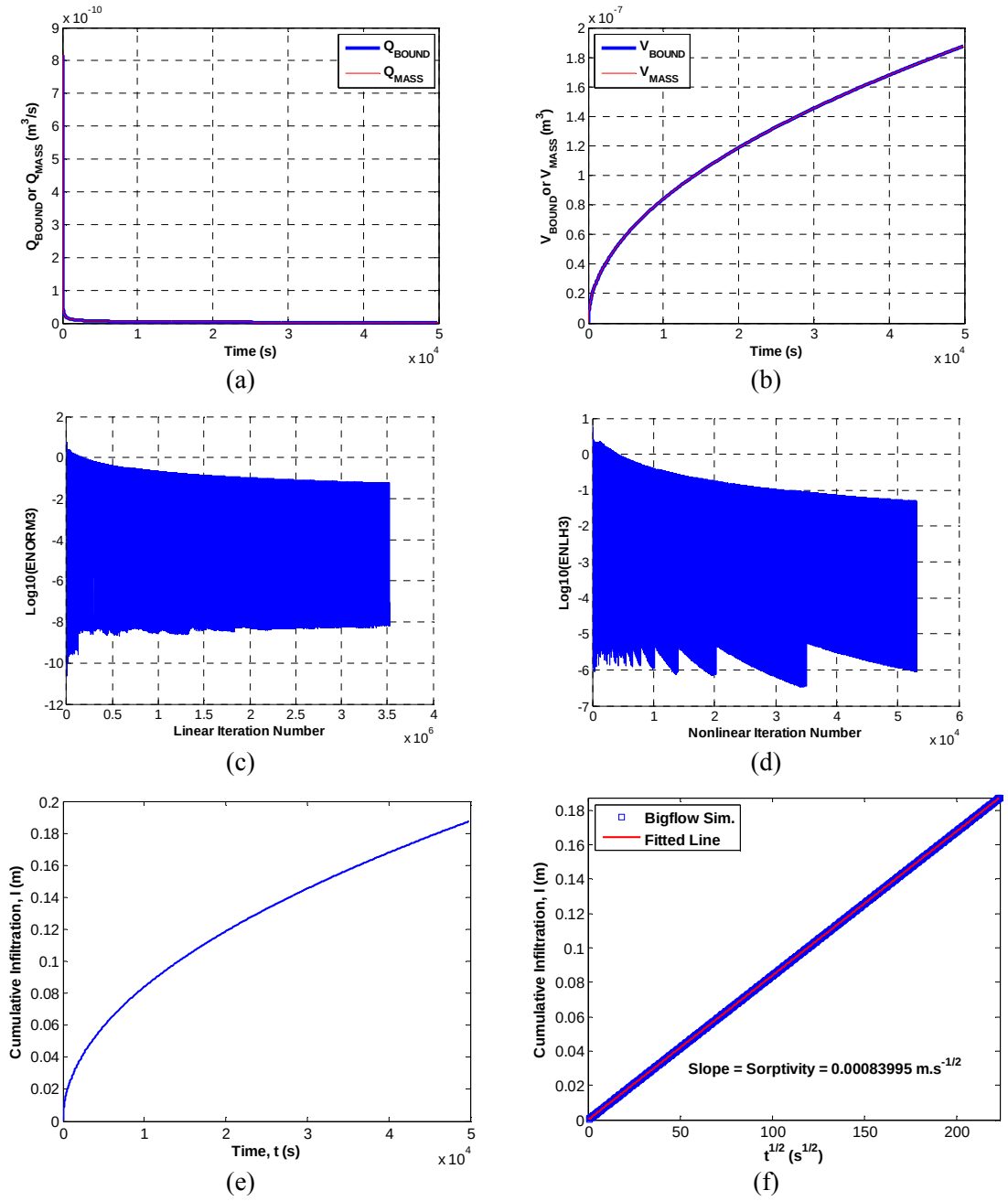

Fig. 4.8: BIGFLOW simulation results for horizontal infiltration case into Guelph loam (PM3): (a) Local mass balance: evolution of Q_{BOUND} and Q_{MASS}. (b) Global volume balance: evolution of V_{BOUND} and V_{MASS}. (c) Linear iteration convergence. (d) Nonlinear iteration convergence. (e) Evolution of the cumulative infiltration. (d) Sorptivity determination by fitting a linear regression line to I versus $\sqrt{t}$ data points.

The following table summarizes the sorptivity values obtained from different methods.

Table 4.2: Sorptivity values comparison

Sorptivity ($m/s^{1/2}$)	**Medium Sand PM1**	**Fine Sand PM2**	**Guelph Loam PM3**
BIGFLOW Simulation (linear fit of the results, see Fig. 4.6(d), Fig. 4.7(d) and Fig. 4.8(d) + Eq. 4.12)	2.028×10^{-3}	3.946×10^{-3}	8.399×10^{-4}
Philip quasi-analytical solution (Matlab program, see Eq. 4.5 to Eq. 4.8)	2.016×10^{-3}	3.801×10^{-3}	8.261×10^{-4}
Parlange expression of sorptivity (Matlab program, see Eq. 4.13)	2.011×10^{-3}	3.91×10^{-3}	8.341×10^{-4}
Percentage of the difference between max. and min. sorptivity values $\frac{S_{MAX}-S_{MIN}}{S_{MIN}} \times 100$	0.8%	3.8%	1.7%
t_{GRAV}, average	101 sec (1.7 min)	671 sec (11.2 min)	51895 sec (864.9 min)

By comparing the results of simulation with those of Philip's and Parlange solution, an excellent agreement is found in terms of the sorptivity values (where the percentage of the difference between the highest and lowest sorptivity values for all porous media is less than 4%).

Vertical infiltration: (1) A-parameter determination and comparison

Fig. 4.9, **Fig. 4.10** and **Fig. 4.11** show the result of the numerical simulation of the vertical infiltration case using BIGFLOW for PM1, PM2 and PM3 respectively.

The *A*-parameter value is obtained from an optimal fit procedure. It represents the slope of the $I/\sqrt{t}$ versus $\sqrt{t}$ relationship [**Fig. 4.9**(d), **Fig. 4.10**(d) and **Fig. 4.11**(d)].

The maximum time of BIGFLOW simulation was about t_{GRAV} for each porous medium. A summary of the results for the three soils is given in Table 4.3.

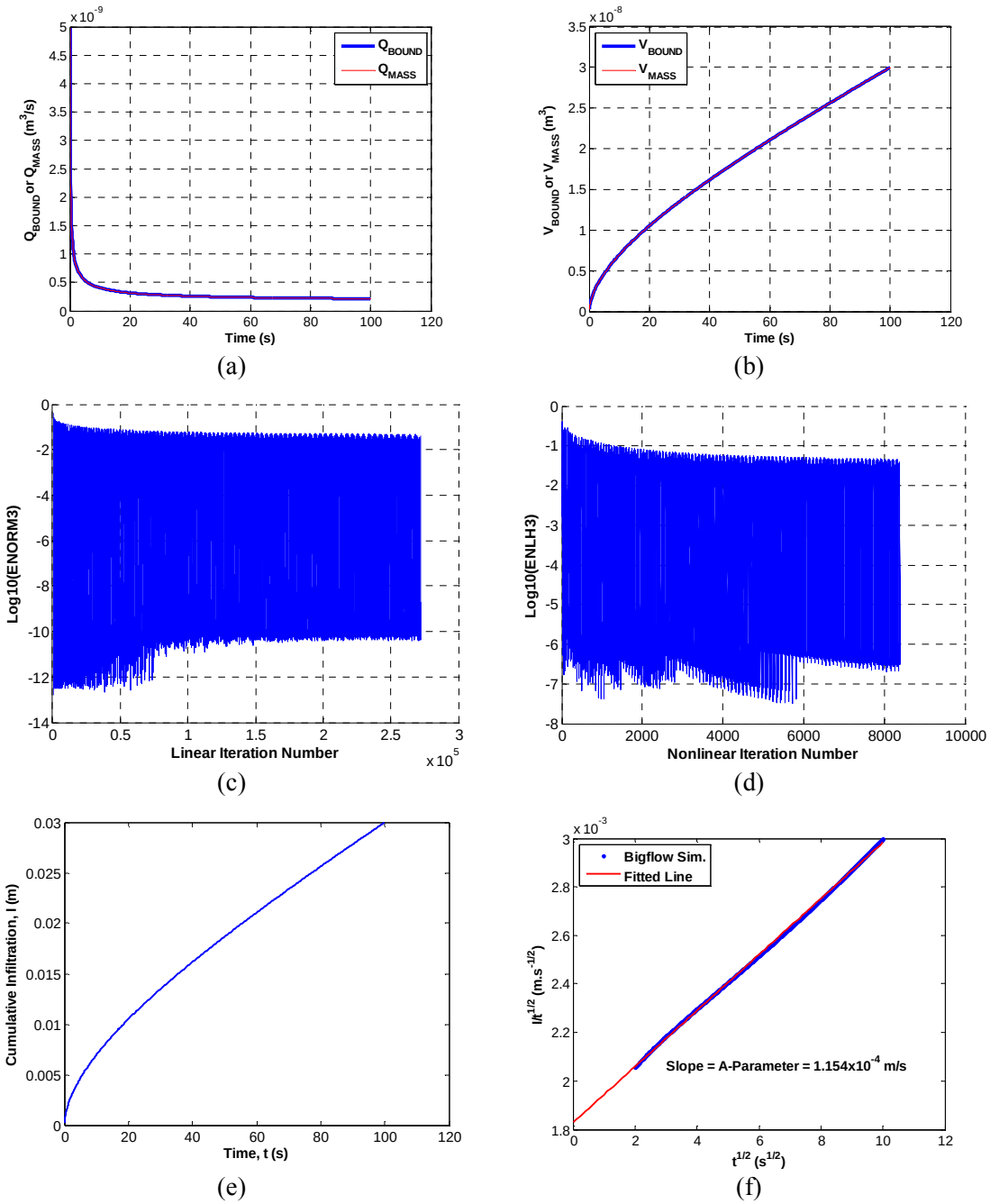

Fig. 4.9: BIGFLOW simulation results for vertical infiltration case into medium sand (PM1): (a) Local mass balance: evolution of Q_{BOUND} and Q_{MASS}. (b) Global volume balance: evolution of V_{BOUND} and V_{MASS} vs. time. (c) Linear iteration convergence. (d) Nonlinear iteration convergence. (e) Evolution of the cumulative infiltration. (d) *A*-parameter determination by linear fitting of the $I/\sqrt{t}$ versus $\sqrt{t}$ relationship.

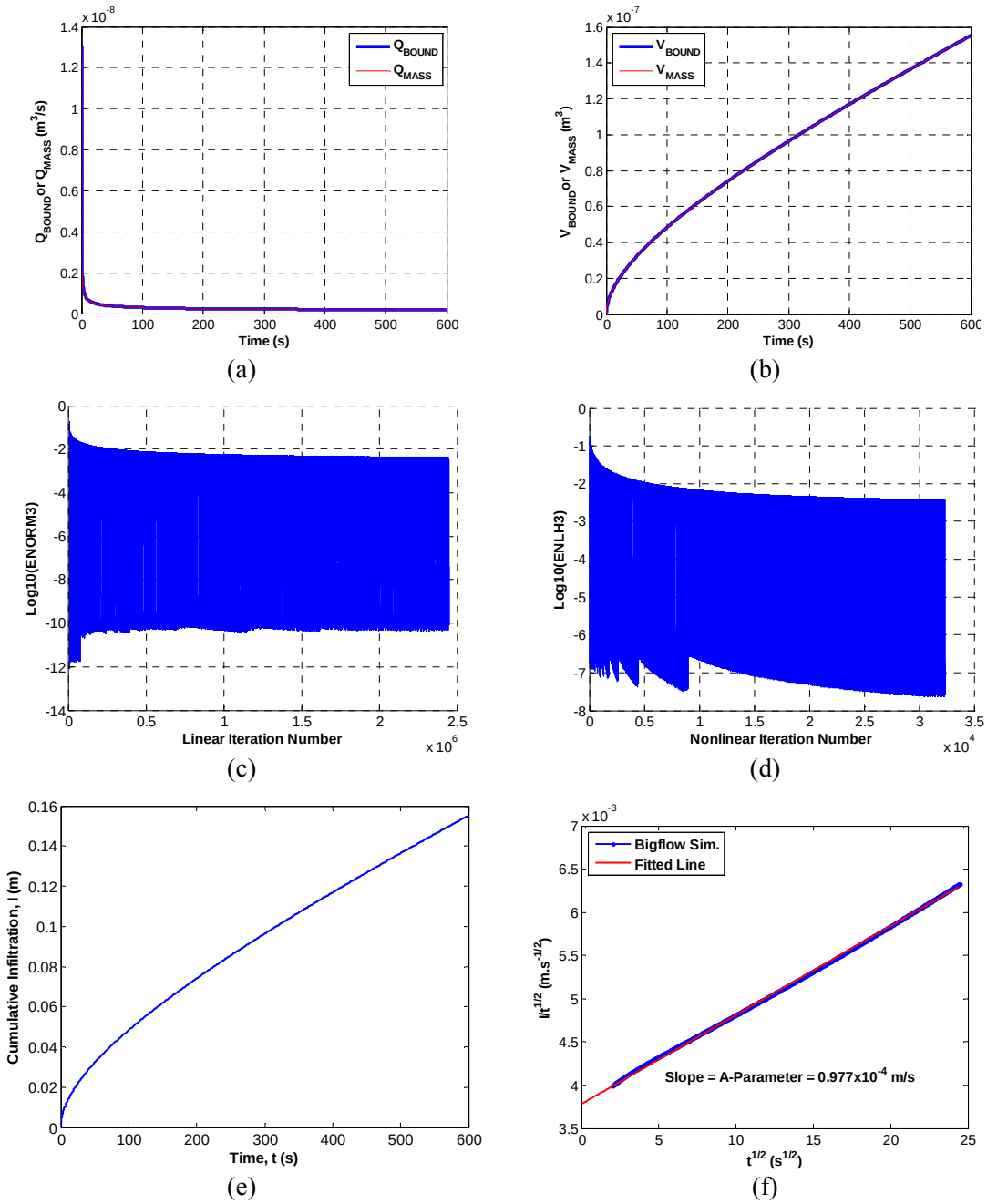

Fig. 4.10: BIGFLOW simulation results for vertical infiltration case into fine sand (PM2): (a) Local mass balance: evolution of Q_{BOUND} and Q_{MASS}. (b) Global volume balance: evolution of V_{BOUND} and V_{MASS} vs. time. (c) Linear iteration convergence. (d) Nonlinear iteration convergence. (e) Evolution of the cumulative infiltration. (d) *A*-parameter determination by linear fitting of the $I/\sqrt{t}$ versus $\sqrt{t}$ relationship.

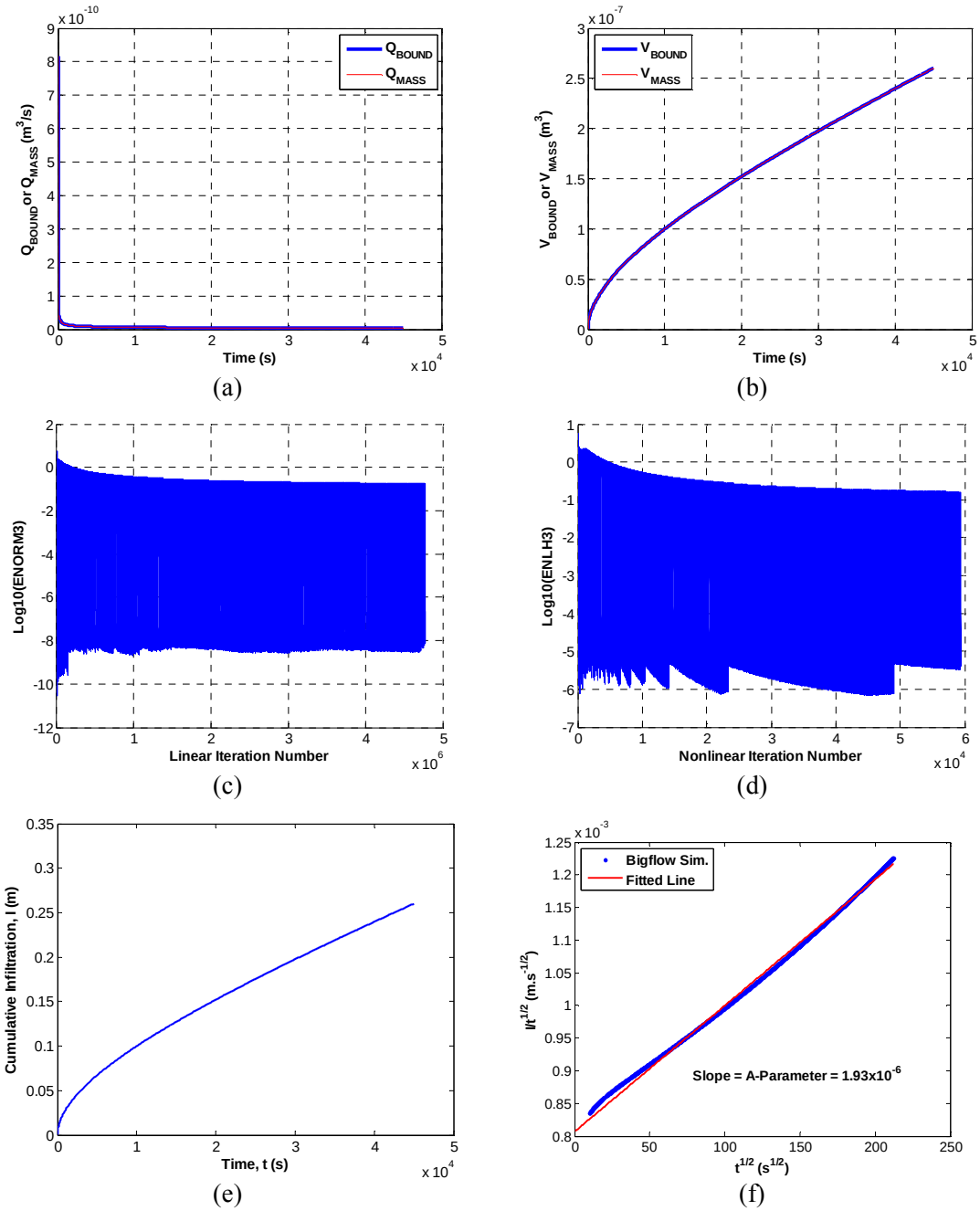

Fig. 4.11: BIGFLOW simulation results for vertical infiltration case into Guelph loam (PM3): (a) Local mass balance: evolution of Q_{BOUND} and Q_{MASS}. (b) Global volume balance: evolution of V_{BOUND} and V_{MASS} vs. time. (c) Linear iteration convergence. (d) Nonlinear iteration convergence. (e) Evolution of the cumulative infiltration. (d) *A*-parameter determination by linear fitting of the $I/\sqrt{t}$ versus $\sqrt{t}$ relationship.

As shown in the previous figures, a good numerical performance was obtained in terms of linear and nonlinear convergence and also in terms of mass balance.

The following table summarizes the results of the *A*-parameter values.

Table 4.3 : Comparison between the *A*-parameter and $\boldsymbol{K_s}$ values

Parameters	**Medium Sand PM1**	**Fine Sand PM2**	**Guelph Loam PM3**
A-parameter (BIGFLOW)(m/s)	1.15×10^{-4}	0.97×10^{-4}	1.93×10^{-6}
K_s (m/s)	2.00×10^{-4}	1.50×10^{-4}	3.66×10^{-6}
A/K_s (%)	57 %	65 %	52 %

From the above table, and for all cases $1/3 < A/K_s < 2/3$ as mentioned in the literature.

Vertical infiltration: (2) Moisture profiles comparison

For the same vertical infiltration simulation described in the previous sub-section, the evolution of the moisture profiles as a function of depth and time $[\theta(z,t)]$ was plotted and compared to Philip's series solution as shown in **Fig. 4.12**, **Fig. 4.13** and **Fig. 4.14**.

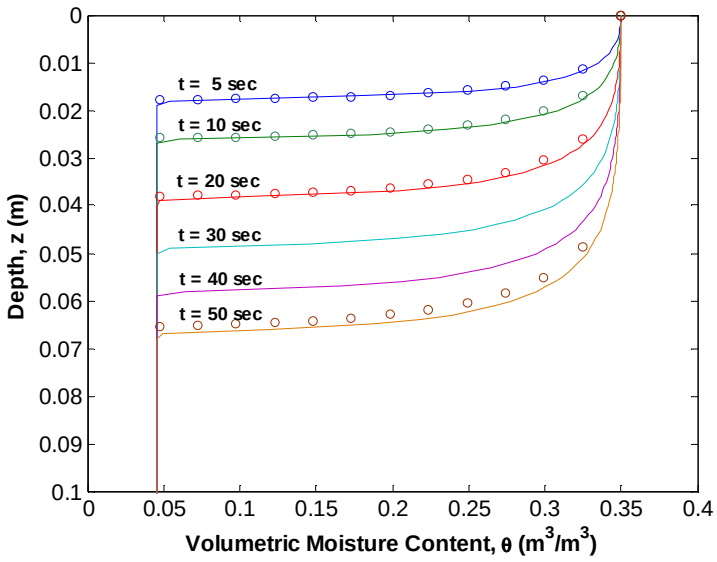

Fig. 4.12: Evolution of moisture profile $\theta(z,t)$for the medium sand (PM1); the figure shows a comparison between the numerical simulation from BIGFLOW (Solid line) and the quasi-analytical solution of Philip (discrete marks).

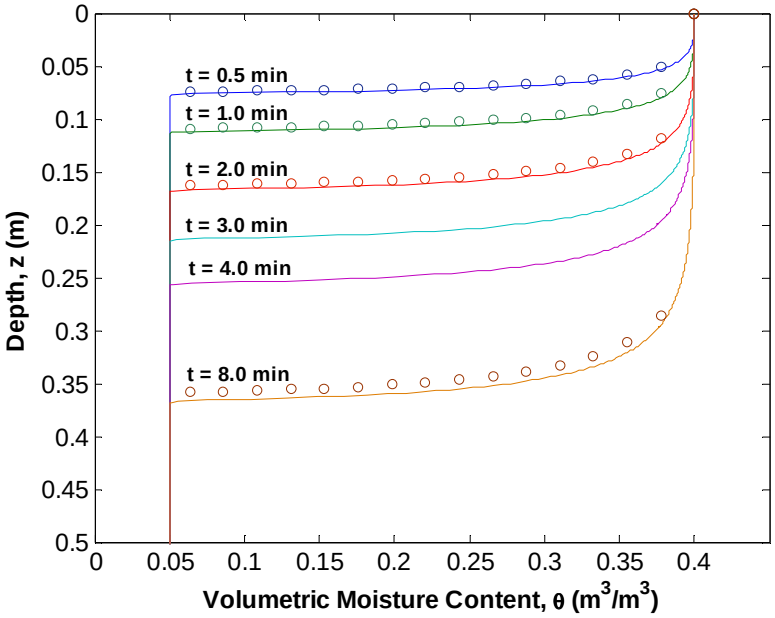

Fig. 4.13: Evolution of moisture profile $\theta(z,t)$for the fine sand (PM2); the figure shows a comparison between the numerical simulation from BIGFLOW (Solid line) and the quasi-analytical solution of Philip (discrete marks).

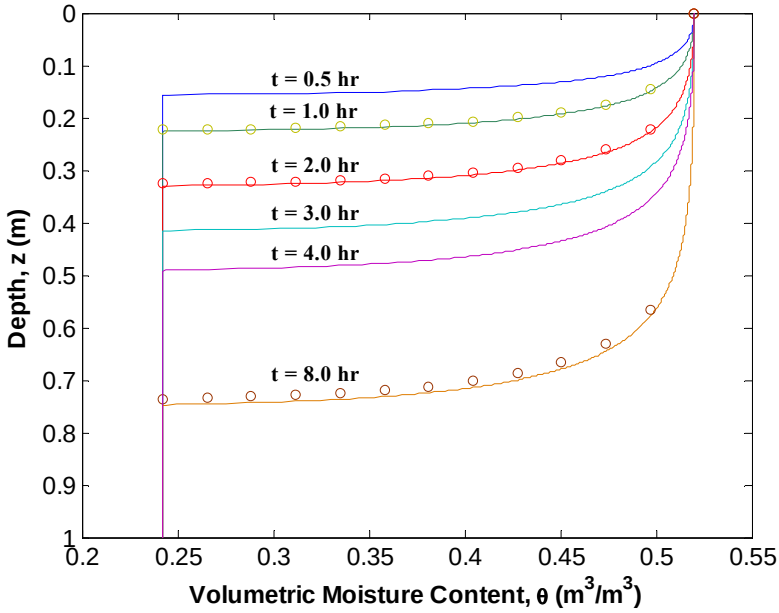

Fig. 4.14: Evolution of moisture profile $\theta(z,t)$for the Guelph loam (PM3); the figure shows a comparison between the numerical simulation from BIGFLOW (Solid line) and the quasi-analytical solution of Philip (discrete marks).

A qualitative comparison between the numerical results and Philip's solution of moisture profiles at selected times shows that in all cases the model matches the quasi-analytical solution values very closely despite some minor over-prediction of the infiltration front during later times.

Chapter 5

Experimental Setup, Sensors Calibration and Sand Properties

5.1 Introduction

In this chapter, a detailed description of a Darcy-scale soil column apparatus and the associated hydro-mechanical system (tide machine) used in the experimental program are given. The whole system simulates the effect of low frequency waves (tides) on a partially saturated 1D porous column by applying an oscillatory pressure (simple harmonic function) at the bottom boundary of a porous column.

The chapter also discusses the methods used to calibrate the measurement sensors (especially tensiometers), and to fill and pack the sand into the column. The properties of the sand (used in the experiment) obtained from various measurements are presented (see also the calibration section in chapter 7)

5.2 Physical model description

The experiment setup consists of a sand column, a hydro-mechanical system (Tide machine) that simulate the effect of low frequency waves, measurement sensors and a data acquisition system for collecting and saving experimental results. A schematic sketch of the experimental setup is shown in **Fig. 5.1**. Photos are shown in **Fig. 5.2**.

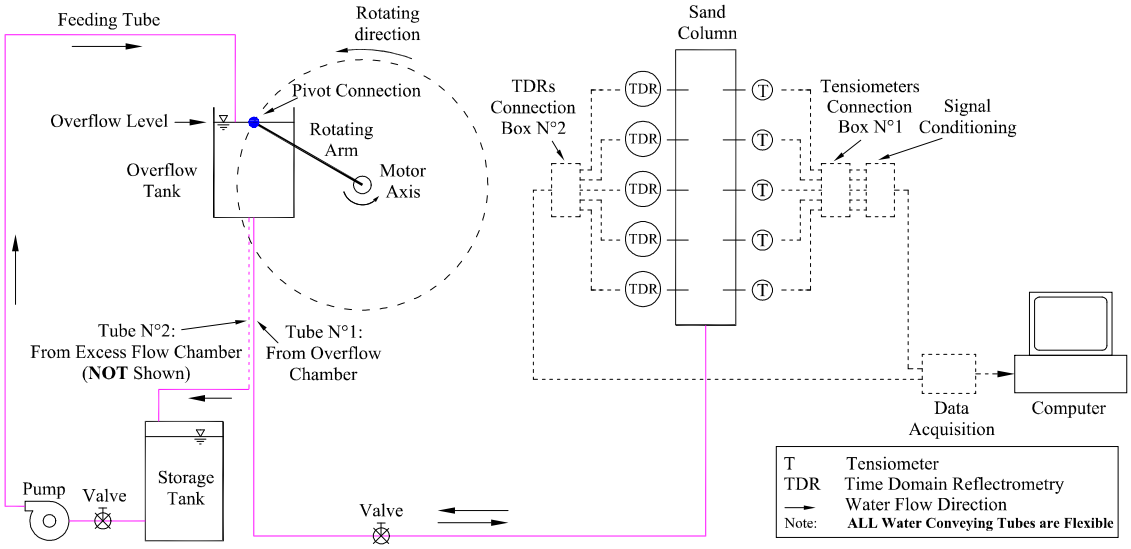

Fig. 5.1: Schematic diagram of the tide machine, soil column and measurement system.

5.2.1 Hydro-mechanical system

The hydro-mechanical system act as a low frequency waves generator. A closed circulating water circuit with mechanical system is designed and manufactured in this thesis to provide an oscillatory driving head (simple harmonic) at the bottom of column that simulate the effect of low frequency waves. The result is a driving head that is almost sinusoidal of the form:

$$h_0(t) = \overline{h_0} + A_0 sin(\omega_0 t) \qquad \textbf{Eq. 5.1}$$

where: $\overline{h_0}$ is the positive time-averaged entry pressure head; A_0 is the amplitude; $\omega_0 = 2\pi/T_P$ is the angular frequency, and T_P is the period of the imposed entry pressure.

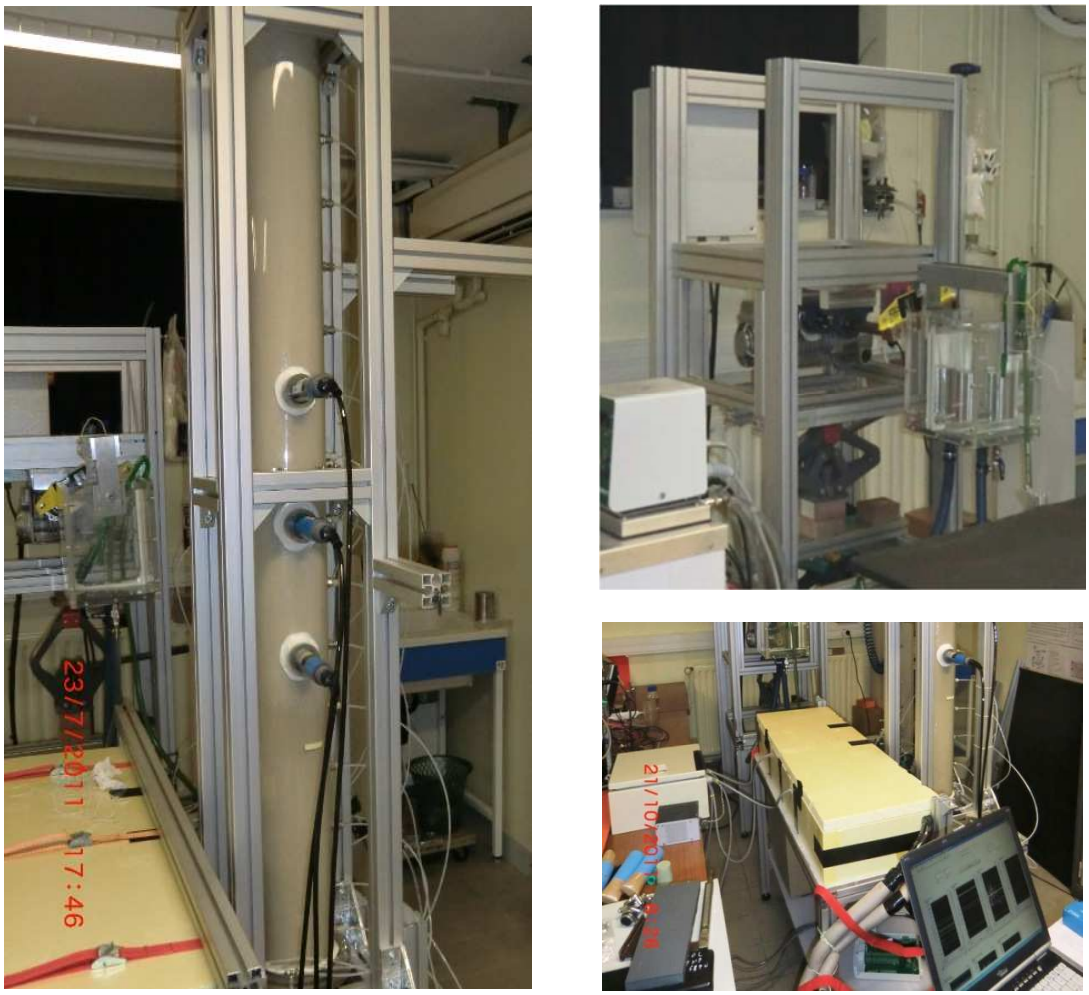

Fig. 5.2: Photographs of the "sand column" experiment conducted at the IMFT laboratory. Left: sand column with the tensiometers and TDR probes; right: the tide generating machine and its supporting structure (above) and a part of the data acquisition system (below).

The feature of this hydro-mechanical system is its flexibility; the system can provide a sinusoidal driving head with the possibility of choosing and changing the mean level, the amplitude and the period of the applied oscillatory pressure.

The following are the main elements of the system: motoreductor, variable Frequency drive, rotating arm with a constant head tank (the assembly function as a variable head reservoir) and a closed water circulating system includes a pump and a storage tank.

5.2.1.1 Motoreductor

The motoreductor provide a slow rotational motion to the rotating arm fixed to its shaft. The motoreductor composed of 0.18 kW, 1500rpm electrical motor and a two-stage reductor with a speed reduction ratio of 1/8000.

A tank with an overflow system is suspended to the rotating arm. By rotating the arm, the tank rotates also, drawing a circle in a vertical plan. By projecting the position of the overflow/free surface with time, a sinusoidal variation of the water level in the overflow tank is obtained (**Fig. 5.3**). Therefore, the outcome is a variable height reservoir that provides a water level (driving head) that is varied with time as a sinusoidal pressure function [$h_0(t) = \overline{h_0} + A_0 sin(\omega_0 t)$]. This oscillatory pressure function can be applied at the bottom of the sand column by means of a flexible tube that connects the variable height reservoir to the bottom of the column (**Fig. 5.1**).

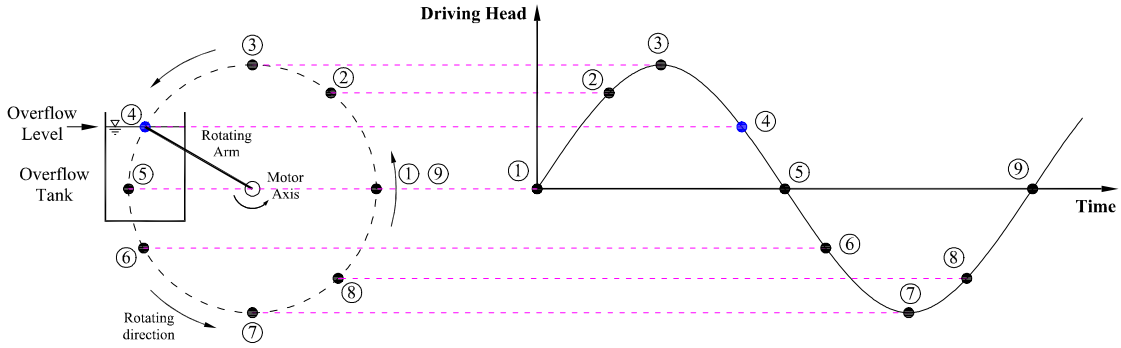

Fig. 5.3: Overflow tank circulation provides a sinusoidal function driving head.

The motoreductor is fixed inside an interior structural frame that can be slide up and down over an exterior frame support. By changing the level of the interior frame, the vertical position of the motoreductor is changed and consequently, the average water level ($\overline{h_0}$) is changed also (**Fig. 5.4**).

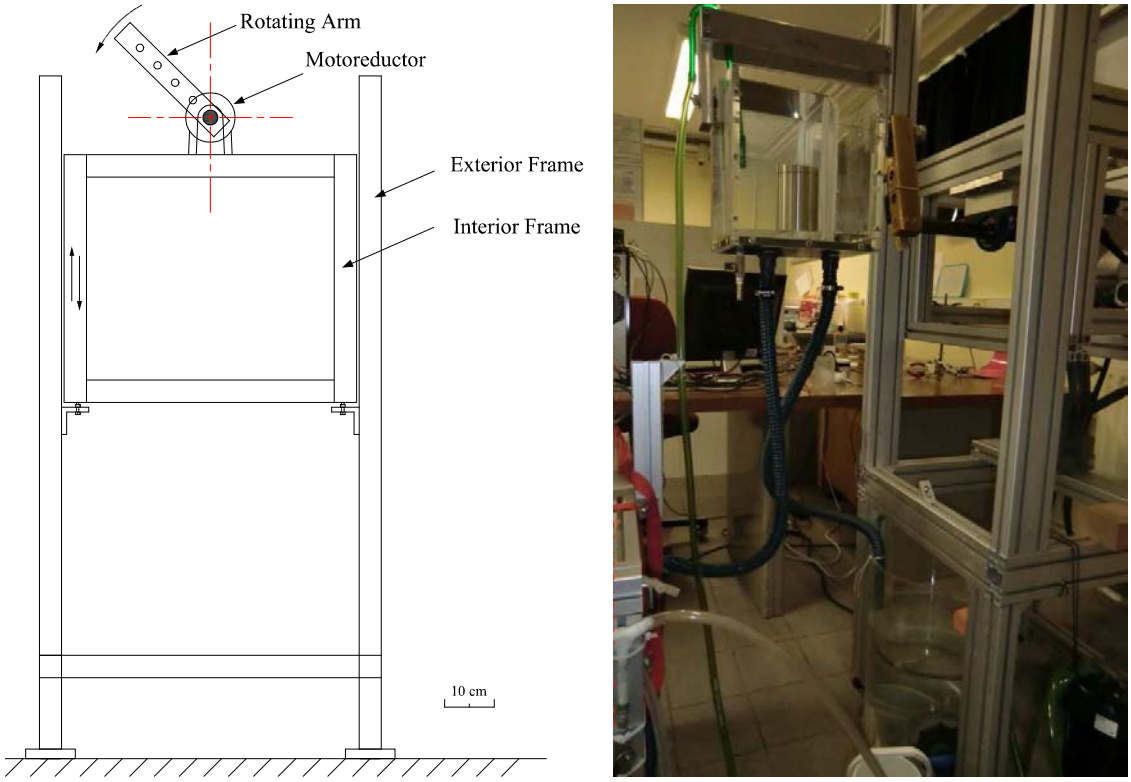

Fig. 5.4: Left: Schematic of the movable support. Right: Photo of the movable support with the motor axe, rotating arm and the moving overflow tank

5.2.1.2 Variable-frequency drive (VFD)

A variable frequency derive is used to control the rotational speed of the motoreductor by controlling the frequency of the electrical power supplied to the motor.

A powerflex40 VFD type was used. The interface of this VFD allows the operator to start and stop the motor and adjust the operating speed. An electrical power frequency range of about 95 to 5Hz can be supplied to the motor. This frequency corresponds to a final rotational speed of about 0.117 rpm (1 revolution per 8.5 min) to 0.006rpm (1 revolution per 3hrs) respectively.

Fig. 5.5 shows the result of calibrating the supplied electrical frequency to the motoreductor rotational speed. The calibration procedure was done by applying a given

frequency to the motor, then recording the time spent by the rotating arm to complete one cycle.

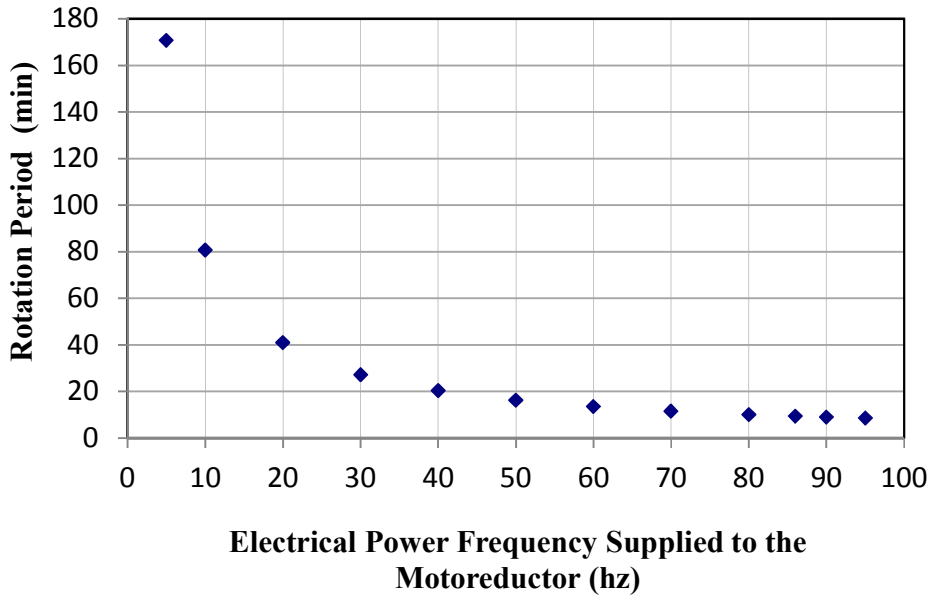

Fig. 5.5: Relationship between the frequency of the electrical power supplied to the motoreductor and the rotation period of the rotating arm.

5.2.1.3 Rotating arm

A rotating arm (made from brass) of 50 × 34 mm in cross section with a length of 240 mm was fabricated as shown in **Fig. 5.6**. Two types of hole were drilled. The first one with 18mm in diameter drilled at one of the arm edge. This hole is used to fix the arm to the motor shaft by two threaded screws placed at the other side of the arm. The second type includes four holes of 20mm in diameter that were drilled at a distance of 50, 100,150 and 200 mm center to center from the first hole. The overflow tank will be connected to one of these four holes depending on the desired amplitude of the applied sinusoidal pressure function.

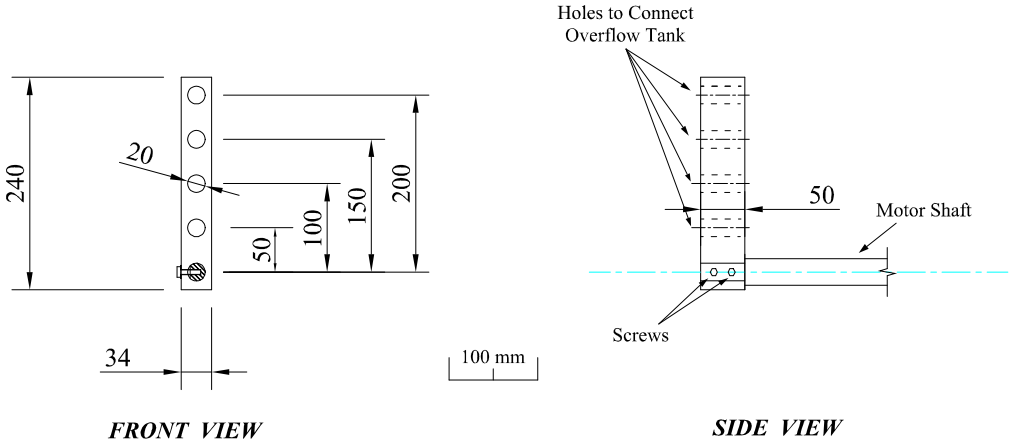

Fig. 5.6: Schematic of the rotating arm (dimensions in mm).

5.2.1.4 Mobile overflow tank

The overflow tank (made from Plexiglas for easy monitoring) contains two chambers separated by an overflow plate. Water will be pumped from the storage tank to the first chamber that has a storage capacity of 7.2 liter. The excess water from the first chamber will be spilled over the overflow plate to the other chamber that returned this excess water back to the storage tank (**Fig. 5.7**). A flexible tube of 25mm diameter connects the bottom outlet of the first chamber (variable level constant head chamber) to the bottom inlet of the sand column.

An important issue is to ensure that the periodic movement of the overflow tank gives a sinusoidal function. To realize this condition, an inverted u-shape hanger as shown in **Fig. 5.7** is used to hold the tank and to make the free surface/overflow surface coincide with the axis of rotation at the connection.

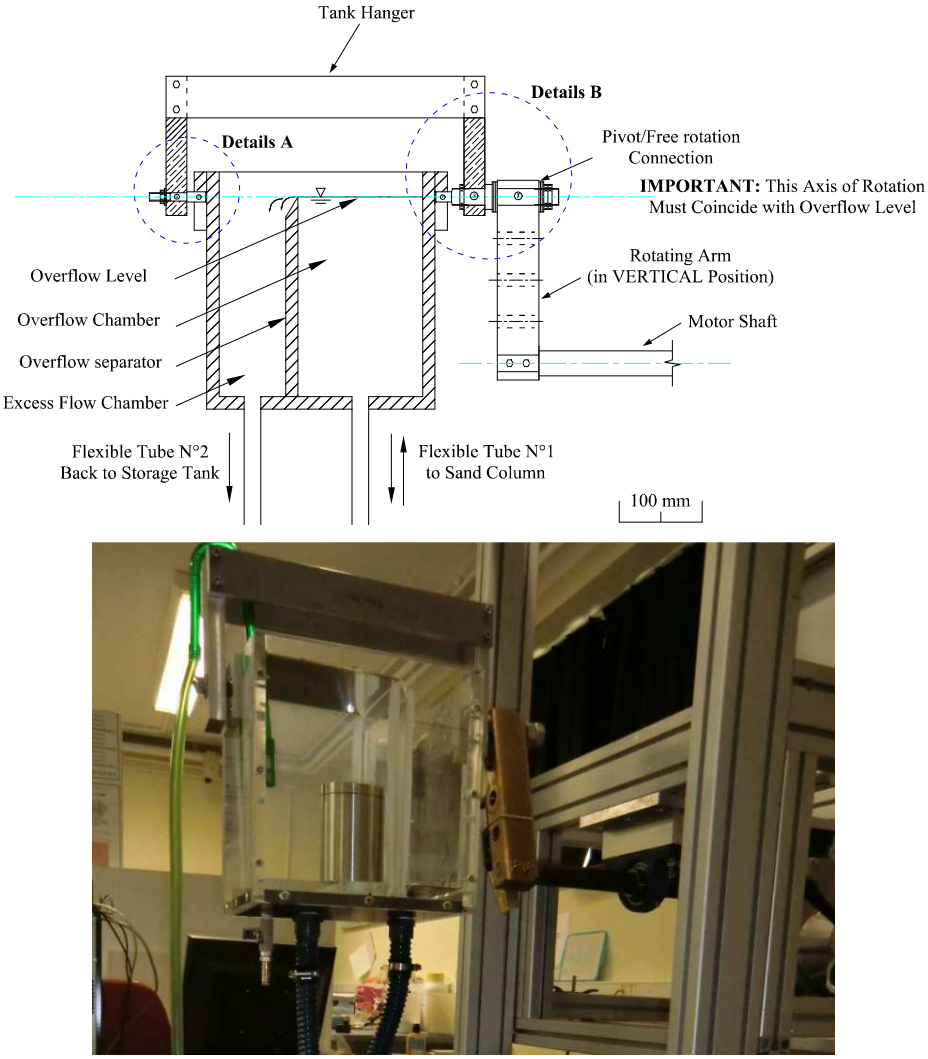

Fig. 5.7: Top: Schematic diagram-side view (Top) and Photo (Below) of the overflow tank.

The connection between the overflow tank and the rotating arm was designed to make a free rotation at the connection. This was achieved by adding cylindrical roller thrust bearing (a ball slewing rings) at each side of the connection (**Fig. 5.8**). This connection makes the tank always in a vertical position under its self weight regardless the orientation of the rotating arm.

Valves are placed between the different components to facilitate controlling the circulating system.

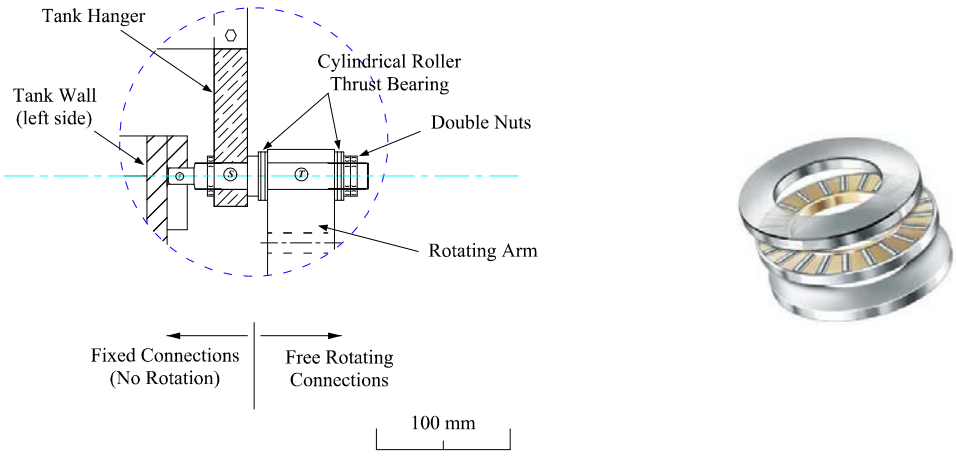

(a) (b)

Fig. 5.8: Pivot/ Free rotating connection details: (a) schematic details ; (b) cylindrical roller thrust bearing.

5.2.1.5 Closed water circulating system:

Water is provided to the overflow tank from a storage tank by a pump that can deliver a flow of 10 L/min (at a head of 1.4m) which is much larger than the expected inflow through the bottom of the sand column.

The excess water is returned back to the storage tank through a flexible 25mm diameter tube that connects the bottom outlet of the excess chamber of the overflow tank to the storage tank (**Fig. 3.1**).

5.2.2 Sand column

The column is made of a clear Perspex cylinder. The top and bottom of the column are provided with acrylic plates. The bottom plate is connected to the hydro-mechanical system (that generates the driving oscillatory pressure head) via a 25 mm flexible tube; where the top cover is used to minimize the effect of the evaporation and is provided with a small opening to assure that an atmospheric pressure acted on the top of the sand column. A perforated screen is place at the bottom of the column to keep a better distribution of flow over the entire cross-sectional area at the bottom of the sand column.

Threaded screws, lock nuts and O-rings seals are used to develop a tight seal between the column and the top and bottom plates. Details of the 1D column are shown in **Fig. 5.9**.

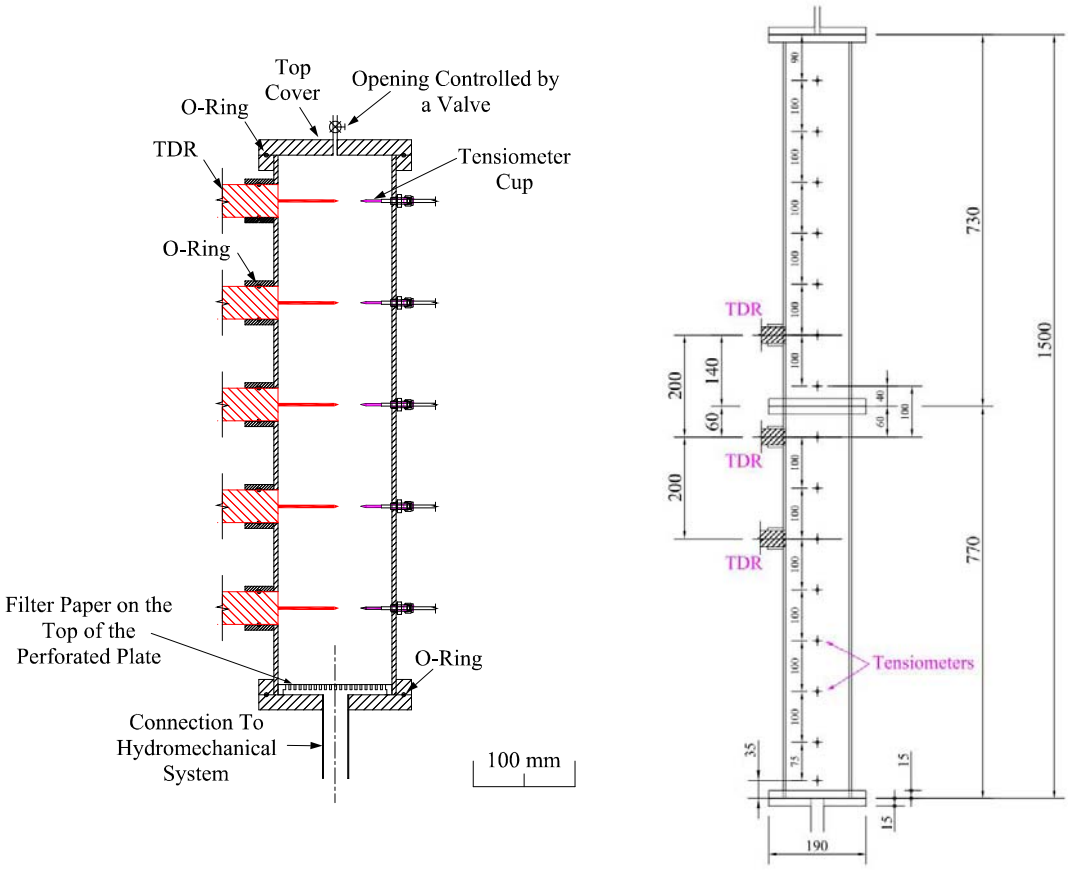

Fig. 5.9: Left: General sand column details (the number and the position of the tensiometers and the TDR probes differs from the actual cases); left: details and dimensions of long column used in the experiments.

Two different columns are used:

- **Short column:** 530 mm high, 112 mm internal diameter and 4mm wall thickness. We started the experiment by this column, then we decide to increase the size (length) of the column to solve some problems facing us with the short column such as: problem regarding the top boundary condition effects, constraints in applying large amplitudes and also modify the method used in the sand filling in order to get a medium which is much more homogeneous.
- **Long Column**: 1500 mm high, 124 mm internal diameter and 5mm wall thickness.

Several ports along the column are produced for the insertion of measurement sensors. A special connection with an O-ring seal is designed and fabricated for the installation of Time Domain Reflectrometry (TDR) probes **(Fig. 5.10)**.

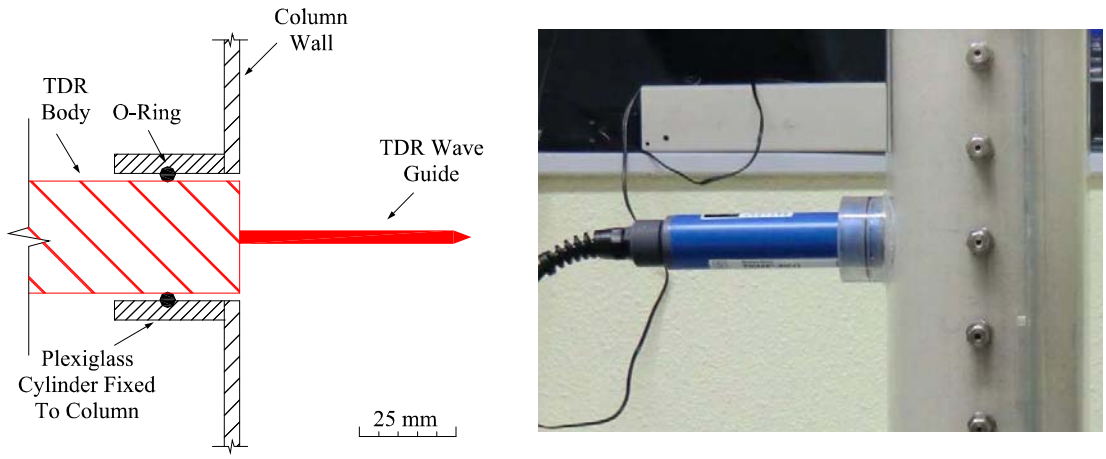

Fig. 5.10: TDR connection: (a) schematic details; (b) fitting picture.

On the other hand SWAGELOK fittings are used to install the tensiometers probes (Fig. 5.11). Plugs are used to seal the ports that are not in use during the experiment.

The connections are checked against leakage by filling the column with water for a few hours.

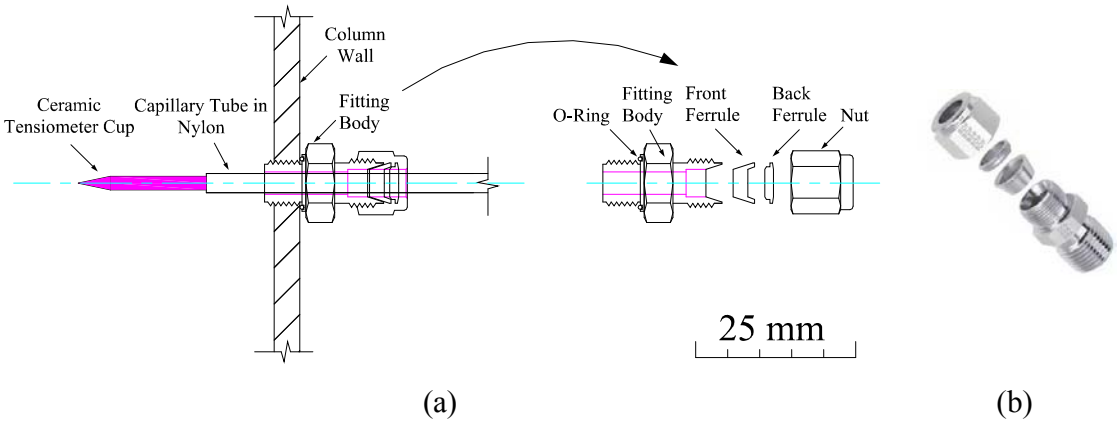

Fig. 5.11: Tensiometer connection: (a) schematic details; (b) picture.

5.2.3 Measurement sensors

Measurements were taken continuously to determine the pore water pressure and the volumetric water content at specific levels along the sand column. Two probes are used: microtensiometer and time domain reflectrometry.

5.2.3.1 Pore water pressure sensors: Tensiometers

Microtensiometer-transducer system is used to measure the pore water pressure of the soil. Each microtensiometer is made of a porous ceramic cup 2.1mm in diameter and 20 mm in length (**Fig. 5.11)**, connected to a differential pressure transducer via a Nylon capillary hydraulic circuit**.** The porous ceramic has a high air entry value[12] of about 150 kPa (1.5 bars).

The pressure transducer is a differential sensor based on a piezoresistive principle, with an operating range from 100 kPa positive pore-water pressure to 100 kPa negative pore-water pressure (+1 to -1 bar) with a response time of 1 msec.

The tensiometer establishes a quasi-equilibrium condition with the soil water system. The porous ceramic cup acts as a membrane through which water flows (WMO, 2008). Water flows in and out of the tensiometer only if the porous cup is saturated with water and therefore it should be remain saturated if it is to function properly. If the cup desaturates, then little or no flow occurs, and air enters the tensiometer and then it stops operating (Hanson and Orloff, 1998) . Consequently, all the pores in the ceramic cup and the Nylon capillary tube are initially filled with de-aerated water. Once in place, the tensiometer will be subject to negative soil water potentials, causing water to move from the tensiometer into the surrounding soil matrix. The water movement from the tensiometer will create a negative potential or suction in the Nylon capillary tube which will be recorded by the pressure transducer. On the other hand, If the soil water potential increases, water moves from the soil back into the tensiometer, resulting in a less negative water potential reading (WMO, 2008).

[12] Air entry value: pressure at which the air can pass through the porous ceramic saturated with water ("bubbling" pressure)

The microtensiometer-transducer system used in the experiment was manufactured by SDEC France (www.sdec-france.com). SDEC France provides WIND system box with an assembly of 6 microtensiometers-transducers.

5.2.3.2 Volumetric water content sensor: TDR[13]

In this experiment, Time Domain Reflectrometry (TDR) probes are used to measure the volumetric soil moisture. The TDR were place horizontally in the soil column. The main components of a TDR system are a voltage pulse generator, the wave guides, and a coaxial cable connecting the waveguide to the instrumentation (Noborio, 2001).

In our study, Trime-pico32 TDR probes are used. Each TDR consist of two parallel rods (that act as a wave guides for the transmission of the TDR-signal) of 110 mm in length and 3.5 mm in diameter with 20mm center to center distance between the rods (**Fig. 5.12**).

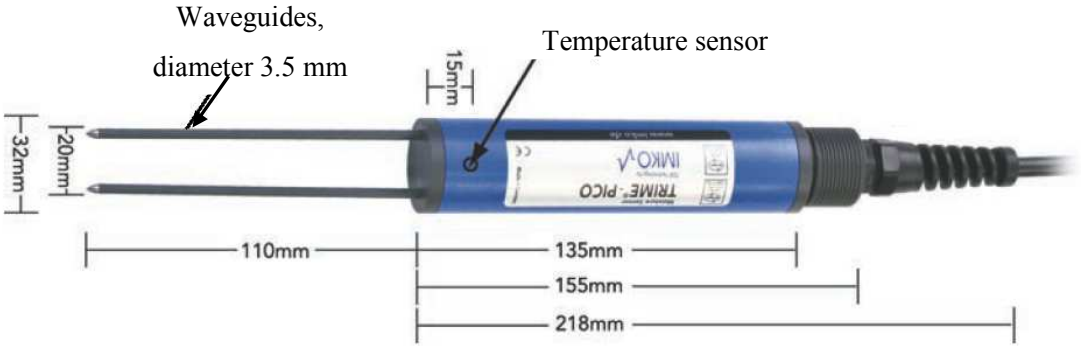

Fig. 5.12: TDR (Trime-Pico 32).

The TDR sensors determine the soil moisture by measuring the dielectric constant of the soil. This constant is an electrical property of the soil that is highly dependent on the soil moisture content. The dielectric constant of dry soil is between 2 and 5, and that of air and water are 1 and 80, respectively. Thus, changes in the soil moisture content change the dielectric constant of the soil.

The dielectric constant of the soil is determined by monitoring the travel of an electromagnetic pulse, which is launched along the waveguide embedded in the soil. The pulse is reflected at the end of the waveguide (WMO, 2008). The travel time

[13] Unfortunately, a sudden break down occurs in the TDR after assembling the system.

required for the pulse to reach the end of the waveguides and back depends on the dielectric constant of the soil. The dielectric constant is calculated by the following equation (Angelaki et al., 2004):

$$\varepsilon = \left(\frac{ct}{2L}\right)^2 \qquad \textbf{Eq. 5.2}$$

Where c is the velocity of electromagnetic waves in free space ($m.s^{-1}$) (3×10^8), t is the transmission time which the wave needs to cross the waveguide and L is the length of the wave guide (m).

5.2.4 Data acquisition system

A continuous and automatically measurement of the volumetric water content and the pore water pressure were ensured through the use of data acquisition system manufactured by National Instruments, NI (www.ni.com). The data acquisition system includes the following components: two connector blocks (NI SCB-68 and NI SCC-68) provides up to 40 differential analog channels, signal conditioning box includes a filter and an amplifier for each pressure transducer output channel, a main USB data acquisition module (NI USB 6225) with maximum sampling rate of 250 kS/s single channel and a portable computer. A USB cable connects the main data acquisition device to the computer (**Fig. 5.13**).

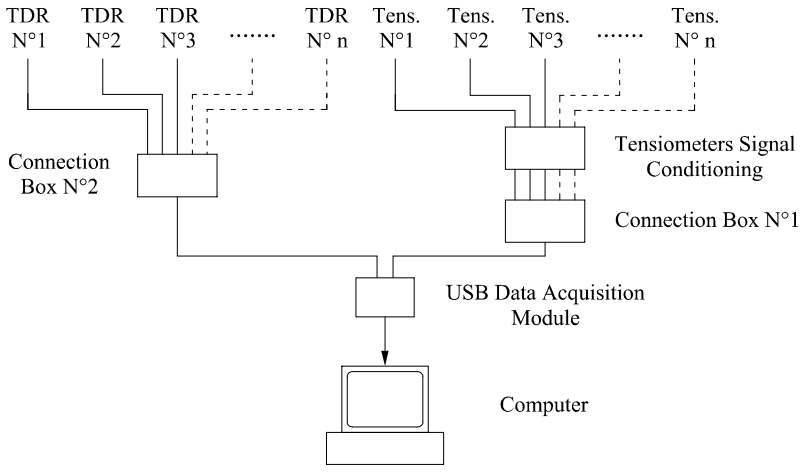

Fig. 5.13: Schematic diagram of the data acquisition system.

The acquired data are stored to the computer through the use of special program written using the LabView software, the final result is a *.lvm extension file that store all the measured data (tensiometers and TDRs readings) as a function of time. This *.lvm file can be opened in MS-excel software (for small size file), transformed into a text file or uploaded in MATLAB workspace for further presentation and interpretation.

5.3 Sensors calibration

5.3.1 Tensiometer-transducer calibration

This calibration of the pressure transducers was one of the challenges facing us during the experimental program. It is a time-consuming and sensitive process and requires special needs and cares to perform and also it should be done separately for each transducers (each pressure transducer have its own calibration model).

The problems with pressure-transducer calibrations appear because of the sensitivity of these transducers to temperature variations in addition to the variation in pressures. Thus each pressure-transducer should be calibrated for both pressure and temperatures.

After many trails, the following is the best model representing the calibration of the pressure-transducer:

$$P_i = a_i \times V + b_i \times T + c_i \qquad \textbf{Eq. 5.3}$$

Where: P is the applied pressure head in (cm) for pressure transducer N°i; V is the measured voltage detected by the pressure-transducer in (mVolts); T is the non-calibrated measured temperature by the temperature sensor in (Volts); a_i, b_i and c_i are the model calibration parameters of the pressure transducer N°i.

The calibration of the pressure transducers is made by taking a series of pressure measurements realized at different temperatures. These measurements allow the determination of the thermal drifting coefficients and the offsets of the calibration model.

The change of temperature is realized by controlling the temperature of the air conditioning of the laboratory room.

The parameters of the calibration model are obtained using the MatLab function ***regress*** which is a multiple linear regression model based on least squares.

Fig. 5.14 shows an example of the resulting calibration models of one pressure transducers (named: B1T1). In this figure, the surface represents the calibration model and the (17) balls represent the calibration points used to find the model through a multiple linear regression method. The resulting calibration model for B1T1 is:

$$P_{B1T1} = 8.46 \times 10^{-2} \times V - 7.36 \times T + 31.7 \qquad \textbf{Eq. 5.4}$$

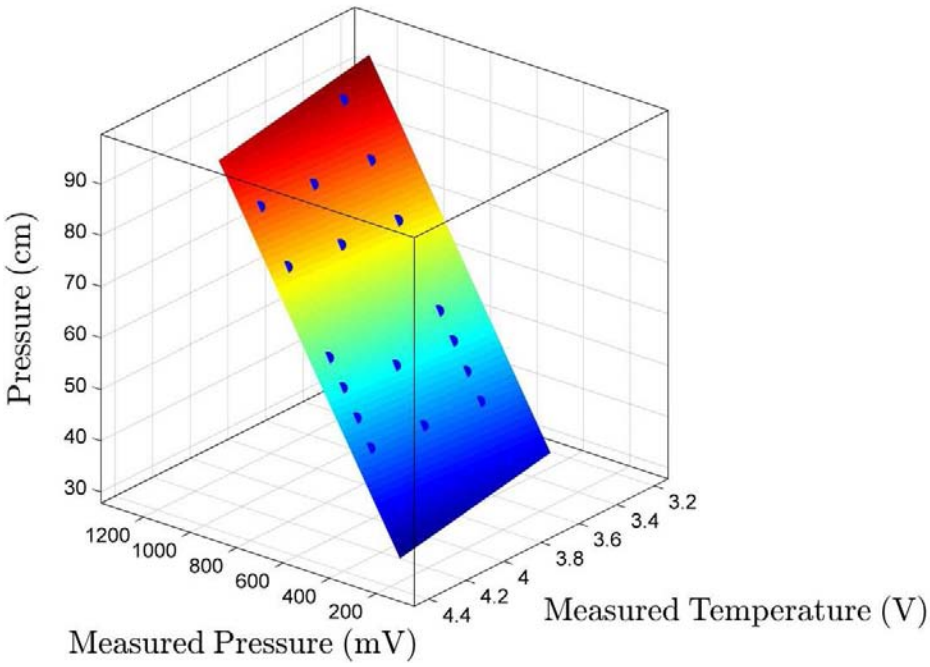

Fig. 5.14: Calibration model of the pressure-transducer named B1T1. The surface represents the calibration model and the (17) balls represent the calibration points used to find the model through a multiple linear regression scheme.

5.3.2 TDR calibration

As mentioned previously, TDR sensors determine the soil moisture by measuring the dielectric constant of the soil. The most widely used relation between soil dielectrics and soil water content was experimentally summarized by (Topp et al., 1980) as follows:

$$\theta = -0.053 + 0.029\,\varepsilon - 5.5 \times 10^{-4}\,\varepsilon^2 + 4.3 \times 10^{-6}\,\varepsilon^3 \qquad \textbf{Eq. 5.5}$$

where (θ) is the volumetric water content (m^3/m^3) and (ε) is the dielectric constant of the soil water system.

This empirical relationship has proved to be applicable in many soils, roughly independent of texture and gravel content (WMO, 2008). However, soil-specific calibration is desirable for soils with low density or with a high organic content.

The calibration of the used Trime-pico32 TDR probes were performed by the manufacturer.

With respect to my experiment, a simple test is conducted before the beginning of the experiment, where the TDR shows approximately 0% moisture in the air and 100% in pure water.

5.4 Sand filling method

To ensure a homogeneous sand column, the filling of the sand should be as uniform as possible. Several filling and packing methods have been reported in the literature. These methods can be categorized based on the moisture condition of the soil (dry, moist, or wet), the method of soil placement (pluviation, spooning, or tubing), and the medium through which the soil is placed (air or water) (Frost, 1989).

In our experiment, a dry packing method was used because of the constraints related to sensors installation and also to simplify the measurement of the porosity and the equivalent capillary length. More precisely in this research, the sand column was prepared using sand raining method through sieve rainer. This method required a minimum manual Intervention and therefore less sensitive to disturbances.

In this method the sand is rained or pluviated into the sand column through multiple sieves or screens placed at top of the column.

The set-up of the sand rainer consists mainly of the following two components as shown in Fig. 5.15 (left):

- Sand funnel (sand hopper) placed at the top of the system and served to center the sand flux on the sieves. The funnel can be provided by an optional pipe to avoid air turbulence influencing the sand flow until it reaches the top of sieves.
- A set of multiple sieves or screens placed on the bottom of the funnel and above the column to be filled. The sieves should have an outer dimension almost the same as the inner dimension of the sand column. These sieves were used to disperse and uniformly distribute the sand over the entire area of the column. This promotes uniformly throughout the soil profile and helps to eliminate the formation of packing irregularities. Note that sieves aperture area and the bottom diameter of the funnel control the rate of sand flow to the column.

Fig. 5.15: Left: Photos of sand raining method used to fill the 1D sand column with four sieves and a funnel. Right: photo of the column bottom during the early stage of the filling process.

The sand filling method is summarized as follows:

- Pour the sand continuously into the sand hopper (funnel) placed on the top of the sieves.
- Keep the continuous feed of sand into the funnel until the column is completely filled with sand.
- Wait over night to minimize the electro-static force produce between the sand grains during the filling process.
- Finally, gently tap the sides of the column with a rubber mallet to compact the sand by vibration until no more volume reduction occurs (we tap for about 3hours). This helped to obtain a uniform bulk density of the sand in the column (consistent sand density properties). In our case this reduces the height of the sand by about 25 mm.

Fig. 5.16 shows the sand column at the end of the filling process.

Fig. 5.16: The sand column at the end of the filling process.

5.5 Sand properties

A commercially available silica sand (named: SILISABLE N°.0) was used in our experiments. It contains high portion of silica (more than 90% SiO_2) with an apparent density of 1.5g/cm^3 and grain size ranging between 0.1 to 0.4 mm. It is almost uniformly sorted and it consists of angular (mostly) to well rounded grains of quartz.

Before using the sand in the experiment, a series of pre-tests are conducted to characterize the sand as follows:

5.5.1 Grain size distribution

The grain size characteristics of the sand used in the experiments were determined by a sieve analysis. In this experiment, a set of sieves is prepared by stacking them one above the other with the largest opening at the top and a catch pan at the bottom. The dry sand is poured at the top of the nested sieves, and then mechanical sieve shaker is used. After the shaking is complete the material on each sieve is weighed.

The results of the sieve analysis are displayed by plotting the percent passing against the sieve opening size as shown in **Fig. 5.17**.

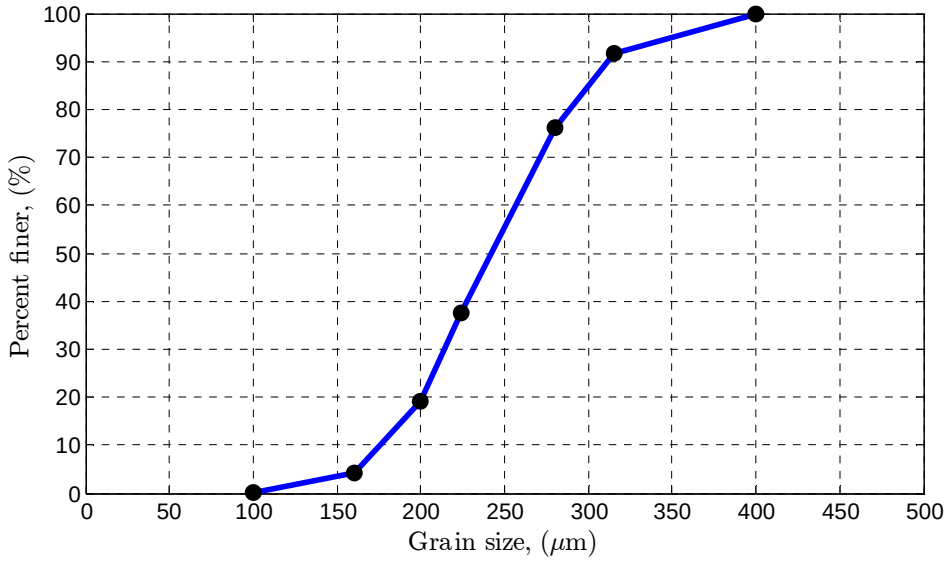

Fig. 5.17: Grain size distribution of the sand used in the experiment.

From the graph, we can deduce the followings:

- D_{10} = the grain diameter for which 10% of the sample (by weight) is finer = 176 μm.
- D_{30} = the grain diameter for which 50% of the sample (by weight) is finer = 242 μm.
- D_{50} = the grain diameter for which 30% of the sample (by weight) is finer = 214 μm.
- D_{60} = the grain diameter for which 60% of the sample (by weight) is finer = 257 μm.

Note that:

- D_{50} is called median grain size and it is the grain diameter for which half the sample (by weight) is smaller and half is larger.
- D_{10} is also called effective grain size and is used to estimate coefficient of permeability.

5.5.2 Sand classification according to USCS

To classify the sand according to the Unified Soil Classification System (USCS), the following two coefficients should be calculated. These coefficients are used to evaluate whether the soil is well graded or poorly graded according to the USCS. The coefficients are:

- C_u = coefficient of uniformity = $D_{10}/D_{60} = 1.46$
- C_c = coefficient of curvature $= D_{30}^2/(D_{10} \times D_{60}) = 1.01$

According to (USCS) classification system the used sand is classified as a poorly graded sand (SP), this mean that the most of the grains of the sand are approximately of the same size (uniformly graded).

With respect to the size range of the sand, it can be considered as fine to medium sand.

5.5.3 Hydraulic conductivity measurement

The hydraulic conductivity of the sand in the column was measured through the idea of constant head test. The sand column was used as a permeameter; and a two overflow (constant head) tanks were attached at the top and the bottom of the column and a constant pressure (ΔH) gradient is imposed across the column as shown in the **Fig. 5.18**.

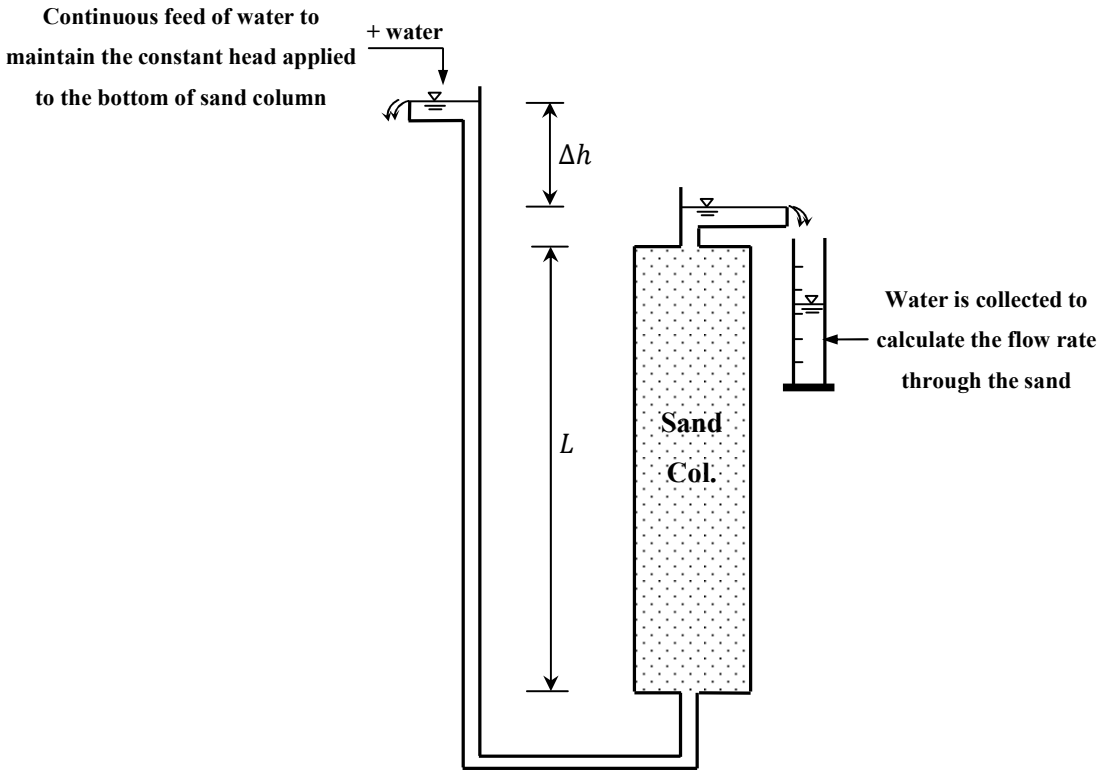

Fig. 5.18: Photos Schematic of the used constant head permeameter test, the cross-sectional area and the length of the sand column is A and L respectively.

It is worth noting that to minimize the effect of entrapped air in the sand column an upward flow through the soil column was applied (bottom total head > top total head).

After a constant flow rate is established (steady-state flow rate had been reached), the outflow water is collected in a measuring cylinder (V), and the duration of the collection period is noted (t).

From Darcy's law, we have:

$$Q = \frac{V}{t} = -AK_{SAT}\frac{\Delta H}{L} \qquad \textbf{Eq. 5.6}$$

where Q is the flow rate, L the length of the column, A its cross-sectional area, and ΔH the head difference causing the flow. Rearranging the above equation:

$$K_{SAT} = -\frac{Q}{A}\cdot\frac{L}{\Delta H} \qquad \textbf{Eq. 5.7}$$

Once all the quantities on the right-hand side of (Eq. 5.7) have been determined from the test, the hydraulic conductivity of the soil can be calculated.

In our case [see the photo in **Fig. 5.19** of the constant head permeability test conducted on the sand column] the dimensions of the sand column are:

- L = total length of the sand in the column = 146.2cm.
- D = diameter of the sand in the column = 12.4cm

And the applied total head difference is:

- ΔH = applied head difference =13.95 cm

The test is repeated two times, the followings are the final results:

- Test N°1: $K_{SAT} = 1.305 \times 10^{-4}$ m/s
- Test N°2: $K_{SAT} = 1.312 \times 10^{-4}$ m/s

With an average value of:

$$K_{SAT} = 1.31 \times 10^{-4} \text{ m/s}$$

Note that, the measurements made using a constant head permeameter are interpreted as hydraulic conductivity values assuming the soil to be uniform and thus the obtained value can be considered as an equivalent global hydraulic conductivity regardless of existing minor/local inhomogeneities. Note also that we assume that the sudden reduction in pressure head that occurs when water passes the inlet (bottom) and outlet (top) of the column have a neglected effect and can be ignored.

Fig. 5.19: Constant head permeability test conducted on the sand column to measure the saturated hydraulic conductivity. Two overflow tanks are attached at the top and bottom of the column

5.5.4 Porosity measurement

The porosity of the sand was measured and it is estimated to have an average value of 0.38. The porosity was estimated in two ways:

- By indirect measurement: using a TDR probe on a saturated sand sample of the same type used in the column.
- By direct measurement on the column: by measuring the water volume needed to fully saturate the bulk sand column (until the top of the sand surface). The porosity can be estimated to be this volume of water divided by the total volume of the column occupied by the sand and water.

5.5.5 Estimation of the equivalent (global) capillary length

The equivalent (global) capillary length is estimated after filling the dry sand in the column. The method of estimation was based on the following:

Wetting the dry sand column from the bottom to a certain constant height by attaching a constant head tank to the bottom of the column. Let us call the constant applied head as $Z_{S_{Applied}}$ [This value ($Z_{S_{Applied}}$) can be interpreted as the height of the water table].

- Wait until reaching to steady state (no further upward flow is detected).
- Measure the total volume of water (V_{Water}) needed to complete the imbibitions until reaching the steady sate. V_{Water} was measured by follow up the drop of the water level in a bottom tank feeding the constant head tank that is attached to the bottom of column.
- Calculate the equivalent total or bulk volume of saturated sand V_{Tot} :

$$V_{Tot} = \frac{V_{Water}}{n} \qquad \textbf{Eq. 5.8}$$

Where (n) is the porosity or the saturated water content (θ_{SAT}) [assuming that θ_{Dry} is neglected]

- Calculate the equivalent saturated height H_{Tot} :

$$H_{Tot} = \frac{V_{Tot}}{A} \qquad \textbf{Eq. 5.9}$$

Where A is the cross sectional area of the column.

- Estimate the equivalent capillary length from $\bar{\lambda}_{Cap}$:

$$\bar{\lambda}_{Cap} = H_{Tot} - Z_{S_{Applied}} \qquad \textbf{Eq. 5.10}$$

In our case, we apply an imbibitions to 5 mm ($Z_{S_{Applied}} = 5\text{mm}$) measured from the bottom of the sand, see **Fig. 5.20**. Following the same procedure described above, we have:

$$\bar{\lambda}_{Cap} = 0.29 \text{ m}$$

Fig. 5.20: Photo of the sand column at the end of the imbibitions step (the imposed water table height is $Z_{S_{Applied}} = 5$mm measured from the bottom of the sand). This photo corresponds to a steady sate conditions.

Chapter 6

Sand Column Experiment: Results, Analysis and Interpretation (at intermediate forcing frequencies)

6.1 Introduction

This chapter presents the experimental results of the oscillatory flows in a 1D porous column. Homogeneous sand column was used to conduct a series of more than 30 experiments with different oscillatory forcing parameters created by the tide machine described in the previous chapter. Pressure measurements were taken at different elevations along the sand column.

The results are presented in terms of the signals of pore water pressure, total pressure, and water table elevation, together with the profiles of pressure and total head. The attenuation, phase lag, and non harmonic structures of the different signals, are also discussed. Preliminary analyses and interpretations of the experimental results, based on the available range of forcing parameters (tidal period, tidal amplitude, and static level) are conducted. This study will be extended and re-analyzed numerically in Chapter 7.

6.2 Summary of the experimental program

Experiments were conducted using the original experimental set-up described previously in chapter 5. Briefly, a Darcy-scale laboratory experiment (tide machine) has been designed and constructed in this thesis at the Fluid Mechanics Institute of Toulouse, IMFT.

The setup consists of a sand column [1.5m height, 0.124 m internal diameter], a hydro-mechanical tide generator system named "tide machine", and measurement sensors (mainly tensiometers), plus a complete data acquisition system operated under the LABVIEW software.

The system generates low frequency waves (tides) on a partially saturated 1D sand column by applying an entry oscillatory pressure (simple harmonic function) at the bottom boundary of the column. The generated entry pressure (driving head) is almost sinusoidal of the form:

$$h_0(t) = \overline{h_0} + A_0 sin(\omega_0 t) \qquad \textbf{Eq. 6.1}$$

where: $\overline{h_0}$ is the positive time-average of the entry pressure head; A_0 is the amplitude; $\omega_0 = 2\pi/T_P$ is the angular frequency, and T_P is the period of the imposed entry pressure.

The design of the system was driven by the desire of making the model as flexible as possible in order to test different set of configurations. Therefore, the manufactured hydro-mechanical system gives the possibility of controlling and changing the mean level ($\overline{h_0}$), the amplitude (A_0) and the period (T_P) of the applied oscillatory pressure.

6.2.1 Initial condition

In all conducted experiments, the initial condition is a linearly distributed pressure head with a water table (h = 0 at the water table), which was chosen to coincide with $\overline{h_0}$ ($\overline{h_0}$ is the time average of the applied oscillatory entry pressure). For example, if the applied entry pressure is: $h_0(t) = 0.5 + 0.1sin(2\pi t/600)$, then, and before starting the oscillations, the static water table inside the sand column is adjusted to a height of 0.5m (measured from the bottom of the sand column) and it is left until it reaches a steady state

condition (until it stabilizes). This adjustment of water table is done by changing the level of the interior frame holding the motor and the overflow tank so that the free water surface of the over flow tank gives this 0.5 m static pressure head without applying any oscillations as shown in **Fig. 6.1** .

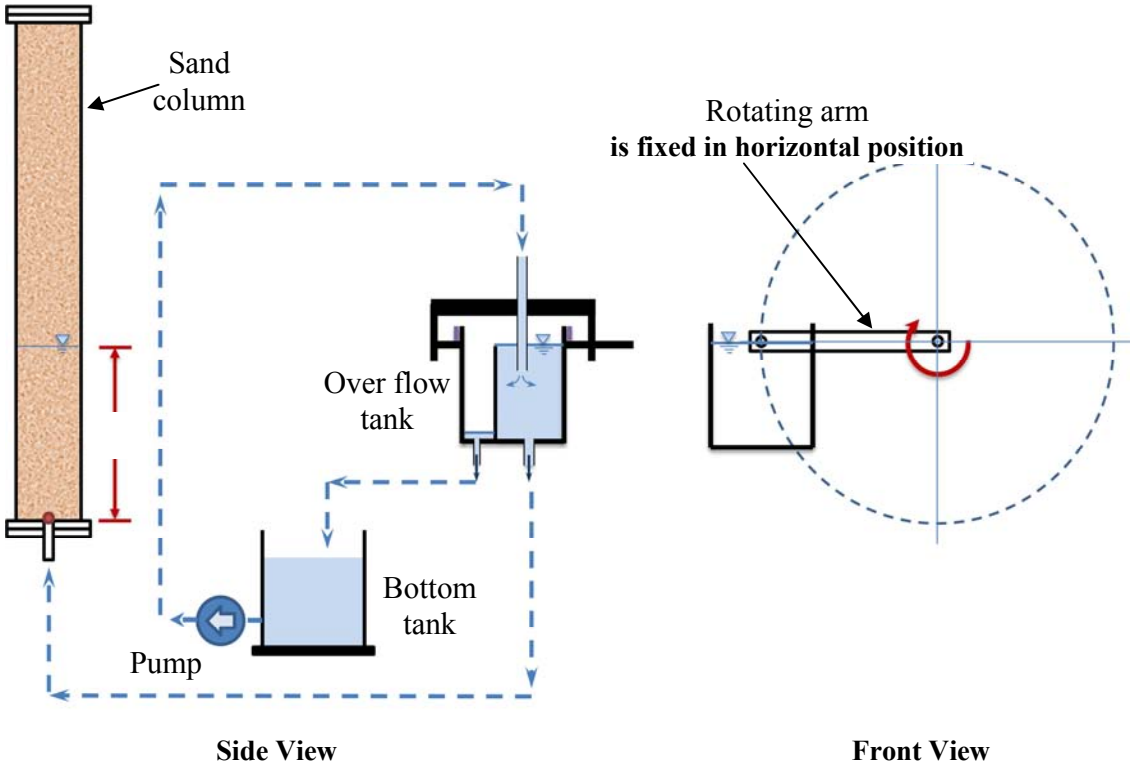

Fig. 6.1: Schema showing the position of the overflow tank in the case of initial condition application.

6.2.2 Experimental program

A series of more than 30 experiments on a short column (0.55 m height) and a long column (1.5 m height) were conducted using the tide machine. For each column, we generate a tidal forcing with different amplitudes ( ), frequencies ( ) or period ( ), and mean water levels ( ). Here in this chapter, we present the results for the long column experiments only. The experiments done on the short column will not be presented due to the constraints discussed previously in section 5.2.2.

The experimental data is summarized in Table 3.1. The parameters range of the entry pressure head were as follows:

- A_0 from 10 to 20 cm.
- $\overline{h_0}$ from 30 to 100cm.
- T_P from about 10 min to 165 min.

6.2.3 General notes

- **Steady oscillations:** For each experiment, the results are presented after reaching a steady oscillatory state (Each experiment was run until a repeatable flow pattern is developed for successive cycles).
- **Data acquisition frequency:** high frequency pressure measurements were chosen. The frequency of measurements is 100 Hz averaged on a span of 10 measures and thus the final results are presented in a 10 Hz frequency. Therefore, almost fine and smooth recorded pressure curves are obtained as shown in the figures presented in this chapter.
- **Time drift:** It was noted from the experimental results that there was a time drift generated by the motoreductor for applied time periods greater than 120min [in our experimental program, this small time drift occurs in the experiments with nominal time period of T_P = 165min, marked by red color in Table 3.1]. For these cases, the entry pressure may not be considered as a simple sine signal. Therefore, we almost choose to not include the results from these experiments in the analyses and discussions hereafter.
- **Acceleration effects:** It was shown in appendix A that the effect of Eulerian and inertial accelerations can be neglected in both experimental and numerical study.

Table 6.1 : Summary of the experiments driving head parameters (the experiments marked by the red color were excluded from the analysis due to time drift problem)

Test N°.	$\overline{h_0}$ (cm)	A_0 (cm)	T_P (min)	T_P Nominal value (min)	Motor frequency (Hz)	Test name
1.	50	10	9.57	10	85	T2
2.			20.38	20	40	T3
3.			30.57	30	26.8	T6
4.			60.51	60	13.6	T5
5.			110.37	110	7.3	T7
6.			164.69	165	4.7	T20
7.		15	9.56	10	85	T25
8.			20.4	20	40	T28
9.			30.63	30	26.8	T26
10.			60.71	60	13.6	T29
11.			110.8	110	7.3	T27
12.			168.84	165	4.7	T30
13.		20	9.56	10	85	T14
14.			20.4	20	40	T15
15.			30.61	30	26.8	T16
16.			60.66	60	13.6	T17
17.			110.9	110	7.3	T18
18.			167.02	165	4.7	T19
19.	30	20	9.55	10	85	T23
20.			20.4	20	40	T32
21.			30.62	30	26.8	T33
22.			60	60	13.6	T34
23.			110.95	110	7.3	T31
24.			164.36	165	4.7	T22
25.	100	10	9.56	10	85	T9
26.			20.38	20	40	T12
27.			30.6	30	26.8	T11
28.			60.63	60	13.6	T10
29.	70	20	9.56	10	85	T39
30.			20.40	20	40	T36
31.			30.62	30	26.8	T38
32.			60.72	60	13.6	T40
33.			110.94	110	7.3	T37

6.3 Experimental results, analysis and interpretation, with extreme cases comparison

In this section, the experimental results and a comparison between extreme cases (in terms of frequencies and within the available range of the conducted experiments) are presented. The results from the experiment are further analyzed and interpreted in terms of the attenuation and the phase lag of the pressure head signals and water table elevation with respect to different entry pressure parameters.

6.3.1 Pressure head time series

Pore water pressure head measurements are taken using the tensiometer-pressure transducer system. As a reminder, the used pressure transducers have an operating range from +1 to -1 bar and therefore we can use the tensiometer-pressure transducer system to measure both positive and negative pore water pressure.

The observed time series of the pressure head measurement at different elevations along the column are shown in **Fig. 6.2** and **Fig. 6.3** for bottom forcing period (T_P) of 10 min and 110 min respectively and similar A_0 = 0.2m and $\overline{h_0}$ = 0.3m. The time in the figures is normalized by the time period (T_P) of the bottom forcing.

Due to the oscillatory entry pressure, we observed spatial and temporal pressure responses along the column. From the pressure head fluctuations along the column we can divide the column into three regions:

- a first region (region I): in the lower part of the column which remains fully saturated during the whole experiment (see the pressure heads at z = 2.5 cm and z = 10 cm: the pressures at these two locations are fluctuated but always positive).
- a second region (region II): in the middle part of the column near $\overline{h_0}$ where the flow is alternating between saturated and unsaturated flows as observed in the pressure head evolution at z = 20, 30 and 40 cm. The pressure at these elevations are sometimes positive (saturated flow) and sometimes negative (unsaturated flow). We can also deduce that the water table (at which h = 0) fluctuates within this region.

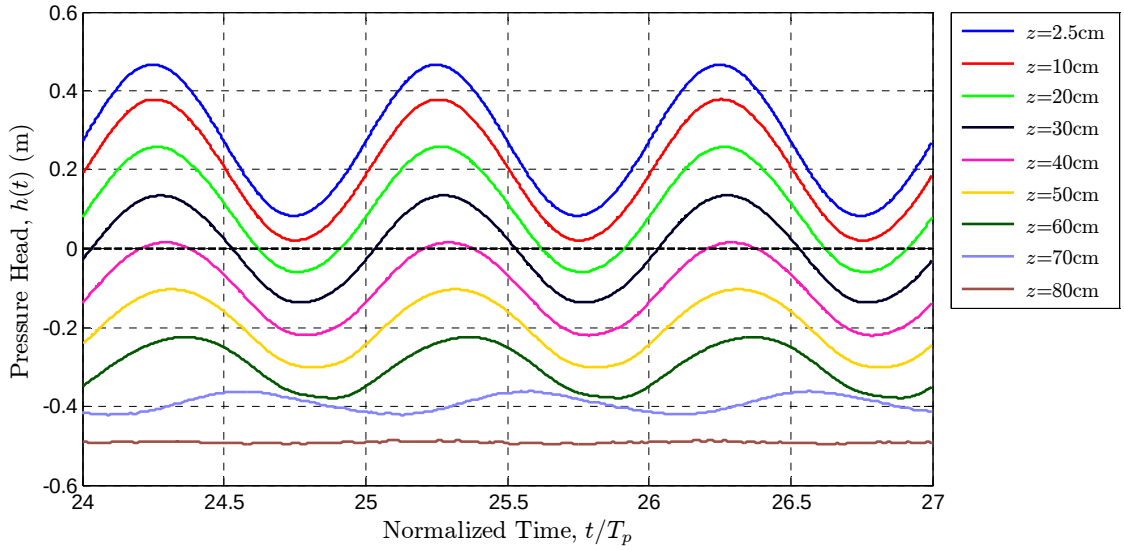

Fig. 6.2: The evolution of the pore water pressure head $[h(z,t)]$ over three time periods at different elevations (z) along the sand column for relatively high frequency bottom forcing pressure with the following parameters: A_0 = 0.2m, $\overline{h_0}$ = 0.3m, T_P = 573sec (9.55min).

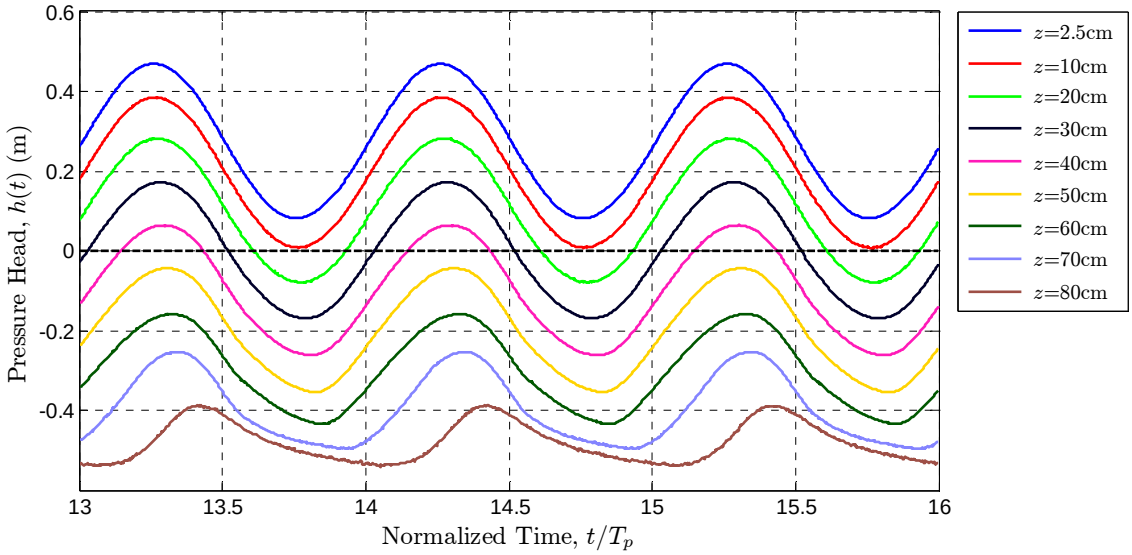

Fig. 6.3: The evolution of the pore water pressure head $[h(z,t)]$ over three periods at different elevations (z) along the sand column for relatively low frequency bottom forcing pressure with the following parameters: A_0 = 0.2m, $\overline{h_0}$ = 0.3m, T_P = 6657sec (110.95min).

- a third region (region III): in the upper part of the column which remains always unsaturated during all times. We can observe this region in the time series of the pressure head at z=50, 60, 70 and 80 cm where the pressure head is always negative.
- We can also define a sub-region in the summit of the third region (the upper part of the column) where the pressure head is negative (unsaturated) but this sub-region did not respond to fluctuations of the bottom forcing. The oscillation of the pressure head was dampened in the higher zone because of the reduced hydraulic conductivity and it is also possible due to the change in the water storage. The pressure in this sub-region matches the hydrostatic pressure and therefore no flux happened there. Note also that the thickness of this NO flow/NO response region increases with increasing bottom forcing frequency; this means that as the frequency of the bottom pressure increases, the damping of the pressure head increases and the thickness of this NO response region increases also.

Moreover, a qualitative inspection of the previous figures shows that as we move away from the applied bottom oscillatory pressure the pressure head amplitude attenuates, the phase lag increases and the shape of the pressure signals becomes more asymmetric. Differences between these observations can be detected between the low (Fig. 6.3) and high frequency (Fig. 6.2) cases. Further interpretation and analysis of these observations are presented in the next sections.

6.3.2 Total head time series

Another presentation of the pore water pressure is to use the total head instead of the pressure head. The presentation of data in terms of total head allows for better interpretation of the results with respect to the attenuations and phase lags. The total head (H) is the sum of the pressure head (h) and the elevation head (z) measured from a given reference. Here, the elevation reference was taken to coincide with the bottom of the sand column.

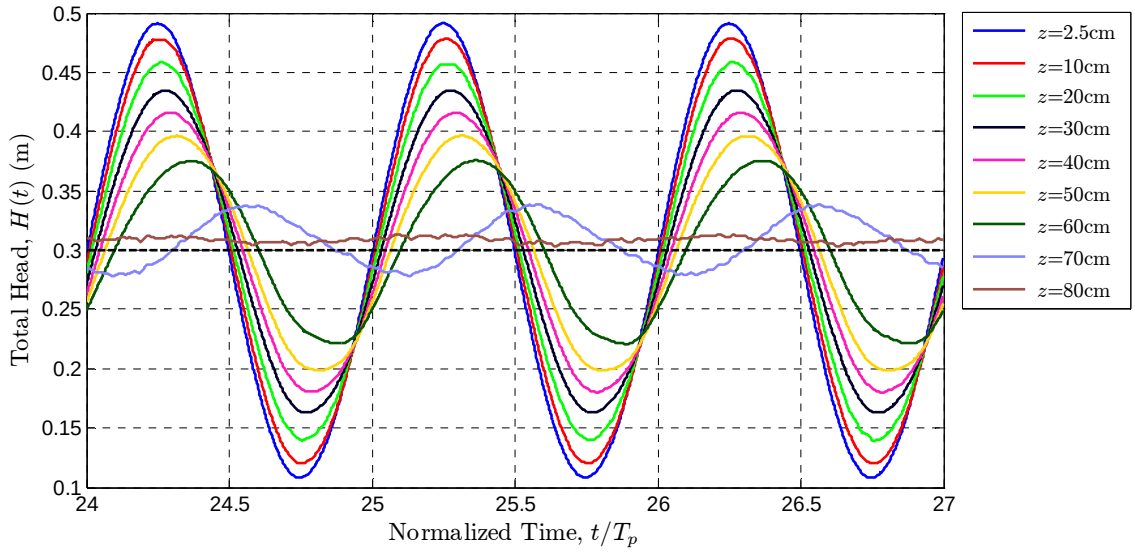

Fig. 6.4: The evolution of the total head $[H(z,t)]$ over three time periods at different elevations (z) along the sand column for relatively high frequency bottom forcing pressure with the following parameters: A_0 = 0.2m, $\overline{h_0}$ = 0.3m, T_P = 573sec (9.55min).

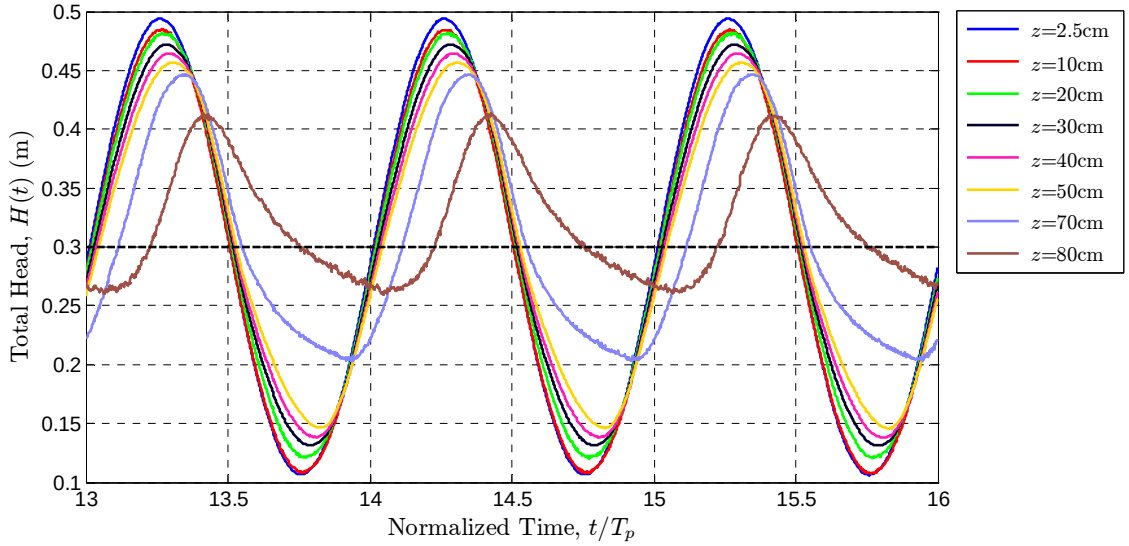

Fig. 6.5: The evolution of the total head $[H(z,t)]$ over three time periods at different elevations (z) along the sand column for relatively low frequency bottom forcing pressure with the following parameters: A_0 = 0.2m, $\overline{h_0}$ = 0.3m, T_P = 6657sec (110.95min).

Fig. 6.4 and **Fig. 6.5** show the evolution of the total head for the same experiments shown previously in **Fig. 6.2** and **Fig. 6.3** respectively. [**Fig. 6.4**: $\overline{h_0}$ = 0.3m, A_0 = 0.2m, T_P=10 min; **Fig. 6.5**: $\overline{h_0}$ = 0.3m, A_0 = 0.2m, T_P=110 min]. In each figure, the time is normalized by the time period (T_P) of the bottom forcing.

From these two figures we can clearly observe the attenuation, phase lag and asymmetry of the total head signals (as in the case of the pressure head) which increase by moving away from the exciting oscillatory pressure applied at the bottom of the column. These three observations will be discussed in more details in the following sub-sections.

6.3.2.1 Total head damping

In order to investigate the attenuation of the total head, *harmonic analysis* for the total head time series along the column were used to extract their amplitudes and phases. This sub-section discusses the attenuation of amplitude, while the next one focuses on the phase lag.

The variation of the amplitude of the total head signals along the column is shown in **Fig. 6.6**. In order to examine the influence of the bottom pressure frequency, the amplitude profiles at five different time periods (T_P) are plotted on the same figure [**Fig. 6.6**]. In the same way, **Fig. 6.7** and **Fig. 6.8** show the influence of different A_0 and $\overline{h_0}$ respectively.

It is observed generally that the amplitude decreases as we move farther from the bottom of the column. Moreover, we have almost linear amplitude drop in the saturated zone near the bottom of the column. In addition, the rate of the amplitude attenuation (dA/dz) in this fully saturated zone:

- decreases as the time period T_P of the bottom pressure increases [**Fig. 6.6**].
- increases with the increase of A_0 [**Fig. 6.7**].
- slightly decreases with the increase of $\overline{h_0}$ [**Fig. 6.8**].

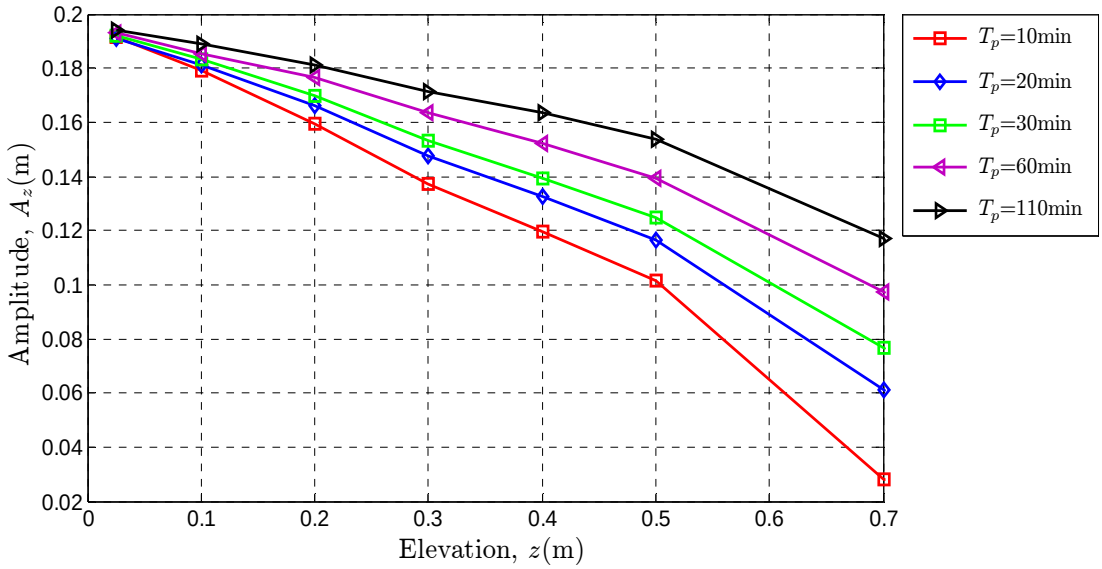

Fig. 6.6: Amplitudes of the pore water pressure versus the elevation (z) along the sand column at different oscillatory bottom forcing frequencies [A_0 = 0.2m, $\overline{h_0}$ = 0.3m, T_P = variable].

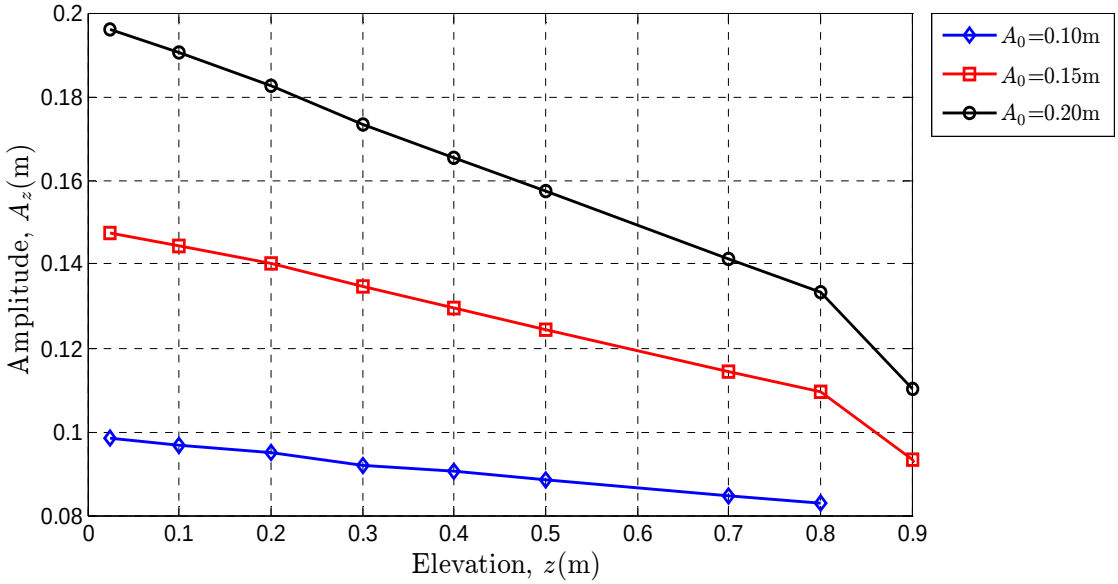

Fig. 6.7: Amplitudes of the pore water pressure versus the elevation (z) along the sand column at different A_0 of the oscillatory bottom forcing [A_0 = variable, $\overline{h_0}$ = 0.5m, T_P = 110min].

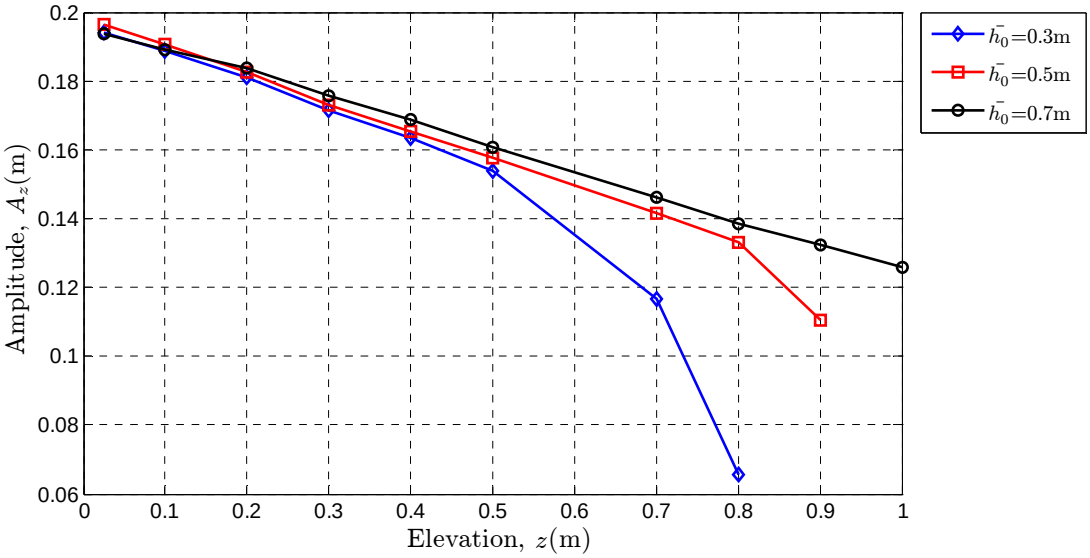

Fig. 6.8: Amplitudes of the pore water pressure versus the elevation (z) along the sand column at different $\overline{h_0}$ of the oscillatory bottom forcing [A_0 = 0.2m, $\overline{h_0}$ = variable, T_P = 110min].

The results shown in the above figures [**Fig. 6.4** to **Fig. 6.8**] are discussed as follows:

- The total head amplitude attenuates as we move away from the bottom of the column. In the saturated zone this damping is largely related to the frictional losses that occur as water flows between the sand grains (resistance to water flow). The total head was almost damped in the upper unsaturated part of the column mainly due to the reduced hydraulic conductivity in this unsaturated region.
- Moreover, we have almost linear amplitude drop in the saturated zone near the bottom of the column in consistency with the linearity of Darcy's head loss law in saturated zones.
- The attenuation of the total head amplitude increases as the frequency of the bottom forcing increases. For example, the total head amplitude at z = 80 cm is almost damped in the relatively high frequency case (T_P=10 min, **Fig. 6.4**); however for the relatively low frequency case (T_P=110 min, **Fig. 6.5**), it is still fluctuating with an apparent amplitude.

- The total head has larger amplitude in the low frequency (slow fluctuation) case because the porous media has more time to respond to the pressure oscillations at the bottom boundary (at very low frequencies, this gives nearly hydrostatic pressure profiles along the column).
- Moreover, with respect to the water content variations, we *can deduce* that in the case of very low tidal waves, there is somewhat like a water volume shift with time with greater fluctuations (it appears as high water content amplitude in the unsaturated zone near the water table). In the contrary the water content may not greatly vary in the case of high frequency waves and the water content profiles will be close to each other at different times within a complete period.

6.3.2.2 Phase lags versus elevation

Fig. 6.4 and **Fig. 6.5** show generally that the phase lag increases as we move farther from the bottom driving head. With more details, **Fig. 6.9** shows the extracted phase lags for the dominant harmonic of total head signals along the sand column. The figure shows also the phase lag profile at five different time periods.

As noted from the figure, the phase lag decreases as the frequency of the bottom forcing decreases. This phase lag (time delay) is related to the response of the porous media to the bottom oscillatory forcing. For example in the extreme case of a very low frequency, a quasi hydrostatic shift occurs with infinitely small phase lag and by increasing the frequency the porous media has no enough time to respond to the applied fluctuations and consequently the phase lag increases.

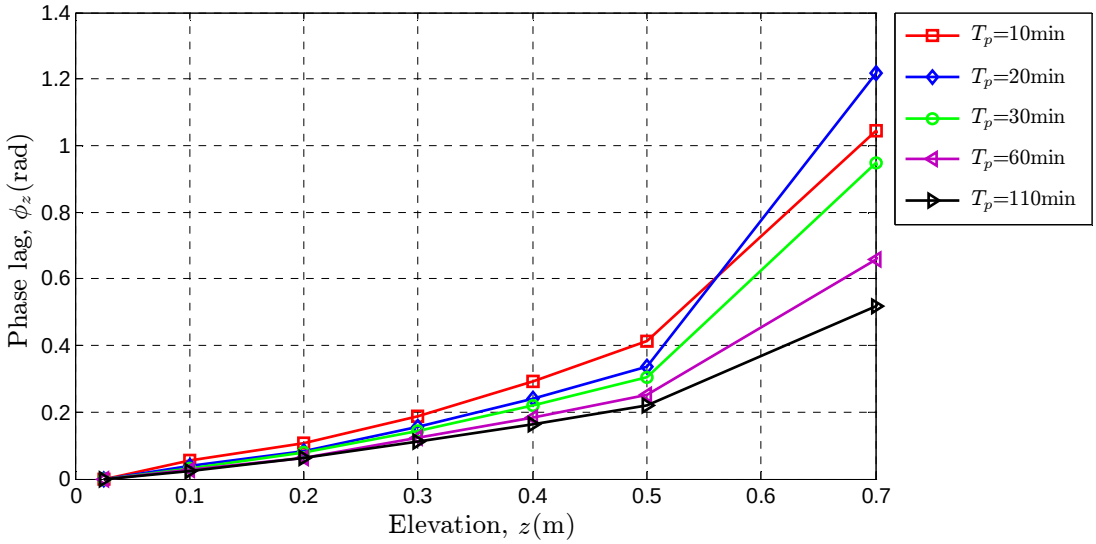

Fig. 6.9: Phase lag of the pore water pressure versus the elevation (z) along the sand column at different oscillatory bottom forcing frequencies [A_0 = 0.2m, $\overline{h_0}$ = 0.3m, T_P = variable].

6.3.2.3 Total head signals asymmetry

- The figures show also that the head signals are asymmetric. This asymmetry is evident in the unsaturated zone and in the case of low frequency (T_P=110 min, **Fig. 6.5**). For example, the shape of the total head signals at z = 70 and 80 cm are asymmetric and skewed with a shorter wetting phase followed by a longer drainage phase.
- This non-harmonic structure of the signals is a sign of the global hysteretic behavior of the porous column (due to for example the competition between the gravity and capillary effects).
- It is worth noting at this stage that the numerical solver (BIGFLOW) shows the same non-harmonic structure of the signals even though it is based on non-local hysteresis formulation of the constitutive relationships [$k(h), \theta(h)$].

6.3.3 Pressure head and total head vertical profiles

Fig. 6.10 and **Fig. 6.11** show the pressure head and the total head vertical profiles respectively at specific times separated by $T_P/8$ within a complete cycle.

The figures confirm the previous interpretations of the time series of the pressure and total heads. The damping of the pressure head (and of course the total head) increases as the frequency of the bottom oscillatory forcing increases (the oscillations become faster). A comparison between the two figures shows that the pressure damps completely at about z = 80 cm for the high frequency case [T_P=10 min, **Fig. 6.10**(a) and **Fig. 6.11**(a)], where it is still fluctuates at about z = 90 cm for the low frequency case [T_P=110 min, **Fig. 6.10**(b) and **Fig. 6.11**(b)]. A qualitative comparison between the envelope of the total head profiles in the two cases emphasizes that the high frequency case has a greater damping rate (tight envelope with steep/large pressure gradient) compared to the low frequency case (spread envelope with relatively mild/low total head gradient).

6.3.3.1 Bottom flux amplitude

Moreover, a qualitative comparison between the bottom fluxes can be deduced. This can be achieved by comparing the total head gradient [$\Delta H/\Delta z$] in the fully saturated zone at the bottom of the column knowing that:

$$q_{Bottom} = K_{SAT} \cdot [\Delta H/\Delta z]_{SAT} \qquad \textbf{Eq. 6.2}$$

From **Fig. 6.11**, it is obvious that there is a higher gradients in saturated zone for the high frequency case [**Fig. 6.11**(a)] compared to the low frequency case [**Fig. 6.11**(b)]. This implies that the bottom flux is higher for the rapid fluctuations compared to the low fluctuations (when the frequency of the driving bottom pressure increases, pressure head losses increase and the amplitude of the fluctuating bottom flux increases too).

It is also noted from the upper unsaturated part of the total head profiles [**Fig. 6.11**] that the total head fluctuated around a new higher time average value which differs from the initial hydrostatic position (0.3m). This indicated that due to the applied fluctuations, a net water volume was stored in this unsaturated region.

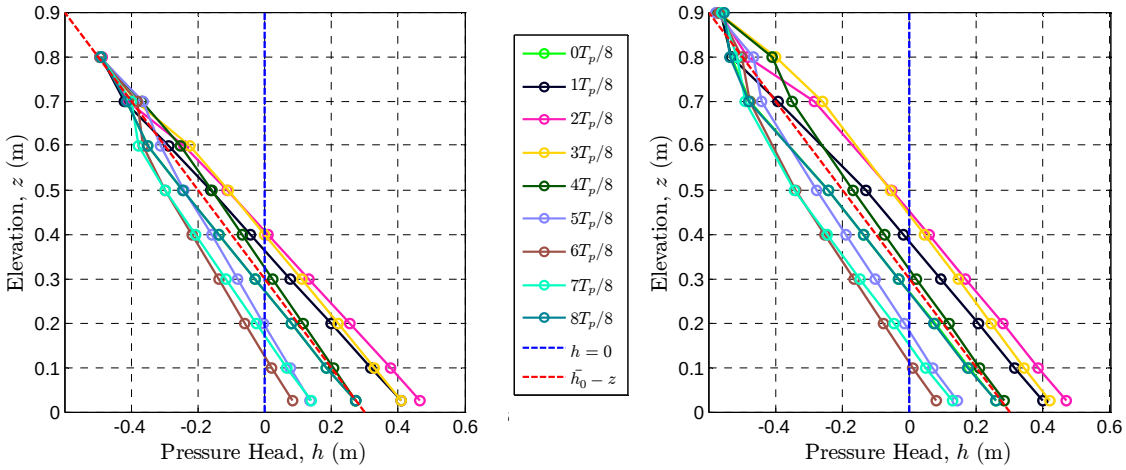

(a) **(b)**

Fig. 6.10: Pressure head profiles $h(z)$ at 9 different times separated by $T_P/8$; the bottom forcing parameters are: A_0 = 0.2m, $\overline{h_0}$ = 0.3m and (a) T_P = 573sec (9.55min); (b) T_P = 6657sec (110.95min). The red dashed line is the hydrostatic pressure head profile.

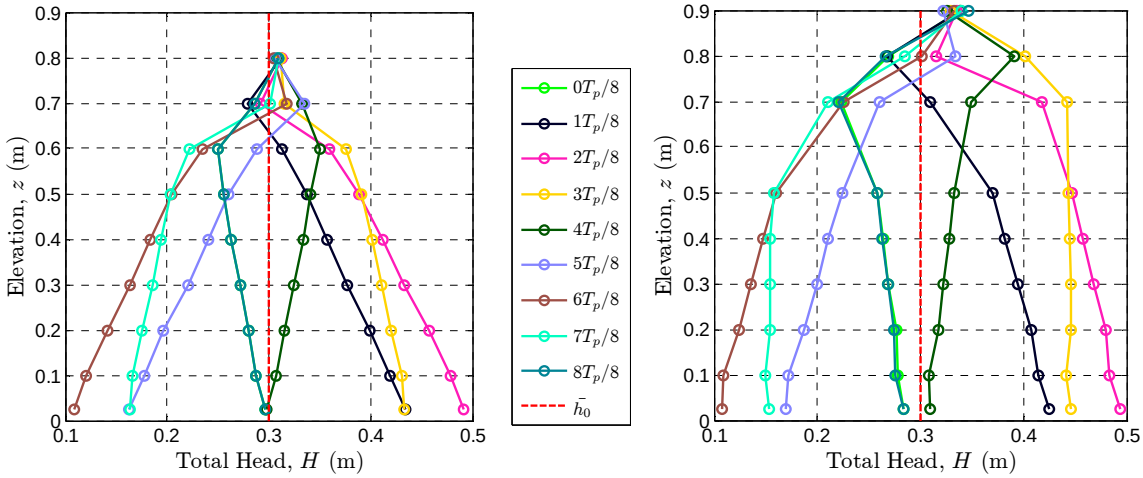

(a) **(b)**

Fig. 6.11: Total head profiles $h(z)$ at 9 different times separated by $T_P/8$; the bottom forcing parameters are: A_0 = 0.2m, $\overline{h_0}$ = 0.3m and (a) T_P = 573sec (9.55min); (b) T_P = 6657sec (110.95min). The red dashed line is the hydrostatic pressure head profile.

6.3.3.2 Flow directions along the column during fluctuations

In this part we will try to answer the following question: does the flow have the same direction throughout the column at a specific instant of time? What happens in the case of a falling or rising water table?

To answer this question, we separate two total head profiles as shown in **Fig. 6.12** for T_P = 573sec (9.55min). The figure shows the profiles at $t = T_P/2$ (during a falling water table) as and $t = T_P$ (during a rising water table rise).

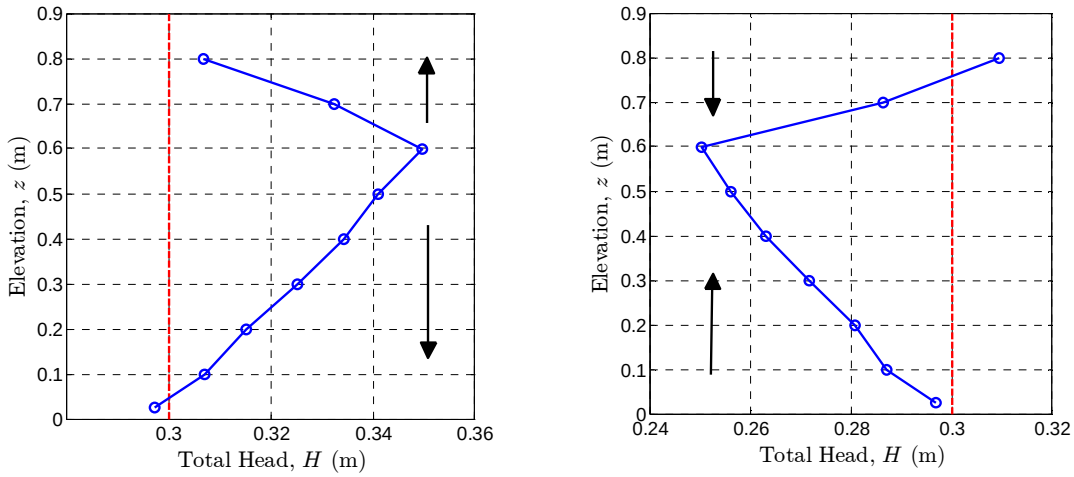

(a) **(b)**

During a falling water table **During a rising water table**

Fig. 6.12: Total head profiles $h(z)$ at (a) $t = T_P/2$ during a falling water table and (b) $t = T_P$ during a rising water table. The presented profiles are for a relatively high frequency bottom forcing with the following parameters: A_0 = 0.2m, $\overline{h_0}$ = 0.3m, T_P = 573sec (9.55min). The arrows in the figure show the flow direction. The red dashed line is the initial hydrostatic condition.

From the above sample figure and by comparing the total head values along the column, we can deduce that the flow direction is not the same along the column at these two times (at other times it may have the same direction and it can also depend on the forcing frequency).

As shown in **Fig. 6.12**(a) and during the falling of the water table, the total head at z = 2.5, 60 and 80cm are 29.7, 34.96 and 30.67 cm respectively which indicates that the flow moves in the upward direction between z = 2.5 and z = 60 cm ($\partial H/\partial z > 0$), and in the

downward direction between z = 60 and z = 80 cm ($\partial H/\partial z < 0$). Therefore, there is a downward flux (as expected) in the bottom part of the column. However, in the upper unsaturated part of the column there is an upward flux even though the water table moves in the downward direction. On the other hand, during the rising of the water table [**Fig. 6.12**(b)], there is an upward flux (as expected) in the bottom part of the column. However, in the upper unsaturated part of the column there is a downward flux even though the water table moves in the upward direction.

It is worth noting that the above fluxes have different magnitudes because of the difference of pressure gradients and also because of the hydraulic conductivities (small hydraulic conductivity in the upper unsaturated zone).

6.3.4 Water table fluctuations

In the sand column experiments, the evolution of the water table elevation [$Z_S(t)$] is not measured directly. However, it can be calculated from pressure head measurements taken at different elevations along the column. The water table elevation is the height at which the pore water pressure equals the atmospheric pressure. If the atmospheric pressure is taken to be the reference pressure; then the water table is the surface or elevation at which the pressure head equals zero.

6.3.4.1 Water table height calculation methods

Based on the experimental results, the water table can be calculated by two methods:

Method 1: by linear interpolation between the two pressure readings at which the pressure sign changes. Therefore, to find the water table at a given instant, we should look for the two tensiometers where the pressure head changes form a positive value (below the water table) to a negative value (above the water table). This method is based on the assumption that the pressure gradient between the two points is linear, and that the capillary fringe is greater than the distance between the successive tensiometers.

Method 2: using Darcy's law in the saturated zone below the water table. The pressure gradient at any specific time is constant in this saturated zone. Thus, the estimation here is exact because the pressure gradient is always linear below the water table. To estimate the gradient in this zone; we rely on the pressure head readings of two points in the saturated zone where the pressure is always positive. A more accurately method is to base the estimation of the pressure gradient in the saturated zone on more than two points (if applicable), then to use the least square regression to find the pressure gradient in this saturated zone. The position of the water table will be the y-intercept of this line.

The two methods were tested and they showed nearly similar results. The analysis hereafter is based on the first method.

Fig. 6.13 shows the evolution of the water table for selected experiments with the following oscillatory bottom forcing parameters A_0 = 0.2m, $\overline{h_0}$ = 0.3m with two different time periods of about 10 min (red curve) and 110 min (blue curve).

By comparing the two curves, we can observe that the amplitude of the water table increases and the phase lag (between the entry pressure and the water table elevation) decreases as the frequency of the bottom forcing decreases. More details on these observations are presented in the next sub-sections.

Moreover, a comparison between the experimental results of the water table fluctuations and the analytical models of (Nielsen and Perrochet, 2000) is presented in Appendix B.

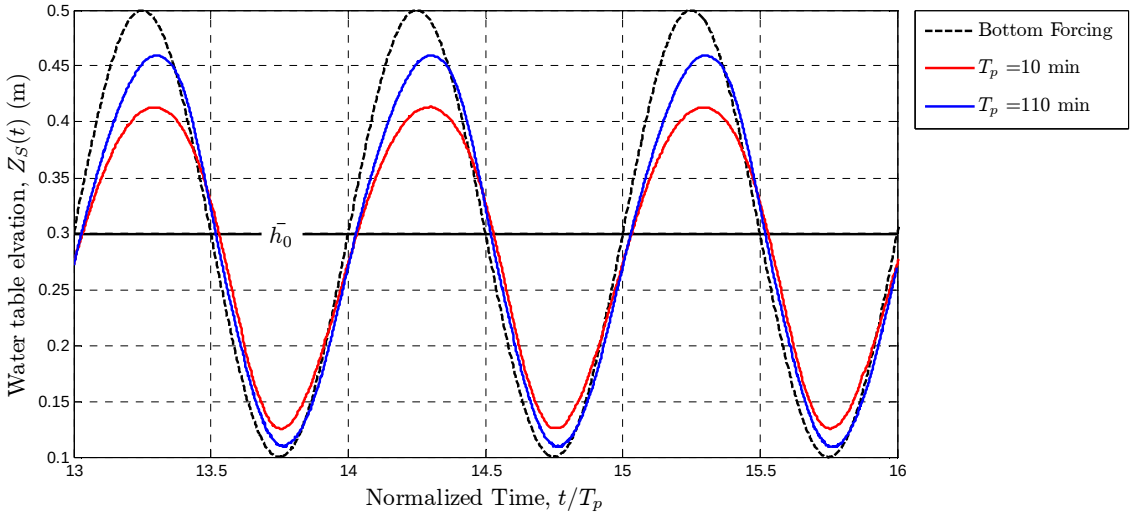

Fig. 6.13: Water table fluctuations $[Z_S(t)]$ over two time periods. The bottom forcing parameters are: A_0 = 0.2m, $\overline{h_0}$ = 0.3m and a variable time period (T_P) of about 110 min (the blue curve) and of about 10 min (the red curve). The dashed black curve is the bottom forcing.

6.3.4.2 Water table amplitude versus frequency

Fig. 6.14 shows the water table amplitudes (extracted from harmonic analysis) versus forcing periods. The figure confirms what was previously observed. The water table amplitude decreases with the decrease of the time period (rapid fluctuations); therefore the sand column can be considered to act as a low pass filter. It is noted from **Fig. 6.14**, that this increase is nonlinear and reaches asymptotically the amplitude of the applied bottom pressure (A_0) at large time period.

The interpretation of this observation bears resemblance to that of the pressure head discussed previously in section 6.3.2. With the increase of the time period of the bottom forcing, the water table height will be close to the imposed bottom pressure. For slow fluctuations, the water table has more time to equilibrate at each instant and the regime will be quasi-static with nearly hydrostatic pressure profile at each instant. On the contrary, for rapid fluctuations the porous medium does not have time to respond to these fluctuations and this leads to small water table fluctuations.

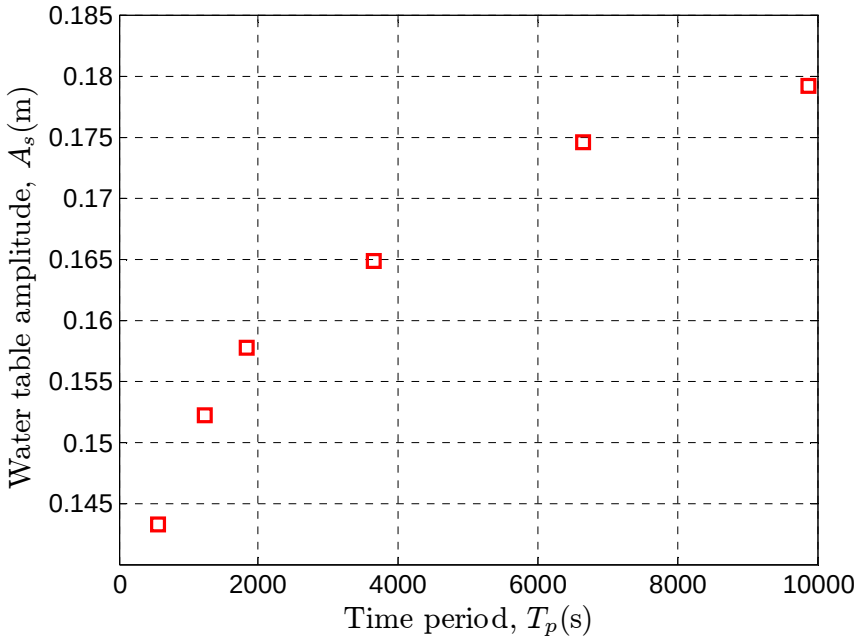

Fig. 6.14: Water table amplitude versus bottom forcing period. [A_0 = 0.2m, $\overline{h_0}$ = 0.3m, T_P = variable].

6.3.4.3 Water table phase lag versus frequency

The phase lag between the time series of the water table height and the applied bottom pressure at different time periods (T_P) is shown in **Fig. 6.15**. It is noted that the phase lag decreases non-linearly with the forcing period. Our guess was that at very large forcing time periods, the static equilibrium is retained instantaneously. Therefore, there is no phase lag (it reaches zero asymptotically) because the porous media and consequently the water table have enough time to respond to the bottom fluctuation.

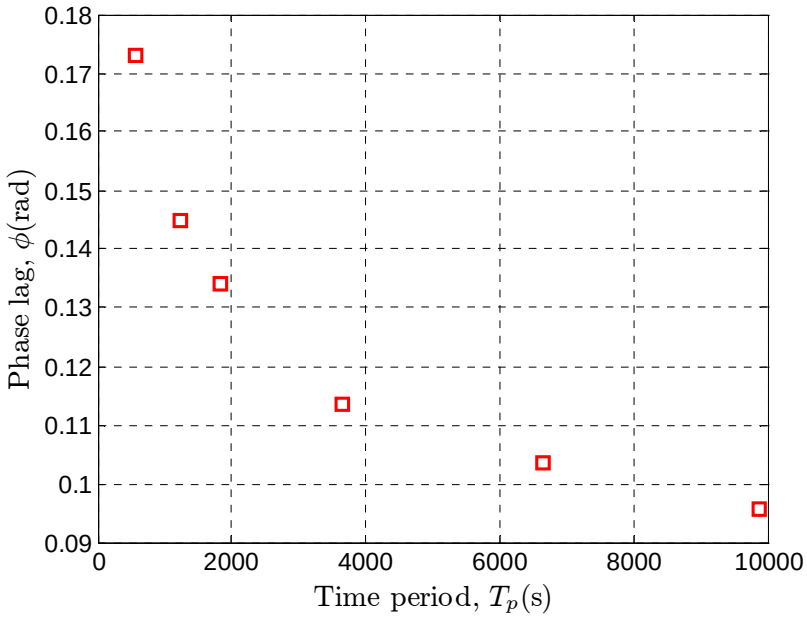

Fig. 6.15: Water table phase lag versus bottom forcing frequency. [A_0 = 0.2m, $\overline{h_0}$ = 0.3m, T_P = variable]

6.3.4.4 Water table time-average position versus frequency

Fig. 6.16 shows the time-average of the water table position versus the time period of the bottom forcing.

Firstly, it is observed from the figure (and within the current range of the conducted experiment) that the time-average position of the water table ($\overline{Z_S}$,) was less than the time average of the fluctuated pressure ($\overline{h_0}$) imposed at the bottom of the 1D column. This is probably due to the particular 1D geometry of our set up and to the effect of the bottom pressure condition. With other geometries, however, an over-elevation of the mean water table height has been observed in the presence of lateral tidal forcing and sloping soil surface (Nielsen, 1990, Turner, 1993b, Cartwright et al., 2004).

Therefore, in our special 1D geometry coupled with a bottom forcing, there is an increased effect of this bottom boundary condition at the instances when the water table height reaches its trough (minimum elevation of the water table) leading to smaller

pressure drop and phase lag, which gives a water table curve that seems to be pulled down when it approaches the bottom of the column. For example for the extreme bottom forcing with: $A_0 = \overline{h_0}$; the numerical simulations shows that the water table reaches the bottom of the sand column at every $t = (3/4) \cdot i \cdot T_P$, $i = 1,2 \cdots$ maximum number of cycles. However, for the same case, it did not reach $A_0 + \overline{h_0}$ at $t = (1/4).i.T_P$. This leads also to a water table signal that is strongly asymmetric which is wide for the maxima and very narrow for the minima (see chapter 8 for example for such signal structure).

Secondly, it appears from the figure that the time-average of the water table increases with the increase of the forcing period of the bottom oscillatory pressure. We expect (not shown experimentally) that at large forcing periods this position will reach $\overline{h_0}$. This is probably because at low frequencies there is a reduced effect of the bottom boundary condition and flow is very small with approximately no pressure loss which results in a water table time series that resemble the applied oscillatory pressure at the bottom of the column.

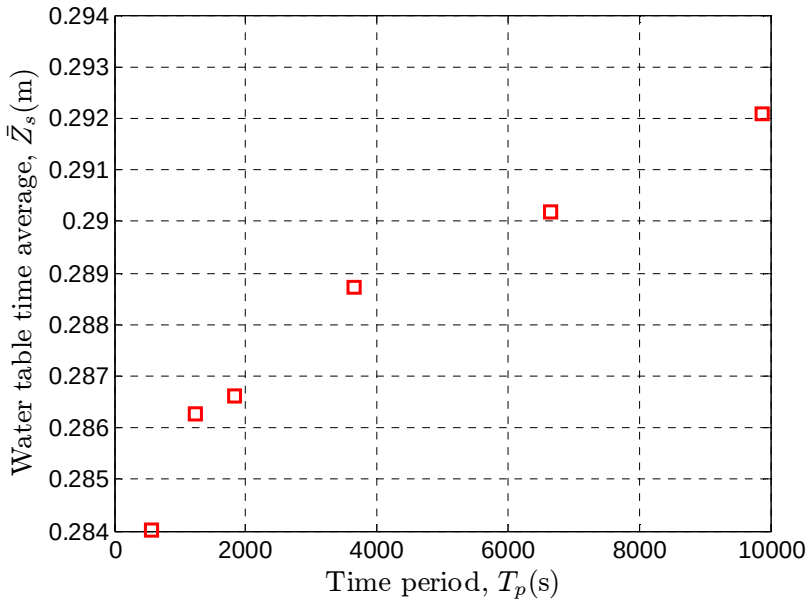

Fig. 6.16: Water table time average versus bottom forcing frequency. [A_0 = 0.2m, $\overline{h_0}$ = 0.3m, T_P = variable]

Chapter 7

Parameters Estimation of the Experimental Sand and an Extended Numerical Study

7.1 Introduction

The first part of this chapter focuses on the parameters estimation of the sand used in the physical experiment, which is accomplished using an inverse problem-based approach with a genetic algorithms. The first part of the chapter also provides a discussion of the achieved calibration results.

In the second part, we use the calibrated sand parameters to extend the experimental study numerically in order to examine the effect of oscillatory forcing and porous media hydraulic parameters outside the available range of the physical experiment. Then we provide an extended numerical parametric study of the frequency response of the water table. One of the objectives is to identify a characteristic frequency separating low and high frequency regimes.

7.2 Parameters estimation of the experimental sand "SilicaSand": The Inverse problem

Parameter estimation (Inverse Problem) with the genetic algorithms optimization technique is used to estimate the soil hydraulic parameters of the sand "Silica-Sand" used in the physical experiment presented in the previous chapters (chapter 5 and 6). In this section, we give an overview of the inverse problem and the genetic algorithm followed by a brief description of the technique used to link the numerical simulator of the variably saturated/unsaturated Richards-based flow equation with the genetic algorithm. The objective function used in the optimization problem is presented and finally the results of the inverse problem are analyzed and discussed.

7.2.1 Overview of the inverse problem and genetic algorithms

In this thesis, genetic algorithms have been used as a tool to get the optimal soil hydraulic parameters for the sand used in the experiment, which enabled the model to match well the measured values. Therefore, we present in the following a brief overview of this technique.

Nowadays, numerical and mathematical models are largely used to analyze groundwater and hydrological systems. These models are parameter-dependent models that are not easily measured.

An attractive procedure for obtaining model parameters in recent years has been through inverse modeling. This approach involves obtaining easily measurable variables (model output), and using this information to estimate a set of unknown model parameters. Inverse procedures usually require optimization of an objective function describing the difference between measured and simulated data (Abbaspour et al., 2001).

Gradient-based local optimization approaches are among the most popular approaches for solving these inverse problems. While these methods are sometimes appropriate, they are not effective for problems that contain several local minima and for problems where the decision space is highly discontinuous or convoluted. For these types of problems,

heuristic global search approaches such as genetic algorithms (GAs) are more effective (Mahinthakumar and Sayeed, 2005).

The primary strengths of nongradient-based techniques such as GAs are the increased flexibility in problem formulation and the capability of handling discontinuities in the decision space. Furthermore, these techniques also have the potential to explore a larger search space, resulting in a more robust search than that of gradient- based approaches (Mahinthakumar and Sayeed, 2005). In the engineering literature, genetic algorithms are well known to be able to solve complex, large and poorly understood optimization problems (Levasseur et al., 2008). GAs are capable of searching the entire solution space with more likelihood of finding the global optimum.

Furthermore, genetic algorithms are able to reach global optima without the dependence on initial guesses, and only using the objective function value. GAs are best used when the objective function is discontinuous, highly nonlinear, stochastic or has unreliable or undefined derivatives.

On the other hand, the GAs method does not guarantee the exact identification of the optimum solution of a problem. However, genetic mechanisms allow to localize an optimum set of solutions close to the optimum in a given search space (Gallagher and Sambridge, 1994)

The genetic algorithm is a search procedure based on the mechanics of natural selection and natural genetics that combines an artificial survival of the fittest with genetic operators. It is initially developed by (Holland, 1975). GAs operate on a population of potential solutions applying the principle of survival of the fittest to produce successively better approximations to a solution. At each generation of a GA, a new set of approximations is created by the process of selecting individuals according to their level of fitness in the problem domain and reproducing them using operators borrowed from natural genetics. This process leads to the evolution of populations of individuals that are better suited to their environment than the individuals from which they were created, just as in natural adaptation (Chipperfield, 1995).

In more details, (Ines and Droogers, 1999) stated that: "GAs consist of three basic operators: the selection, crossover and mutation". They summarized the GAs steps as follows:

- First, GAs start by randomly generating an initial population of possible solutions. The population size is the number of individuals that are allowed in the population maintained by a GA. If the population size is too large, the GA tends to take longer to converge on a solution.
- Each individual is evaluated based on its performance with respect to some fitness function that represents the environment. Using this measure, individuals compete in a selection process where the fittest survives and is selected to enter the mating pool; the lesser-fit individual dies. These best individuals are called parents.
- The selected individuals (parents) are assigned a mate randomly. Genetic information is exchanged between the two parents by crossover to form offspring. The parents are then killed and replaced in the population by the offspring to keep the population size stable. Reproduction between the individuals takes place with a probability of crossover. If a randomly generated number is less than the probability of crossover, crossover happens, otherwise not, and the parents enter into the new population.
- To maintain diversity, some of the genes are subjected to mutation to keep the population from premature convergence.
- Selection, crossover and mutation are repeated for many generations, with the expectation of producing the best individual(s) that could represent the optimal or near optimal solution to the problem under study.

In this thesis, the MATLAB genetic algorithm toolbox is used to solve the optimization problem. MATLAB was also used to write a script that combines this toolbox with the numerical code BIGFLOW. This is described in the next section.

7.2.2 Coupling genetic algorithms with numerical simulation

A MatLab script (named MLGA) is written in this thesis to automatically perform optimization and link the numerical code (BIGFLOW), which solves the Richards' equation, to the MatLab genetic algorithm function (GA) in order to find the optimal parameter set. MLGA performs the following steps (**Fig. 7.1**):

- Run the GA to generate an initial population, which is a set of individuals; each of which represents a single set of sand hydraulic parameters β. The constraints here are usually the upper and lower bounds on the unknown parameters.
- MLGA prepares the input file required to run BIGFLOW. This input file contains the latest set of the sand-hydraulic parameters (individual) created by the genetic algorithm function.
- MLGA executes automatically BIGFLOW for the created input file. At the end of the 'forward' numerical simulation, the resulted pressure head at all time steps will be available in the form of output file.
- MLGA reads and analyses this output file to get the water table height (The final result is a water table height time series).
- MLGA calculates the objective function that compares the measured and the modeled water table height (see the objective function section)
- The steps (2 to 5) are repeated for all individuals in the current population.
- The GA evaluates these objective function values, followed by applying the operations (selection, crossover and mutation) to generate a new population.
- These steps (2-7) are repeated for the new population until an acceptable solution is found or some other stopping condition has been reached.
- Finally, MLGA Returns the best-so-far individual.

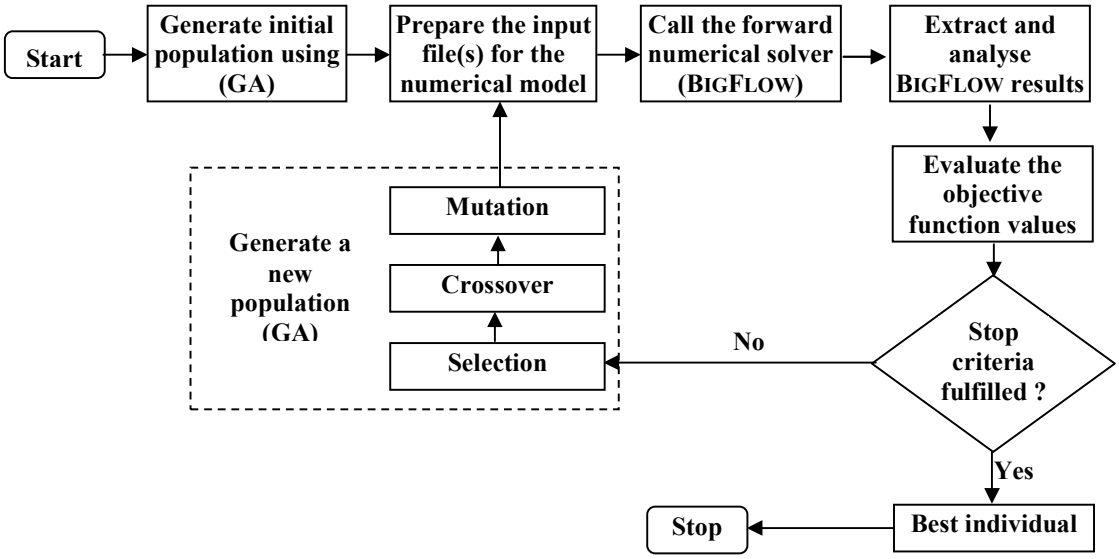

Fig. 7.1: Flowchart of the optimization procedure linking the genetic algorithm(GA) to numerical model (BIGFLOW).

7.2.3 Objective function

Our objective of using the inverse problem is to find the soil hydraulic parameter set β that minimizes the root means square errors (RMSE) between measured and simulated water table heights. The model formulation is as follows:

$$F(\beta) = \left[\frac{1}{N}\sum_{n=1}^{n=N}\left|Z_{s_{MES}}(t_n) - Z_{s_{SIM}}(\beta, t_n)\right|^P\right]^{1/P} \qquad \textbf{Eq. 7.1}$$

Where F is the objective function; N is the total number of measurements over time ; $Z_{s_{MES}}(t_n)$ is the measured water table height at time $t = t_n$; $Z_{s_{SIM}}(\beta, t_n)$ is the corresponding simulated value; P is a power value taken to be 2 (RMSE) and β is the vector of the input soil-hydraulic parameters used in the numerical model, $\beta = \{K_{SAT}, \alpha, n\}$ which are the parameters to be optimized.

Note that our objective function is based on the water table heights as both saturated and unsaturated zones contribute/interfere in the positioning of the water table.

Generally speaking, the use of the absolute differences as the objective function (P=1 in Eq. 7.1) tends to overemphasize numerous small events while the use of higher power ($P \geq 3$) overemphasizes the larger events (tends to be more sensitive to largest errors). In our analysis, an intermediate power value (P=2) is chosen.

7.2.4 Inverse problem prior information and the proposed parameter range

The experiments are evaluated by inverse simulation of the flow process using the Richards equation as the flow model, and the van Genuchten/Mualem parameterization for the hydraulic properties. For modeling purposes, it is assumed that the sand used in the physical experiment is isotropic and homogeneous.

By the optimization techniques described previously, we seek to estimate the following soil-hydraulic parameters:

- K_{SAT} : saturated hydraulic conductivity.
- α : van Genuchten unsaturated parameter that can be related to the inverse of an average capillary length scale of the porous media (see chapter 3 for more details on this parameter).
- n : van Genuchten unsaturated parameter, related to the pore size distribution of the porous media or the rate of change of the de-saturation zone of the soil water characteristic curve (see chapter 3 for more details on this parameter).

On the other hand, the saturated water content (θ_{SAT}) was excluded from the optimization and was fixed at the measured value of 0.38. The residual water content (θ_r) is set to the value of 0.02 [calibrated by (Wang, 2010) in her wetting/imbibitions experiment].

Upper and lower bounds are applied as constraints on the parameters to be optimized see Table 7.1. The proposed range of the hydraulic parameters is based on previous qualitative calibration done by (Wang, 2010) for the same sand which she used in an imbibitions/wetting experiment and also on the measured or estimated values done in this thesis (see chapter 5). Moreover, the parameters ranges were chosen to be in the physically expected range for this fine sand.

Table 7.1 : The upper and lower bounds of **s**oil hydraulic parameters (applied in the optimization problem) and measured versus calibrated parameter values.

Parameters	**Estimated or measured values**	**Old calibration (Wang, 2010)***	**Range used in the optimization**	**Optimization results**
K_{SAT} (m/s)	1.31E-4	1.5E-4	1.0E-4 to 5.0E-4	**3.23E-4**
α (m^{-1})	3.4	4.6	2.5 to 10	**2.8**
n	—	5	1.5 to 5.5	**2.88**
λ_{CAP} (m)	0.29	0.21		**0.308**

(*) these values was captured from the calibration done by (Wang, 2010) for the same sand used in our experiment; she did a qualitative calibration (based on images) for her wetting/imbibition experiment .

7.2.5 Inverse problem results and discussion

The conducted inverse modeling was based on calibrating the numerical model with experiment N°.T32 which has the following forcing parameters:

- A_0 = 0.2m
- $\overline{h_0}$ = 0.3m.
- T_P = 1223.9 s.

The results of calibration give the following soil hydraulic parameters:

- $K_{SAT} = 3.23 \times 10^{-4}$m/s
- $\alpha = 2.8$ m^{-1}
- $n = 2.88$

Fig. 7.2 shows the results of the inverse optimization by comparing the observed and the simulated water table height.

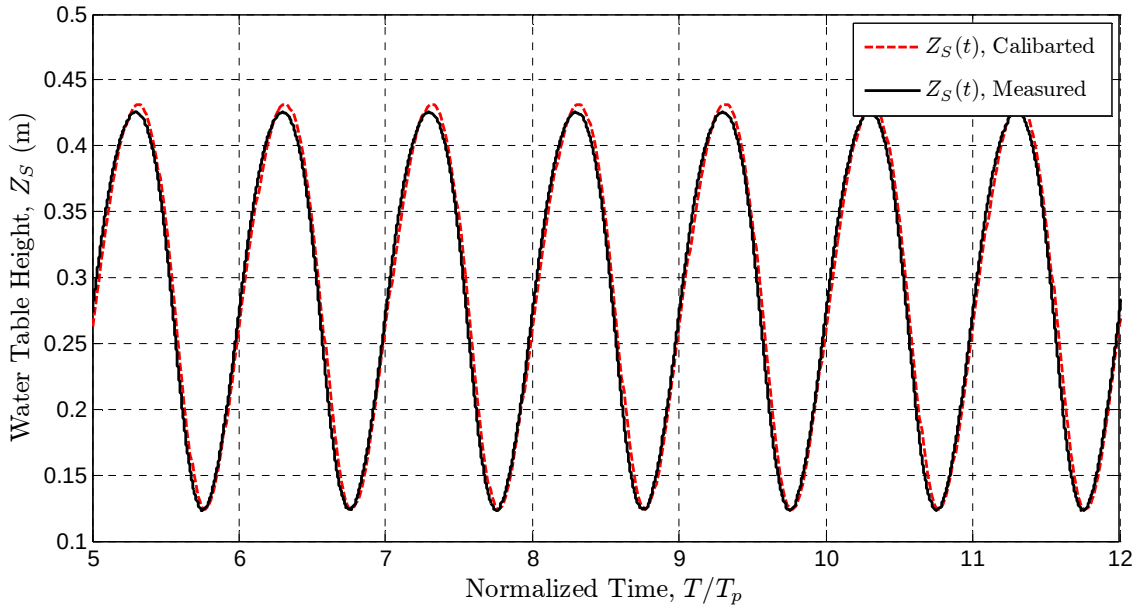

Fig. 7.2: Observed versus calibrated water table height. The bottom forcing pressure parameters are: A_0 = 0.2m, $\overline{h_0}$= 0.3m, T_P = 1223.95 sec (20.4min).

From the above figure [**Fig. 7.2**], it is clear that the calibrated water table height match well the observed one.

To validate the results of calibration we run the model using the calibrated parameters at different bottom non-calibrated frequencies (different T_P). **Fig. 7.3** shows the measured and modeled water table amplitude at different time periods. It is noted from the figure that the numerical calibrated model does not fully match the observed values. In fact, a perfect match is impossible for the following reasons:

- The numerical model assumes that the column is perfectly homogeneous; however this is not the real case. Even if we take care as much as possible to get a homogeneous sand column in the physical experiment, it is impossible to get such a perfect homogeneous column and the presence of small local heterogeneity is possible. On the other hand, it is also possible that the porosity varies along the height of the column due to the effect of the sand own weight.

- The numerical model does not take into account the effect of hysteresis that may have occurred during the drainage and imbibition cycles. This may affect the numerical results of this highly dynamic problem.
- The effect of the bottom boundary (the perforated plate and the screen) is not taken into account in the numerical model.
- It is also possible that the measurement based on the tensiometer/pressure transducers system is not highly accurate, these pressure transducers are sensitive to temperature and even when we included the temperature in the calibration procedure, there were still some errors in the calibration model. Moreover, the presence of air bubbles near the tensiometers affects its reading.

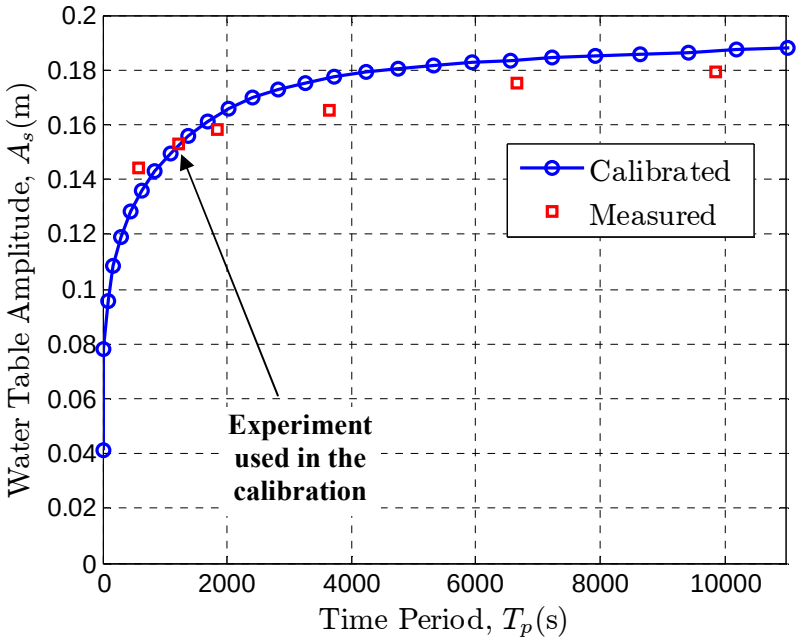

Fig. 7.3: Water table amplitude versus bottom forcing period. Other bottom forcing parameters are: Amplitude = 0.2m, mean bottom pressure= 0.3m.

The above factors can contribute to make the measured and the modeled water table time series not completely matched. Finally, I would like to finish with the statement of (Oreskes et al., 1994):" *it is impossible to validate a numerical model because modeling is only an approximation of reality*".

7.3 Extended numerical study and time characteristic identification

In this section, we extend our experimental study numerically in order to examine the effect of oscillatory forcing and porous media hydraulic parameters outside the available range of the physical experiments.

For this purpose, we use the sand parameters calibrated in the previous section together with another soil named "Guelph Loam" with the following hydraulic parameters ($K_{SAT} = 3.66 \times 10^{-6}$ m/s; θ_S= 0.52; θ_r= 0.218; α = 1.15m^{-1}; n = 2.03).

In addition, a parametric study with synthetic soil hydraulic parameters (derived from the calibrated sand) is also presented and discussed.

This extended numerical study can be implemented using either the numerical code BIGFLOW described in chapter 4 or the multi-front Green and Ampt model that is developed in chapter 8.

It is worth noting that the effect of Eulerian and inertial accelerations can be neglected in this extended numerical study as it is shown in Appendix A.

7.3.1 Effect of the bottom forcing parameters: Frequency analysis and time characteristic identification

The focus here is to study the effect of the time period (T_P) of the oscillatory forcing mainly on the water table height ($Z_S(t)$). The effect of the time period on the water table height will be measured in terms of the mean water table height ($\overline{Z_S}$) and the Root Mean Square (RMS) of the water table height (σ_{Z_S}). It is worth noting that the RMS can be used as an estimation of the amplitude of the fluctuating water table.

Multiple simulations with variable bottom forcing time period (T_P) are conducted; for each simulation the mean and the RMS of the water table height are extracted, the results are shown in **Fig. 7.4**, **Fig. 7.5**, **Fig. 7.6**, **Fig. 7.7**. The figures are plotted on log-scale for the time period axis. From these figures, we can conclude the following:

A) Characteristic Time period (or equivalently characteristic frequency)

- Remarkably, in **Fig. 7.4** and **Fig. 7.6**, it can be seen that the behavior of $\overline{Z_S}$ vs. T_P is non monotonic for both soils, sand and loam. This points out the existence of a characteristic frequency. In other words, there appears a characteristic frequency that separates two frequency regimes (low / high frequency regimes) for each of these soils. For the calibrated SilicaSand (**Fig. 7.4**), the characteristic period (T_P^*) is 81s, or about 1.3 min; and for the Guelph Loam (**Fig. 7.6**), the characteristic period (T_P^*) is 1681s, or about 1/2 hour.
- Moreover, looking at the frequency dependence of σ_{Z_S} from **Fig. 7.5** and **Fig. 7.7**, let us define the characteristic period that corresponding to σ_{Z_S} of about ½ the RMS amplitude of the bottom pressure forcing (σ_{h_0}). We obtain T_P^* around 80 s for the SilicaSand (Fig. 7.5), and around 1700s for the Guelph Loam (Fig. 7.7). These values are very close to the previous ones obtained by looking at the minimum of $\overline{Z_S}$ vs. period.
- Conversely, if we look at the characteristic periods identified previously, we find that for the SilicaSand (**Fig. 7.5**) the T_P^* =81s corresponds to σ_{Z_S}=0.1867 m which is approximately the half of the RMS of the bottom pressure forcing ($\sigma_{Z_S}/\sigma_{h_0}$= 0.528). Similar results are found for the Guelph loam (**Fig. 7.7**) the T_P^*=1681s corresponds to =0.1865 m which is approximately the half of the RMS of the bottom forcing ($\sigma_{Z_S}/\sigma_{h_0}$= 0.527). These amplitude ratios are very stable, close to 50% for both different soils (sand and loam).
- These results are also confirmed from the parametric study that is conducted on 9 other synthetic soils (see next section), with an amplitude ratios ($\sigma_{Z_S}/\sigma_{h_0}$) ranging around 50% (48% to 53%). Therefore, for all soils used in the parametric study, the characteristic period (defined from the minimum of $\overline{Z_S}$) corresponds to water table RMS amplitude of about 50% the RMS amplitude of the bottom pressure forcing.
- However, more work needs to be done to relate this remarkable characteristic period (or frequency) to the saturated and unsaturated soil parameters.

B) Under-elevation of the mean water table height:

- Note also that in Fig. 7.4 and Fig. 7.6**,** the mean water table height ($\overline{Z_S}$) remains below the static level $\overline{h_0}$ = 0.50 m for all frequencies (or equivalently, for all periods T_P). Thus, we observe here an "under-elevation" phenomenon. This effect is most probably influenced by the specific type of geometry and boundary condition used in the present study (namely, vertical oscillations are forced in the system by applying an oscillating pressure at the bottom). With other geometries, however, an over-elevation of the mean water table height has been observed in the presence of lateral tidal forcing and sloping soil surface (Nielsen, 1990, Turner, 1993b, Cartwright et al., 2004).
- The results of this under-elevation in $\overline{Z_S}$ in these numerical simulations confirm what is noted previously in the experimental study (see section 6.3.4.4).

C) High and low frequency limits:

- The high and low frequency limits of $\overline{Z_S}$ are also of interest. It appears from Fig. 7.4 and Fig. 7.6**,** that the infinite frequency limit for the mean water table height is the static level 0.50 m - although physically, the infinite frequency limit is not strictly valid because acceleration terms are neglected in the Darcy-Richards model used in this work. It is quite clear, on the other hand, that the mean water table height attains the static value $\overline{h_0}$ in the limit of very low frequency ($T_P \to \infty$).
- Similarly, for the water table amplitude; **Fig. 7.5** and **Fig. 7.7** shows that the amplitude of the water table reach the amplitude of the bottom forcing at very low frequencies ($T_P \to \infty$) in consistency with the experimental results (see section 6.3.4.2). This can be explained that at larger periods (T_P), there is more time to adapt to changing water table levels, and to equilibrate to quasi-hydrostatic state.

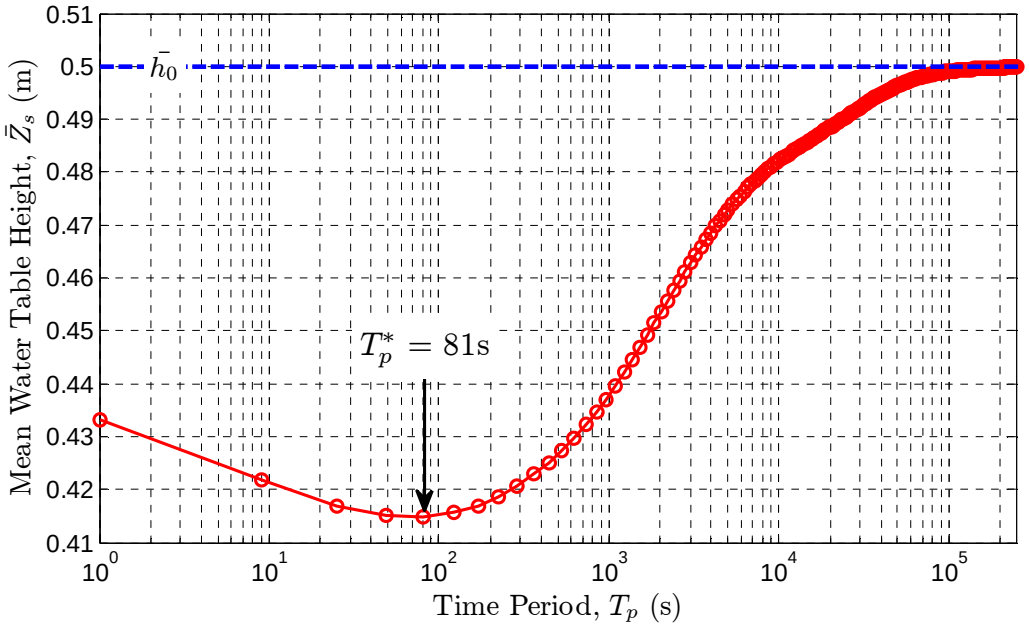

Fig. 7.4: Mean water table height ($\overline{Z_S}$) vs. the time period (T_P) of the bottom forcing for the calibrated SilicaSand. Other bottom forcing parameters are: A_0 = 0.5 m, $\overline{h_0}$= 0.5m.

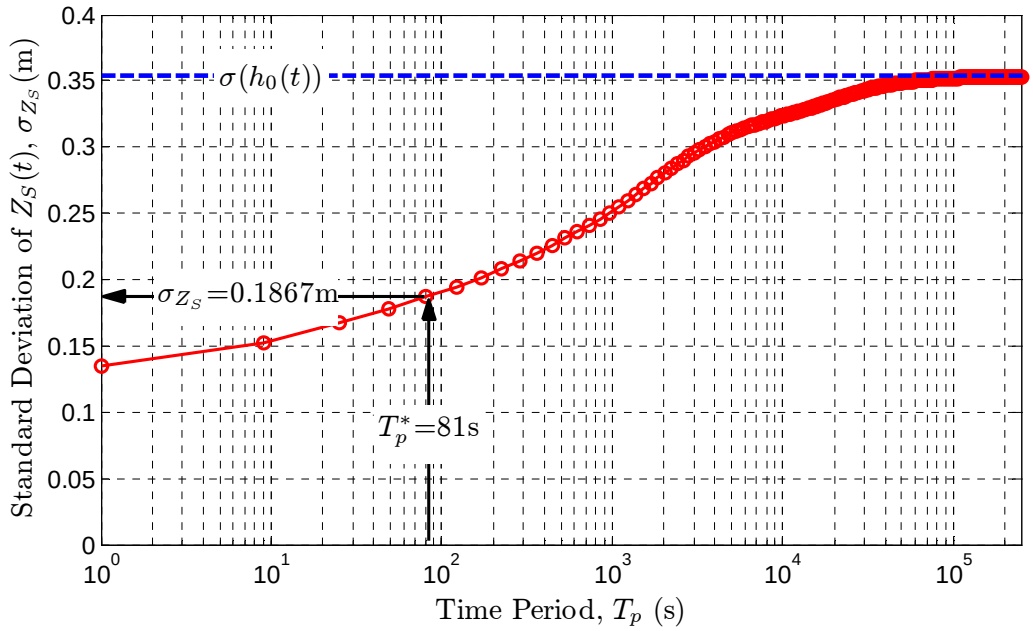

Fig. 7.5: Root mean square of the water table height (σ_{Z_S}) vs. the time period (T_P) of the bottom forcing for the calibrated SilicaSand. Other bottom forcing parameters are: A_0 = 0.5 m, $\overline{h_0}$= 0.5m.

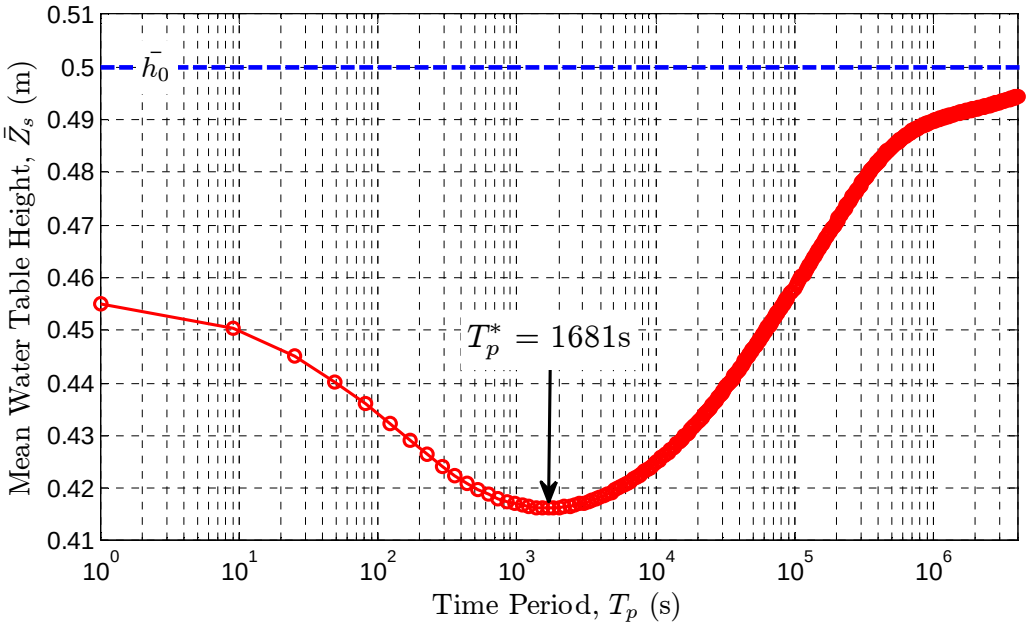

Fig. 7.6: Mean water table height ($\overline{Z_S}$) vs. the time period (T_P) of the bottom forcing for the Guelph Loam. Other bottom forcing parameters are: A_0 = 0.5 m, $\overline{h_0}$= 0.5m.

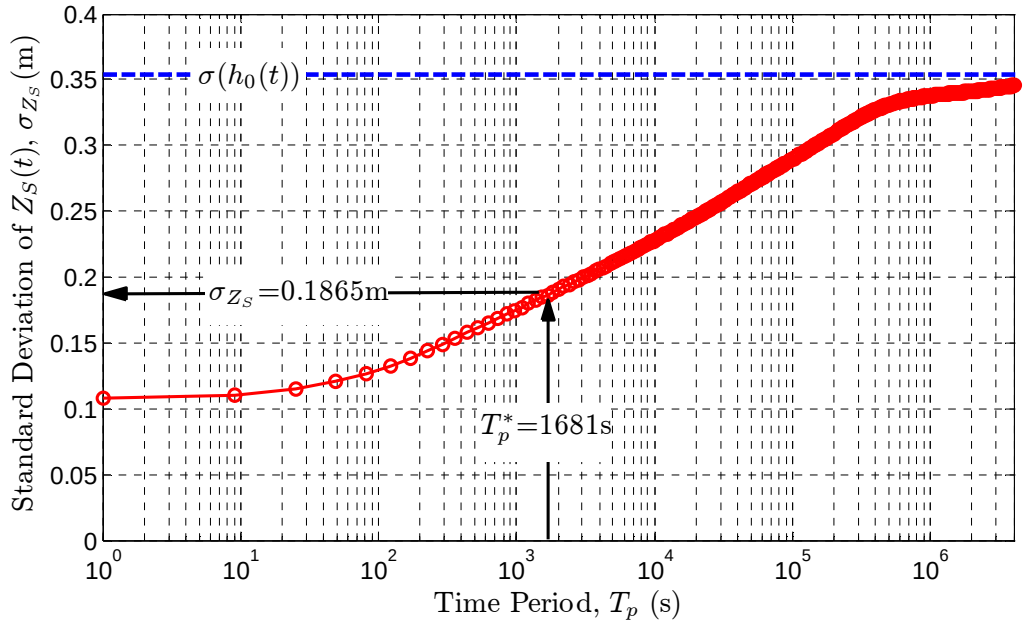

Fig. 7.7: Root mean square of the water table height (σ_{Z_S}) vs. the time period (T_P) of the bottom forcing for the Guelph Loam. Other bottom forcing parameters are: A_0 = 0.5 m, $\overline{h_0}$= 0.5m.

7.3.2 Effect of porous media parameters: Parametric study

In this section, we investigate the effect of the soil hydraulic parameters on the water table fluctuations. For this purpose, we conduct a parametric study on synthetic soils derived from the calibrated SilicaSand. The saturated hydraulic conductivity (K_{SAT}), the saturated water content (θ_S) and a capillary length related parameter (α of the van Genuchten model) are the parameters consider in this study.

7.3.2.1 The effect of the saturated hydraulic parameter (K_{SAT}):

Three synthetic soils which differ only in their K_{SAT} values (1×10^{-4}; 5×10^{-4} and 10×10^{-4}m/s) are used to study the effect of the K_{SAT} on the water table fluctuations. **Fig. 7.8** and **Fig. 7.9** show the results in terms of the mean ($\overline{Z_S}$) and the standard deviation of the water table height respectively.

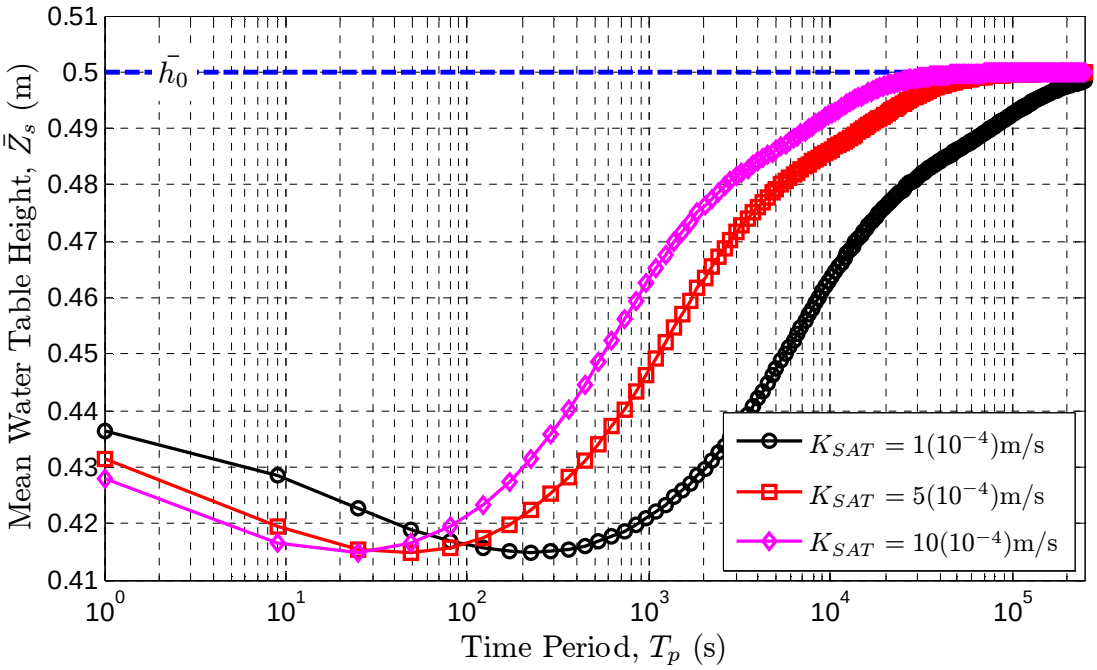

Fig. 7.8: Mean water table height ($\overline{Z_S}$) vs. the time period (T_P) of the bottom forcing for different K_{SAT} values. Other bottom forcing parameters are: A_0 = 0.5 m, $\overline{h_0}$= 0.5m.

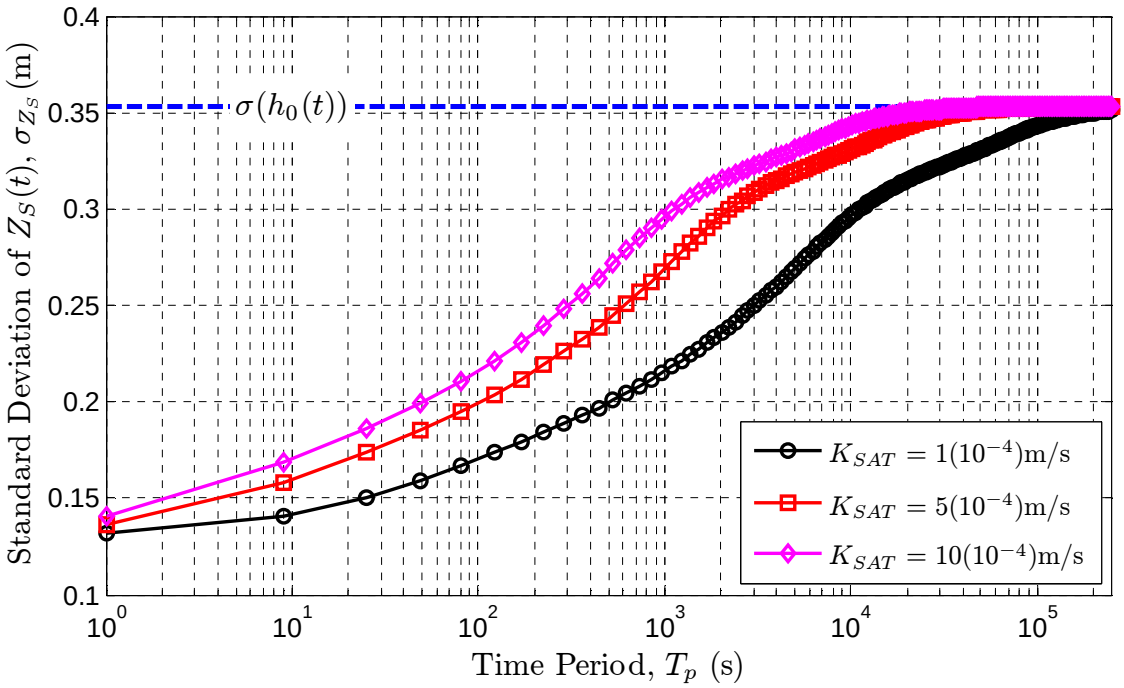

Fig. 7.9: Root mean square of the water table height (σ_{Z_S}) vs. the time period (T_P) of the bottom forcing for different K_{SAT} values. Other bottom forcing parameters are: A_0 = 0.5 m, $\overline{h_0}$= 0.5m.

As it is expected, as the saturated hydraulic conductivity increases, the water movement through the porous medium will be easier; and this reflects directly on the water table fluctuations leading to higher water table amplitude as shown in **Fig. 7.9** and a smaller characteristic period (T_P^*) as shown in **Fig. 7.8**.

7.3.2.2 The effect of the saturated water content (θ_S):

Fig. 7.10 and **Fig. 7.11** shows that the saturated water content plays a minor effect on the water table fluctuations. The figures also show that this is true over large range of frequencies.

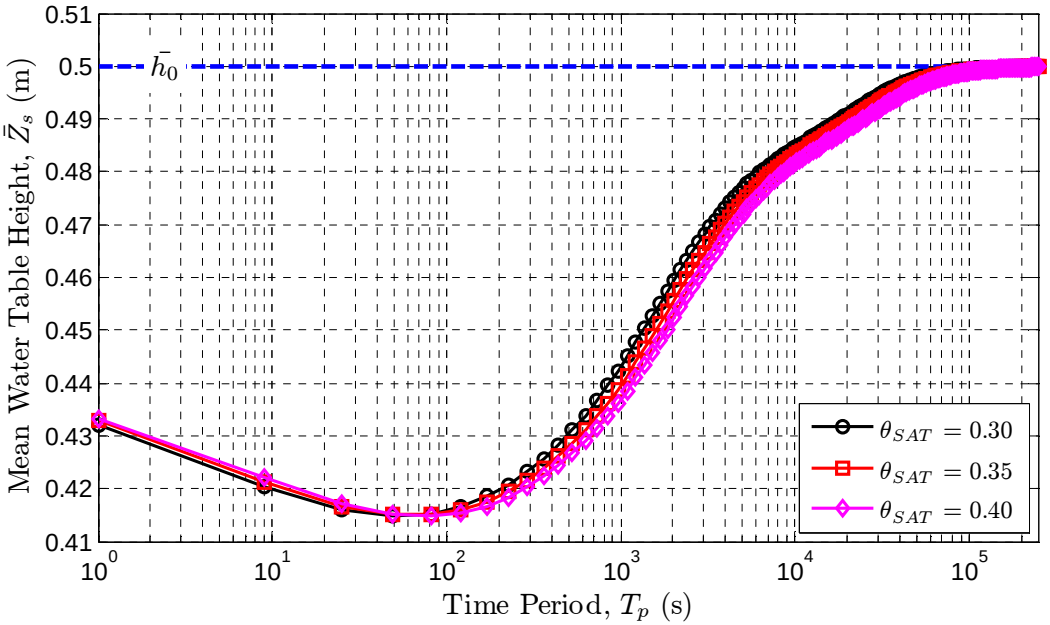

Fig. 7.10: Mean water table height ($\overline{Z_S}$) vs. the time period (T_P) of the bottom forcing for different θ_S values. Other bottom forcing parameters are: A_0 = 0.5 m, $\overline{h_0}$= 0.5m.

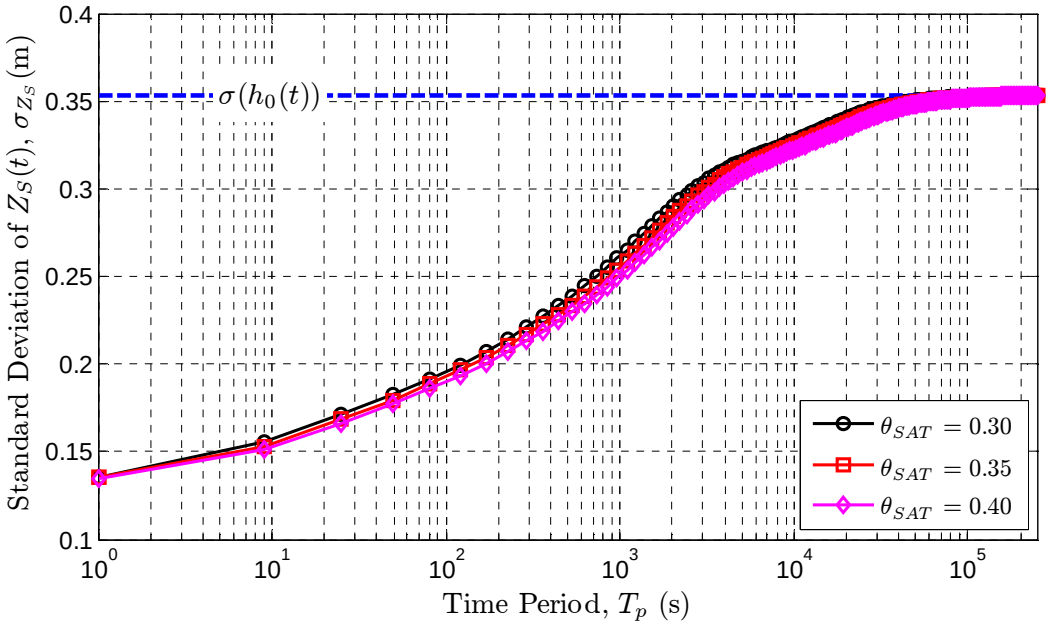

Fig. 7.11: Root mean square of the water table height (σ_{Z_S}) vs. time period (T_P) of the bottom forcing for different θ_S values. Other bottom forcing parameters are: A_0 = 0.5 m, $\overline{h_0}$= 0.5m.

7.3.2.3 The effect of the capillary fringe height:

The effect of the length of capillary fringe can be studied using the inverse of the parameter (α) of the van Genuchten model. As described previously in chapter 3 (section 3.3.6), the inverse of the (α) parameter provides an estimate of the height of the capillary fringe (λ).

Three soils with different α values (2.5, 5 and 10 m^{-1}) corresponds to a capillary length (λ) of about (0.4, 0.2 and 0.1m) are used in the analysis. **Fig. 7.12** and **Fig. 7.13** show the effect of the (α) parameter (or inversely the capillary length) on the water table fluctuations.

By comparing the red (λ=0.4m) and the magenta curves (λ=0.1m) in the figures below (**Fig. 7.12** and **Fig. 7.13**), the capillary fringe has significant effect for high frequency fluctuations; and this effect reduces for low forcing frequencies, as both curves coincides for forcing periods larger than about 1200 sec (or 20 min).

It is also noted from **Fig. 7.13** that the soil with the larger capillary fringe (red curve with λ=0.4m) has a larger water table amplitude (for high frequency range) compared to the other soils. This means that at high forcing frequencies, soils with thicker capillary fringe leads to smaller water table amplitude attenuations.

This result is in consistent with the literatures describing other types of geometry (2D and 3D beaches with vertical and sloping) and having lateral oscillatory forcing. (Horn, 2006) stated that: "Field and laboratory observations have shown that natural groundwater waves usually propagate faster and decay more slowly in aquifers with a capillary fringe"

Moreover, it is noted from **Fig. 7.12** that soils with thicker capillary fringe have a smaller characteristic periods (T_P^*). More work needs to be done to quantify the relationship between this characteristic period (or frequency) and the saturated and the unsaturated soil parameters (work in progress).

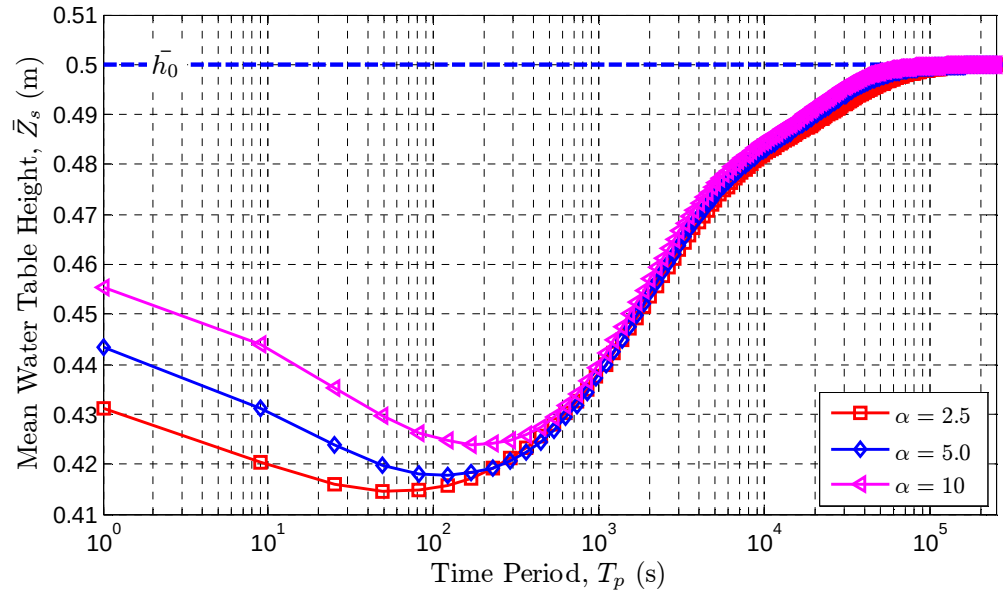

Fig. 7.12: Mean water table height ($\overline{Z_S}$) vs. the time period (T_P) of the bottom forcing for different α values. Other bottom forcing parameters are: A_0 = 0.5 m, $\overline{h_0}$= 0.5m.

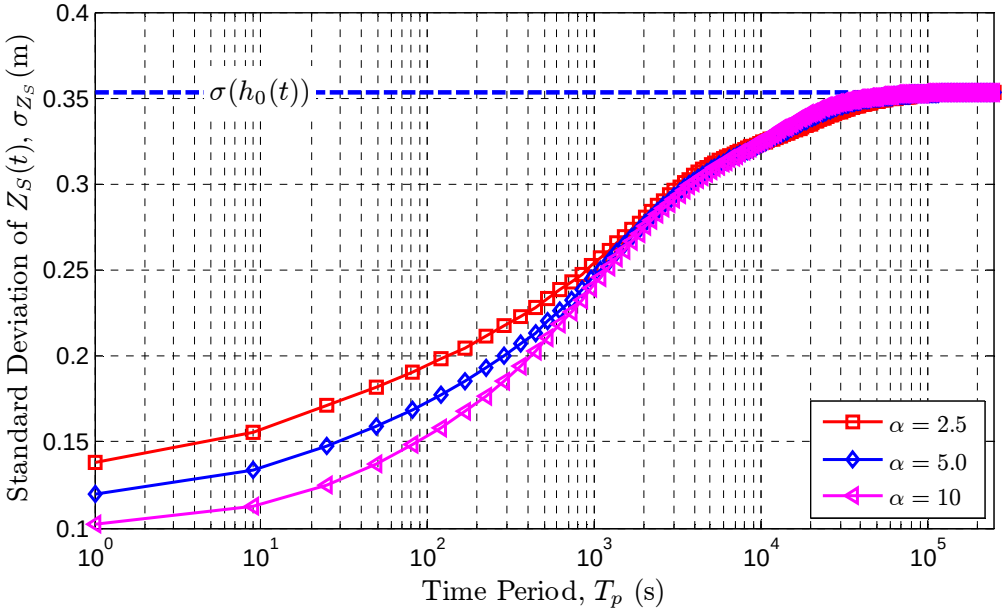

Fig. 7.13: Root mean square of the water table height (σ_{Z_S}) vs. time period (T_P) of the bottom forcing for different α values. Other bottom forcing parameters are: A_0 = 0.5 m, $\overline{h_0}$= 0.5m.

Chapter 8

Generalized Green-Ampt approach to 1D oscillatory flows in partially saturated /unsaturated media: capillary effects in beach hydrodynamics (semi-analytical and numerical studies)

This Chapter represents an article submitted to an international scientific journal "*under reviewing*".

Generalized Green-Ampt approach to 1D oscillatory flows in partially saturated/unsaturated media: capillary effects in beach hydrodynamics (semi-analytical and numerical studies)

Khalil Alastal, Rachid Ababou, Dominique Astruc

Abstract

Semi-analytical multi-front solutions of water table response due to periodic forcing in a partially saturated vertical porous column are developed, tested and compared to finite volume solutions of the Richards equation for partially saturated / unsaturated flow with non linear water retention and conductivity curves (θ(h), K(h)). The multi-front solutions are useful for capturing parametrically the frequency response of the vertical column to tidal oscillations while taking into account both capillary and gravitational effects. Vertical oscillations are examined, accounting for unsaturated flow above the oscillating water table as well as saturated flow below it. The multi-front models are conceived as successive generalizations of the Green-Ampt piston flow approach. The single front model is an "inverted" Green-Ampt model, with an abrupt front separating the saturated and dry regions. It is adapted to the case of an oscillatory pressure imposed at the bottom of the column (rather than a fixed pressure imposed at the top). The N-front models (N≥2) further generalize this concept, using a (θ(h), K(h)) parametrization to take into account the capillary properties of the unsaturated medium. The resulting systems of ODE's are non linear with time variable coefficients (non autonomous ODE systems). The solutions obtained for $N \approx 10$ fronts are satisfactory both in terms of water table fluctuations and moisture profiles, even for fine grained soils (Guelph Loam). They are computed much faster than space-time discretized solutions of the non linear Richards PDE. For sandy soils, even the 2-front solution (N=2) is satisfactory in terms of water table response $Z_S(t)$. The 2-front model itself is a significant improvement on the single front Green-Ampt model, and it appears potentially useful for analyzing the response of unsaturated flow systems under various types of oscillatory and transient forcing. Overall, the N-front method is useful for exploring the frequency response of the water table to tidal forcing. To illustrate this capability, we discuss the results of a parametric study of mean water table height *vs.* frequency for the Guelph Loam.

Keywords

Green-Ampt piston flow model; tidal beach hydrodynamics; capillary effects; Richards equation; unsaturated porous media; multi-front model.

1. Introduction and literature review

In coastal hydrodynamics, oscillations of groundwater flow and water table elevation in beaches have been recognized to influence the morphological processes and sediment transport of the swash zone (erosion and accretion) [1,2]. The oscillatory flow regime can also control the biological conditions, nutrient cycling and contaminant movement near the water table [3,4]. These oscillations also affect the stability of structures founded on soils and sands [5]. Such oscillation phenomena also take place in river banks near estuaries, in harbor dykes, etc. The porous media involved in these oscillatory phenomena may have various grain size distributions. In many cases, due to fine grained features, capillary effects intervene significantly, and one must account for the time variable unsaturated wetting and drainage phenomena above the oscillating water table.

Thus a reliable and simple model that predicts the space-time response of groundwater flow and water table elevation in the presence of unsaturated capillary effects, would be very useful for studying the nonlinear response of groundwater flow and water table elevation to, say, periodic forcing. In this paper we will focus specifically on the case of tidal forcing at the bottom of a vertical column, without taking into account wave hydrodynamics, but taking into account both saturated and unsaturated flow dynamics in the porous column.

Many models have been developed to predict the water table fluctuations in response to periodic forcing [5,6,7,8,9,10,11]. Most of the proposed models are based on the Dupuit-Boussinesq equation of plane groundwater flow [12,13], which is derived from Darcy's law and mass conservation assuming (i) vertically hydrostatic pressure (plane flow), and (ii) instantaneous wetting/drainage of the moving water table (the unsaturated zone is totally dry at all times). The models based on (i) and (ii) can predict space-time propagation of water table fluctuations horizontally (Z_S (x,y,t)), but they are limited to planar flow within the saturated region, and also, they totally neglect any capillary effect on water table fluctuations.[1]

[1] Note: a vertical flow model Zs(t) based solely on the second hypothesis is conceivable, but it would be limited to merely ensuring mass conservation between the bottom boundary and the mobile water table.

Recent laboratory and field studies show that capillarity affects water table dynamics over a wide range of frequencies, including tidal frequencies [14,15,16,17]. As the water table fluctuates, the pressure distribution above the water table will change, and thus an apparent local water exchange across the water table occurs [18].

Parlange and Brutsaert [19] proposed a correction of the Dupuit-Boussinesq equation to take into account capillary effects above the water table. Barry et al. [20] used the technique of (Parlange and Brutsaert) and showed that the influence of the capillary fringe increases with oscillation frequency. Another author, Li et al. [18], developed a modified kinematic boundary condition for the water table, which takes capillarity effects into account.

Most of the above-cited modification techniques were based in some way on the Green-Ampt (G-A) "piston flow" approximation [21]. The latter assumes that the equivalent capillary fringe is completely saturated with water, and that the sharp interface between the capillary fringe and the dry medium is characterized by a fixed suction head called "wetting front suction" and denoted Ψ_{FRONT} or Ψ_F [19]. Strictly speaking, the classical G-A model is limited to the case of vertical downward infiltration under constant positive pressure imposed at soil surface, although some variants have been introduced in the literature.[2] Now, the classical G-A infiltration problem and the tidal oscillations considered in this work are both vertical flow configurations, but they differ in two important aspects: (1) the time-varying boundary condition considered in this work is an oscillatory "tidal" pressure; and (2) the tidal pressure condition is imposed at the bottom boundary (not at the top) so that the forcing in our tidal problem is alternately co- and contra-gravitational (while G-A infiltration is co-gravitational at all times).

Thus, Nielsen and Perrochet [14,15] analyzed a tidal oscillation problem similar to ours, and they attempted to include capillary effects in their analyses. At first, they accounted for the effects of the capillary fringe above a vertically oscillating water table by introducing an equivalent (integral) capillary fringe height hc(t), which leads to a differential equation similar to the G-A model. They proposed to solve this equation for

[2] Note: anticipating on the next sections, it can be mentioned here that the multi-front models introduced in this paper are themselves extensions of the Green-Ampt approach.

small amplitude using complex variables. The result of their linearized small amplitude model is expressed in terms of a (real or complex) dynamic effective porosity "n_D", which accounts the total equivalent saturated height in the column (water table height + equivalent thickness of the capillary fringe). The authors compared their complex effective porosity model to a laboratory experiment conducted on a vertical column, and they also introduced a small amplitude model based directly on the Green-Ampt piston flow approximation expressed in terms of front suction, which they named "Hc". In order to obtain better fit with the experiment, other modifications were introduced (e.g., an empirical hydraulic conductivity $K < K_S$ was introduced in the equivalent capillary fringe zone). Overall, the proposed analytical models are limited to small amplitude scenarios and/or contain empirical parameters. The authors [14,15] conclude that (i) the various variants of the small amplitude G-A models do not match the experimental data very well (in terms of amplitude and phase of the frequency response); (ii) the results of the "dynamic effective porosity" (n_D), from their equivalent integral capillary fringe model, cannot be matched simultaneously for amplitude and phase for any real value of "n_D", but the match becomes good with an empirically fitted complex-valued " n_D". Note: this boils down to fitting empirically the amplitude decay and phase shift in a G-A type solution of water table fluctuations.

Other works in the literature extended the G-A approximation in various ways, e.g. for infiltration under time varying conditions (quite different from oscillatory water table problems as reviewed above), and also, for layered soils, for multidimensional flow configurations, etc. These are briefly reviewed below.

Warrick et al. [22] used and solved a slightly modified form of the G-A infiltration equation for the case of irrigation under time-variable ponded depth. They compared the results to field observations in two irrigated plots: (a) input water depth "d" = $h_{SURF}(t)$, and (b) output cumulative infiltration I(t). Their solution technique is to discretize the non linear Green-Ampt ODE with relatively coarse time steps, such that the prescribed ponded depth $h_{SURF}(t)$ is assumed constant within each step (piecewise constant). The solution of this variable time G-A infiltration was also compared to a numerical finite element solution of Richards equation with the HYDRUS1D code. The results were close in terms of infiltration depth I(t), but it should be noted (along with the authors) that the

effect of time variability is not strong in this type of ponded infiltration scenario: indeed the solutions I(t) obtained with time varying ponded depth (HYDRUS1D, G-A) and with constant mean ponded depth (G-A) were all quite close. The conclusion of the authors is that time variability of ponded depth does not have a great effect on the resulting cumulative infiltration I(t).

The latter observation should be related to our previous remarks concerning co-gravity flows versus contra-gravity flows. The flow system studied by Warrick et al. [22] is co-gravity at all times (despite time variability at soil surface). In the tidal case, we have alternating co-/contra-gravity flow.

At this point, it may be useful to consider a technical mathematical issue that emerges from the above reviewed works. It concerns the "discretization" of the Green-Ampt model in various situations and for various purposes. Indeed, in the remainder of the present work, we will propose to improve on the classical G-A approach by discretizing the state variables themselves (the water contents and the suctions, and consequently the unsaturated permeability along the profile). In comparison, we have seen just above that Warrick et al. [22] propose to discretize the G-A model in time to reformulate it as a classical G-A model under piecewise constant conditions. The resulting nonlinear ODE can then be solved either by numerical integration or, say, by explicit Runge-Kutta finite differences in time[3]. On the other hand, in finite element or finite volume methods (HYDRUS1D code, BIGLOW3D code) the non linear Richards PDE (Partial Differential Equation) is discretized in both time *and* space.

Ma et al. [23] empirically adapted and discretized the G-A model for infiltration in layered soils, based on previous work which appears to have been published in a journal in Chinese language ("*Han et al. 2001, Chinese J. of EcoAgriculture*"). Their modification leads to a layer-discretized G-A infiltration equation governing the wetting front elevation $Z_F(t)$ as it passes through each layer, taking into account, in this process, the different effective saturations and effective harmonic mean conductivities as the wetting front moves downwards. Some parameters of the governing equation were

[3] Note: in all such cases, when the resulting equations boil down to single integrals or to integrable 1rst order ODE's, we refer to these as quasi-analytical or semi-analytical solutions.

determined empirically, e.g., the ratio of actual measured moisture volume divided by total saturated volume. The results obtained for a 5-layer soil compared favorably with numerical solutions of the Richards equation (HYDRUS1D code), but only in terms of infiltration rate and cumulative infiltration I(t). However, tracking down the motion of the wetting front was less successful, in comparison with experimental results.

Kacimov et al. [24] consider also the case of infiltration in a vertically heterogeneous soil using the Green-Ampt approach, but they differ in two ways from the previous study: they treat the case of a continuously stratified soil, and their approach is more formal (quasi-analytical). The authors take into account a continuously varying saturated conductivity $K_S(z)$ and wetting front suction $\Psi_F(z)$, the latter being considered as a capillary parameter of the soil. This leads to a nonlinear ODE (Ordinary Differential Equation), which they end up solving numerically for the case of exponentially varying $K_S(z)$ and $\Psi_F(z)$ (using MATHEMATICA's "NDSolve" package). The authors also introduce randomness in the exponential profile $K_S(z)$ and briefly analyze the results in a probabilistic framework (mean and dispersion variance of the infiltration process).

Selker et al. [25] treat the case of infiltration into vertically stratified soils using the Green-Ampt approach and a parametrization of heterogeneity based on pore size distribution. Considering a continuously variable pore size with depth, both $K_S(z)$ and $\Psi_F(z)$ vary with depth. More precisely, these authors use a relationship between $K_S(z)$ and $\Psi_F(z)$ in terms of pore size distribution, and they assume for simplicity that $\theta s(z)$ is nearly constant based on field evidence. The resulting quasi-analytical model is applied to monotonic variation with depth (linear, power law and exponential).

Chen and Young [28] developed a G-A infiltration model orthogonally to the surface, in the case of a sloping soil surface. Technically, their flow solution is 1D, although the flow direction is not vertical. The flow domain is semi-infinite normally to slope. The sloped soil G-A solution resembles the classcial G-A solution (semi-analytical). The authors use it for studying hypothetical hydrologic scenarios of ponded infiltration. They also extend the model to treat the case of steady or transient rainfall (before and after ponding). One of their conclusions is that, under constant ponding head, the infiltration rate normal to the sloping surface is enhanced by the slope angle compared to the case of

a horizontal soil. But this effect is only significant at early times when capillary effects dominate over gravity. At later times, or as $t \to \infty$, the gravitational infiltration rate does not depend on slope angle. These results have consequences on run-off over sloping soils in watershed hydrology.

Note, in the present paper, we focus on time variability and tidal oscillations, rather than heterogeneity; however, it will be interesting in future to consider combining the previously reviewed extensions of the Green-Ampt approach for stratified soils, and for sloping soils, with the oscillatory multi-front model that is developed in the remainder of this paper.

Finally, it is also worth noting that the G-A piston flow approximation has also been applied in the literature to multi-dimensional flow systems. For instance, the G-A approach has been used to analyze the multidimensional growth of a wetting bulb at the bottom of a falling head permeameter: see Regalado et al. [26], whose work is based on Philip [27].

The remainder of this article is organized as follows.

In **Section 2**, we present briefly the configuration of the oscillatory flow system to be studied analytically and numerically in the rest of the paper. It consists in a vertical soil column comprising a water table forced by an oscillating pressure at bottom. This concept is illustrated by a brief description of an actual experiment, including an instrumented soil column connected to a "tide machine" (the complete results from this set of experiments are currently being analyzed).

In **Section 3**, we present a series of successive generalizations of the Green-Ampt approach, starting with the single front model (in the first subsection) and ending up with a general multi-front or "N-front" model. The single front model is, in a sense, an "inverted" and "oscillatory" version of the classical Green-Ampt infiltration model. The 2-front and then the N-front models constitute further extensions, where the N fronts are defined based on the nonlinear pressure-dependent curves ($\theta(h)$, $K(h)$), i.e., respectively, water content vs. pressure and hydraulic conductivity vs. pressure. The resulting equations are nonlinear systems of 1rst order ODE's. We focus on large amplitude oscillations of the entry pressure head, up to 100% compared to the static height of the

water table (most of the cases presented in this paper are based on this extreme case). The results of the 2-front and of the 20-front model are discussed, including comparison tests with numerical finite volume solution of the nonlinear Richards equation (PDE).

Section 4 discusses in detail the parametrization of the single front, 2-front, and more generally the N-front models. For instance, the front suction ψ_F is a parameter of the single front model, and it is computed from the unsaturated properties K(h) and/or θ(h) of the unsaturated soil. This concept is extended to the N suctions at the N fronts. Other parameters intervene. All parameters of the proposed multi-front model are presented and discussed in this section.

Section 5 discusses the performance of the single front, the 2-front, and the multi-front model (the latter with N = 20) for two different soils (fine sand "SilicaSand", and Guelph Loam) and for very large amplitude of the entry pressure. The models are compared to a refined solution of the Richards PDE using the implicit finite volume code BIGFLOW. The comparisons are based on water table height Z_S (t) and bottom flux q_0 (t) (signals).

Section 6 presents a brief summary of the work, and discusses various extensions and perspectives. It is pointed out that the multi-front approach is also a good approximation of the Richards equation, not only in terms of water table signals, but also in terms of water content vertical profiles (for $N \geq 10$ to 20 fronts). This section also illustrates a possible application of the multi-front approach to parametric study of the frequency response to tidal forcing (behavior of the mean water table height vs. frequency for the Guelph Loam).

2. Oscillatory flow in 1D porous column

In this article, we consider a partially saturated 1D porous column under “dynamic” conditions. The dynamic effect is simulated by an oscillatory "entry pressure head" or “driving head” imposed at the bottom face of the column. It can be expressed as:

$$h\left(z=0,t\right)=h_0(t)=\overline{h_0}+A_0 sin\left(\omega_0 t\right) \qquad 1$$

where:

- $\overline{h_0}$ is the positive time-averaged entry pressure head, chosen to coincide with the initial hydrostatic level in the column;
- A_0 is the amplitude of the entry pressure;
- $\omega_0 = 2\pi / T_P$ is the angular frequency, and
- T_P is the period of the imposed entry pressure.

Experimentally this driving head can be generated by a tide machine connected to the bottom of the column as described in [29]. This concept is illustrated by the schematic in **Fig. (1)**, describing an actual instrumented soil column and the associated tide machine. This experiment was conducted at the Institut de Mécanique des Fluides de Toulouse; the results of which are still being analyzed (some of these experimental results were reported in [29]).

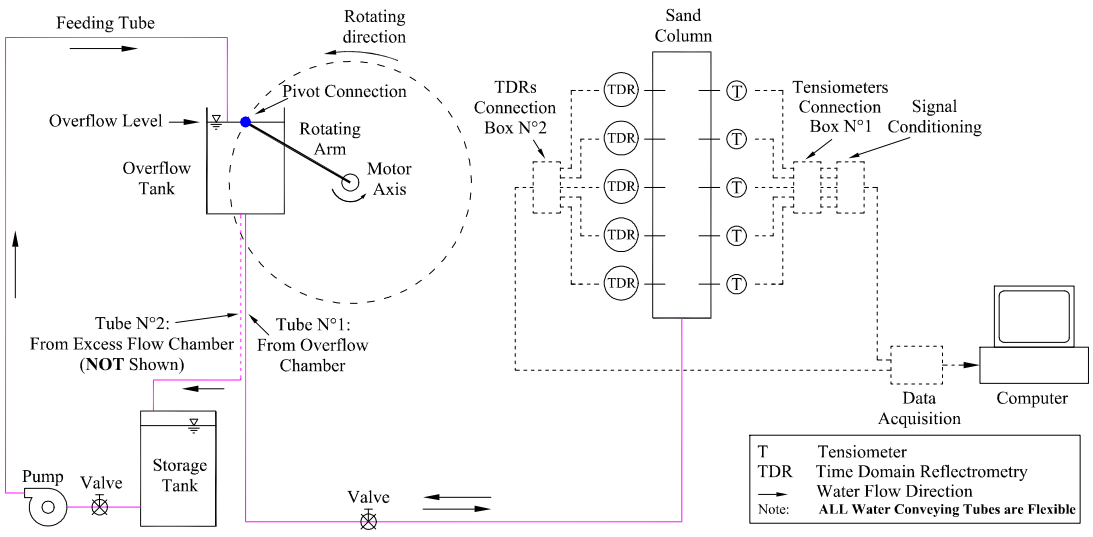

Fig. 1: Schematic diagram of the tide machine, soil column and measurement system.

3. Generalised Green-Ampt models for vertical oscillatory flows

3.1. The classical Green-Ampt model (vertical infiltration downwards)

The Green-Ampt model [21] has been the focus of many interests because of its simplicity and satisfactory performance for a variety of hydrological applications [23,30]. It was originally developed to study one dimensional (1D) vertical infiltration into homogeneous porous medium of infinite depth. The Green-Ampt infiltration model assumes piston flow, with a sharp wetting front that separates the saturated zone from the unsaturated zone. This wetting front is characterized by a constant suction head (considered a parameter of the soil), and it propagates downward into the soil under the combined action of capillary pressure gradient and gravity. Initially, the soil is assumed to have a constant, uniform water content profile.

As we have seen earlier, a number of studies have focused on extending the Green-Ampt model to other applications. In this article, the Green-Ampt (G-A) model is generalized to deal with 1D oscillatory flow in partially saturated/unsaturated porous media, taking into account unsaturated capillary effects on the oscillation process as realistically as possible. In fact, several generalized versions of the G-A model are developed for oscillatory flow, starting below with the basic single front model, and ending up with the general multi-front or N-front model.

3.2. The Green-Ampt or single front model, extended to oscillatory flows

The purpose of this first basic model is to provide a semi-analytical solution for water table height fluctuations, and also, to provide a basis for further extensions (multi-front). This model is basically an "inverted" version of the classical Green-Ampt infiltration model. A pressure condition is imposed at bottom (instead of top), and the model is further extended to accommodate periodic fluctuations of the imposed bottom pressure. Thus, strictly speaking, the so-called "wetting front" is in fact either wetting or draining, depending on time. This model is also called "single front" model because, as in the classical G-A approach, it is based on the movement of a single front ($Z_F(t)$).

Accordingly, based on the usual Green-Ampt piston flow hypotheses, we assume that:

- There exists a well defined "wetting front" separating the fully saturated and the totally dry regions, as shown in **Fig. (2),** where the dashed line represents the GA approximation.
- The wetting front is assumed to be characterized by some effective, constant suction head ψ_F, or pressure head h_F, with $\psi_F = -h_F$.

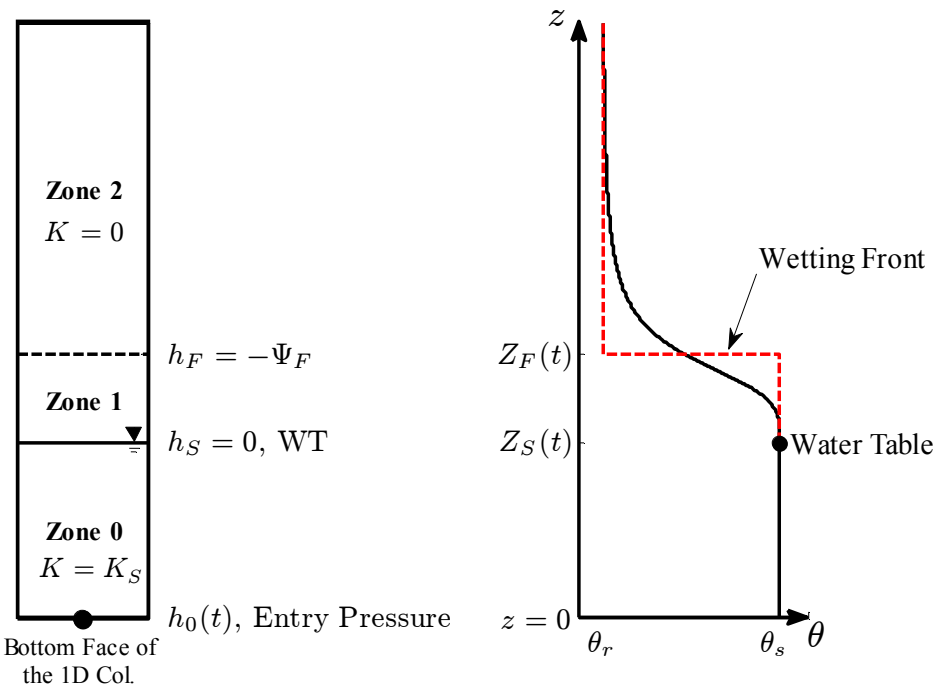

Fig. 2: schematic diagram of the single front model. On the left: 1D porous column shows the water table ($Z_S(t)$) and the wetting front ($Z_F(t)$) elevations where the suction heads are 0 and ψ_F respectively. On the right: the instantaneous water content profile with Green-Ampt approximation (dashed line).

The free surface (water table) is itself characterized by h = 0 (zero pressure head relative to air pressure). Both the wetting front elevation, $Z_F(t)$, and the free surface elevation, $Z_S(t)$, move in response to the oscillating bottom pressure head.

Note that the entry pressure head is assumed in this work to be a simple harmonic (sine or cosine function); the response of the wetting front and water table may also be analyzed with the same techniques when the forcing is a more complex signal containing, say, both discrete and continuous spectra (not just a simple harmonic).

Our single-front model approximation divides the soil column into three zones, labeled i = (0,1,2) from bottom to top, each zone having *a priori* its own hydraulic conductivity and water content (Ki, θi):

- **Zone 0**: this zone is totally saturated; it extends from the bottom of the column ($z = 0$) to the moving water table ($z = Z_S(t)$); in this zone, $K_0 = K_S$, $\theta_0 = \theta_S$.
- **Zone 1**: this zone extends from the moving water table ($z = Z_S(t)$) to the moving wetting front ($z = Z_F(t)$); it represents a wet or quasi-saturated transition zone between the totally saturated Zone 0 and the totally dry Zone 2; the properties of this zone are $K_1 = K_S$ and $\theta_1 = \theta_S$, although lower values can be assumed empirically (say $K_1 \le K_S$).
- **Zone 2**: this last zone is the totally dry region extending from the wetting front ($z = Z_F(t)$) up to infinity; it is a semi-infinite zone; the flux is null in this zone, since we choose $K_2 = 0$ and $\theta_2 = \theta_r$.

Let us now develop the governing equations under these assumptions, using mass conservation principles and Darcy's flux-gradient law (a simplified version of Navier-Stokes' conservation of momentum).

3.2.1. Darcy's flux-gradient equation for the single front model

Now, let us apply Darcy's equation to calculate the vertical fluxes q(z,t).

The flux $q_0(t)$ in the saturated *Zone 0* is constant in space, and is given by:

$$q_0(t) = -K_0\left(\frac{\partial h}{\partial z} - g\right) = -K_S\left(\frac{0 - h_0(t)}{Z_S(t)} - g\right) = K_S\left(\frac{h_0(t)}{Z_S(t)} + g\right) \qquad 2$$

where $Z_S(t)$ is the water table elevation; $h_0(t)$ is the bottom entry pressure head. Note that "g" represents unit gravity, with $g = -1$ if the Oz axis is directed upwards (as is the case here). In fact, the solution is also generalized in terms of the gravity vector g :

- $g = -1$ in the present case (pressure fluctuations at bottom, z directed upwards).
- $g = +1$, e.g., for variable-head ponded infiltration, with z directed downwards.
- $g = 0$, e.g. for horizontal flow model and/or in the absence of gravity.

The flux $q_1(t)$ in the quasi-saturated transition *Zone 1* is also constant in space, given by:

$$q_1(t) = -K_1\left(\frac{h_F - 0}{Z_F(t) - Z_S(t)} - g\right) = K_S\left(\frac{\psi_F}{Z_F(t) - Z_S(t)} + g\right) \qquad 3$$

where $h_F = -\psi_F$ is the constant suction head at the sharp wetting front (it should be considered a parameter characterizing, mainly, the unsaturated soil properties).

3.2.2. Mass conservation equations for the single front model

On the other hand, let us apply the mass conservation equation locally around the moving water table ($\boldsymbol{z = Z_S(t)}$). This yields:

$$q_0(t) - q_1(t) = (\theta_0 - \theta_1)\cdot\frac{dZ_S}{dt} \qquad 4$$

where θ_0 and θ_1 are the water content in the zone 0 and 1 respectively. However, both of these equal the saturated water content (θ_S) based on the Green–Ampt assumptions. Therefore for this simple single front model:

$$q_0(t) = q_1(t) \qquad 5$$

Now, applying the mass conservation equation through the moving wetting front ($z = Z_F(t)$):

$$q_1(t) - q_2(t) = (\theta_1 - \theta_2)\cdot\frac{dZ_F}{dt} \qquad 6$$

where q_2 and θ_2 are the flux and water content in the dry zone 2 ($q_2 = 0$, $\theta_2 = \theta_r$); and $\theta_1 = \theta_S$. Then:

$$q_1(t) = (\theta_S - \theta_r)\cdot\frac{dZ_F}{dt} \qquad 7$$

Combining Eq. (3), (5) and (7):

$$\frac{dZ_F}{dt} = \frac{K_S}{\theta_S - \theta_r}\left(\frac{\psi_F + h_0(t)}{Z_F(t)} + g\right) \qquad 8$$

Eq. (8) is an ordinary differential equation (ODE) that can be solved in the time domain for our assumed initial condition: $Z_F(t=0) = \overline{h_0} + \psi_F$. This equation, together with the

initial condition, is solved for the unknown wetting front height as a function of time using the ODE MATLAB solver package (ODE45 for example).

Once $Z_F(t)$ is determined, Eq. (5) is solved to obtain the water table height $Z_S(t)$:

$$Z_S(t) = Z_F(t)\left(\frac{h_0(t)}{h_0(t)+\psi_F}\right) \qquad 9$$

Finally, either Eq. (2) or Eq. (3) may be applied to calculate the bottom flux [$q_0(t)$ *or* $q_1(t)$].

3.3. The two-front model

In this section, the novel two-front model is considered. The water content is approximated by two sharp fronts instead of one. Our expectation is to modify the results by approximate the characteristic curves by two fronts instead of only one, **Fig. (3)**. Each front represents an equipotential line (of suction head) that moves with time as a response to the bottom entry fluctuating pressure head.

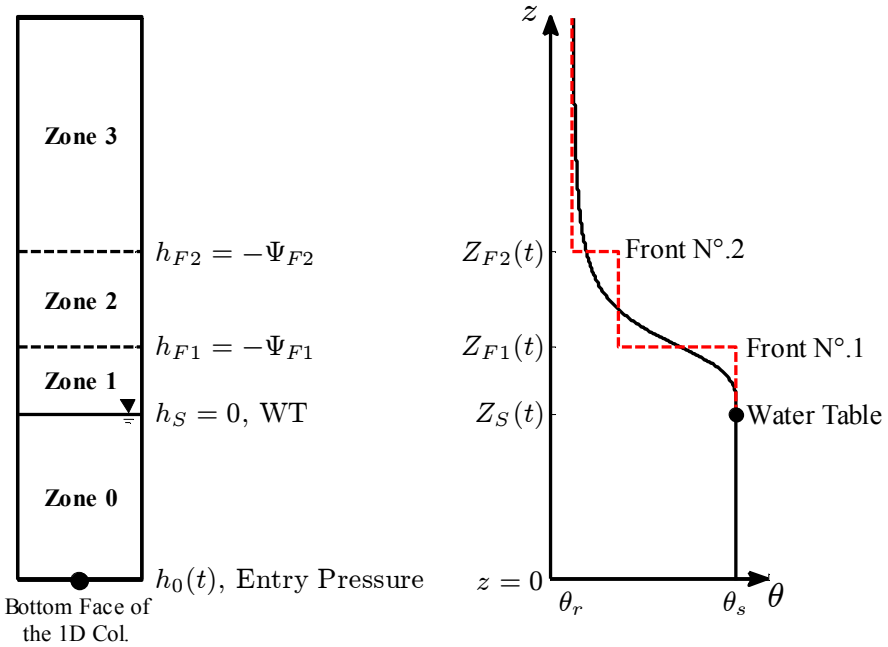

Fig. 3: Schematic diagram of the two-front model approximation. On the left: 1D porous column shows the water table ($Z_s(t)$) and the two fronts ($Z_{F1}(t), Z_{F2}(t)$) elevations where the suction heads are 0, ψ_{F1} and ψ_{F2} respectively. On the right: the instantaneous water content profile with two-front model approximation (dashed line).

The two-front model approximation divides the column into four regions:

- **Zone 0**: it is a totally saturated zone extending from the bottom of the column ($z = 0$) to the moving water table ($z = Z_S(t)$); with $K_0 = K_S$, $\theta_0 = \theta_S$
- **Zones 1** and **2**: They are comprised between the moving water table ($z = Z_S(t)$) and the second moving wetting front ($z = Z_{F2}(t)$). These zones can be considered as "stepped" transition zones from the totally saturated zone to the totally dry zone. The parameters are: $K_1 = K_S$ and $K_2 < K_S$; $\theta_1 = \theta_S$ and $\theta_2 < \theta_S$.
- **Zone 3**: This is the totally dry region, it is a semi-infinite zone starting above the second moving front ($z = Z_{F2}(t)$); the flux is null in this zone, and the parameters are: $K_3 = 0$; $\theta_3 = \theta_r$.

3.3.1. Darcy's equation for the two-front model

Now, let us apply Darcy's law to determine the flux in each zone of the two front model.

- Flux in zone 0, $q_0(t)$

$$q_0(t) = -K_0\left(\frac{\partial h}{\partial z} - g\right) = -K_S\left(\frac{0 - h_0(t)}{Z_S(t)} - g\right) = K_S\left(\frac{h_0(t)}{Z_S(t)} + g\right) \qquad 10$$

- Flux in zone 1, $q_1(t)$

$$q_1(t) = -K_1\left(\frac{\partial h}{\partial z} - g\right) = -K_1\left(\frac{h_{F1} - 0}{Z_{F1}(t) - Z_S(t)} - g\right) = K_1\left(\frac{\psi_{F1}}{Z_{F1}(t) - Z_S(t)} + g\right) \qquad 11$$

- Flux in zone 2, $q_2(t)$

$$q_2(t) = -K_2\left(\frac{\partial h}{\partial z} - g\right) = -K_2\left(\frac{h_{F2} - h_{F1}}{Z_{F2}(t) - Z_{F1}(t)} - g\right) = K_2\left(\frac{\psi_{F2} - \psi_{F1}}{Z_{F2}(t) - Z_{F1}(t)} + g\right) \qquad 12$$

The flux is null in the dry zone 3 ($q_3(t) = 0$).

3.3.2. Mass conservation equations for the two-front model

On the other hand, let us apply the mass conservation equation locally around each moving front (including the water table).

- Mass conservation equation traversing the moving water table ($z = Z_S(t)$):

$$q_0(t) - q_1(t) = (\theta_S - \theta_1) \cdot \frac{dZ_S}{dt} \quad 13$$

- Mass conservation equation traversing the first moving front ($z = Z_{F1}(t)$):

$$q_1(t) - q_2(t) = (\theta_1 - \theta_2) \cdot \frac{dZ_{F1}}{dt} \quad 14$$

- Mass conservation equation traversing the second moving front ($z = Z_{F2}(t)$):

$$q_2(t) - 0 = (\theta_2 - \theta_r) \cdot \frac{dZ_{F2}}{dt} \quad 15$$

Eqs. (13), (14) and (15) can be written in matrix form as follow:

$$\begin{bmatrix} \theta_S - \theta_1 & 0 & 0 \\ 0 & \theta_1 - \theta_2 & 0 \\ 0 & 0 & \theta_2 - \theta_r \end{bmatrix} \begin{Bmatrix} dZ_S / dt \\ dZ_{F1} / dt \\ dZ_{F2} / dt \end{Bmatrix} = \begin{Bmatrix} q_0(t) - q_1(t) \\ q_1(t) - q_2(t) \\ q_2(t) \end{Bmatrix} \quad 16$$

where θ_1 is usually equal to θ_S (therefore the "mass matrix" on the left hand side is usually singular). This is a system of differential algebraic equations (DAE) that we solve using the ODE MATLAB package "ODE15S" based on multistep finite difference schemes, adapted for stiff non linear algebraic differential systems possibly with a singular mass matrix (alternatively, we have also used "ODE23T"). The system is subjected to the following initial condition:

$$\begin{cases} Z_S(t=0) = \overline{h_0} \\ Z_{F1}(t=0) = \overline{h_0} + \psi_{F1} \\ Z_{F1}(t=0) = \overline{h_0} + \psi_{F2} \end{cases} \quad 17$$

Once the evolution of the water table height ($Z_S(t)$) and front elevations ($Z_{F1}(t)$, $Z_{F2}(t)$) were determined; then eq. (10), (11) and (12) can be applied to calculate the fluxes.

3.4. The multi-front model

In this section, we generalize the inverse Green-Ampt model to the multi-front model. The unsaturated profiles, K(z) and θ(z), are approximated by *N* fronts as shown **Fig. 4**. With this parametrization of the multi-front model, we expect that the accuracy of the

results will be improved as the transition zone is divided (approximated) by a larger number of "fronts" over the height of the 1D column. As a consequence, the profiles K(z) and θ(z) will also be more refined.

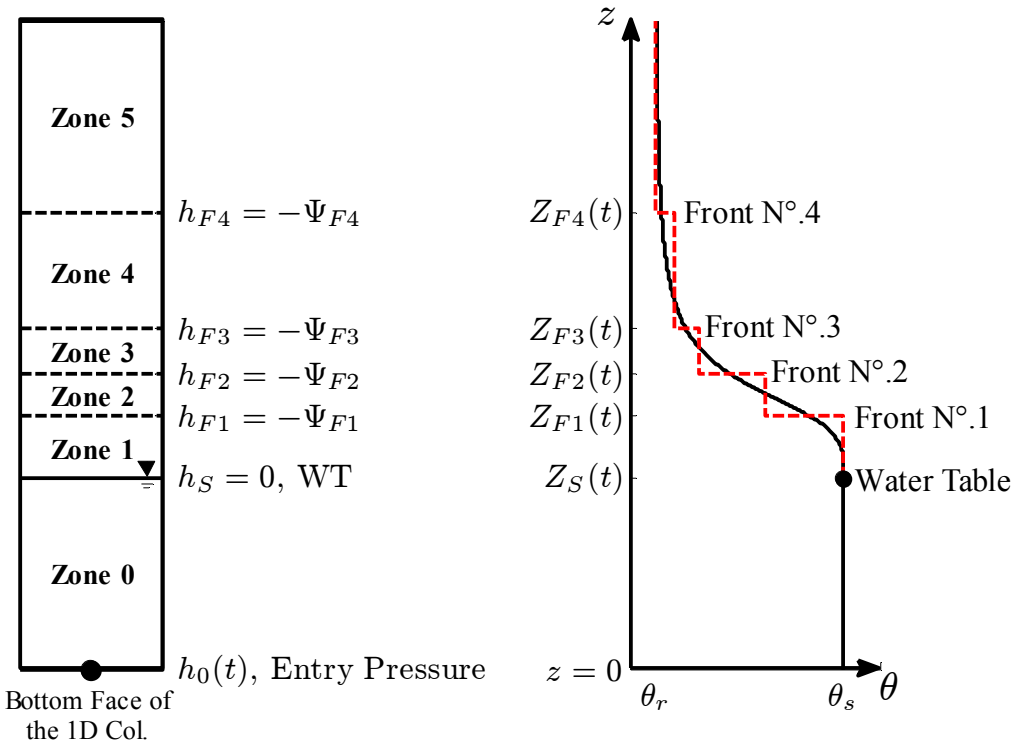

Fig. 4: Schematic diagram of a multi-front model approximation with four fronts (for clarity we show only 4 fronts). On the left: 1D porous column shows the water table ($Z_s(t)$) and the four successive fronts at elevations of ($Z_{F1}(t)$, $Z_{F2}(t)$, $Z_{F3}(t)$ and $Z_{F4}(t)$) where the suction heads are 0, ψ_{F1}, ψ_{F2}, ψ_{F3} and ψ_{F4} respectively. On the right: the instantaneous water content profile with multi-front model approximation (dashed line).

The multi-front approximation divides the 1D column into N+2 regions

- **Zone 0**: it is a totally saturated zone extending from the bottom of the column ($z = 0$) to the moving water table ($z = Z_S(t)$); parameters: $K_0 = K_S$, $\theta_0 = \theta_S$
- **Zones 1** to **N**: These zones are comprised between the moving water table ($z = Z_S(t)$) and the last (Nth) moving front ($z = Z_{F_N}(t)$). They are the N transition zones from the totally saturated zone to the totally dry one. The parameters of each zone (number j) are $K_j \leq K_S$ and $\theta_j \leq \theta_S$.

- **Zone N+1**: This is the totally dry region; it is a semi-infinite dry zone above the N^{th} moving front ($z = Z_{F_N}(t)$); the flux in this zone is null, and the parameters are: $K_{N+1} = 0$, $\theta_{N+1} = \theta_R$.

3.4.1. N-front model: applying Darcy's equation for each zone

- Applying Darcy's law for Zone 0:

$$q_0(t) = K_S\left(\frac{h_0(t)}{Z_S(t)} + g\right) \tag{18}$$

- In the same manner the flux in the Zone 1:

$$q_1(t) = K_1\left(\frac{\psi_{F1}}{Z_{F1}(t) - Z_S(t)} + g\right) \tag{19}$$

- For the remaining Zones (Zone i, $2 \le i \le N$)

$$q_i(t) = K_i\left(\frac{\psi_{F_i} - \psi_{F_{i-1}}}{Z_{F_i}(t) - Z_{F_{i-1}}(t)} + g\right) \tag{20}$$

- For the top dry zone (zone $N+1$) : $q_{N+1}(t) = 0$

3.4.2. N-front model: applying mass conservation through the fronts

Moreover, applying the mass conservation equation through the moving water table, and through the other N fronts (interfaces), we obtain the following results.

- Mass conservation equation traversing the moving water table $(z = Z_S(t))$:

$$q_0(t) - q_1(t) = (\theta_S - \theta_1)\cdot\frac{dZ_S}{dt} \tag{21}$$

- Mass conservation equation traversing the i-th moving front $(1 \le i \le N-1)$:

$$q_i(t) - q_{i+1}(t) = (\theta_i - \theta_{i+1})\cdot\frac{dZ_{Fi}}{dt} \tag{22}$$

- Mass conservation equation traversing the last (Nth) moving front $(z = Z_{F_N}(t))$:

$$q_N(t) - 0 = (\theta_N - \theta_r)\cdot\frac{dZ_{F_N}}{dt} \tag{23}$$

The above equations can be arranged in the following matrix form:

$$\begin{bmatrix} \theta_S-\theta_1 & 0 & \cdots & 0 & 0 \\ 0 & \theta_1-\theta_2 & \ldots & 0 & 0 \\ \vdots & \vdots & \ddots & \vdots & \vdots \\ 0 & 0 & \ldots & \theta_{N-1}-\theta_N & 0 \\ 0 & 0 & \ldots & 0 & \theta_N-\theta_r \end{bmatrix} \begin{Bmatrix} dZ_S/dt \\ dZ_{F_1}/dt \\ \vdots \\ dZ_{F_{N-1}}/dt \\ dZ_{F_N}/dt \end{Bmatrix} = \begin{Bmatrix} q_0(t)-q_1(t) \\ q_1(t)-q_2(t) \\ \vdots \\ q_{N-1}(t)-q_N(t) \\ q_N(t) \end{Bmatrix} \quad 24$$

This is a system of differential algebraic equations (DAE) that can be solved by the ODE package of MATLAB (ODE15S) subject to the following initial condition:

$$\begin{cases} Z_S(t=0)=\overline{h_0} \\ Z_{F_1}(t=0)=\overline{h_0}+\psi_{F_1} \\ \vdots \\ Z_{F_N}(t=0)=\overline{h_0}+\psi_{F_N} \end{cases} \quad 25$$

Once the evolution of the water table height ($Z_S(t)$) and the fronts elevations ($Z_{F_1}(t)$, $Z_{F_2}(t) to Z_{F_N}$) are determined; then eq. (21), (22) and (23) can be applied to calculate the fluxes between the moving fronts, including also the bottom flux ($q_0(t)$).

4. Generalized Green-Ampt models parameters

The performance of the proposed models depends largely on the suitable estimation of the model parameters. These parameters are the constant suction head (ψ_F) at each front, the hydraulic conductivity (K) and the water content (θ) between the successive fronts.

4.1. The single front model parameters

The single front model parameter [the front suction (ψ_F)] can be related to soil hydraulic characteristics. Two expressions for ψ_F were suggested as follows:

- ψ_F corresponds to the point of the inflection of the water retention curve [$\theta(h)$] at which the specific moisture capacity [$C(h)=\partial\theta(h)/\partial h$] is maximum as shown in Fig. (5). The suction head at this point can be treated as a global capillary length scale of the porous media which is defined by Ababou [31]:

$$\psi_F = \frac{1}{\alpha}\left(1-\frac{1}{n}\right)^{\frac{1}{n}} \quad 26$$

Where α and n are the van Genuchten model parameters.

- Another estimation of the wetting front suction is altered form Neuman [32] suggestion of the wetting front suction for the 1D infiltration:

$$\psi_F = \int_0^{\infty} K_r(\psi)\, d\psi \qquad 27$$

This approximation is shown in Fig. (6)

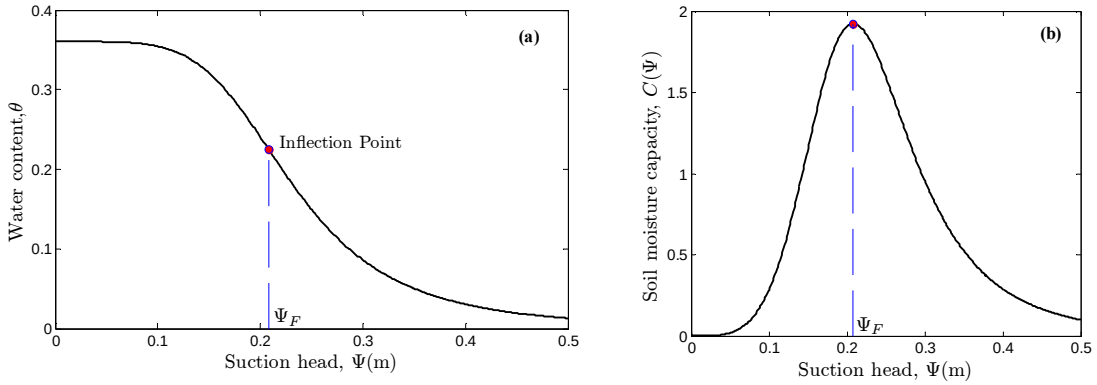

Fig. 5: (a) Water retention curve showing the point of inflection; (b) The corresponding to the maximum soil moisture capacity.

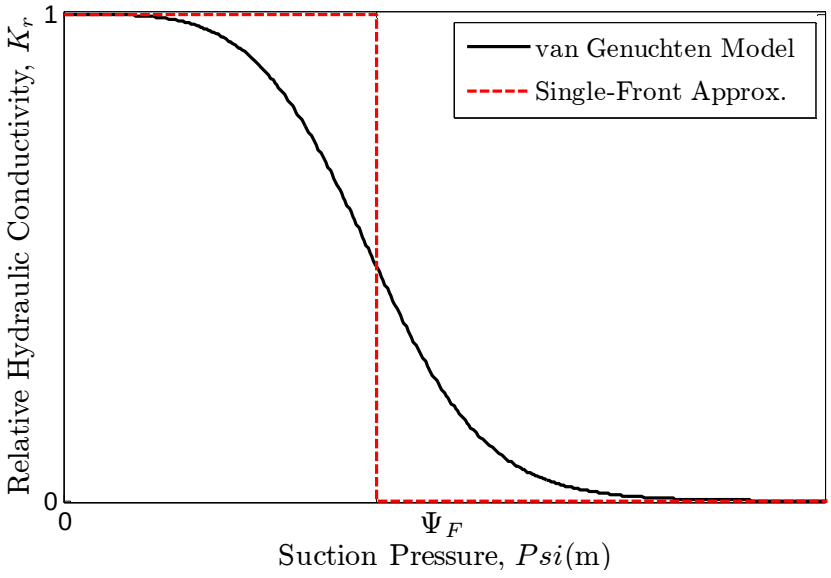

Fig. 6: Relative hydraulic conductivity curve with the Single-front model approximation.

4.2. The two-front model parameters

Here, we suggest a theoretical expression to obtain the parameters of the two-front model. The proposed method relates the two-front suction heads ψ_{F1} and ψ_{F2} to the soil characteristics. It is based on maintaining the area under the relative hydraulic conductivity curve $K_r(\psi)$ given by eq. (27) above and rewritten here $\left[\int_0^{\infty} K_r(\psi)\,d\psi\right]$.

In the same manner, for the two-front model, we assume that:

- There is an intermediate suction head (ψ_{Inter}) between the two-front suction heads (ψ_{F1}) and (ψ_{F2}) as shown in Fig. (10). A good approximation of ψ_{Inter} can be taken to be equal to ψ_F for the single front model [see eq. (27)]. However we can take any other value.
- The area under the $K_r(\psi)$ curve equals the area under the two-front approximation. This assumption is valid for the whole suction range [0 to ∞] and also for the sub regions: from [0 to ψ_{Inter}] and from [ψ_{Inter} to ∞]

Thus applying the second assumption between [0 to ψ_{Inter}] to obtain ψ_{F1}:

$$\int_0^{\psi_{Inter}} K_r(\psi)\,d\psi = \psi_{F1}\cdot 1 + (\psi_{Inter} - \psi_{F1})\cdot K_{r2} \qquad 28$$

And applying the second assumption between [ψ_{Inter} to :] to obtain ψ_{F2}:

$$\int_{\psi_{Inter}}^{\infty} K_r(\psi)\,d\psi = (\psi_{F2} - \psi_{Inter})\cdot K_{r2} \qquad 29$$

Where $K_{r2} = K_r(\psi_{Inter})$ and ψ_{Inter} is an intermediate value between ψ_{F1} and ψ_{F2}.

Note that the value of the hydraulic conductivity and the water content are:

- K_S and θ_S below the first front [between $Z_S(t)$ and $Z_{F1}(t)$].
- $K(\psi_{Inter})$ and $\theta(\psi_{Inter})$ between the first and second front [between $Z_{F1}(t)$ and $Z_{F2}(t)$] as shown explicitly in Fig. (7).

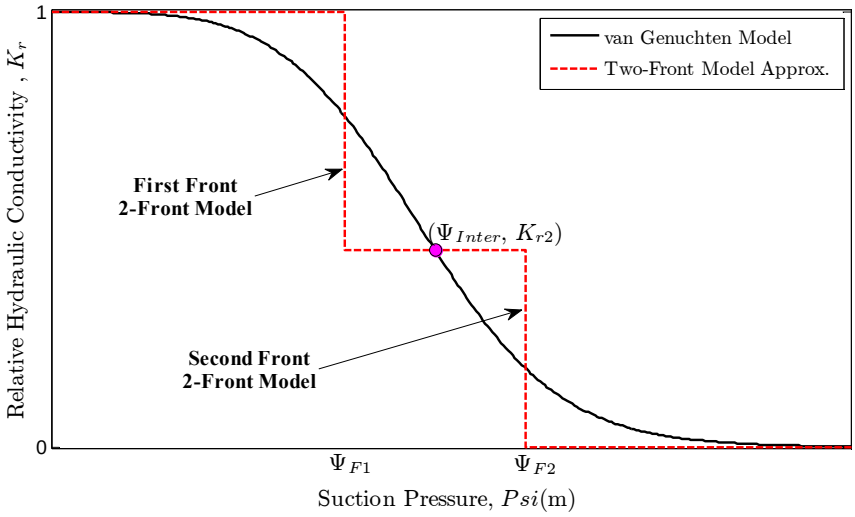

Fig. 7: Relative hydraulic conductivity curve with the two-front model approximation.

4.3. The multi-front model parameters

The parameters of the multi-front model are obtained by a similar method to the one used for the two-front model parameters estimation. For N fronts, the estimation of the model parameters can be summarized as follows [see Fig.(8)]:

- Discretize the relative hydraulic conductivity curve $K_r(\psi)$ by N intermediate suction values [ψ_{Inter1} to ψ_{InterN}]. Where $\psi_{Inter1} = 0$.
- Calculate the relative hydraulic conductivities K_{r_i} at the intermediate suctions. [$K_{r_1} = K_r(\psi_{Inter1})$ to $K_{r_N} = K_r(\psi_{InterN})$]
- Calculate the suction head at each front [ψ_{F1} to ψ_{FN}] by keeping the area under the $K_r(\psi)$ curve equals the area under the model approximation. This step is repeated between each successive intermediate suction values. Thus, to obtain the suction front ψ_{F_i} of the front number i, where i=1,2,…., N -1, we have:

$$\int_{\psi_{Inter_i}}^{\psi_{Inter_{i+1}}} K_r(\psi)\,d\psi = \left(\psi_{Inter_{i+1}} - \psi_{Inter_i}\right)\cdot K_{r_{i+1}} + \left(K_{r_i} - K_{r_{i+1}}\right)\cdot\left(\psi_{F_i} - \psi_{Inter_i}\right) \qquad 30$$

- For the last front ψ_{F_N}

$$\int_{\psi_{Inter_N}}^{\infty} K_r(\psi)\,d\psi = \left(K_{r_N}\right)\cdot\left(\psi_{F_N} - \psi_{Inter_N}\right) \qquad 31$$

Note that the value of the hydraulic conductivity and the water content are:

- K_S and θ_S between the water table and the first front [between $Z_S(t)$ and $Z_{F1}(t)$].
- $K\left(\psi_{Inter_i}\right)$ and $\theta(\psi_{Inter_i})$ between front number (i) and front number $(i-1)$, where $i=2,3,\ldots,N$ as shown in Fig. (8).

It is worth mentioning that other method to discretize the multi-front model can be used such as: discretize the water content [$\theta(\psi)$] into N equally space segments or discretize directly the suction head (ψ) then find the corresponding υ and *K*.

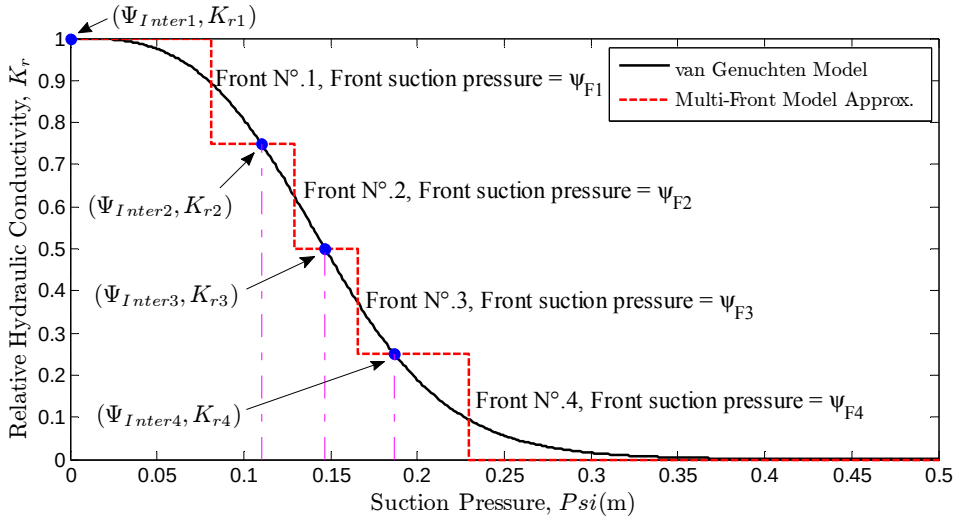

Fig. 8: Relative hydraulic conductivity curve with the multi-front model approximation. Four fronts are shown (to clarify the figure).

5. Validation tests, comparison and performance of the single & multi-front models

To evaluate the proposed models, the solutions obtained from the models are compared to true solutions. Here, the true solution is assumed to be represented by the numerical solution of the Richards equation using BIGFLOW 3D code briefly described below (section 5.1).

Two different soils, namely fine sand (SilicaSand) and Guelph loam (GL), were used in this study to evaluate the performance of the three models. The fine sand and the loam

are from [33]. The soil water retention curves are presented in Fig. (9). The curves indicated that the fine sand has a sharp transition from the saturated to the dry water content (Green-Ampt soil behavior). In contrast with the Guelph loam which have gradual transition behavior.

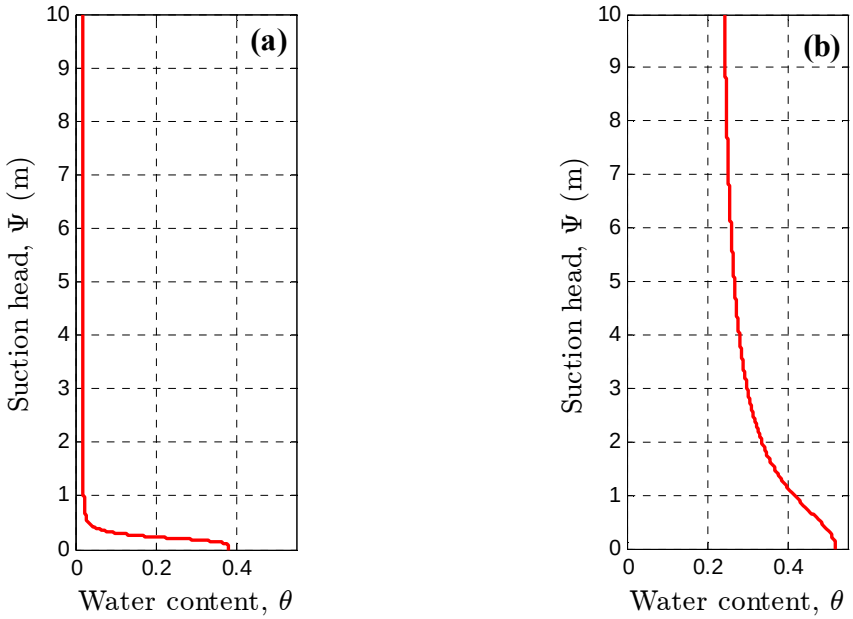

Fig. 9: Water retention curves for the used porous media. (a) Fine Sand "SilicaSand"; (b) Guelph Loam.

The soil hydrodynamic parameters are summarized in Table 1; the unsaturated hydrodynamic properties of the soils are described with the soil water retention model of van Genuchten [34] in combination with the functional model of hydraulic conductivity model proposed by Mualem [35].

Table 1: Hydraulic parameters of porous media used in the study

Parameters	Fine sand "SilicaSand" [33]	Guelph Loam [33]
K_s (m/s)	1.5×10^{-4}	3.66×10^{-6}
θ_s (m^3/m^3)	0.38	0.52
θ_r (m^3/m^3)	0.02	0.218
α (m^{-1})	4.6	1.15
n	5	2.03

The validation of each of the models proposed in this study (the Green-Ampt based multi-front models) is done by comparing the evolution of water table height ($Z_S(t)$) and bottom flux ($q_0(t)$) obtained from these models, to those obtained by a refined numerical simulation based on fully implicit finite volumes with a regular mesh (BIGFLOW 3D). For the numerical solver (BIGFLOW), the spatial gridding vertically involves 150 to 200 nodes or more, depending on the case tested. It should be noted that the multi-front or generalized G-A solutions are computed in a semi-infinite vertical domain, whereas the finite volume solution requires a finite column length with either dry suction or zero flux condition at the top. Here the chosen boundary condition was zero flux at the top of the column (preliminary tests were performed with the Richards / Bigflow solver to ensure that the results were not sensitive to column height, i.e., that the numerical column was long enough to emulate the case of a semi-finite column).

For all cases, the tidal effect is simulated by an oscillatory "entry pressure head" of the form given in eq. (1) and re-written here: $h_0(t) = \overline{h_0} + A_0 sin(\omega_0 t)$ with the following parameters: $\overline{h_0}$ = 0.5m , A_0 = 0.5m , $\omega_0 = 2\,pi / T_p$ with a period T_p of a 10 min (600sec). Note that the amplitude was chosen to be maximum ($A_0 / \overline{h_0}$ =1) to examine an extreme case.

All columns were considered homogeneous, isotropic, and of semi-infinite height with $\overline{h_0}$ chosen to coincide with the initial hydrostatic level.

5.1. Numerical code description (finite volume solution of Richards equation)

Numerical simulations are conducted using the Bigflow 3D finite volume flow code that has been widely documented, tested and benchmarked [36,37,38]. Bigflow is based on generalized Darcy-type equation, with a mixed formulation of mass conservation, capable of simulating various types of flows within the same domain. It is of the form:

$$\begin{cases} \dfrac{\partial\theta(h,\vec{x})}{\partial t} = -\vec{\nabla}\bullet\vec{q} \\ \vec{q} = -\vec{K}\left(h,\vec{\nabla}H,\vec{x}\right)\vec{\nabla}H \\ H = h + \vec{g}(\vec{x})\bullet\vec{x} \end{cases} \qquad 32$$

where only the first equation is actually solved (after insertion of the second and third equations). The first equation expresses mass conservation with a known water retention curve $\theta(h)$; the second equation is a generalized nonlinear flux-gradient law with tensorial hydraulic conductivity/transmissivity (K); and the third equation is the relation between total head (H) and pressure head or water depth (h) via a normalized gravitational vector (g).

In the case of 3D flow in partially saturated/unsaturated media, 'h' is the pressure head relative to atmospheric pressure [L], $K(h)$ is the unsaturated conductivity [LT^{-1}], and $\theta(h)$ is volumetric water content [L^3/L^3].

BIGFLOW 3D can consider any functional unsaturated nonlinear model. In this article, the Van Genuchten / Mualem (VGM) model is used to describe the constitutive relationships [$\theta(h)$, $K(h)$] as follows.

The water retention function is:

$$\frac{\theta(h)-\theta_r}{\theta_s-\theta_r} = \frac{1}{\left[1+\left(-\alpha h\right)^n\right]^m} \qquad 33$$

where θ_r is the residual water content; θ_s is the saturated water content; α, n are the model shape parameters corresponding to average capillary length and the pore size distribution respectively ; and with m related to n by $m = 1-(1/n)$. The corresponding function for the unsaturated hydraulic conductivity is:

$$K(h) = K_s \frac{1}{\left(1+\left(-\alpha h\right)^n\right)^{m/2}}\left(1-\left[1-\frac{1}{\left(1+\left(-\alpha h\right)^n\right)}\right]^m\right)^2 \qquad 34$$

where K_s is the saturated hydraulic conductivity. The remaining variables and parameters were defined earlier.

5.2. Performance of the single front model

Fig. (10) and (11) illustrate the comparison between the exact solution (obtained by the numerical code) and the single front model for the fine sand and the Guelph loam respectively.

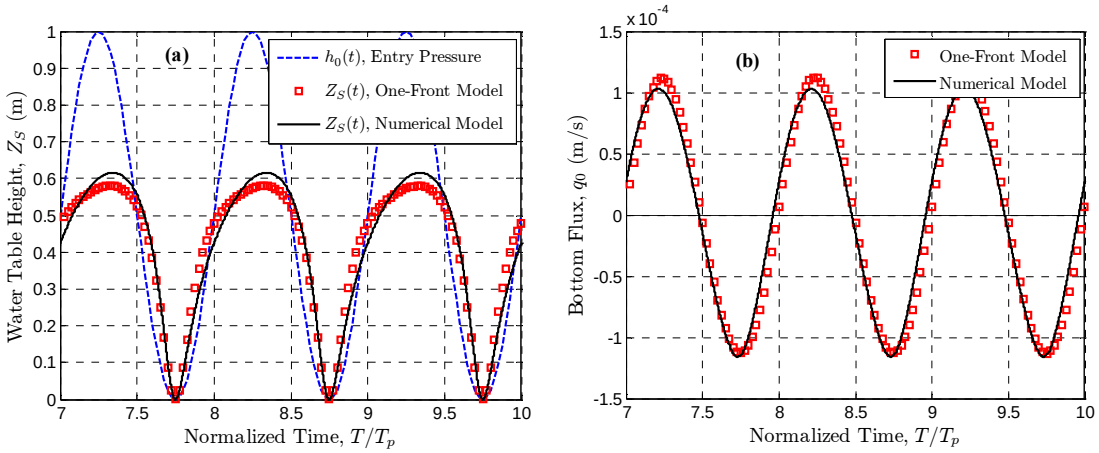

Fig. 10: Tidal oscillations in the SilicaSand: single front model vs. Richards. (a) Evolution of the water table height $Z_S(t)$; (b) Evolution of the bottom flux $q_0(t)$. Bold line: quasi-exact output signals obtained from a refined numerical solution of Richards equation; square symbols : semi-analytical solution of single-front model. The parameters of the entry bottom pressure $h_0(t)$ are: A_0=0.5m, $\overline{h_0}$=0.5m and T_p=600s. The suction head at the wetting front is calculated by eq. 27 in the text.

In the case of the fine sand, the single front model was reasonably close to the exact solution whether accounting for the evolution of the water table or the bottom flux. On the other hand, for the Guelph loam the single front model fails to follow the true solution as shown in Fig. (11).

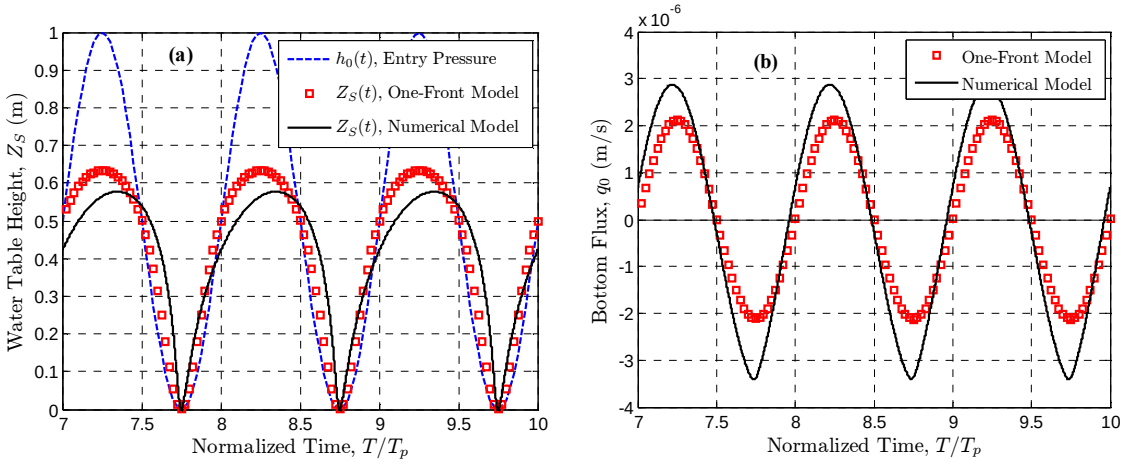

Fig. 11: Tidal oscillations in the Guelph Loam: single front model vs. Richards. (a) Evolution of the water table height $Z_S(t)$; (b) Evolution of the bottom flux $q_0(t)$. Bold line: quasi-exact solution obtained from numerical solution of Richards equation; square symbols : solution of the single-front model. Parameters of the entry bottom pressure $h_0(t)$: A_0 =0.5m, $\overline{h_0}$ =0.5m, T_p =600s. The suction head at the wetting front is calculated by eq. 27 in the text.

These results were expected. The water retention curve for the fine sand has a small transition between the saturated and the unsaturated zones with an elevated value of van Genuchten parameter (n) making a steep water retention curve [Fig. (9)]. This steep curve is close to the sharp front approximation of the single front model and consequently, the single front model work well for this type of soils.

On the other hand, the Guelph loam has a water retention curve with large transition zone and the approximation of this relation by the single front model didn't give a good agreement.

As a summary, for highly dynamic boundary condition, the single front model approximation has reasonable results in the case of soils that compatible to the original Green-Ampt assumptions. However, it may not be so useful for soils that are far away from these assumptions.

5.3. Performance of the two-front model

In this section, we consider the performance of the two-front model. Fig. (12) and (13) show the efficiency of this novel two-front model for the fine sand and the Guelph loam respectively.

A qualitative comparison of the results with the previous single front model shows that the two-front approximation give a better results either in terms of the water table or the bottom flux fluctuations. The modifications/improvements are more obvious in the case of the Guelph loam compared to the previous one-front model.

Our expectations that the results can be improved more if we optimized the two-front model parameters. For this purpose, an optimization procedure was used to look for the best model parameter (ψ_{Inter}) to reduce the root mean square (RMS) of the difference between the two-front model and the true (numerical) model.

The two-front model was coupled with the MatLab genetic algorithm code. Fig. (14) shows the improved results that can be obtained with the optimized parameters for the Guelph loam.

Therefore, the successful performance of the two-front model depends largely on the appropriate values of the model parameters.

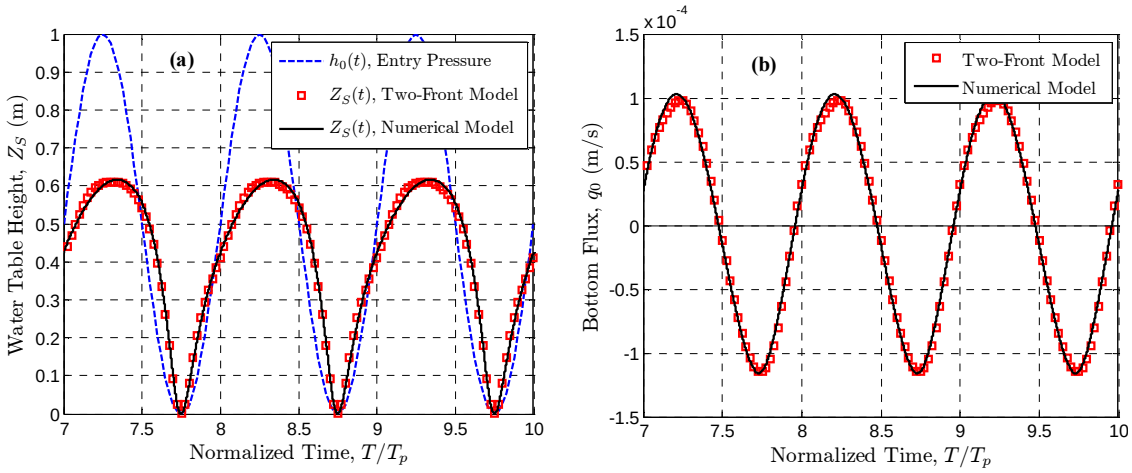

Fig. 12: Tidal oscillations in the SilicaSand: two-front model vs. Richards. (a) Evolution of water table height $Z_S(t)$; (b) Evolution of bottom flux $q_0(t)$. Bold line: quasi-exact solution obtained from numerical solution of Richards equation; square symbols : the two-front model. The parameters of entry bottom pressure $h_0(t)$ are: A_0 =0.5m, $\overline{h_0}$ =0.5m and T_p =600s. The suction heads at the two fronts are calculated with eqs. 27, 28 and 29.

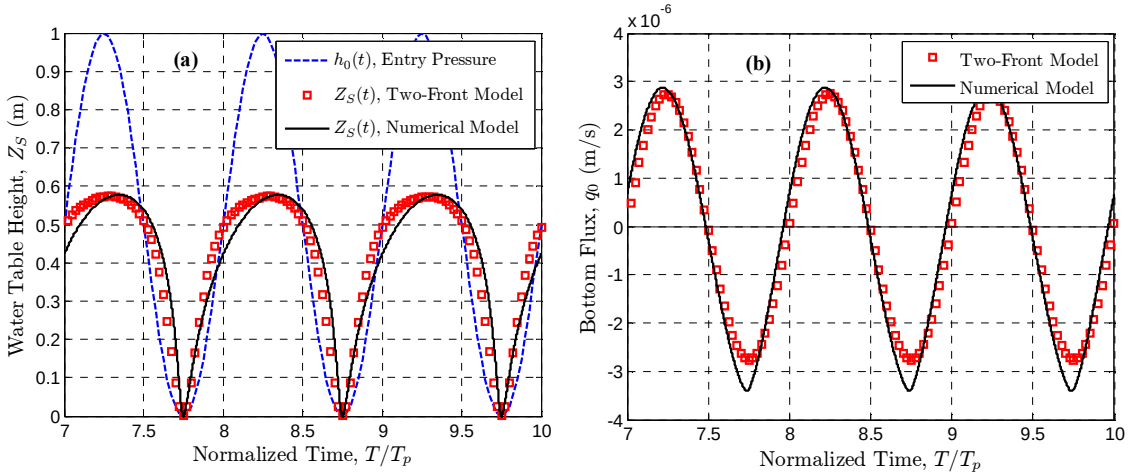

Fig. 13: Tidal oscillations in the Guelph Loam: two-front model vs. Richards. (a) Evolution of water table height $Z_S(t)$; (b) Evolution of bottom flux $q_0(t)$. Bold line: quasi-exact solution obtained from numerical solution of Richards equation; square symbols : the two-front model. The parameters of entry bottom pressure $h_0(t)$ are: A_0 =0.5m, $\overline{h_0}$ =0.5m and T_p =600s. The suction heads at the two fronts are calculated with eqs. 27, 28 and 29.

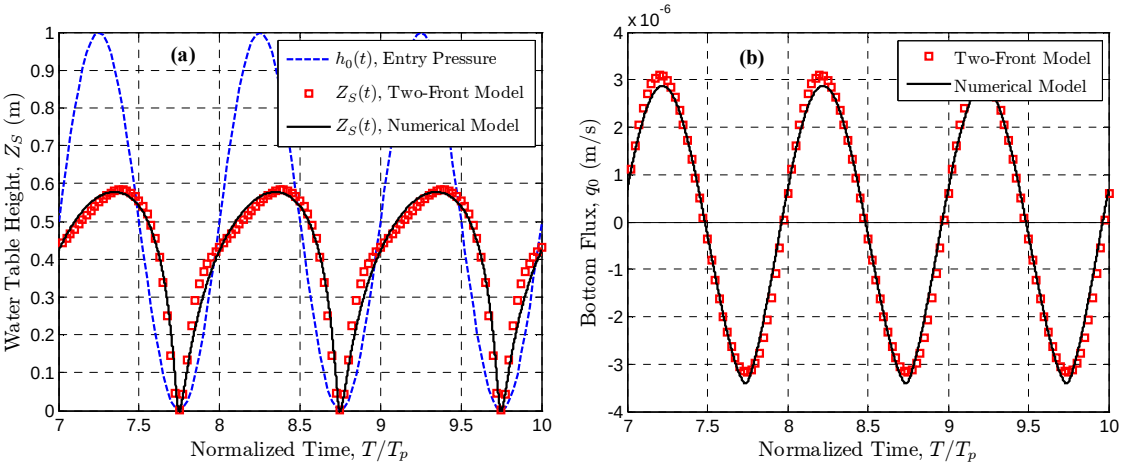

Fig. 14: Tidal oscillations in the Guelph Loam: two-front model with optimized parameter vs. Richards. (a) Evolution of water table height $Z_S(t)$; (b) Evolution of bottom flux $q_0(t)$. Bold line: quasi-exact solution obtained from numerical solution of Richards equation; square symbols : the optimized two-front model. The parameters of entry bottom pressure $h_0(t)$ are: A_0 =0.5m, $\overline{h_0}$ =0.5m and T_p =600s.

5.4. Performance of the Multi-front model

Fig. (15) and Fig. (16) show the evolution of the water table and the bottom fluxes as obtained from the multi-front and numerical models.

A full agreement was achieved between the multi-front model and the true solution. The multi-front model could be used as a substitute for the numerical solution of the Richards equation in the case of 1D simulation subjected to highly dynamic boundary conditions with a successful performance. Overall, our results indicate that this excellent performance can be achieved regardless of the type of saturated/unsaturated hydraulic characteristics of the porous media (coarse sand, fine sand, loam, etc.).

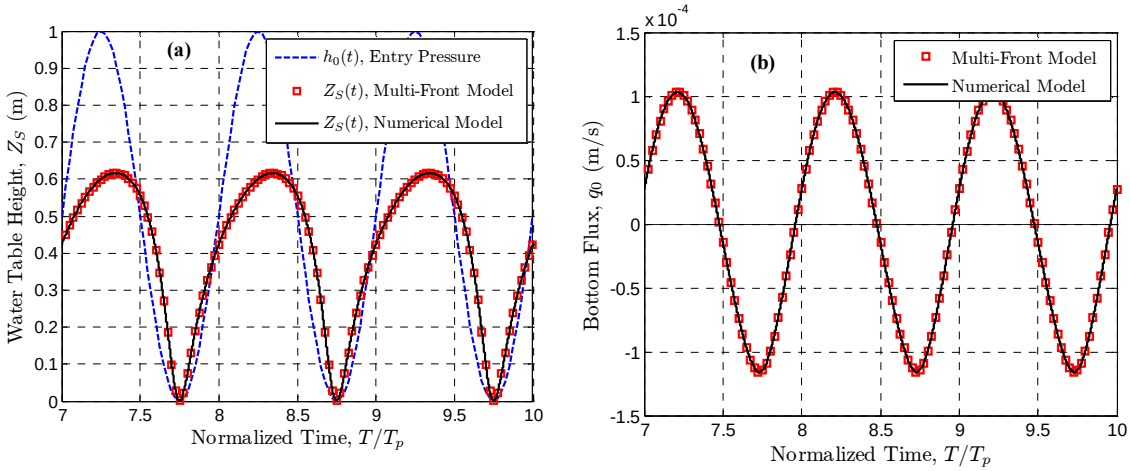

Fig. 15: Tidal oscillations in the SilicaSand: multi-front model vs. Richards. (a) Evolution of water table height $Z_S(t)$; (b) Evolution of bottom flux $q_0(t)$. Bold line: quasi-exact solution obtained from numerical solution of Richards equation; square symbols : the multi-front model (N=20 fronts were used). The parameters of entry bottom pressure $h_0(t)$ are: A_0 =0.5m, $\overline{h_0}$ =0.5m and T_p =600s.

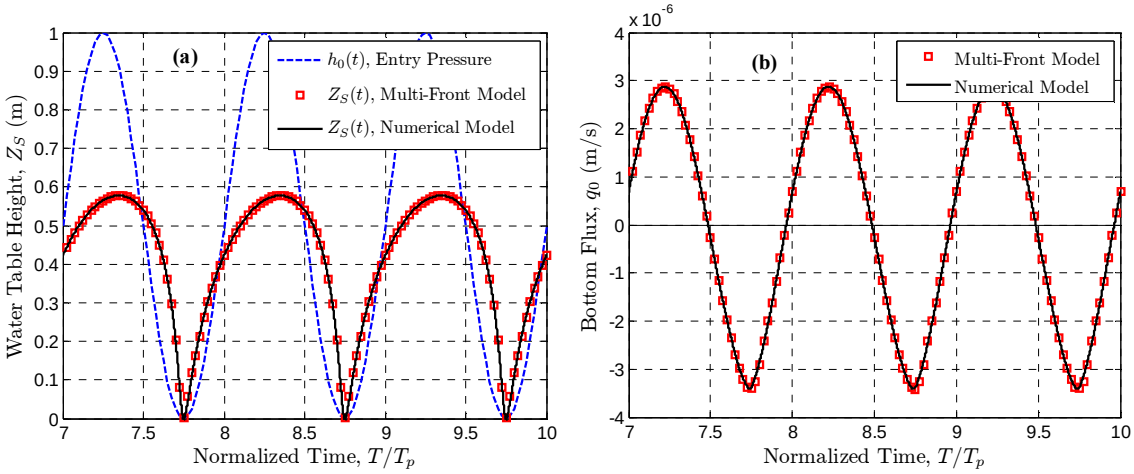

Fig. 16: Tidal oscillations in the Guelph Loam: multi-front model vs. Richards. (a) Evolution of water table height $Z_S(t)$; (b) Evolution of bottom flux $q_0(t)$. Bold line: quasi-exact solution obtained from numerical solution of Richards equation; square symbols : the multi-front model (N=20 fronts were used). The parameters of entry bottom pressure $h_0(t)$ are: A_0 =0.5m, $\overline{h_0}$ =0.5m and T_p =600s.

6. Conclusions and outlook

In summary, a multi-front model which generalizes the Green-Ampt piston flow approach was developed and tested for vertical oscillatory flows in this paper. The set up is a partially saturated vertical column, including a water table, tidally forced via a sinusoïdal pressure signal imposed at the bottom of the column (experimentally, this can be realized using a tide machine as described in **Fig. 1**). In this paper, we focus on large amplitude oscillations. The amplitude of entry pressure head is up to 100% relative to the static height of the water table (most of the tests presented in this paper are based on this extreme case).

In beach hydrodynamics, the objective is to analyze the non linear time response or the frequency response of the system (here a vertical soil column) in terms of pressure, moisture, water table elevation and flux (profiles and signals). Indeed, it was shown that the N-front model, with reasonably small N on the order of 10 or even less (depending on the type of soil) yields accurate solutions in terms of output signals q_0(t) and Z_S (t).

Furthermore, other numerical investigations indicate that the multi-front model can also give accurate solutions, not only in terms of water table and flux signals, but also in

terms of vertical profiles θ(z,t) and h(z,t), and this for all types of soils. An example is shown in **Fig.17** for the case of the Guelph Loam, with N=20 fronts. In fact, the fit is almost as good for N=10 instead of 20 fronts. Many other cases (not shown here) indicate that the 20-front solution profiles are indeed quite close to the numerical profiles obtained from a finite volume solution of Richards equation, with about 200 nodes for vertical discretization in the latter. Moreover, the 20-front solution requires only 1/10th the CPU time of the 200 node finite volume solution, which makes it easier to conduct parametric studies with the multi-front method.

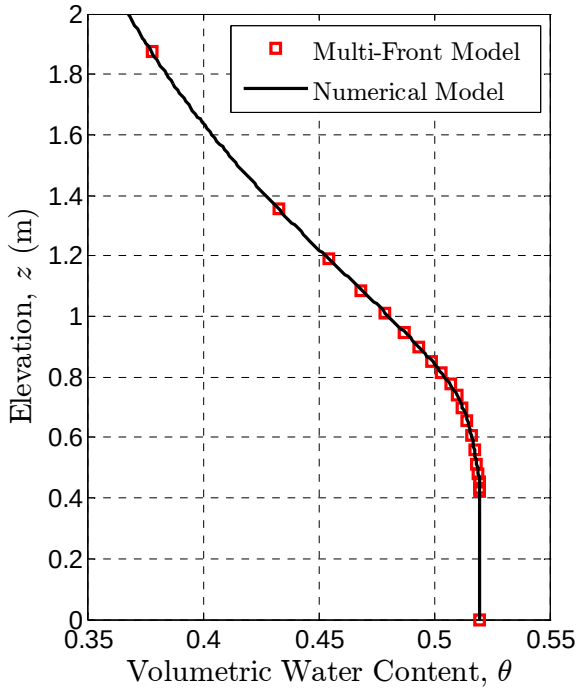

Fig. 17: Water content profile θ(z,t) at time t = 3000 s = 5 T_p , for the Guelph Loam. The square symbols represent the multi-front model with N = 20 fronts; the solid line is the implicit finite volume solution of Richards equation obtained numerically with the Bigflow code. The parameters of the periodic bottom pressure are: A_0 = 0.5 m, $\overline{h_0}$ = 0.5 m and T_p = 600 s.

For example, **Fig. 18** shows one result from a parametric study of frequency response, conducted on the Guelph Loam using the 20-front model. The mean water table height

($\overline{Z_S}$) is plotted versus the period (T_p) of the oscillating pressure $h_0(t)$ imposed at the bottom of the column.

Remarkably, in **Fig. 18**, it can be seen that the behavior of $\overline{Z_S}$ vs. T_p is non monotonic, pointing out the existence of a characteristic frequency for that soil. In other words, there appears a characteristic frequency that separates low / high frequency regimes for this soil (in **Fig. 18**, the characteristic period T_p is about 1800 s, or 1/2 hour).

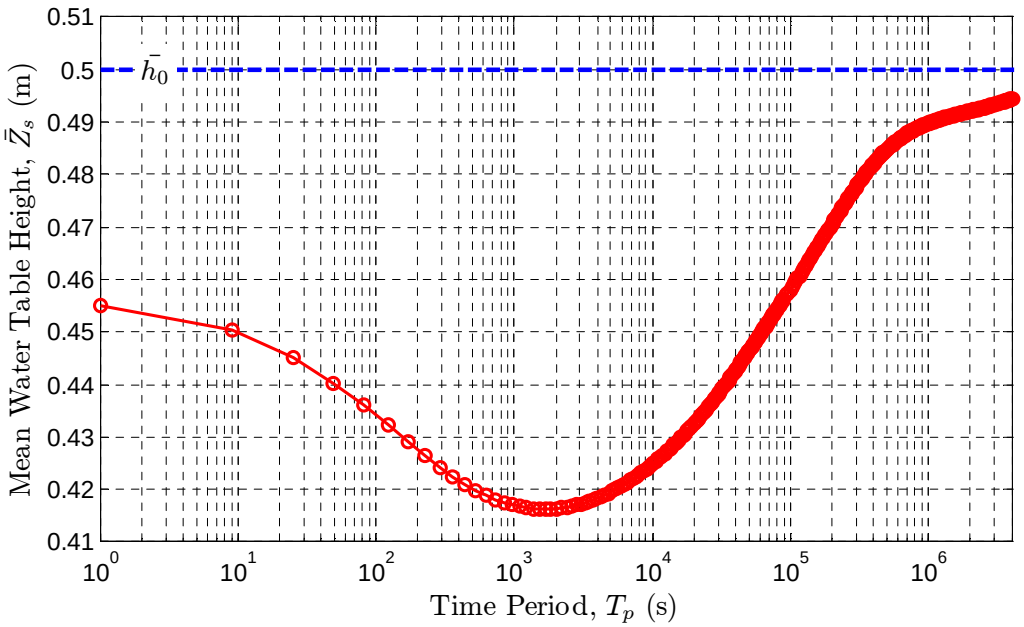

Fig.18: Example of frequency response analysis using the multi-front model (here with N=20 fronts). This figure shows a plot of the mean water table height ($\overline{Z_S}$) vs. period (T_p) for the Guelph Loam. The period T_p (abscissa) is that of the oscillating pressure $h_0(t)$ imposed at the bottom of the column. In this case, the amplitude of $h_0(t)$ was A_0 = 0.50 m and the mean static pressure was $\overline{h_0}$ = 0.5 m.

Note also that the mean water table height ($\overline{Z_S}$) remains below the static level $\overline{h_0}$ =0.50 m for all frequencies (or equivalently, for all periods T_p). Thus, we observe here an "under-elevation" phenomenon due to vertical capillary effects. This effect is most probably influenced by the specific type of geometry and boundary condition used in the present study (namely, vertical oscillations are forced in the system by applying an

oscillating pressure at the bottom). With other geometries, however, an over-elevation of the mean water table height has been observed in the presence of lateral tidal forcing and sloping soil surface [5,39,40].

The high and low frequency limits of $\overline{Z_S}$ are also of interest. It appears from Fig. 18 that the infinite frequency limit for the mean water table height is the static level 0.50 m - although physically, the infinite frequency limit is not strictly valid because acceleration terms are neglected in the Darcy-Richards model used in this work. It is quite clear, on the other hand, that the mean water table height attains the static value $\overline{h_0}$ in the limit of very low frequency ($T_p \to \infty$).

The multi-front model is currently being exploited along these lines, towards a more systematic investigation and parametric study of the frequency response of soil columns in response to tidal forcing, depending on tidal amplitude, static level, and soil parameters such as Ks, θs, and capillary length scale (ongoing work).

Another interesting feature of the multi-front approach developed in this paper is the simple 2-front model. It was demonstrated that the 2-front model can give reasonable solutions - at least compared to the single front Green-Ampt model - in terms of entry flux $q_0(t)$ and water table height $Z_S(t)$. Thus, because of its simplicity, and given the favorable results of tests presented in this paper, it is thought that the 2front model is useful in its own sake as an analytical tool for studying water table oscillations in the presence of capillary effects (ongoing work).

Finally, other extensions to be considered for future work for the generalized G-A or multi-front approach may involve transient problems with non periodic forcing (time signals, wave spectra), and also, multidimensional geometries, including: soil surface slopes, bedrock slopes, slanted river banks, and internal heterogeneities (stratified soils, composite dykes, beach drainage systems, etc).

See for instance [25,41] concerning Green-Ampt infiltration approaches for stratified soils, [28] concerning Green-Ampt infiltration with a sloping surface. See also [19] concerning a Green-Ampt correction of the planar groundwater flow equation, combining

horizontal groundwater flow with vertical exchange through the unsaturated zone above the water table.

In beach hydrodynamics, previous investigations [40] clearly show that several questions still remain open, e.g., concerning the mean over-elevation of water tables compared to static levels. Indeed, several factors intervene together: multidimensional geometry, beach slope, but also, capillary effects during unsaturated wetting/drainage cycles. A multi-front approach might be developed for studying such multidimensional systems.

It is thought that some of the above-mentioned approaches - dealing with geometric or multidimensional extensions of the Green-Ampt model - might be useful in the context of coastal and beach hydrodynamics, and that they can be enhanced based on the two-front and multi-front methods tested in this work.

7. References

[1] Baird AJ, DP Horn. Monitoring and Modelling Groundwater Behaviour in Sandy Beaches. Journal of Coastal Research. 12 1996 630-40.
[2] Jeng DS, HT Teo, DA Barry, L Li. Two-Dimensional Approximation for Tidal Dynamics in Coastal Aquifers: Capillarity Correction. Journal of Engineering Mechanics. 131 2005 534-41.
[3] Chen H, G Pinder. Investigation of Groundwater Contaminant Discharge into Tidally influenced Surface-water Bodies: Theoretical Analysis. Transport in Porous Media. 89 2011 289-306.
[4] Hinz C. Analysis of unsaturated/saturated water flow near a fluctuating water table. Journal of Contaminant Hydrology. 33 1998 59-80.
[5] Nielsen P. Tidal dynamics of the water table in beaches. Water Resour Res. 26 1990 2127-34.
[6] Baird AJ, T Mason, DP Horn. Validation of a Boussinesq model of beach ground water behaviour. Marine Geology. 148 1998 55-69.
[7] Kang H-Y, P Nielsen. WATERTABLE DYNAMICS IN COASTAL AREAS. Proceedings of the International Conference on Coastal Engineering; No 25 (1996): Proceedings of 25th Conference on Coastal Engineering, Orlando, Florida, 1996. 1996.
[8] Raubenheimer B, RT Guza, S Elgar. Tidal water table fluctuations in a sandy ocean beach. Water Resour Res. 35 1999 2313-20.
[9] Song Z, L Li, J Kong, H Zhang. A new analytical solution of tidal water table fluctuations in a coastal unconfined aquifer. Journal of Hydrology. 340 2007 256-60.
[10] Teo HT, DS Jeng, BR Seymour, DA Barry, L Li. A new analytical solution for water table fluctuations in coastal aquifers with sloping beaches. Advances in Water Resources. 26 2003 1239-47.

[11] Xia Y-q, H-l Li, MC Boufadel. A new perturbation solution of groundwater table fluctuations in tidal beaches. Journal of Hydrodynamics, Ser B. 22 2010 55-60.
[12] Dupuit J. Etudes Théoriques et Pratiques sur le Mouvement des Eaux dans les Canaux Découverts et à Travers les Terrains Perméables. 2nd ed. Dunod, Paris, 1863.
[13] Boussinesq J. Recherches théoriques sur l'écoulement des nappes d'eau infiltrées dans le sol et sur le débit des sources. CR Académie des Sciences, Journal de Mathématiques pures et appliquées. 11 1904 363-94.
[14] Nielsen P, P Perrochet. Watertable dynamics under capillary fringes: experiments and modelling. Advances in Water Resources. 23 2000 503-15.
[15] Nielsen P, P Perrochet. Watertable dynamics under capillary fringes: experiments and modelling [Advances in Water Resources 23 (2000) 503–515]. Advances in Water Resources. 23 2000 907-8.
[16] Turner I. The Total Water Content of Sandy Beaches. Journal of Coastal Research. 1993 11-26.
[17] Werner AD, DA Lockington. Influence of hysteresis on tidal capillary fringe dynamics in a well-sorted sand. Advances in Water Resources. 26 2003 1199-204.
[18] Li L, DA Barry, JY Parlange, CB Pattiaratchi. Beach water table fluctuations due to wave run-up: Capillarity effects. Water Resour Res. 33 1997 935-45.
[19] Parlange JY, W Brutsaert. A capillarity correction for free surface flow of groundwater. Water Resour Res. 23 1987 805-8.
[20] Barry DA, SJ Barry, J-Y Parlange. Capillarity correction to periodic solution of the shallow f ow approximation. in: CB Pattiaratchi, (Ed.). Mixing Processes in Estuaries and Coastal Seas Coastal and Estuarine Studies. American Geophysical Union, Washington, DC1996. pp. 496–510.
[21] Green WH, GA Ampt. Studies on soil physics, 1: The flow of air and water through soils. J Agric Sci. 4 1911 1–24.
[22] Warrick AW, D Zerihun, CA Sanchez, A Furman. Infiltration under Variable Ponding Depths of Water. Journal of Irrigation and Drainage Engineering. 131 2005 358-63.
[23] Ma Y, S Feng, D Su, G Gao, Z Huo. Modeling water infiltration in a large layered soil column with a modified Green-Ampt model and HYDRUS-1D. Comput Electron Agric. 71 2010 S40-S7.
[24] Kacimov A, O Abdalla. Water table response to a tidal agitation in a coastal aquifer: The Meyer–Polubarinova-Kochina theory revisited. Journal of Hydrology. 392 2010 96-104.
[25] Selker JS, J Duan, J-Y Parlange. Green and Ampt infiltration into soils of variable pore size with depth. Water Resour Res. 35 1999 1685-8.
[26] Regalado CM, A Ritter, J Álvarez-Benedí, R Muñoz-Carpena. Simplified Method to Estimate the Green–Ampt Wetting Front Suction and Soil Sorptivity with the Philip–Dunne Falling-Head Permeameter. Vadose Zone Journal. 4 2005 291-9.
[27] Philip JR. Approximate analysis of falling-head lined borehole permeameter. Water Resour Res. 29 1993 3763-8.
[28] Chen L, MH Young. Green-Ampt infiltration model for sloping surfaces. Water Resour Res. 42 2006 W07420.
[29] Alastal K, R Ababou, D Astruc. Partially saturated oscillatory flow under tidal conditions in homogeneous and layered soil columns: experiment and simulations.

Proceedings of the Second Coastal and Maritime Mediterranean Conference; Tangier, Morocco, 2011. 2011.
[30] Liu G, JR Craig, ED Soulis. Applicability of the Green-Ampt Infiltration Model with Shallow Boundary Conditions. Journal of Hydrologic Engineering. 16 2011 266-73.
[31] Ababou R. Approaches to Large Scale Unsaturated Flow in Heterogeneous, Stratified, and Fractured Geologic Media, Report NUREG/CR 5743. U.S. Nuclear Regulatory Commission, Government Printing Office, Washington D.C., U.S.A.1991. pp. 150 pp.
[32] Neuman SP. Wetting front pressure head in the infiltration model of Green and Ampt. Water Resour Res. 12 1976 564-6.
[33] Alastal K, R Ababou, D Astruc. Partially saturated oscillatory flow in a sandy beach (numerical modeling). XVIII International Conference on Water Resources (CMWR), CIMNE, Barcelona 20102010.
[34] van Genuchten MT. A Closed-form Equation for Predicting the Hydraulic Conductivity of Unsaturated Soils. Soil Sci Soc Am J. 44 892-8.
[35] Mualem Y. A new model for predicting the hydraulic conductivity of unsaturated porous media. Water Resour Res. 12 1976 513-22.
[36] Ababou R, A Al-Bitar. Coupled Surface/Subsurface Flow Systems: Numerical Modeling. in: CJG Darnault, (Ed.). Overexploitation and Contamination of Shared Groundwater Resources. Springer Netherlands2008. pp. 105-17.
[37] Ababou R, AC Bagtzoglou. BIGFLOW: A Numerical Code for Simulating Flow in Variably Saturated, Heterogeneous Geologic Media (Theory and User's Manual, Version 1.1), Report NUREG/CR-6028. U.S. Nuclear Regulatory Commission, Government Printing Office, Washington D.C., U.S.A.1993. pp. 139 pp.
[38] Bailly D, R Ababou, M Quintard. Geometric characterization, hydraulic behavior and upscaling of 3D fissured geologic media. Mathematics and Computers in Simulation. 79 2009 3385-96.
[39] Turner I. Water table outcropping on macro-tidal beaches: A simulation model. Marine Geology. 115 1993 227-38.
[40] Cartwright N, P Nielsen, L Li. Experimental observations of watertable waves in an unconfined aquifer with a sloping boundary. Advances in Water Resources. 27 2004 991-1004.
[41] Kacimov AR, S Al-Ismaily, A Al-Maktoumi. Green-Ampt One-Dimensional Infiltration from a Ponded Surface into a Heterogeneous Soil. Journal of Irrigation and Drainage Engineering. 136 2010 68-72.

Chapter 9

Conclusions and Perspectives

This chapter comprises the major conclusions for the whole thesis, together with recommendations and perspectives for future research (outlook).

9.1 Conclusions

The response of porous media to tidal fluctuations was studied in this thesis experimentally, numerically and analytically.

In chapter 4 (numerical studies):

- The numerical code (BIGFLOW 3D) used in solving the 3D variably saturated/unsaturated Richards equation was modified in this thesis to deals with the time varying pressure head boundary conditions. This code is validated against Philips series solution of 1D continuous infiltration through a semi-infinite homogeneous soil. The results on three different soils (medium sand, fine sand and a loam) show a good matching between the numerical and Philip's quasi-analytical results in terms of the sorptivity, and hydraulic conductivity values and also in comparing the two solutions with respect to water content profiles at selected times.
- Moreover, the previous validation test was chosen as it addresses the concept of sorptivity. This concept presents an important integral variable which links water retention and hydraulic conductivity characteristics and it may be helpful in obtaining a time-scale characteristic for porous medium t_{GRAV} which can be define as the time for which the gravity forces are supposed to become predominant over the capillary forces. Comparison between the t_{GRAV} values of the different soil shows distinct differences (1.7 min for medium sand, 11.2 min for fine sand and 864.9 min for the loam).

In chapter 5 and 6 (experimental studies):

- A tidal machine was designed and fabricated in this thesis at the IMFT. This machine can generate tidal oscillations which can be applied to 1D, 2D and 3D flow problems into porous media. This machine also shows its capability to be coupled with other forcing types: for example, in the thesis of (Caplain, 2011) the tide machine is coupled perfectly with a wave generator to study the combined effect of waves and tides on beach or cliff erosion. Moreover, the tide machine is a flexible apparatus that

gives the possibility of controlling and changing the mean level, the amplitude and the period of the applied oscillatory pressure.

- In this thesis, a series of more than 30 experiments on a sand column (1.5 m height) were conducted using this tide machine. For each experiment, we generate a tidal forcing with different amplitudes A_0, frequencies ω_0, and mean water levels $\overline{h_0}$. The results of these experiments are summarized and discussed below.
- The pressure evolution $h(z,t)$ and the phase lag $\varphi(z)$ along the experimental column were investigated. Based on the pressure measurements, the column can be divided into 3 zones: (1) totally saturated zone at all times; (2) variably saturated/ unsaturated mixed zone; (3) totally unsaturated zone at all times (including an upper dry zone which does not response to bottom fluctuations). As we move away from the bottom oscillatory pressure, the amplitude $A(z)$ of total head $H(z,t)$ is attenuated, the phase lag $\varphi(z)$ increases, and the temporal structure of the signals becomes more asymmetrical (skewed).
- In the saturated zone, this attenuation is related to the frictional losses that occur as water flows through the sand grains, whereas in the unsaturated zone, the reduced hydraulic conductivity enhances the attenuation even more. It is observed also that the amplitude of total head decreases linearly in the saturated zone, as expected from the linearity of Darcy's head loss law in saturated zones. Moreover the attenuation rate dA/dz decreases with increasing time period. One possible explanation is that, for larger periods (T_P), there is more time for water contents and pressures to adapt to changing water table levels, and to equilibrate to quasi-hydrostatic state. In fact, as $T_P \rightarrow \infty$, it is expected that the pressure profiles become nearly hydrostatic; they are just slowly translated in time.
- The total head signals were observed to be more asymmetrical (and less harmonic) as one moves up into the active part of the unsaturated zone (moderately dry) with a shorter wetting phase followed by a longer drainage phase. This non-harmonic structure of the signals is a sign of the global hysteretic behavior of the porous column (due to for example the competition between the gravity and capillary

effects). It is worth noting that the numerical solver (BIGFLOW) shows the same non-harmonic structure of the signals even though it is based on non-local hysteresis formulation of the constitutive relationships $[k(h), \theta(h)]$.

- The bottom flux, $q_0(t)$, was analyzed indirectly (in the experiment) by looking at the total head gradient (grad H) in the saturated zone. The amplitude of bottom flux appears to increase with frequency. Also, it was observed from grad H measurements that, at some specific times, the vertical flux changes sign (direction) along the column. We provided examples where we have an upward water table movement, while at the same time, we have a downward flux in some part of the unsaturated zone (meaning that the "information" of changing direction of the water table motion, has not yet "reached" this zone).
- It is also inferred from the experimental results that, as the frequency of the bottom pressure increases, the water content profiles do not vary greatly in time, and they stay close to each other at all times. This means that, by increasing the applied forcing frequency, the porous medium "does not have enough time" to respond to these high frequency forcing.
- The response of the water table height to the applied tidal forcing in terms of amplitude damping and phase lag was analyzed. The water table amplitude increases with the increase of time period T_P (lower frequencies); therefore the porous column acts as a low pass filter. It is noted that this amplitude increase is nonlinear, and it can be inferred that at very low frequency the amplitude of the water table reached asymptotically the amplitude of the applied bottom pressure (A_0). This is obviously a quasi-hydrostatic low frequency regime (see the previous discussion about total head signals).
- It is also noted that the phase lag decreases non-linearly with increase of the time period of the bottom tidal forcing. Our expectation that at very large time periods, the static equilibrium is retained instantaneously. Therefore, there is no phase lag (it reaches zero asymptotically) because the porous media and consequently the water table have enough time to response to the bottom fluctuation.

- The mean water table height ($\overline{Z_S}$) was also analyzed from the experiments. The results show that $\overline{Z_S}$ was less than the time average of the fluctuating pressure imposed at the bottom of the column ($\overline{h_0}$). This under-elevation is probably due to the effect of the bottom pressure condition: the distance between the water table and the pressure boundary becomes minimal when the water table reaches its trough, and is maximal when the water table reaches its peak. The difference $\overline{h_0} - \overline{Z_S}$ decreases with increasing period (T_P) and vanishes as $T_P \to \infty$ (quasi-static regime).

In chapter 7 (optimal calibration)

- Parameter estimation of the sand used in the experimental study was done using optimization modeling by the genetic algorithm. The genetic algorithm available in the MATLAB software was coupled with the numerical code (BIGFLOW) in order to automatize the optimization process. The parameters were calibrated for a given frequency in the column experiment, and the simulation results were then compared to experimental results obtained for other frequencies. The results generally show a good match in terms of the time series of water table heights. These calibrated parameters were then used to extend the study numerically.

In chapter 8 (quasi-analytical multi-front model):

- A family of quasi-analytical multi-front solutions was developed for the tidal oscillation problem, as an extension of the Green-Ampt piston flow approximation. This leads to nonlinear, non-autonomous systems of Ordinary Differential Equations with initial conditions (dynamical systems).
- The multi-front solutions were tested by comparing them with a refined finite volume solution of the Richards equation (BIGFLOW). Multi-front solutions are at least 100 times faster, and the match is quite good even for a loamy soil (Guelph Loam) with strong capillary effects. The number of fronts required for good accuracy is small, no more than N≈10 to 20 at most. For coarse soils (sands), even the 2-front

solution can give good results in terms of water table signal. A large set of multi-front simulations was then produced in order to analyze water table and flux fluctuations for a broad range of forcing frequencies. The results were analyzed in terms of means and amplitudes of the output variables, $Z_S(t)$ and $q_0(t)$. They indicate the existence, for each porous medium, of a characteristic frequency separating low frequency and high frequency flow regimes.

9.2 Perspectives for future researches (outlook)

Finally, as an outlook for the study of beach hydrodynamics and groundwater interactions, it will be interesting and useful to consider, in a future work the following extensions:

- The column experiment can include direct measurement of water contents. In addition, using a CCD (Charged Coupled Device) camera together with the time-domain reflectometer (TDR) to find a calibration curve relating the gray scales from the CCD camera to the water content from TDR measurements. The benefit of the calibration relationship is to provide a follow up of the water content distribution along the column rather that at local points.

  At the time of this writing, a preliminary set of optical CCD measurements were performed on the column experiment (ongoing work, see appendix C).

- The experimental study can be extended to more complex 2D geometry: an experiment involving a 2D slab of soil with a vertical/sloping sand beach has been recently constructed and instrumented, see **Fig. 9.1**. This experiment will include a study of 2D capillary effects with various slope angles. It will include a CCD camera, and at least one TDR probe for calibrating the optical measurements (ongoing work).

Fig. 9.1: Photo of the 2D experiment; the photo show also the tide machine used to generate the tidal forcing on the beach face.

- Moreover, with the availability of 2D experimental results, the coupling between the surface and the subsurface flow could also be studied numerically in 2D and 3D cases under the effect of tidal oscillations with vertical or sloping beaches using the idea of macro-porous media (to be discussed and validated). Comparisons between the numerical and the 2D slab experimental results can be done to test these ideas.
- Other extensions to be considered for future work concern the generalized Green-Ampt or multi-front approach. These extensions may include other transient problems with non periodic forcing (time signals, wave spectra), and also, multidimensional geometries, including: soil surface slopes, bedrock slopes, slanted river banks, and internal heterogeneities (stratified soils, composite dykes, beach drainage systems, etc).
- Finally, the influence of fine stratification and/or local hysteresis could be re-examined and compared to the global hysteretic behavior of the porous medium (Note that a global hysteretic behavior of the partially saturated system was observed both

experimentally and numerically. This was explained by the nonlinearity of $\theta(h)$ and $K(h)$ and to the competition of capillarity and gravity).

Conclusions et Perspectives (en français)

1. Conclusions

Dans ce travail de thèse, on a étudié expérimentalement, numériquement et quasi-analytiquement la réponse hydrodynamique de milieux poreux à des fluctuations tidales, imposées par le biais d'une pression oscillatoire. L'objectif était d'étudier les fluctuations verticales de la nappe ainsi que l'écoulement non saturé sus-jacent, en prenant en compte:

- les pertes de charge dans la zone saturée;
- la surface libre mobile;
- les gradients de pression capillaire dans la zone non saturée.

On a mis en œuvre des expérimentations sur colonnes de sols, équipées de tensiomètres à céramique poreuse pour mesurer les pressions positives et les succions. On a induit des écoulements oscillants dans la colonne en imposant une pression oscillatoire positive au bas de la colonne grâce à une machine à marée à bras rotatif. Ces résultats ont été analysés en termes de déphasages, d'atténuations, de moyennes, etc. Les résultats expérimentaux ont servi aussi à caler certains paramètres hydrodynamiques du sol de la colonne afin de procéder par la suite à des simulations numériques sur un éventail plus large de paramètres (niveau statique de la nappe, amplitude du forçage, fréquence du forçage, et type de sol: sable fin, limon, etc.).

Enfin, on a développé une nouvelle classe de solutions quasi-analytiques (différentielles ordinaires) des écoulements saturés/insaturés. Ces solutions, de type

"multi-front", ont été obtenues en généralisant l'approche "écoulements piston" de Green et Ampt, et en l'adaptant au cas des oscillations tidales (y compris de forte amplitude). Les solutions de ces systèmes multi-front sont testées et comparées aux solutions volumes finis de l'équation de Richards sur maille fine. Les solutions multi-front s'avèrent dix fois plus rapides à calculer, et leur accord avec l'EDP de Richards est excellent même pour un sol limoneux à fort effet capillaire (le nombre de fronts requis reste modéré, N≈10 à 20 au plus).

Grâce à ces performances, la méthode multi-front a pu alors être utilisée pour générer un grand nombre de simulations oscillatoires, afin d'analyser les fluctuations du flux d'entrée $q_0(t)$, et du niveau de la nappe $Z_S(t)$, pour une très large gamme de fréquences de forçages. Les résultats, exprimés en termes de moyennes et d'amplitudes des variables hydrodynamiques ($q_0(t)$,$Z_S(t)$) font apparaître assez nettement une fréquence caractéristique, qui dépend des propriétés hydrodynamiques du milieu poreux, et qui sépare les régimes d'écoulement "haute fréquence" / "basse fréquence" dans le poreux.

2. Perspectives

Finalement, concernant l'étude des interactions mer/nappe en hydrodynamique côtière, il sera intéressant de considérer les extensions suivantes :

- Expérimentations en colonnes sur des milieux poreux granulaires ayant une plus large distribution de tailles de grains (et une plus grande proportion de fines) que le "SilicaSable" utilisé jusqu'ici.
- Mise en oeuvre complète du protocole expérimental de mesures optiques des teneurs en eau (que ce soit en colonne ou en bi-plaque). Ce protocole combine une acquisition d'images par caméra CCD et l'utilisation d'une sonde TDR pour caler (ne serait-ce que partiellement) la relation entre niveaux de gris et teneurs en eau. Un ensemble de mesures optiques par CCD ont déjà été effectuées à titre préliminaire sur

la colonne expérimentale utilisée dans cette thèse, et également, sur le bi-plaque expérimental décrit ci-dessous (travail expérimental en cours, voir appendice C).

- L'étude expérimentale sur colonne ne s'intéresse qu'aux oscillations verticales. Elle devrait être complétée par une expérience sur maquette à géométrie plus complexe.

  Une nouvelle expérimentation 2D sur maquette bi-plaque, représentant en section verticale une plage de sable inclinée avec sa nappe connectée à la mer, a été récemment construite et instrumentée par nos soins dans le laboratoire du Groupe d'Etudes Milieux Poreux à l'IMFT (recherche collaborative en cours, en vue d'une extension de ce travail de thèse).

  Noter que, bien que cette expérience 2D n'ait pas encore été mise en œuvre, elle a déjà fait l'objet de tests préliminaires, notamment avec la caméra CCD. La maquette bi-plaque est remplie de sable, et les capteurs tensiométriques sont déjà positionnés. Les oscillations du niveau de la "mer" dans ce système provoqueront des écoulements oscillatoires tant horizontaux que verticaux dans le massif poreux. On cherche à comprendre notamment les effets combinés de la pente de la plage et des gradients de pression capillaires dans un tel système bi-dimensionnel.

- La simulation numérique de l'expérimentation bidimensionnelle sur plage inclinée (décrite ci-dessus) fera intervenir un couplage direct entre le système de pleine eau ("mer") et le poreux ("plage"), le couplage prenant place à l'interface entre les deux (surface inclinée de la plage). Pour traiter ce problème, on utilisera le concept de milieu macro-poreux, déjà testé et implanté dans le modèle numérique BIGFLOW 3D.

- Enfin, d'autres extensions théoriques sont prévues suite à ce travail, concernant notamment la méthode multi-front (ou "Green-Ampt généralisée). Cette méthode peut être développée dans deux directions différentes, quasi-analytique (e.g. pour la méthode à 2 fronts), ou bien numérique (lorsque $N \approx 10$ ou plus). Les extensions de la méthode multi-front, analytiquement ou numériquement, pourront inclure:

  - A) les problèmes transitoires à forçage non périodique (signaux réels, signaux aléatoires, spectres composites, variations brusques, etc.);

- B) les problèmes à géométrie multidimensionnelle et/ou hétérogène (sols et berges à surfaces inclinées, multi-couches inclinés, sols stratifiés, digues poreuses composites, plages avec systèmes de drainages, etc.).

Dans toutes les extensions considérées, les effets capillaires, gravitaires et géométriques sont combinés, et le principal challenge de l'analyse sera de départager les contributions et les interactions entre ces différents effets en réponse aux sollicitations.

References

1. ABABOU, R. 1988. *Three-dimensional flow in random porous media.* PhD Thesis.
2. ABABOU, R. 1991. Approaches to Large Scale Unsaturated Flow in Heterogeneous, Stratified, and Fractured Geologic Media, Report NUREG/CR 5743. U.S. Nuclear Regulatory Commission, Government Printing Office, Washington D.C., U.S.A.
3. ABABOU, R. 2008. Quantitative Stochastic Hydrogeology: The Heterogeneous Environment. *In:* DARNAULT, C. J. G. (ed.) *Overexploitation and Contamination of Shared Groundwater Resources.* Springer Netherlands.
4. ABABOU, R. & AL-BITAR, A. 2004. Salt water intrusion with heterogeneity and uncertainty: mathematical modeling and analyses. *In:* CASS, T. M. & GEORGE, F. P. (eds.) *Developments in Water Science.* Elsevier.
5. ABABOU, R. & AL-BITAR, A. 2008. Coupled Surface/Subsurface Flow Systems: Numerical Modeling. *In:* DARNAULT, C. J. G. (ed.) *Overexploitation and Contamination of Shared Groundwater Resources.* Springer Netherlands.
6. ABABOU, R. & BAGTZOGLOU, A. C. 1993. BIGFLOW: A Numerical Code for Simulating Flow in Variably Saturated, Heterogeneous Geologic Media (Theory and User's Manual, Version 1.1), Report NUREG/CR-6028. U.S. Nuclear Regulatory Commission, Government Printing Office, Washington D.C., U.S.A.
7. ABABOU, R., GELHAR, L. W. & HEMPEL, C. 1992a. Serial and parallel performance on large matrix systems. *Cray channels* 14**,** 22-25.
8. ABABOU, R., SAGAR, B. & WITTMEYER, G. 1992b. Testing procedures for spatially distributed flow models. *Advances in Water Resources,* 15**,** 181-198.
9. ABABOU, R., SAGAR, B. & WITTMEYER, G. 1992c. Testing Procedures for Spatially Distributed Flow Models. *Advances in Water Resources,* 15**,** 181-198.
10. ABABOU, R. & TRÉGAROT, G. 2002. Coupled modeling of partially saturated flow: macro-porous media, interfaces, variability. *In:* S. MAJID HASSANIZADEH, R. J. S. W. G. G. & GEORGE, F. P. (eds.) *Developments in Water Science.* Elsevier.
11. ABBASPOUR, K. C., SCHULIN, R. & VAN GENUCHTEN, M. T. 2001. Estimating unsaturated soil hydraulic parameters using ant colony optimization. *Advances in Water Resources,* 24**,** 827-841.
12. AL-RAOUSH, R. & PAPADOPOULOS, A. 2010. Representative elementary volume analysis of porous media using X-ray computed tomography. *Powder Technology,* 200**,** 69-77.
13. ANGELAKI, A., SAKELLARIOU-MAKRANTONAKI, M. & TZIMOPOULOS, C. 2004. Laboratory Experiments and Estimation of Cumulative Infiltration and Sorptivity. *Water, Air, & Soil Pollution: Focus,* 4**,** 241-251.
14. ARAMPATZIS, G., TZIMOPOULOS, C., SAKELLARIOU-MAKRANTONAKI, M. & YANNOPOULOS, S. 2001. Estimation of unsaturated f ow in layered soils with the f nite control volume method. *Irrigation and Drainage,* 50**,** 349-358.

15. BAILLY, D., ABABOU, R. & QUINTARD, M. 2009. Geometric characterization, hydraulic behavior and upscaling of 3D fissured geologic media. *Mathematics and Computers in Simulation,* 79**,** 3385-3396.
16. BAIRD, A. J. & HORN, D. P. 1996. Monitoring and Modelling Groundwater Behaviour in Sandy Beaches. *Journal of Coastal Research,* 12**,** 630-640.
17. BAIRD, A. J., MASON, T. & HORN, D. P. 1998. Validation of a Boussinesq model of beach ground water behaviour. *Marine Geology,* 148**,** 55-69.
18. BEAR, J. 1972. *Dynamics of Fluids in Porous Media*, American Elsevier Publishing Company, Inc.
19. BOUTT, D. F. 2010. Poroelastic Loading of an Aquifer Due to Upstream Dam Releases. *Ground Water,* 48**,** 580-592.
20. CAPLAIN, B. 2011. *Étude expérimentale de l'érosion d'un massif de sable cohésif par une houle monochromatique.* PhD Thesis, Institut National Polytechnique de Toulouse (INPT).
21. CARTWRIGHT, N., NIELSEN, P. & LI, L. 2004. Experimental observations of watertable waves in an unconfined aquifer with a sloping boundary. *Advances in Water Resources,* 27**,** 991-1004.
22. CARTWRIGHT, N., NIELSEN, P. & PERROCHET, P. 2005. Influence of capillarity on a simple harmonic oscillating water table: Sand column experiments and modeling. *Water Resour. Res.,* 41**,** W08416.
23. CHEN, H. & PINDER, G. 2011. Investigation of Groundwater Contaminant Discharge into Tidally influenced Surface-water Bodies: Theoretical Analysis. *Transport in Porous Media,* 89**,** 289-306.
24. CHIPPERFIELD, A. J. 1995. The MATLAB Genetic Algorithm Toolbox. *IEE Colloquium on Applied Control Techniques Using MATLAB.*
25. DAGAN, G. 1967. Second-order theory of shallow free-surface flow in porous media. *The Quarterly Journal of Mechanics and Applied Mathematics,* 20**,** 517-526.
26. DIETRICH, P., HELMIG, R., SAUTER, M., HÖTZL, H., KÖNGETER, J. & TEUTSCH, G. (eds.) 2005. *Flow and transport in fractured porous media*: Springer Berlin Heidelberg New York.
27. FREDLUND, D. G. & XING, A. 1994. Equations for the soil-water characteristic'curve. *Canadian Geotechnical Journal,* 31**,** 521-532
28. FREEZE, R. A. & CHERRY, J. A. 1979. *Groundwater*, Prentice Hall Inc., Englewood Cliffs.
29. FROST, J. D. 1989. *Studies on the Monotonic and Cyclic Behavior of Sands.* Ph.D. Dissertation, Purdue University.
30. FUENTES, C., HAVERKAMP, R. & PARLANGE, J.-Y. 1992. Parameter constraints on closed-form soilwater relationships. *Journal of Hydrology,* 134**,** 117-142.
31. GALLAGHER, K. & SAMBRIDGE, M. 1994. Genetic algorithms: a powerful tool for large-scale nonlinear optimization problems. *Comput. Geosci.,* 20**,** 1229-1236.

32. GAU, H., HSIEH, C. & LIU, C. 2006. Application of grey correlation method to evaluate potential groundwater recharge sites. *Stochastic Environmental Research and Risk Assessment,* 20**,** 407-421.
33. GENUCHTEN, M. T. V., LEIJ, F. J. & YATES, S. R. 1991. The RETC code for quantifying the hydraulic functions of unsaturated soils. Riverside, California: U.S. Department of Agriculture, Agricultural Research Service.
34. GRANT, U. S. 1948. Influence of the water table on beach aggradation and degradation. *Journal of Marine Research Volume,* 7**,** 655-660
35. GREEN, W. H. & AMPT, G. A. 1911. Studies on Soil Phyics. *The Journal of Agricultural Science,* 4**,** 1-24.
36. HANSON, B. & ORLOFF, S. 1998. Measuring Soil Moisture.
37. HINZ, C. 1998. Analysis of unsaturated/saturated water flow near a fluctuating water table. *Journal of Contaminant Hydrology,* 33**,** 59-80.
38. HODNETT, M. G. & TOMASELLA, J. 2002. Marked differences between van Genuchten soil water-retention parameters for temperate and tropical soils: a new water-retention pedo-transfer functions developed for tropical soils. *Geoderma,* 108**,** 155-180.
39. HOLLAND, J. H. 1975. *Adaptation in natural and artificial systems : an introductory analysis with applications to biology, control, and artificial intelligence,* Ann Arbor, University of Michigan Press.
40. HORN, D. P. 2006. Measurements and modelling of beach groundwater flow in the swash-zone: a review. *Continental Shelf Research,* 26**,** 622-652.
41. HORTON, R. E. 1940. An approach toward a physical interpretation of infiltration capacity. *Soil Science Society of America Proceedings,* 5**,** 399-417.
42. INES, A. V. M. & DROOGERS, P. 1999. Inverse modelling in estimating soil hydraulic functions: a Genetic Algorithm approach. *Hydrol. Earth Syst. Sci.,* 6**,** 49-66.
43. JENG, D. S., SEYMOUR, B. R., BARRY, D. A., PARLANGE, J. Y., LOCKINGTON, D. A. & LI, L. 2005a. Steepness expansion for free surface flows in coastal aquifers. *Journal of Hydrology,* 309**,** 85-92.
44. JENG, D. S., TEO, H. T., BARRY, D. A. & LI, L. 2005b. Two-Dimensional Approximation for Tidal Dynamics in Coastal Aquifers: Capillarity Correction. *Journal of Engineering Mechanics,* 131**,** 534-541.
45. KACIMOV, A. & ABDALLA, O. 2010. Water table response to a tidal agitation in a coastal aquifer: The Meyer–Polubarinova-Kochina theory revisited. *Journal of Hydrology,* 392**,** 96-104.
46. KANG, H.-Y. & NIELSEN, P. 1996. WATERTABLE DYNAMICS IN COASTAL AREAS. *Proceedings of the International Conference on Coastal Engineering; No 25 (1996): Proceedings of 25th Conference on Coastal Engineering, Orlando, Florida, 1996.*

47. LANYON, J. A., ELIOT, I. G. & CLARKE, D. J. 1982. Groundwater-level variation during semidiurnal spring tidal cycles on a sandy beach. *Marine and Freshwater Research,* 33**,** 377-400.
48. LEONG, E. C. & RAHARDJO, H. 1997. Review of Soil-Water Characteristic Curve Equations. *Journal of Geotechnical and Geoenvironmental Engineering,* 123**,** 1106-1117.
49. LEVASSEUR, S., MALÉCOT, Y., BOULON, M. & FLAVIGNY, E. 2008. Soil parameter identification using a genetic algorithm. *International Journal for Numerical and Analytical Methods in Geomechanics,* 32**,** 189-213.
50. LI, L., BARRY, D. A., PARLANGE, J. Y. & PATTIARATCHI, C. B. 1997a. Beach water table fluctuations due to wave run-up: Capillarity effects. *Water Resour. Res.,* 33**,** 935-945.
51. LI, L., BARRY, D. A. & PATTIARATCHI, C. B. 1997b. Numerical modelling of tide-induced beach water table fluctuations. *Coastal Engineering,* 30**,** 105-123.
52. LI, L., BARRY, D. A., STAGNITTI, F. & PARLANGE, J. Y. 2000a. Groundwater waves in a coastal aquifer: A new governing equation including vertical effects and capillarity. *Water Resour. Res.,* 36**,** 411-420.
53. LI, L., BARRY, D. A., STAGNITTI, F., PARLANGE, J. Y. & JENG, D. S. 2000b. Beach water table fluctuations due to spring–neap tides: moving boundary effects. *Advances in Water Resources,* 23**,** 817-824.
54. LU, N. & LIKOS, W. J. 2004. *Unsaturated soil mechanics*, John Wiley & Sons, Inc., Hoboken, New Jersey.
55. MAHINTHAKUMAR, G. & SAYEED, M. 2005. Hybrid Genetic Algorithm---Local Search Methods for Solving Groundwater Source Identification Inverse Problems. *Journal of Water Resources Planning and Management,* 131**,** 45-57.
56. MILLER, C. T., ABHISHEK, C. & FARTHING, M. W. 2006. A spatially and temporally adaptive solution of Richards' equation. *Advances in Water Resources,* 29**,** 525-545.
57. NIELSEN, P. 1990. Tidal dynamics of the water table in beaches. *Water Resour. Res.,* 26**,** 2127-2134.
58. NIELSEN, P., ASEERVATHAM, R., FENTON, J. D. & PERROCHET, P. 1997. Groundwater waves in aquifers of intermediate depths. *Advances in Water Resources,* 20**,** 37-43.
59. NIELSEN, P. & PERROCHET, P. 2000a. Watertable dynamics under capillary fringes: experiments and modelling. *Advances in Water Resources,* 23**,** 503-515.
60. NIELSEN, P. & PERROCHET, P. 2000b. Watertable dynamics under capillary fringes: experiments and modelling [Advances in Water Resources 23 (2000) 503–515]. *Advances in Water Resources,* 23**,** 907-908.
61. NIELSEN, P. & TURNER, I. L. Year. Groundwater Waves and Water Exchange in Beaches. *In:* EDGE, B. L., ed., 2000 Sydney, Australia. ASCE, 184-184.

62. NIELSEN, P. 1999. Groundwater Dynamics and Salinity in Coastal Barriers. *Journal of Coastal Research* , 15, 732-740.
63. NOBORIO, K. 2001. Measurement of soil water content and electrical conductivity by time domain reflectometry: a review. *Computers and Electronics in Agriculture,* 31**,** 213-237.
64. ORESKES, N., SHRADER-FRECHETTE, K. & BELITZ, K. 1994. Verification, Validation, and Confirmation of Numerical Models in the Earth Sciences. *Science,* 263**,** 641-646.
65. PARLANGE, J.-Y. 1975. On solving the flow equation in unsaturated soils by optimization: Horizontal infiltration. *Soil Sci. Soc. Am. Proc.,* 39**,** 415-418.
66. PARLANGE, J.-Y., STAGNITTI, F., STARR, J. L. & BRADDOCK, R. D. 1984. Free-surface flow in porous media and periodic solution of the shallow-flow approximation. *Journal of Hydrology,* 70**,** 251–263.
67. PARLANGE, J. Y. & BRUTSAERT, W. 1987. A capillarity correction for free surface flow of groundwater. *Water Resour. Res.,* 23**,** 805-808.
68. PHILIP, J. R. 1957. The theory of infiltration: 1. The Infiltration equation and its solution. *Soil Science Society of America Journal,* Vol. 83**,** pp. 435-448.
69. PHILIP, J. R. 1969. The theory of inf ltration. *Adv. Hydrosci,* 5**,** 215-296.
70. PHILIP, J. R. 1973. Periodic Nonlinear Diffusion: An Integral Relation and its Physical Consequences. *Australian Journal of Physics,* 26**,** 513-520.
71. RAUBENHEIMER, B., GUZA, R. T. & ELGAR, S. 1999. Tidal water table fluctuations in a sandy ocean beach. *Water Resour. Res.,* 35**,** 2313-2320.
72. REINSON, J. R., FREDLUND, D. G. & WILSON, G. W. 2005. Unsaturated flow in coarse porous media. *Can. Geotech. J.,* 42**,** 252–262
73. RICHARDS, L. A. 1931. Capillary conduction of liquids through porous mediums. *Physics,* 1**,** 318-333.
74. ROBERTS, M., TREFRY, M., FOWKES, N., BASSOM, A. & ABBOTT, P. 2011. Water-table response to tidal forcing at sloping beaches. *Journal of Engineering Mathematics,* 69**,** 291-311.
75. SILLERS, W. S., FREDLUND, D. G. & ZAKERZAHEH, N. 2001. Mathematical attributes of some soil–water characteristic curve models. *Geotechnical and Geological Engineering,* 19**,** 243-283.
76. SONG, Z., LI, L., KONG, J. & ZHANG, H. 2007. A new analytical solution of tidal water table fluctuations in a coastal unconfined aquifer. *Journal of Hydrology,* 340**,** 256-260.
77. STOJSAVLJEVIC, J. D., JENG, D. S., SEYMOUR, B. R. & POKRAJAC, D. 2012. Higher Order Analytical Solutions of Water Table Fluctuations in Coastal Aquifers. *Ground Water,* 50**,** 301-307.
78. SUN, J., LI, J., LIU, Q. & ZHANG, H. 2011. Approximate Engineering Solution for Predicting Groundwater Table Variation During Reservoir Drawdown on the Basis of the Boussinesq Equation. *Journal of Hydrologic Engineering,* 16**,** 791-797.

79. TEO, H. T., JENG, D. S., SEYMOUR, B. R., BARRY, D. A. & LI, L. 2003. A new analytical solution for water table fluctuations in coastal aquifers with sloping beaches. *Advances in Water Resources,* 26**,** 1239-1247.
80. TOPP, G. C., DAVIS, J. L. & ANNAN, A. P. 1980. Electromagnetic determination of soil water content: Measurements in coaxial transmission lines. *Water Resour. Res.,* 16**,** 574-582.
81. TRÉGAROT, G. 2000. *Modélisation couplée des écoulements à saturation variable avec hétérogénéités, forcages et interfaces hydrologiques.* PhD Thesis, Institut National Polytechnique de Toulouse (INPT).
82. TURNER, I. 1993a. The Total Water Content of Sandy Beaches. *Journal of Coastal Research***,** 11-26.
83. TURNER, I. 1993b. Water table outcropping on macro-tidal beaches: A simulation model. *Marine Geology,* 115**,** 227-238.
84. TURNER, I. L., COATES, B. P. & ACWORTH, R. I. 1997. Tides, Waves and the Super-elevation of Groundwater at the Coast. *Journal of Coastal Research,* 13**,** 46-60.
85. VALIANTZAS, J. D. 2010. New linearized two-parameter infiltration equation for direct determination of conductivity and sorptivity. *Journal of Hydrology,* 384**,** 1-13.
86. VAN GENUCHTEN, M. T. 1980. A closed-form equation for predicting the hydraulic conductivity of unsaturated soils. *Soil Science Society of America Journal,* 44(5)**,** 892-898.
87. VAUCLIN, M., HAVERKAMP, R. & VACHAUD, G. 1979. *Résolution numérique d'une équation de diffusion non linéaire. Application à l'infiltration de l'eau dans les sols non saturés.*, Presses Universitaires de Grenoble, France.
88. WANG, Y. 2010. *Experimental and Numerical Study of Hydrodynamic Oscillations in Partially Saturated Porous Media* PhD Thesis, Institut National Polytechnique de Toulouse (INPT).
89. WANG Y., ABABOU, R. & MARCOUX, M. 2008. Oscillatory Flows and Wave Propagation in Porous Media : Partially Saturated Free Surface Hydraulics. *IAHR International Groundwater Symposium* Istanbul, Turkey.
90. WERNER, A. D. & LOCKINGTON, D. A. 2003. Influence of hysteresis on tidal capillary fringe dynamics in a well-sorted sand. *Advances in Water Resources,* 26**,** 1199-1204.
91. WMO 2008. Guide to Meteorological Instruments and Methods of Observation. *In:* ORGANIZATION, W. M. (ed.) Seventh edition ed.
92. XIA, Y.-Q., LI, H.-L. & BOUFADEL, M. C. 2010. A new perturbation solution of groundwater table fluctuations in tidal beaches. *Journal of Hydrodynamics, Ser. B,* 22**,** 55-60.
93. ZHU, Y. 2007. *Modeling spatial and temporal variations of surface moisture content and groundwater table fluctuations on a fine-grained beach, padre island, texas.* PhD, Louisiana State University.

Appendices

Appendix A

The Effect of Acceleration

A.1 Introduction

In this appendix, the effect of the acceleration are discussed, or in other words do we need to add other acceleration terms to our mathematical model that based only on Darcy's equation.

A.2 From Navier-Stokes equation to Darcy's equation:

This section is based on personal communication with R. ABABOU 2012.

Let us start by Navier-Stokes momentum equation:

$$\rho_0 \frac{\partial \vec{V}}{\partial t} + \rho_0 (\vec{V} \cdot \nabla)\vec{V} = -(\vec{\nabla} p + \rho_0 g \vec{\nabla} z) + \mu \nabla^2 \vec{V} \qquad \textbf{Eq. A.1}$$

Where ρ_0 is the density of water, $\vec{V}$ is the average velocity, p is the pressure, g is the gravity acceleration and μ is the dynamic viscosity

The first two terms of the left hand side presents the Eulerian and inertial accelerations respectively.

Moreover, the viscous dissipation term on the right-hand side ($\mu\nabla^2\vec{V}$) becomes proportional to $\vec{V}$ upon averaging over many pores, and therefore we can write:

$$\mu\nabla^2\vec{V} = -\mu\frac{\phi\vec{V}}{k} \qquad \textbf{Eq. A.2}$$

Where ϕ is porosity (which will be considered here as the saturated water content θ) and k is the permeability [m^2] and it is related to the hydraulic conductivity by $K = k\rho g/\mu$ and . Note also that the microscopic velocity ($\vec{V}$) is related to the macroscopic flux density ($\vec{q}$) through $\vec{q} = \theta\vec{V}$.

Now using the above relations and neglecting all types of acceleration in the original Navier-Stokes equation, we obtain Darcy's equation as follows:

$$\vec{q} = -\frac{k}{\mu}\left(\vec{\nabla}p + \rho_0 g\vec{\nabla}z\right) \qquad \textbf{Eq. A.3}$$

or in the form of head:

$$\vec{q} = -K\vec{\nabla}(h+z) = -K\vec{\nabla}H \qquad \textbf{Eq. A.4}$$

where h is the pressure head [m] and H is the total head [m].

Now let us return to the starting question of the acceleration effects.

A.3 Analysis of the Eulerian acceleration under oscillatory flows:

To consider the Eulerian acceleration ($\partial\vec{q}/\partial t$) only, we will neglect the inertial effect ($\rho_0\left(\vec{V}\cdot\nabla\right)\vec{V}$) from the Navier-Stokes equation, therefore after arranging the equation we get:

$$\frac{1}{\theta g}\frac{\partial\vec{q}}{\partial t} + \frac{1}{K}\vec{q} = -\vec{\nabla}H \qquad \textbf{Eq. A.5}$$

And assume also for simplicity that the medium is fully saturated ($K = K_S\,; \theta = \theta_S\,; h \geq 0$), and let us named the hydraulic gradient as $J = -\vec{\nabla}H$.

By Fourrier analysis in the frequency space, we have:

$$q(z,t) = \hat{q}(z,\omega)e^{i\omega t} \qquad \textbf{Eq. A.6}$$

and

$$J(z,t) = \hat{J}(z,\omega)e^{i\omega t} \qquad \textbf{Eq. A.7}$$

Now Eq. A.5, Eq. A.6 and Eq. A.7 we obtain:

$$\frac{i\omega}{\theta_S g}\hat{q} + \frac{1}{K_S}\hat{q} = \hat{J} \qquad \textbf{Eq. A.8}$$

or

$$\hat{q}(\omega) = \frac{\hat{J}(\omega)\, K_S}{1 + \frac{i\omega K_S}{\theta_S g}} \qquad \textbf{Eq. A.9}$$

or

$$\hat{q}(\omega) = \hat{J}(\omega)\ K(\omega) \qquad \textbf{Eq. A.10}$$

where

$$K(\omega) = \frac{K_S}{1 + \frac{i\omega K_S}{\theta_S g}} \qquad \textbf{Eq. A.11}$$

Let us define $\Omega = (\omega K_S)/(\theta_S g)$ as a dimensionless frequency number; then this complex $K(\omega)$ have the following modulus and phase

$$|K(\omega)| = \frac{K_S}{\sqrt{1+\Omega^2}} \qquad \textbf{Eq. A.12}$$

$$\varphi(\omega) = \tan^{-1}(\Omega) = \tan^{-1}\left(\frac{\omega K_S}{\theta_S g}\right) \qquad \textbf{Eq. A.13}$$

We note that as $\Omega \to 0$, $|K(\omega)| \to K_S$ and $\varphi(\omega) \to 0$ and this is the case of no Eulerian acceleration effect.

Therefore, the key of this analysis is the dimensionless frequency number (Ω) which can be treated as the ratio between a characteristic time period ($T_{Char} = K_S/\{\theta_S g\}$) which depends on the porous medium only to the time period of the applied fluctuation (T_p):

$$\Omega = \frac{T_{Char}}{T_p} \quad and \quad T_{Char} = \frac{K_S}{\theta_S g} \qquad \textbf{Eq. A.14}$$

Therefore $\Omega \to 0$ when either $T_p \gg T_{Char}$.

By applying this analysis to our calibrated SilicaSand with:

$K_S = 3.23 \times 10^{-4}$ m/s

$\theta_S = 0.38$ m^3/m^3

We obtain T_{Char}= 8.6778e-005 s. This value is very small with respect to both:

- the smallest T_p applied in the numerical parametric study (1s).
- the smallest T_p applied in the experimental study (about 600s).

Therefore we can conclude that in our study the Eulerian acceleration ($\partial\vec{q}/\partial t$) can be neglected.

Note that (Polubarinova, 1962) proposed a similar analysis and concluded also, based on T_{Char}, that $\partial\vec{q}/\partial t$ was negligible for her applications.

A.4 Analysis of the inertial acceleration:

This section is focused on the effect of inertial acceleration [the second term in the left-hand side of the Navier-Stokes equation, $(\vec{V}\cdot\nabla)\vec{V}$], this term can be written as follows (Ward-Forchheimer):

$$(\vec{V}\cdot\nabla)\vec{V} = C_1 \frac{\vec{V}.\|\vec{V}\|}{\sqrt{k/\theta}} \qquad \textbf{Eq. A.15}$$

By substituting this equation in the Navier-Stokes equation and also neglecting the Eulerian acceleration, we obtained:

$$\rho_0 C_1 \frac{\vec{V}.\|\vec{V}\|}{\sqrt{k/\theta}} = -(\vec{\nabla}p + \rho_0 g\vec{\nabla}z) - \mu\frac{\phi\vec{V}}{k} \qquad \textbf{Eq. A.16}$$

Or in terms of the flux density ($\vec{q}$):

$$\rho_0 C_1 \frac{\vec{q}.\|\vec{q}\|}{\theta^{3/2}\sqrt{k}} = -\left(\vec{\nabla}p + \rho_0 g\vec{\nabla}z\right) - \mu\frac{\vec{q}}{k} \qquad \textbf{Eq. A.17}$$

By rearranging the above equation, then we obtained the following expression of the Darcy-Ward-Forchheimer head loss law:

$$\left(1 + C\frac{\rho_0}{\mu}\sqrt{k}\,\|\vec{q}\|\right)\vec{q} = -\left(\vec{\nabla}p + \rho_0 g\vec{\nabla}z\right) \qquad \textbf{Eq. A.18}$$

where ($C = C_1/\theta^{3/2} \sim 1$) is the constant of Ergun (dimensionless); and

$$Re = C\frac{\rho_0}{\mu}\sqrt{k}\,\|\vec{q}\| = C\sqrt{\frac{\rho_0 K_S}{\mu g}}\,\|\vec{q}\| \qquad \textbf{Eq. A.19}$$

is the Reynolds-Darcy Number

Note that if $Re \ll 1$ then Eq. A.18 becomes Darcy's law and the inertial effect can be neglected.

By applying this analysis to our calibrated "SilicaSand" with:

$K_S = 3.23 \times 10^{-4}$ m/s

$\nu = \mu/\rho_0 = 10^{-6}$ m^2/s

then $Re = 5.7\,\|\vec{q}\|$

and note for all our simulations $\|\vec{q}\| < K_S$, therefore $Re \ll 1$ and the inertial effects can be neglected in our study.

A.5 References:

1. Theory of Ground Water Movement. P. Ya. Polubarinova-Kochina. Translated from the Russian edition by J. M. Roger de Wiest. Princeton University Press, Princeton, N.J., 1962.

Appendix B

Experiment versus Analytical Model (Complex Effective Porosity)

B.1 Introduction

The objective of this appendix is to compare our experimental study (presented in Chapter 6) to the model based on the complex effective porosity concept described in the following two articles:

- NIELSEN, P. & PERROCHET, P. 2000a. Watertable dynamics under capillary fringes: experiments and modelling. *Advances in Water Resources,* 23**,** 503-515.
- CARTWRIGHT, N., NIELSEN, P. & PERROCHET, P. 2005. Influence of capillarity on a simple harmonic oscillating water table: Sand column experiments and modeling. *Water Resour. Res.,* 41**,** W08416.

B.2 Complex effective porosity

Nielsen and Perrochet (Nielsen and Perrochet, 2000a, Nielsen and Perrochet, 2000b) introduced the concept of a complex effective porosity which describes the relationship between periodic fluctuations in the equivalent saturated height of total moisture (the sum of the water table height and the equivalent thickness of the capillary fringe) and those fluctuations of the water table height only. The complex effective porosity is defined by:

$$n_\omega \frac{dZ_S}{dt} = n \frac{dh_{tot}}{dt} \qquad \textbf{Eq. B.1}$$

where n_ω is the complex effective porosity; $n = \theta_s - \theta_r$ is the effective porosity; θ_s is the saturated water content; θ_r is the residual water content; Z_S is the water table height; $h_{tot}(t) = Z_S(t) + h_c(t)$ is the equivalent saturated height of total moisture; Z_S is the water table height; h_c is the equivalent thickness of the capillary fringe.

(Cartwright et al., 2004) stated that: "n_ω is complex in nature so as to mathematically account for the fact that fluctuations in the total moisture (h_{tot}) are both damped and lag those in the water table (Z_S). These two processes are accounted for by $|n_\omega|$ and Arg$\{n_\omega\}$ respectively". (Cartwright et al., 2005) found experimentally a definitive dependence of the effective porosity on $\omega\lambda_{Cap}/K_S$. They recommend the following expression for n_ω which obtained by an empirical curve fit to their experimental data:

$$n_\omega = \frac{n}{1 + 2.5\left(i\frac{n\omega\lambda_{Cap}}{K_S}\right)^{2/3}} \qquad \textbf{Eq. B.2}$$

They noted also that the form of this equation is similar but still clearly different from the model that they derived based on Green-Ampt approximation (linearized 1st order perturbation of Green-Ampt):

$$n_\omega = \frac{n}{1 + i\frac{n\omega\lambda_{Cap}}{K_S}} \qquad \textbf{Eq. B.3}$$

where λ_{Cap} is afixed parameter, similar to the classical Green-Ampt front suction (ψ_F).

Moreover, (Nielsen and Perrochet, 2000a) derived a differential equation for the water table height which is obtained from Darcy's law and mass conservation :

$$n\frac{dh_{tot}}{dt} = K_S\frac{h_0(t) - Z_S(t)}{Z_S(t)} \qquad \textbf{Eq. B.4}$$

or equivalently using the concept of the complex effective porosity:

$$n_\omega\frac{dZ_S}{dt} = K_S\frac{h_0(t) - Z_S(t)}{Z_S(t)} \qquad \textbf{Eq. B.5}$$

For small amplitude oscilation ($A_s \ll \overline{h_0}$), the above equation can be linearised as follows:

$$n_\omega\frac{dA_S}{dt} = \frac{K_S}{\overline{h_0}}(A_0(t) - A_S(t)) \qquad \textbf{Eq. B.6}$$

Where A_S is the amplitude of the water table; A_0 is the amplitude of the bottom forcing and $\overline{h_0}$ is the bottom forcing timde average.

Eq. B.6 with simple harmonic forcing has the following frequency response function:

$$F(\omega) = \frac{1}{1 + i\left(\omega n_\omega\overline{h_0}/K_S\right)} \qquad \textbf{Eq. B.7}$$

corresponding to the amplitude ratio:

$$|F(\omega)| = \frac{A_s}{A_0} = \frac{1}{\sqrt{1 + (\omega n_\omega\overline{h_0}/K_S)^2}} \qquad \textbf{Eq. B.8}$$

And phase lag for the water table relative to the bottom forcing:

$$\phi_S = tan^{-1}(\omega n_\omega\overline{h_0}/K_S) \qquad \textbf{Eq. B.9}$$

(Nielsen and Perrochet, 2000a) in their Appendix (B) derived also a weakly non-linear solution through a perturbation technique; this solution indicates that the mean of the water table height ($\overline{Z_S}$) will be below the mean of the bottom forcing ($\overline{h_0}$) by an underelevation $\Delta\overline{Z_S}$ ($\overline{\eta_2}$ in their notation) given by:

$$\Delta\overline{Z_S} = \frac{A_S^2}{2\overline{h_0}}n_I\frac{\omega\overline{h_0}}{K_S} \qquad \textbf{Eq. B.10}$$

B.3 Comparison between our experimental results and the analytical models of Nielsen et al.:

In this section, the experimental results of the water table amplitude and phase lag were compared to the analytical results of : the Green-Ampt model (Eq. B.3) and the complex effective porosity model (Eq. B.2) as shown in **Fig. B.1** and **Fig. B.2**.

From thses two figures it is obsereved that:

- the Green-Ampt model (red curves) failed to match the experimental results especially in the comparison of the phase lag.
- the complex effective porosity model follows the the same trend as the experimental results for both amplitude ratio and phase lag. The discrepancy between the complex effective porosity model and the experimental results may be related to the fact that our experimental sand (SilicaSand) do not match greatly the empirical fit done by (Cartwright et al., 2005) and also to simplification of the linearized solution.

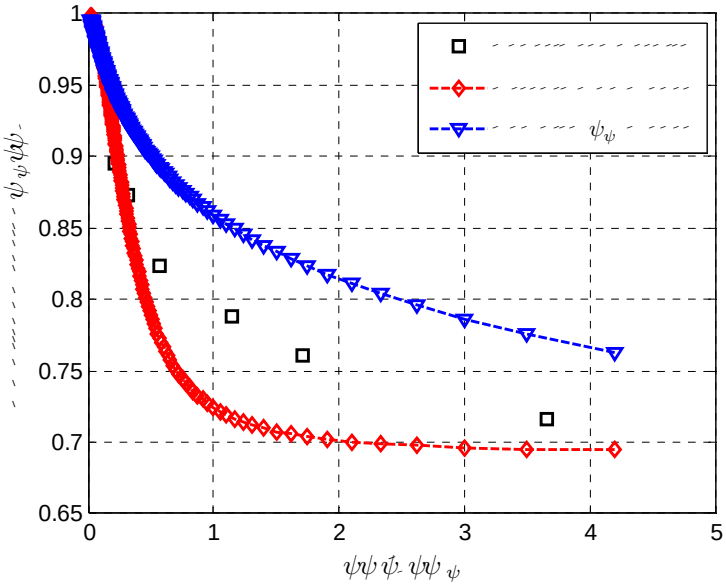

Fig. B.1: Amplitude ratios (A_s/A_0) of the water table and the bottom forcing versus a dimensionless frequency ($n\omega\overline{h_0}/K_s$).

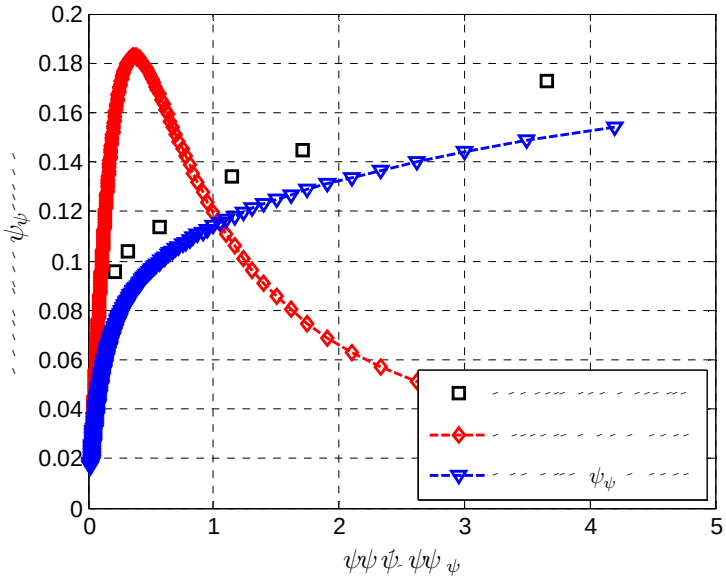

Fig. B.2: Water table phase lag (ϕ_s) relative the bottom forcing versus a dimensionless frequency ($n\omega\overline{h_0}/K_S$).

We also compared the under-elevation ($\Delta\overline{Z_S}$) of the mean water table relative to the mean bottom forcing observed experimentally to the under-elevation calculated from Eq. B.10. The comparison was shown in **Fig. B.3**.

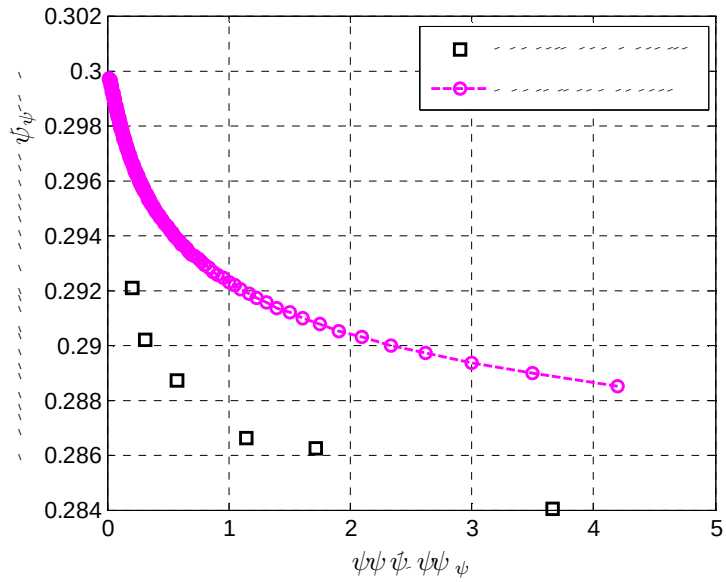

Fig. B.3: The under-elevation ($\Delta\overline{Z_S}$) of the mean water table relative to the mean bottom forcing versus a dimensionless frequency ($n\omega\overline{h_0}/K_S$).

B.4 References:

1. CARTWRIGHT, N., NIELSEN, P. & LI, L. 2004. Experimental observations of watertable waves in an unconfined aquifer with a sloping boundary. *Advances in Water Resources,* 27**,** 991-1004.
2. CARTWRIGHT, N., NIELSEN, P. & PERROCHET, P. 2005. Influence of capillarity on a simple harmonic oscillating water table: Sand column experiments and modeling. *Water Resour. Res.,* 41**,** W08416.
3. NIELSEN, P. & PERROCHET, P. 2000a. Watertable dynamics under capillary fringes: experiments and modelling. *Advances in Water Resources,* 23**,** 503-515.
4. NIELSEN, P. & PERROCHET, P. 2000b. Watertable dynamics under capillary fringes: experiments and modelling [Advances in Water Resources 23 (2000) 503–515]. *Advances in Water Resources,* 23**,** 907-908.

Appendix C

Preliminary Optical Measurement of the Water Contents $[\theta(z,t)]$ using CCD camera

C.1 Introduction

The objective of this appendix is to present preliminary results of the optical measurement of the water content using CCD camera.

The CCD camera is used to get a series of images during the experimental study of the oscillatory flow through the partially saturated/ unsaturated porous column. The calibration process of these images includes two main stages:

- Optical calibration: which includes image correction in order to eliminate the effect of the light environment on the images and also to normalized the gray scale of the image series.
- Gray level versus water content calibration: in this stage the normilized gray scale are transformed into an equivelent water content through a calibration model.

The first calibration stage was done for all optical measurements; however, we are currently looking for a suitable gray scale versus water content calibration model and we have identified several possible models in the literature (work in progress).

C.2 Sample of the optical measurement results:

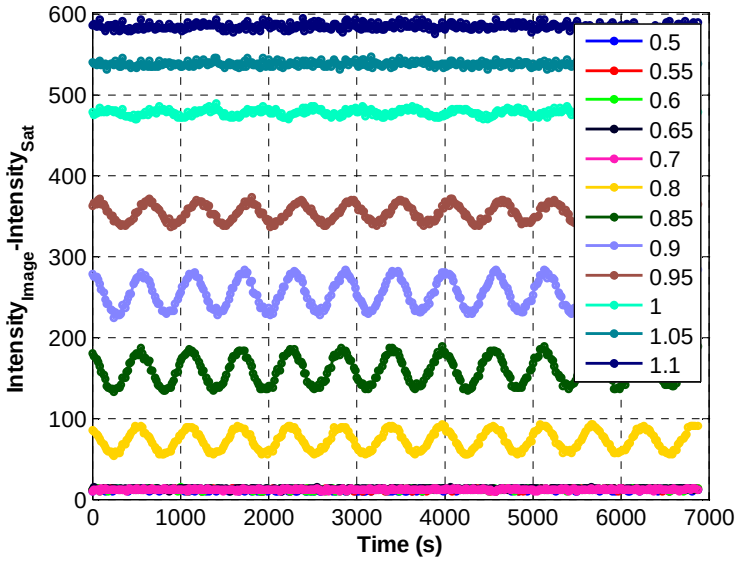

Fig. C.1: The evolution of the gray scale level at different elevations along the column. The parameters of the bottom forcing are: A_0 = 0.15 m, $\overline{h_0}$ = 0.5 m, $\boldsymbol{T_P}$ **=10min**

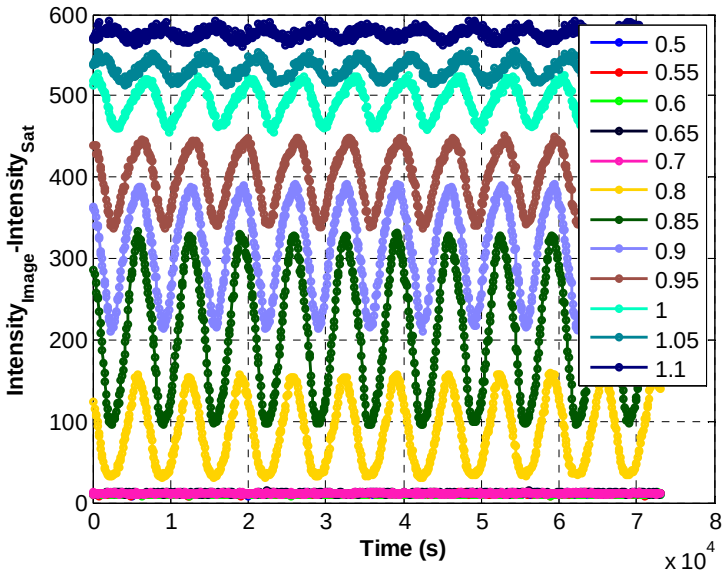

Fig. C.2: The evolution of the gray scale level at different elevations along the column. The parameters of the bottom forcing are: A_0 = 0.15 m, $\overline{h_0}$ = 0.5 m, $\boldsymbol{T_P}$ **=110min**

At least, a qualitative comparison can be inferred from the previous two figures as follows:

- As expected there are no gray scale fluctuations (or equivalently water content fluctuations) up to a level of 70 cm for the two cases.
- The water content fluctuations damped completely at a level of about 1.0 m for a bottom forcing period of T_P =10min; and to a level higher than 1.1 m for a bottom forcing period of T_P =110min. This observation was expected and confirmed also by the pressure measurement using the tensiometers.
- As the time period of the bottom forcing decreased (rapid fluctuations), the attenuation of the water content amplitude increased. This confirmed that the porous column acts as a low pass filter.

Appendix D

Partially Saturated Oscillatory Flow in a Sandy Beach (Numerical Modeling)

This appendix is a conference paper presented at "XVIII International Conference on Water Resources (CMWR), CIMNE, Barcelona, Spain, 21-24 June 2010":

Alastal K., Ababou R. and Astruc D. (2010): "Partially saturated oscillatory flow in a sandy beach (numerical modeling)". XVIII International Conference on Water Resources (CMWR), CIMNE, Barcelona 21-24 June 2010.

XVIII International Conference on Water Resources
CMWR 2010
J. Carrera (Ed)
CIMNE, Barcelona 2010

PARTIALLY SATURATED OSCILLATORY FLOW IN A SANDY BEACH (NUMERICAL MODELING)

Khalil ALASTAL, Rachid ABABOU and Dominique ASTRUC

Institut de Mécanique des Fluides de Toulouse (IMFT),
Allée du Professeur Camille Soula, 31400 Toulouse, France.
Email addresses: alastal@imft.fr, ababou@imft.fr, astruc@imft.fr.

Key words: Porous media, numerical modeling, partially saturated flow, Richards equation, free surface oscillations, sorptivity.

Summary. In this paper, numerical modeling of oscillatory flow in 1D porous column is developed, validated and interpreted in terms of space-time scales in order to assist in the design and interpretation of 1D and 2D laboratory experiment.

1 INTRODUCTION

Surface/subsurface flow interactions concern a wide range of applications, from beach morphodynamics (swash zone), to harbor engineering and hydrology (e.g., man-made structures such as porous dykes and earth dams).

In the context of beach dynamics, two types of periodic 'forcing' will be considered:

1. low frequency / long tidal waves (approximated as quasi-static reservoir oscillations);
2. high frequency / short waves (complex nonlinear surface wave dynamics, including: overspill, run up/run down processes, and erosion near the swash zone).

In this paper, oscillatory flow in the presence of a sandy beach is studied numerically using Richards's equation for unsaturated or partially saturated flow, with oscillatory pressure-based boundary conditions. With this in mind, the numerical simulations and analyses are currently being conducted as follows:

- Validation test for the numerical procedure through 1D infiltration problem.
- Analyses of sudden recharge and drainage on a 1D porous column.
- Analyses of forced oscillations in a partially saturated 1D column, and interpretation in terms of space-time scales. This will help in defining the appropriate scales for a more complex 2D slab experiment.

2 NUMERICAL MODELING USING BIGFLOW

The 3D finite volume flow code 'BIGFLOW' has been widely described, documented, tested and benchmarked[1,2,3]. The equational model of BIGFLOW is a generalized Darcy-type equation, with a mixed formulation of mass conservation, capable of simulating various types of flows within the same domain. It is of the form:

$$\begin{cases} \dfrac{\partial \theta(h,\vec{x})}{\partial t} = -\vec{\nabla} \bullet \vec{q} \\ \vec{q} = -\vec{\vec{K}}\left(h, \vec{\nabla} H, \vec{x}\right)\vec{\nabla} H \\ H = h + \vec{g}(\vec{x}) \bullet \vec{x} \end{cases} \tag{1}$$

where only the first equation is actually solved (after insertion of the second and third equations). The first equation expresses mass conservation with a known water retention curve $\theta(h)$; the second equation is a generalized nonlinear flux-gradient law with tensorial hydraulic conductivity/transmissivity (K); and the third equation is the relation between total head (H) and pressure head or water depth (h) via a normalized gravitational vector (g).

3 SOIL PARAMETERS & CHARACTERISTIC SPACE-TIME SCALES

In the case of 3D flow in partially saturated/unsaturated media, 'h' is the pressure head relative to atmospheric pressure [L], $K(h)$ is the unsaturated conductivity [LT^{-1}], and $\theta(h)$ is volumetric water content [L^3/L^3]. Two main functional models were considered in BIGFLOW 3D for the nonlinear curves: *Van Genuchten / Mualem (VGM)* and *Exponential (EXP)*. In this paper, VGM model is used. Other important relations can be derived from these properties such as[4]: moisture capacity $C(h)$; hydraulic diffusivity $D(h)$; gravitational speed $U(h)$; and capillary dispersion length $\lambda(h)$. The global capillary length scale of the soil can be defined via the point of maximum moisture capacity, i.e., the inflexion point of $\theta(h)$, which leads to[4]:

$$\lambda_{CAP} = \frac{1}{\alpha}\left(1 - \frac{1}{n}\right)^{1/n} \tag{2}$$

where "α" is the Van Genuchten pressure scaling parameter (inverse length units), and "n" is the Van Genuchten/Mualem exponent (dimensionless positive real number). The λ_{CAP} values obtained for the 3 soils considered in this work can be found in the Table 1 below. Finally, note that several characteristic time scales can be formed (gravitational, capillary,…): we use only one of them here, the time scale "t_{GRAV}", as explained immediately below (infiltration tests).

4 VALIDATION TESTS WITH CONTINUOUS UNSATURATED INFILTRATION

In this section, 1D continuous infiltration through a deep homogeneous soil is used to validate the numerical procedure, using the Van Genuchten/Mualem model in BIGFLOW 3D. The numerical results are compared with those of Philip's series solution, which was programmed in Matlab after the method of Vauclin et al.[5]. Permeability and sorptivity are identified from the numerical cumulative infiltration rate via an optimal fit procedure, and compared to the actual permeability and sorptivity (the latter is deduced from other parameters through Parlange's expression).

4.1 Theoretical background

Over the past years, numerous analytical and semi-empirical equations for 1D inf ltration have been developed[6]. Philip[7] has shown that a nonlinear solution can be obtained by a time expansion procedure in the case of a constant water content imposed at the surface. He derived the following series solution for the cumulative infiltration $I(t)$ [L] :

$$I(t) = St^{1/2} + (A_2 + K_0)t + A_3 t^{3/2} + A_4 t^2 + \cdots \tag{3}$$

where K_0 is the initial hydraulic conductivity [$L.T^{-1}$], t is time [T] , S is the sorptivity [$L.T^{-1/2}$]. The sorptivity 'S' and the A's depend on the initial (θ_0) and boundary (θ_1) conditions. Sorptivity characterizes the ability of the soil to absorb water by capillary diffusion (in the absence of gravity). In practice, it is sufficient to use the two-parameter equation of the form:

$$I(t) = St^{1/2} + At \tag{4}$$

One of the problems involved in Philip's solution is that the time series solution becomes divergent for large times no matter how many terms are developed. Thus the above solution is only valid for a limited time range. The time limit is mostly set at t_{GRAV} (a time for which the gravity forces are supposed to become predominant over the capillary forces):

$$t_{GRAV} = \left(\frac{S(\theta_1, \theta_0,)}{K_1 - K_0}\right)^2 \tag{5}$$

A different solution was proposed by Parlange[8] resulting in the following sorptivity expression:

$$S^2 = \int_{\theta_0}^{\theta_1} [\theta_1 + \theta - 2\theta_0] D(\theta) d\theta \tag{6}$$

where D is moisture diffusivity $D = K/C = K\ dh/d\theta$ [$L^2.T^{-1}$].

4.2 Validation test

A 1D column with the initial and boundary conditions shown in figure 1 is used for simulating the 1D infiltration problem in BIGFLOW code. Table 1 shows the hydraulic characteristics of the porous media used in the simulation.

Parameters		Soil No.1 Fine Sand	Soil No.2 Medium Sand	Soil No.3 Loam
K_{sat} (m/s)		2.7×10^{-4}	2.0×10^{-4}	3.66×10^{-6}
θ_{sat}		0.411	0.35	0.52
θ_{dry}		0.0073	0.0147	0.218
VGM model parameters	α (m^{-1})	5.85	11.47	1.15
	$1/\alpha$ (cm)	17.08	8.71	86.95
	λ_{CAP} (cm)	15.34	6.11	62.25
	n	3.32	1.98	2.03

Table 1: Hydraulic characteristics of porous media.

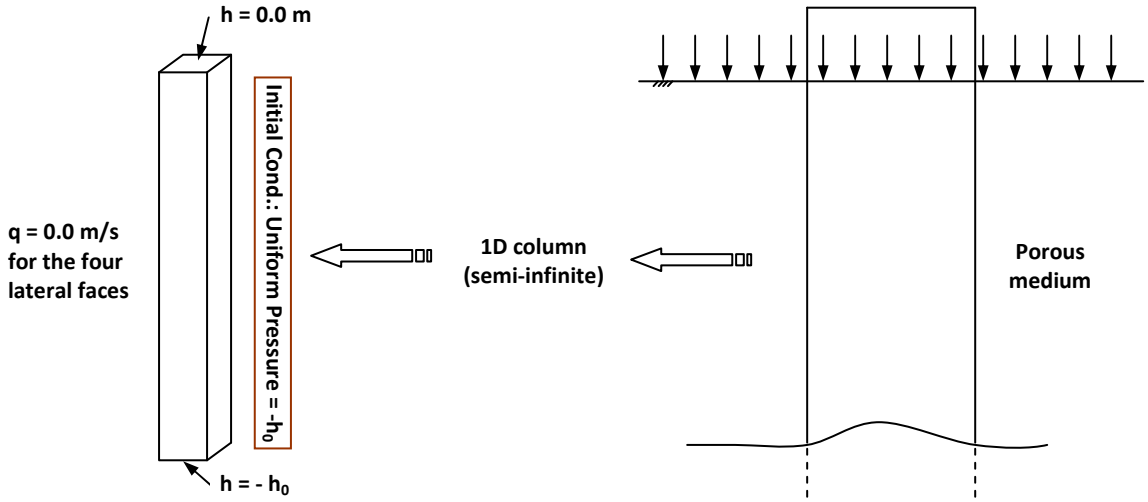

Figure 1: Initial and boundary conditions used in the infiltration test for the 3 soils.

4.3 Results and analysis

Simulation results of the infiltration test for soil No.1 (fine sand) are presented in figure 2. The y-intercept and the slope of $I/\sqrt{t}$ versus$\sqrt{t}$ curve give the *S* and *A* values (see equation 4). The maximum time of BIGFLOW simulation is about t_{GRAV}. A summary of the results for the three soils is given in Table 2.

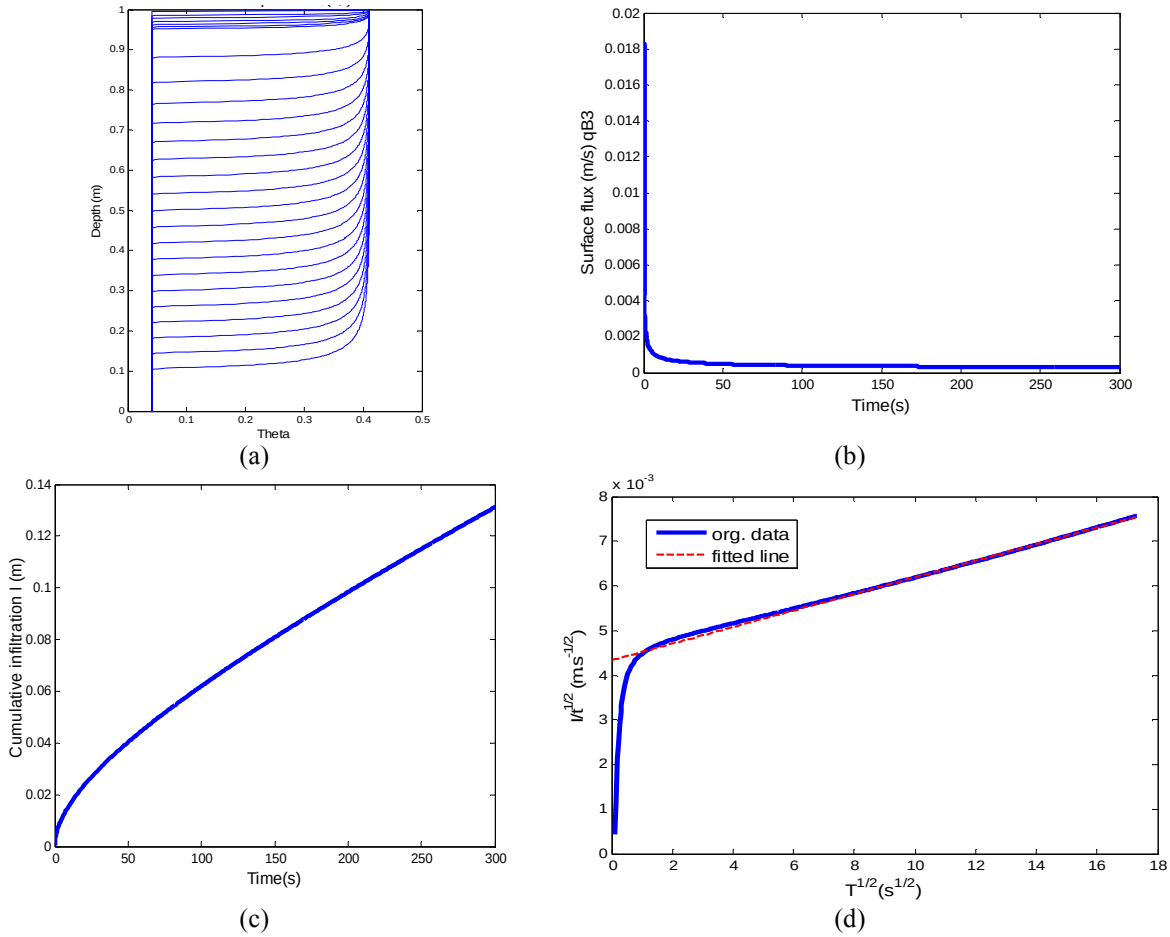

Figure 2: Bigflow results of the infiltration problem. (a) evolution of moisture profiles θ(z,t), (b) surface flux versus time, (c) Cumulative infiltration versus time, (d) $I/\sqrt{t}$ versus $\sqrt{t}$ including the fitting parameters.

Infiltration Parameters	Soil No.1 Fine Sand	Soil No.2 Medium Sand	Soil No.3 Loam
A (m/s)	1.686×10^{-4}	1.121×10^{-3}	1.762×10^{-6}
A/K_{sat} (%)	62.4	56.05	48.14
S, Sorptivity (m/$s^{1/2}$) BIGFLOW	4.48×10^{-3}	1.815×10^{-3}	8.712×10^{-4}
S, Sorptivity (m/$s^{1/2}$) Parlange	4.57×10^{-3}	1.908×10^{-3}	8.682×10^{-4}
S, Sorptivity (m/$s^{1/2}$) Philip/Vauclin	4.15×10^{-3}	1.898×10^{-3}	8.498×10^{-4}
t_{grav}, average (sec)	266	88	55643

Table 2: Infiltration parameters' results obtained from different methods.

By comparing the simulation results with those of Philip's and Parlange solutions, a good agreement is found in terms of sorptivity values. Note that the simulation results were analysed through an optimal fit procedure, providing that a very short initial phase of the simulated infiltration is removed (indeed the initial flux in this experiment is infinite in theory).

The results also show that for all cases: $1/3 < A/K_{SAT} < 2/3$ as mentioned in the literature[9].

5 NUMERICAL EXPERIMENTS & ANALYSES – UNSATURATED DYNAMICS

Numerical simulations are conducted with the BIGFLOW 3D code in a partially saturated 1D porous column under highly "dynamic" conditions. The following cases are studied: **(1)** sudden recharge and drainage processes; **(2)** forced periodic oscillations. In what follows, we present only the results for soil N°3 (Loam). In all simulations, suitable numerical parameters were chosen to obtain good numerical results in terms of mass balance (net boundary flux versus mass flux), and convergence of both nonlinear solver (Incremental Picard) and matrix solver (Preconditioned Conjugate Gradients with Diagonal Scaling).

5.1 Sudden recharge and sudden drainage:

A hydrostatic pressure is applied as an initial condition, with the free surface located at z = 0.5m (z is elevation from the bottom). A sudden recharge process is obtained by applying a constant pressure boundary condition at the bottom of the column (z = 0), with positive pressure "h_{BC}" greater than the initial hydrostatic pressure ($h_{BC} = h_{IN} + 0.10$ m). The resulting free surface at infinite time (steady state) should be located at z = 0.5 + 0.1 = 0.6 m. On the other hand, another numerical experiment is also conducted, this time for sudden drainage process. A bottom pressure condition is applied such that $h_{BC} = h_{IN} - 0.10$ m. The resulting free surface in the column should then descend from z = 0.5m initially to z = 0.5 - 0.1 = 0.4 m at infinite time (steady state). The maximum time of simulation is chosen to be $t_{MAX} = 10^5$sec ($t_{MAX} \approx 2t_{GRAV} \approx 1$day). Figure 3 shows the free surface position versus time for the two cases.

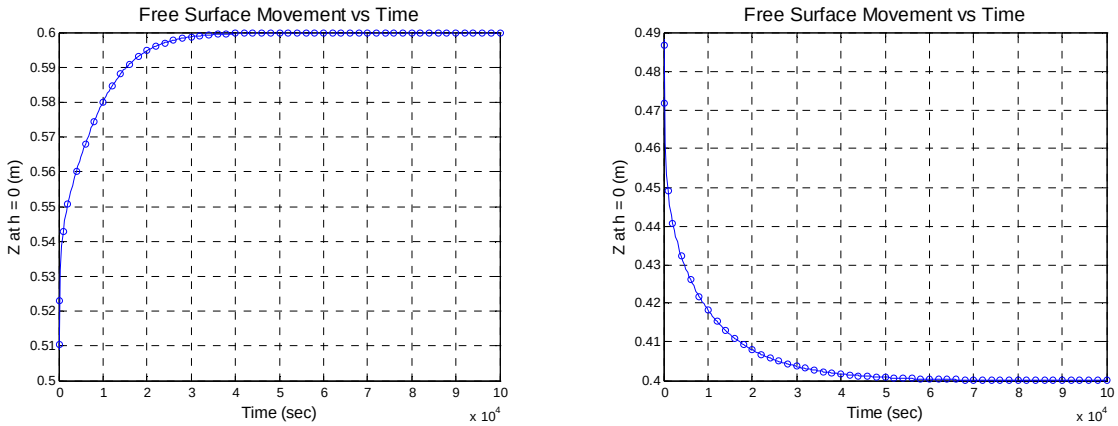

(a) (b)

Figure 3: Free surface position versus time for (a) sudden recharge, (b) sudden drainage.

The benefit of the above recharge and drainage simulations is that they provide information on the response time scale of the partially saturated soil column. This response time can then be used for selecting the appropriate periods for the case of periodic forcing, i.e., short waves

and long tidal waves, idealized by a periodic pressure condition applied at the bottom of the column.

Thus, in the case of forced oscillations, if the applied pressure wave has a quarter-period $T_p/4 = 0.5 \times 10^4$ sec and an amplitude of 0.10 m, then referring to the above recharge/drainage simulations, it is expected that this periodic wave will generate a free surface wave of about 0.06m amplitude (less than the amplitude 0.10m of the applied wave). Therefore this period corresponds to a "high frequency/short wave" type at least in terms of the hydrodynamic response of this soil. On the other hand, if the quarter-period of the applied pressure wave is larger, say $T_p/4 = 6 \times 10^4$ sec, with the same amplitude, then we expect that the free surface will oscillate with nearly the same amplitude and phase as the applied bottom pressure wave. This period corresponds to a "low frequency / long wave" type, in terms of soil response. See the ensuing discussion in the next section.

5.2 Forced oscillations:

To study the effect of forced oscillations, a sinusoidal pressure wave of the form $h(t) = h_0 + A\sin(\omega t)$ is imposed at the bottom face of the porous column; where: h_0 is the average pressure head of the wave, chosen to coincide with the initial hydrostatic level (0.5m); "A" is the amplitude of the pressure wave (A = 0.1m, same as the head variation imposed in the sudden recharge/drainage problems); $\omega = 2\pi/T_P$ is the angular frequency; and T_P is the period of the wave. As suggested previously, two different wave periods are chosen, the "short wave" period T_{P1} = 20 000sec, and the "long wave" period T_{P2} = 240 000sec. Figures 4 and 5 show the results of simulations for periods T_{P1} and T_{P2}, respectively. Note that the ratio A/h_o is less than 1, so the oscillatory bottom pressure remains always positive ($\forall t$).

The simulation results confirm our expectations as stated previously. For the "short wave" (T_{P1}), the oscillations of the free surface height Z(t) do not follow the pressure wave applied at the bottom. The amplitude of the free surface is 0.055m, only slightly less than the value 0.06m obtained for the sudden recharge case, This slight discrepancy between the two cases (periodic/sudden) is not unsurprising given the gradual versus abrupt changes imposed at the bottom boundary (compare the two cases at time $t = T_{P1}/4$ = 5000sec).

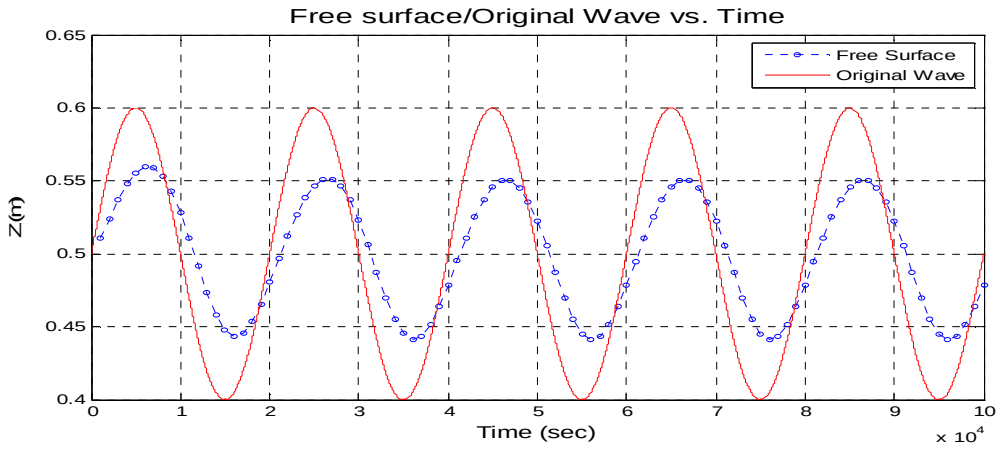

Figure 4: Comparison between free surface position (dotted line) and the applied pressure wave (solid line) versus time for the "short" period, T_{P1} = 20 000 sec ≈ t_{GRAV} / 3 (Loam soil N°3).

On the other hand, for the "long wave" (T_{P2}), the oscillations of the free surface height Z(t) are almost identical with those of the bottom pressure (indistinguishable with respect to the amplitude, but still slightly distinct in terms of phase lag). In total, these results confirm that the two chosen periods, short and long, have very different effects in terms of the response of the unsaturated soil column (free surface height movements Z(t)).

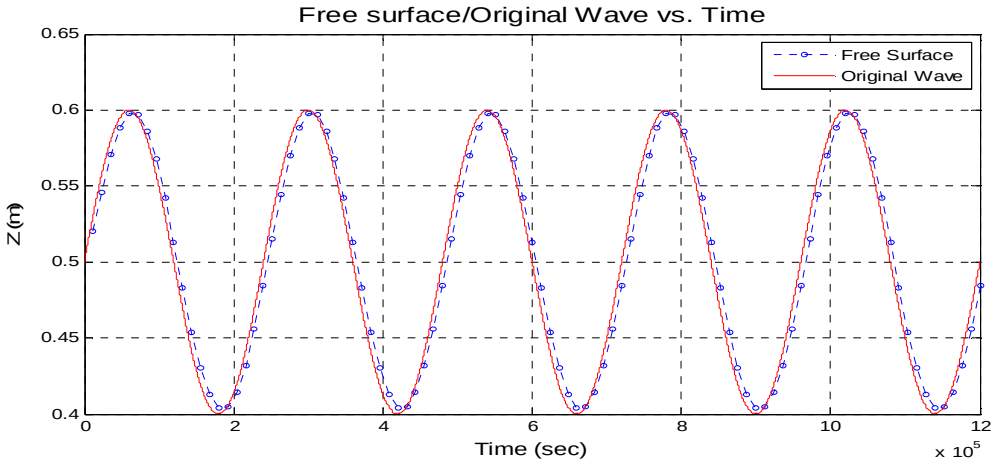

Figure 5: Comparison between free surface position (dotted line) and the applied pressure wave (solid line) versus time for the "short" period, T_{P2} = 240 000 sec ≈ $4t_{GRAV}$ (Loam soil N°3).

The next step is to study the effects of the period (T_P) and the average height (h_0) of the applied bottom pressure wave, on the phase lag (*delay*) between this input wave and the free surface wave Z(t). For this purpose, two sets of numerical simulations were conducted with a range of T_P and h_0 values. **Figure 6** shows the final result of these simulations. First, from figure 6(a), it is clear that the phase lag (*in radians*) between the two waves decreases as the wave period T_P increases. Indeed, this is because; by increasing T_P, more time is given for the free surface to follow the applied wave and therefore, a lower phase difference is obtained. Secondly, from figure 6(b), we can deduce that as the average pressure wave height (h_0) applied at the bottom increases, the phase lag increases also. This may be due to several effects which are currently being analyzed (note that the column has finite height and a zero flux condition is imposed on top).

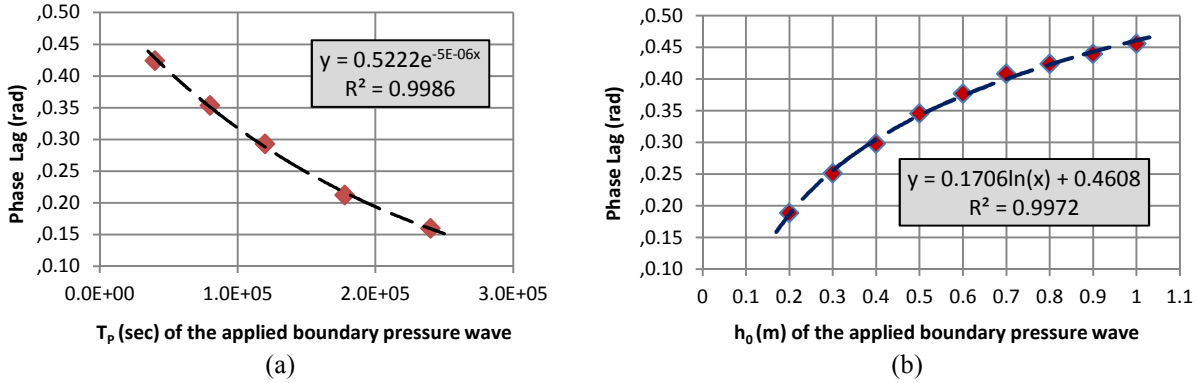

(a) (b)

Figure 6: Phase lag plotted versus (a) pressure wave period T_P, and (b) average pressure wave height h_0. The ordinate is the phase lag between the boundary pressure and the resulting free surface wave (Loam soil N°3).

Further investigations are done to study the effect of the amplitude (of the applied pressure wave at the bottom boundary (*A*)) on the free surface evolution. Figure 7(a) shows that as the amplitude [*nominalised by* h_0] increases, the phase lag between the two waves decreases. It is also noted from figure 7(b) that as the amplitude of the applied boundary pressure wave approaching the average wave height, the resulting free surface is no longer symmetric; this is because the effect of the bottom boundary condition becomes dominant.

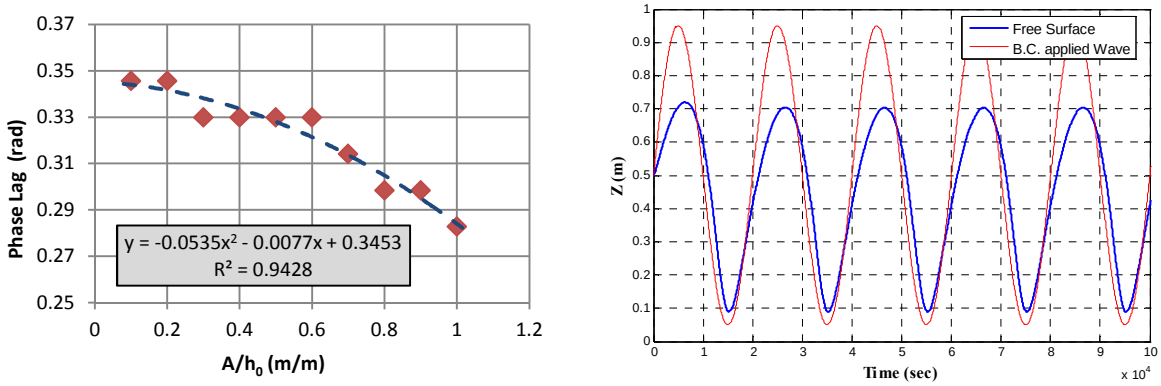

(a) (b)

Figure 7: (a) The effect of the amplitude A on the phase lag between the applied boundary pressure wave and the resulting free surface wave. (b) The evolution of the resulting free surface compared to that of the pressure wave applied at the bottom boundary for $A/h_0 = 0.9$ (Loam soil N°3).

6 "EULERIAN" PRESSURE ANALYSIS (POINT TO POINT ANALYSIS):

In this part, instead of analysing the free surface evolution (as in the previous section), we are interested in interpreting the results focusing on pressure evolution h(z,t) at a specific level "z" as a result of an applied pressure wave h(0,t) at the bottom boundary. In what follows, we present the results for a new fine sand ($K_{SAT}=1.5\times10^{-4}$, $\theta_{SAT} = 0.38$, VGM parameters: $\alpha = 4.6\ m^{-1}$, $n = 5$).

Figure 8 shows the pressure evolution at four different points along the column [(a) h(0,t), (b) h(0.5,t), (c) h(0.7,t) and (d) h(0.85,t)] as a result of an oscillatory pressure boundary condition [$h(0,t) = 0.5 + 0.1\sin(wt)$]. These figures clearly show the damping effect on the applied pressure wave through the length of column. Moreover, it is observed that the effect of the bottom boundary pressure wave disappears at height $z = 1.1m$ from the bottom of the column (at $z = 1.1m$ ➔ $h = -0.6m$ for all $t \leq t_{MAX\ SIMULATION}$).

Additionally, by analysing the phase lag along the column in the fully saturated zone (from z=0 to z=0.4m) and in the variably saturated zone (between z=0.4 and z=0.6m), we can deduce from figure 9(a) that by moving further away from the bottom boundary, the phase lag increases superlinearly (up to a point). This may be due to several effects combining darcian friction losses and unsaturated capillary zone dynamics. This particular behaviour is not completely elucidated at this time, and requires further investigation.

On the other hand, figure 9(b) shows that as the average height (h_0) of the applied pressure wave increases, the phase lag between this boundary pressure wave and the pressure obtained at a height $z=h_0$ increases also. This result confirms what was previously obtained in Section 5 for the phase lag between the bottom pressure and the resulting free surface height.

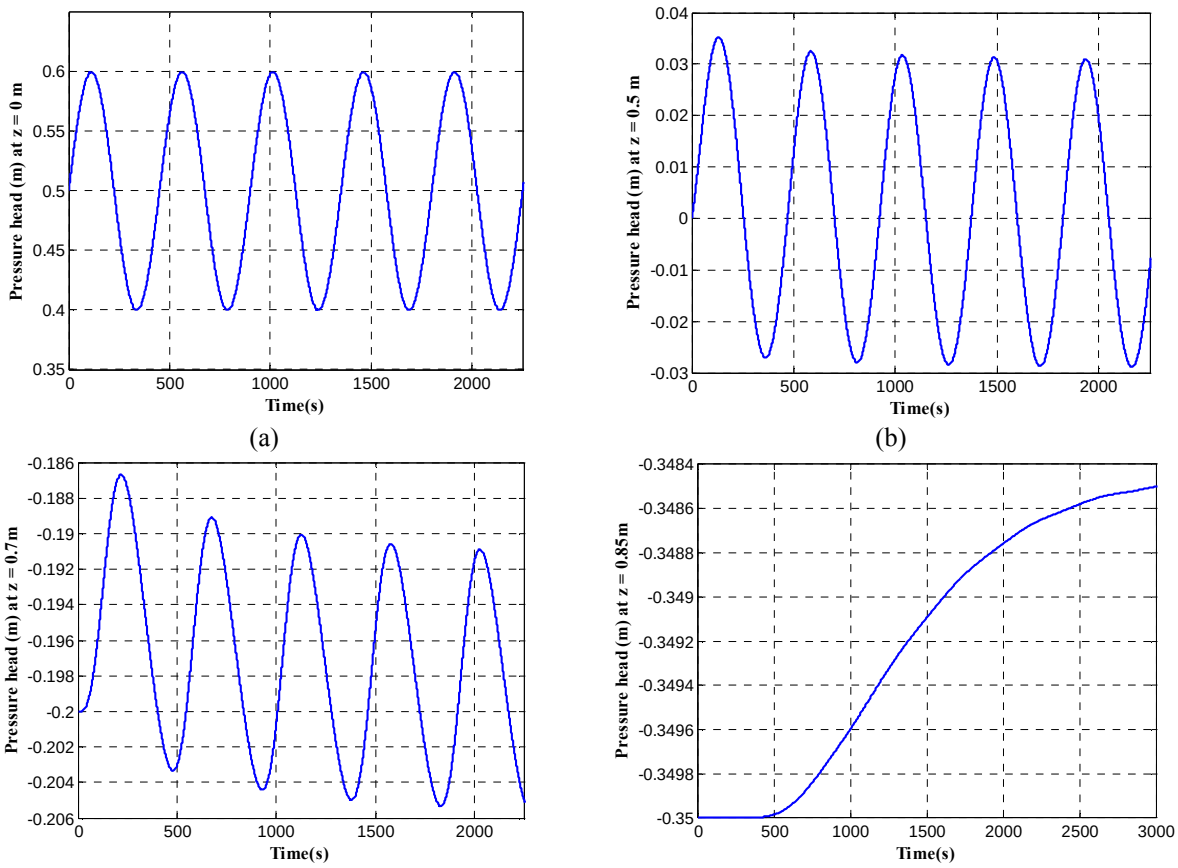

Figure 8: Pressure evolution along the fine sand column at (a) the bottom boundary z =0m, (b) z = 0.5m, (c) z= 0.7m, (d) z = 0.85m. The parameters of the applied bottom boundary pressure wave are: A = 0.1m, h_0 = 0.5m, Tp = 450sec.

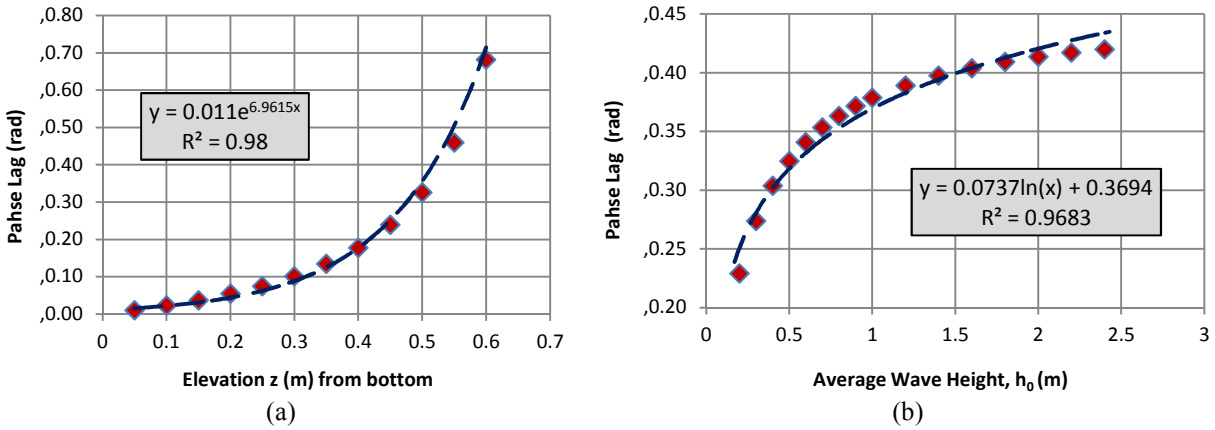

Figure 9: (a) Phase lag evolution along the fine sand column (vertical profile) for wave parameters A = 0.1m, h_0 = 0.5m, Tp = 450sec. (b) Phase lag versus average pressure wave height h_0 for wave parameters A = 0.1m, h_0 = variable, Tp = 450sec (this is the phase lag between boundary pressure and the resulting pressure at height z = h_0).

7 CONCLUSIONS

In this paper, a set of numerical modeling was conducted to study the effect of vertical oscillatory flow in a 1D partially saturated porous column. Through these simulations, two wave types can be distinguished (low frequency waves / high frequency waves) by an appropriate comparison with the characteristic time scale of the soil.

Furthermore, the resulting oscillations of the free surface height Z(t) were analyzed and the simulations illustrate the effect of wave frequency on phase delay. In addition to that, the pressure evolution and the phase lag along the column are also analysed.

The results of these numerical experiments will assist in the design and interpretation of laboratory experiments, including a 1D partially saturated column experiment, as well as a more complex 2D slab experiment.

REFERENCES

[1] Ababou R. and A.C. Bagtzoglou, *BIGFLOW: A numerical code for simulating flow in variably saturated, heterogeneous geologic media (Theory and user's manual, version 1.1)*". Report NUREG/CR-6028, U.S. Nuclear Regulatory Commission, Government Printing Office, Washington D.C., U.S.A., 139 pp., (1993).

[2] Ababou R. and A. Al-Bitar, *Coupled Surface / Subsurface Flow Systems : Numerical Modeling.* Chap. 7 in "Overexploitation & Contamination of Shared Groundwater Resources". NATO-ASI: Adv. Stud. Instit. Series, C.J.G. Darnault (ed.), Springer Science & Business Media BV, pp. 105-117, (2008).

[3] Bailly D., R. Ababou and M. Quintard , *Geometric Characterization, Hydraulic Behavior and Upscaling of Fissured Geologic Media*. Journal of Mathematics and Computers in Simulation, Special Issue MAMERN 2007, 79 3385–3396. Elsevier B.V, (2009).

[4] Ababou R., *Approaches to Large Scale Unsaturated Flow in Heterogeneous, Stratified, and Fractured Geologic Media*. Report NUREG/CR-5743, U.S. Nuclear Regulatory Commission, Government Printing Office, Washington DC, 150 pp., (1991).

[5] Vauclin M., R. Haverkamp and G. Vachaud, *Résolution numérique d'une équation de diffusion non linéaire. Application à l'infiltration de l'eau dans les sols non saturés*. Presses Universitaires de Grenoble, France, (1979).

[6] Espinoza R.D., *Infiltration*, Chap. 6 in "The Handbook of Groundwater Engineering", edited by Jacques Delleur, CRC Press LLC, (1999).

[7] Philip J.R., *The theory of infiltration*. Adv. Hydrosci. 5: 215-305, (1969).

[8] Parlange J.-Y., *On solving the flow equation in unsaturated soils by optimization: Horizontal infiltration*. Soil Sci. Soc. Am. Proc. 39: 415-418, (1975).

[9] Haverkamp R., F. Bouraoui, C. Zammit, and R. Angulo-Jaramillo, *Soil Properties and Moisture Movement in the Unsaturated Zone*, Chap. 5 in "The Handbook of Groundwater Engineering", edited by Jacques Delleur, CRC Press LLC, (1999).

Appendix E

Partially Saturated Oscillatory Flow Under Tidal Conditions in Homogeneous and Layered Soil Columns (Experiment and Simulations).

This appendix is a conference paper presented at "2nd Coastal and Maritime Mediterranean Conference (CM2), Tangier – Morocco, 22-24 November 2011":

Alastal K., Ababou R. and Astruc D. (2011): "Partially saturated oscillatory flow under tidal conditions in homogeneous and layered soil columns (experiment and simulations)". Proceedings of the Second Coastal and Maritime Mediterranean Conference; Tangier, Morocco, 2011. PARALIA editor.

Partially saturated oscillatory flow under tidal conditions in homogeneous and layered soil columns (experiment and simulations)

Khalil ALASTAL [1], Rachid ABABOU [1], Dominique ASTRUC [1]

1. Institut de Mécanique des Fluides de Toulouse (CNRS / Université de Toulouse : INPT – UPS). 1 Allée du Professeur Camille Soula, F-31400 Toulouse, France. E-*ababou@imft.fr; alastal@imft.fr ; astruc@imft.fr*

Abstract:
Surface/subsurface flow interactions concern a wide range of applications, from beach morphodynamics (swash zone), coastal aquifers (seawater intrusion and tidal effects), to harbour engineering and hydrology (e.g., man-made structures such as porous dykes and earth dams). The aim of this paper is to study numerically and experimentally the oscillatory flow in a sandy beach under tidal / low frequency forcing. In this short paper, we only describe the principle of the experiments, and then we focus in more detail on numerical simulations and analyses. For the numerical simulation, we use Richards's equation for variably saturated/unsaturated flow in a 1D porous column, with oscillatory pressure boundary conditions at the bottom of the column. Numerical simulations and analyses are conducted for the following cases: 1) homogeneous column, 2) heterogeneous 2-layer column (currently being extended to other heterogeneities).

Keywords:
Coastal hydrodynamics – Oscillations – Numerical modelling – Richards – Unsaturated flow – Layers - Porous media – Beach - Laboratory experiment – Tide machine.

1. Introduction

We focus on oscillatory flows in partially saturated porous media, such as beaches. Our study in this paper concerns 1D vertical flow under tidal forcing, numerically and experimentally. In this short paper, we only describe the principle of the experiments, and then we focus in more detail on numerical simulations and analyses.

Numerical simulations are conducted using the BIGFLOW 3D finite volume flow code that has been widely described, documented and tested (ABABOU & BAGTZOGLOU, 1993 : http://www.osti.gov/bridge/servlets/purl/10168217-yoTsuT/10168217.pdf). It was used to model oscillatory flows (WANG, 2010). BIGFLOW is based on generalized Darcy and mixed form mass conservation equations. Here, the Van Genuchten / Mualem (VGM) model is used to describe the constitutive relationships [θ(h), K(h)].

After a brief description of the laboratory experiment, the results of the numerical simulations in a partially saturated 1D porous column under “dynamic” conditions are

presented. The tidal effect is simulated by an oscillatory "entry pressure head" imposed at the bottom face of the column. It can be expressed as:

$$h(t) = h_0 + A_0 \sin(\varpi_0 t) \quad (1)$$

where: "h_0" is the positive time-averaged entry pressure head, chosen to coincide with the initial hydrostatic level in the column; "A_0" is the amplitude of the pressure wave; $\varpi_0 = 2\pi/T_0$ is the angular frequency, and T_0 is the period of the imposed entry pressure. Several periods have been tested, both experimentally and numerically. With respect to the heterogeneity of the soil column, the following cases are studied: (1) homogeneous column (experiment and simulations; (2) two layered column (simulations). The latter work is currently being extended to the case of stratified or multi-layer columns.

2. Laboratory experiment on tidal oscillations in a sand column (summary)

A Darcy-scale laboratory experiment (tide machine) has been designed and constructed at the Fluid Mechanics Institute of Toulouse (IMFT). The system generates low frequency waves (tides) on a partially saturated 1D porous column by applying an oscillatory pressure (simple harmonic function) at the bottom boundary of the column.

The setup consists of a sand column, a hydro-mechanical tide generator system or "tide machine"), and measurement sensors including TDR probes and porous cup tensiometers, plus a complete data acquisition system operated under LabView. A schematic sketch of the experimental setup is shown in figure 1a, and a photograph of one of the sand columns is shown in figure 1b.

The manufactured hydro-mechanical system is a flexible one that gives the possibility of controlling and changing the mean level, the amplitude and the period of the applied oscillatory pressure.

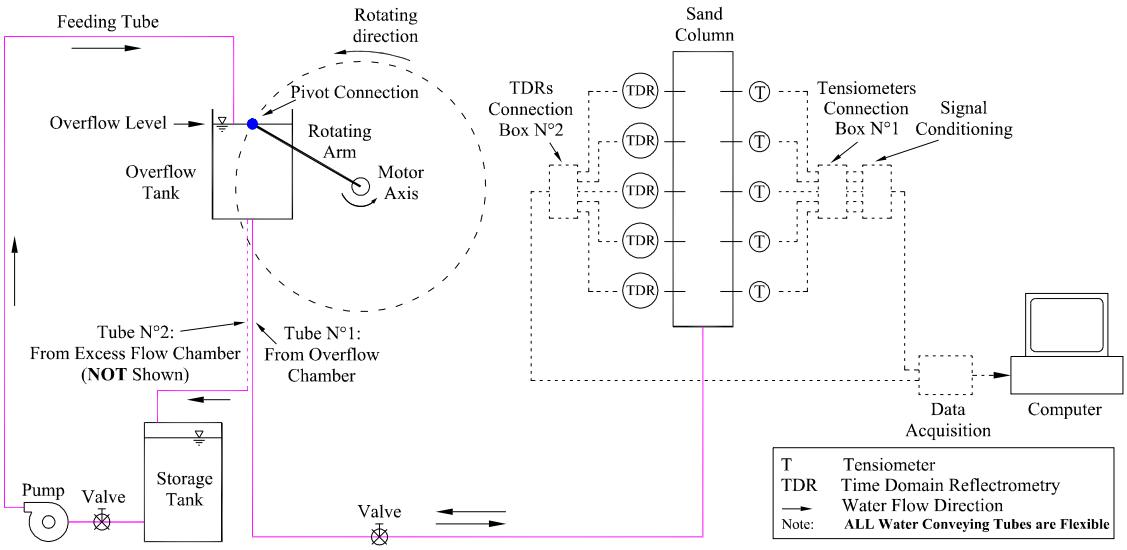

Figure 1a. Schematic diagram of the tide machine, soil column and measurement system.

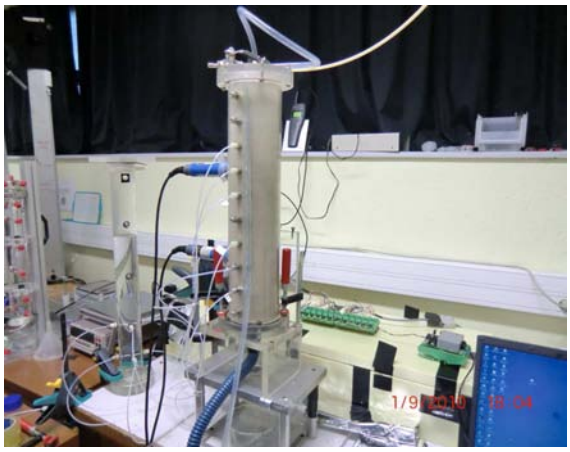

A small sample of the sand used in the column.

Two views of sand column with tensiometers, TDR probe, and (below) the reservoir.

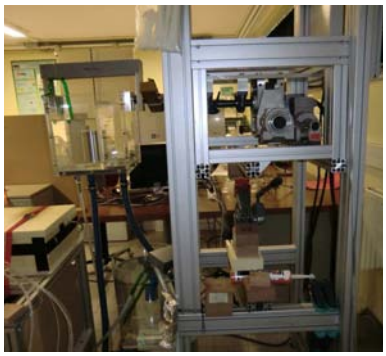

Tide machine : reservoir (left); rotating engine and its supporting structure (right).

Figure 1b. Photographs of the "short column" experiment conducted at the IMFT laboratory (part of a set of tidal flow experiments in sand beaches).

A series of more than 30 experiments on short column (0.55 m height) and long column (1.5 m height) were conducted using this tide machine. For each column, we generate a tidal forcing with different amplitudes A_0, frequencies ϖ_0, and mean water levels h_0.

3. Tidal simulations in a homogeneous sand column

We have conducted a parametric study, involving 11 numerical simulations of cyclic flow in the saturated/unsaturated column, with oscillatory pressure imposed at the bottom of the column (see equation 1). A fine sand (FS) is used to illustrate some results in this section. The characteristics of the fine sand are: $K_{SAT}=1.5\times10^{-4}$ m/s; $\theta_{SAT}=0.38$; and for the unsaturated parameters (VGM model): $\alpha=4.6$ m^{-1}; $n=5$.

Figure 2 shows the time evolution of the total hydraulic head $H(z, t) = h(z,t) + z$, at different elevations "z" along the column, for an amplitude $A_0 = 0.10$m and an average water level $h_0 = 0.50$ m (relative amplitude $A_0/h_0 = 20\%$). We clearly see the effects of attenuation (damping) along the column. Other results for the same sand show a phase shift of the pressure signal that increases nonlinearly with "z" (ALASTAL *et. Al.*, 2010).

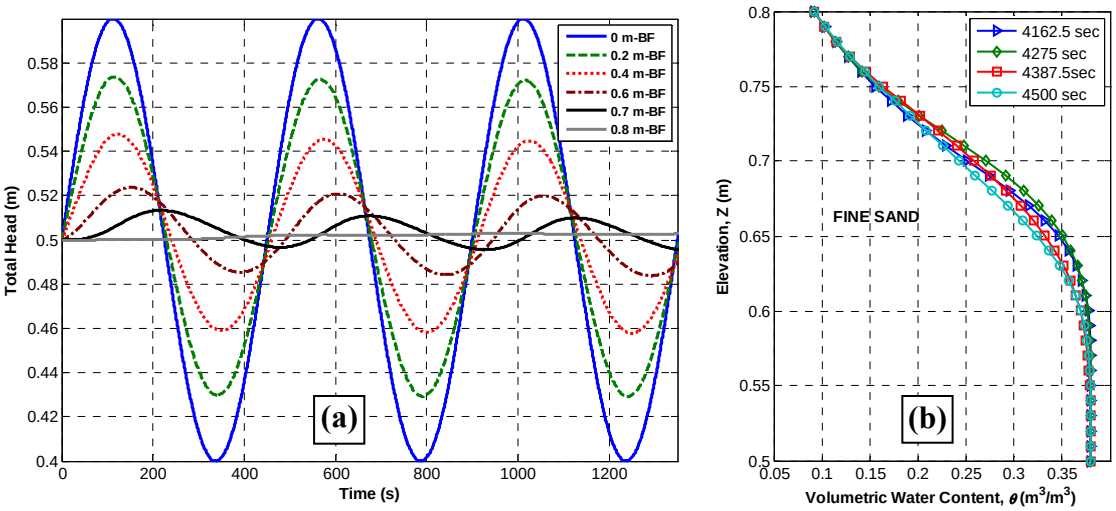

Figure 2. ***(a)*** *Evolution of the total head H(t) at 6 positions along the fine sand column.* ***(b)*** *Water Content profiles θ(z) at 4 different times separated by $T_0/4$. Parameters of the input pressure signal: A_0 =0.1m, h_0 =0.5m, T_0 =450s.*

Figure 3 shows the effect of input parameters (A_0, T_0, h_0) on the amplitude attenuation along the column. We see in Figure 3 that the amplitude A(z) of pressure h(z,t) decreases linearly with elevation "z" in the saturated part of the column. This can be partially explained by the linearity of Darcy's head loss law in the saturated zone. In addition, the attenuation rate (the gradient dA/dz) increases non-linearly with the mean static level h_0. Other observations: (1) dA/dz increases with A_0 (Figure 3a), (2) dA/dz decreases with T_0 (Figure 3b), and (3) dA/dz increases with h_0 (Figure 3c,d).

4. Tidal simulations in a heterogeneous sand column: two-layer case

We consider now a two-layer column. The bottom layer is a medium sand with $K_{SAT}=2.0\times10^{-4}$ m/s, θ_{SAT}= 0.35, et $\alpha=11.47\text{m}^{-1}$, n =1.98. The top layer is a loam (Guelph loam) with $K_{SAT}=3.66\times10^{-6}$ m/s, θ_{SAT}=0.4, et $\alpha=1.15\ \text{m}^{-1}$, n=2.03. The interface between the two layers is located at elevation z = 57.5 cm.

The input oscillatory pressure is: $h(0,t)=0.50+0.25\times\sin(\varpi_0 t)$ at z=0, so the relative amplitude is quite large here (A_0/h_0 = 50%).

Figure 4(a) shows the evolution of the total load H(t) at different elevations along the two-layer column: z = 0 (input signal), z = 30cm (always saturated), z = 57cm and 58 cm (interface), z = 70 cm (always unsaturated). The elevation of the free surface Zs(t) is also plotted: we noted that the column is always saturated from z = 0 to 35 cm, and always unsaturated for z ≥ 65cm. The signals H(t) are not harmonic, even in the permanently saturated zone (z = 30cm). In addition, we remark that H(t) increases sharply at certain times, which correspond to the crossing of the sand/loam interface by the ascending free surface (this occurs once per cycle).

Figure 4(b) shows the evolution of water contents on both sides of the interface around z = 57.5cm. Periods of saturation are marked in bold. It is noted that the water content varies much greater in the Medium Sand than in the Guelph loam at the interface. The latter is almost still saturated unlike the sand which drains more easily.
Figure 4(c) shows the water contents profiles θ(z) for 8 different times separated by $T_0/8$. Clearly, water content oscillations are greater in the sand than in the loam layer.

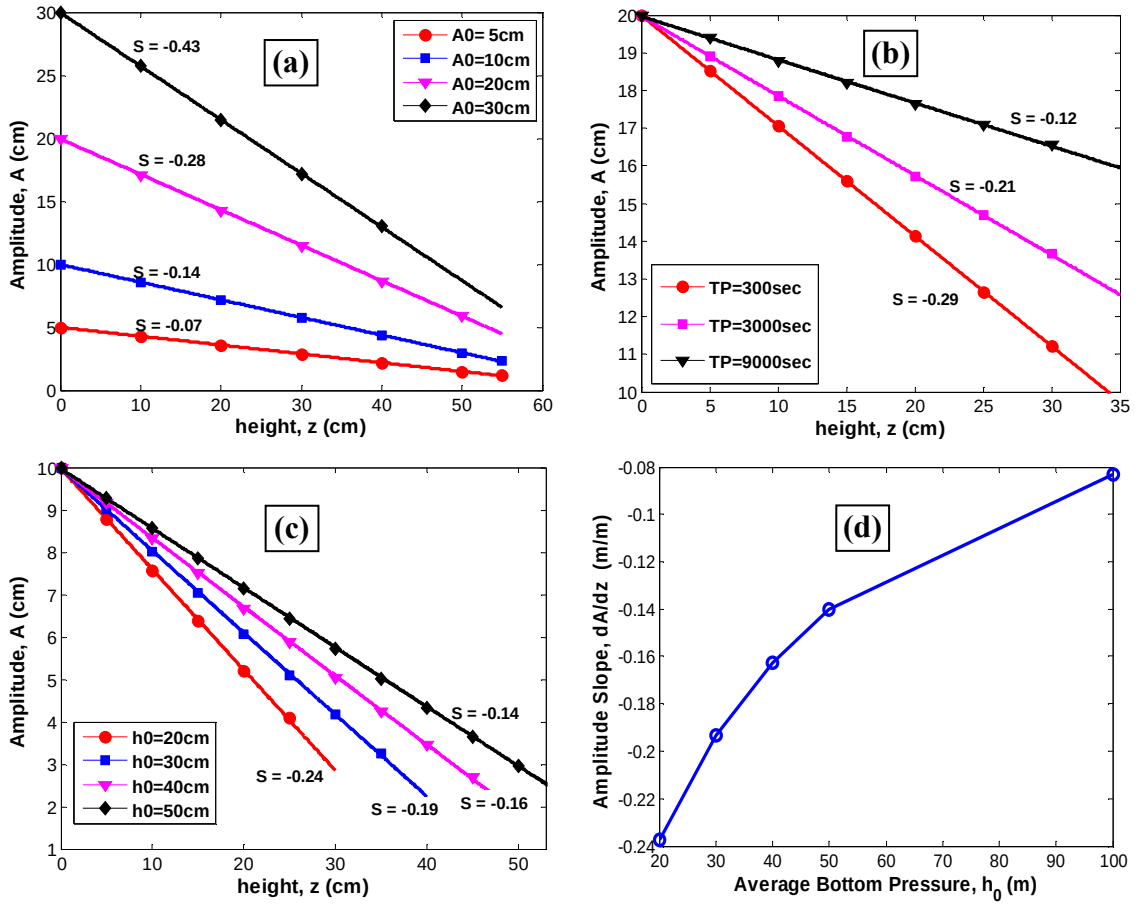

Figure 3. Parametric study of the attenuation of pressure amplitude A(z) with height "z" along the column (in the saturated zone only): ***(a)*** *effect of the amplitude A_0 of the entry pressure (h_0 = 50cm , T_0 = 450s);* ***(b)*** *effect of the period T_0 (h_0 = 50cm);* ***(c)*** *effect of the mean static level h_0 (T_0 = 450s, A_0 = 10cm);* ***(d)*** *decay rate dA/dz plotted versus h_0.*

5. Conclusions

A series of physical and numerical experiments was conducted on a 1D porous column to study partially saturated oscillatory flow under tidal conditions. Results show the damping and phase shift of the pressure signals along the column. A parametric study quantified the effects of entry pressure parameters on the amplitude damping. Other

numerical simulations in a 2-layer column show distinct dynamic behavior in terms of water content for each layer. Other types of heterogeneities are currently under study.

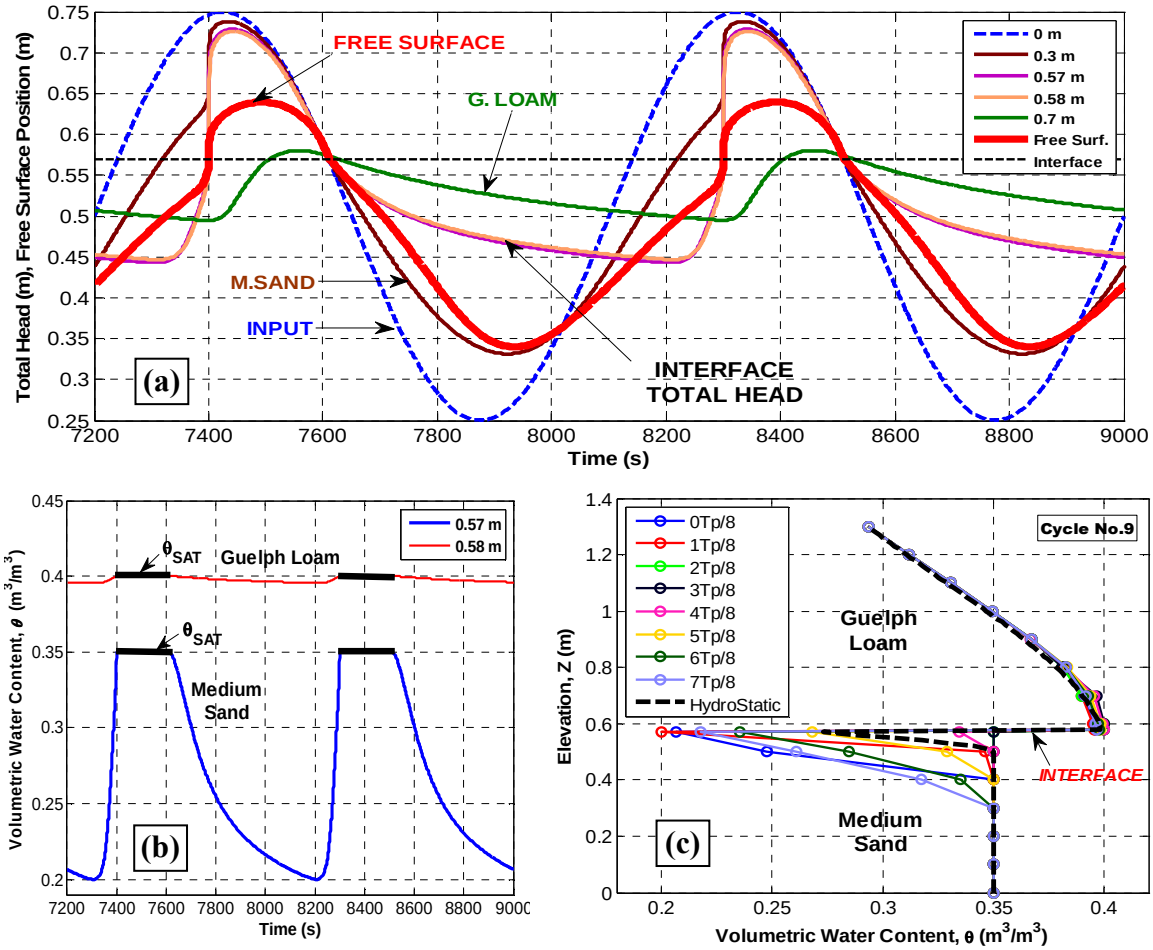

***Figure 4**. Evolutions in the two-layer column over two cycles. **(a)** Total head H(t) at different elevations along the column (input signal in dotted curve, and elevation of the free surface Zs(t) in thick line). **(b)** Time evolution θ(t) of volumetric water content of Medium Sand and Guelph Loam on each side of the interface (z=0.57m and 0.58m). **(c)** Water Content profiles θ(z) for 8 different times separated by $T_0/8$. Parameters of the input signal at the bottom of the column: A_0 = 0.25m, h_0 = 0.5m, T_0 = 900s.*

5. References

ALASTAL K., ABABOU R., ASTRUC D. (2010). *Partially saturated oscillatory flow in a sandy beach (numerical modeling)*. XVIII Internat. Conf. Water Resources, CMWR 2010. J. Carrera (Ed). Barcelona.

WANG Y. (2010). *Experimental and Numerical Study of Hydrodynamic Oscillations in Partially Saturated Porous Media.* Doctoral thesis. Université de Toulouse / Institut National Polytechnique. Toulouse, France, 16 Sept. 2010, 347 p.